Title

Investigation of Coupled Processes and Impact of High Temperature Limits in Argillite Rock

Authors

Zheng, Liange
Rutqvist, Jonny
Steefel, Carl
et al.

Publication Date

2014-08-18

Investigation of Coupled Processes and Impact of High Temperature Limits in Argillite Rock

Fuel Cycle Research & Development

Prepared for

U.S. Department of Energy
Used Fuel Disposition Campaign

Liange Zheng
Jonny Rutqvist
Carl Steefel
Kunhwi Kim
Fei Chen
Victor Vilarrasa
Seiji Nakagawa
James Houseworth
Jens Birkholzer
Lawrence Berkeley National Laboratory

August, 2014

FCRD-UFD-2014-000493

Revision 2
12/20/2012

APPENDIX E

FCT DOCUMENT COVER SHEET [1]

Name/Title of Deliverable/Milestone/Revision No.	Investigation of Coupled Processes and Impact of High Temperature Limits in Argillite Rock
Work Package Title and Number	Argillite Disposal R&D International – LBNL FT-14LB080606
Work Package WBS Number	1.02.08.06
Responsible Work Package Manager	James E. Houseworth (signature on file) (Name/Signature)

Date Submitted 08/15/2014

Quality Rigor Level for Deliverable/Milestone[2]	☐ QRL-3	☐ QRL-2	☐ QRL-1 ☐ Nuclear Data	☒ Lab/Participant QA Program (no additional FCT QA requirements)

This deliverable was prepared in accordance with Lawrence Berkeley National Laboratory
(Participant/National Laboratory Name)

QA program which meets the requirements of
☒ DOE Order 414.1 ☐ NQA-1-2000 ☐ Other

This Deliverable was subjected to:

☐ Technical Review ☐ Peer Review

Technical Review (TR)	**Peer Review (PR)**
Review Documentation Provided	**Review Documentation Provided**
☐ Signed TR Report or,	☐ Signed PR Report or,
☐ Signed TR Concurrence Sheet or,	☐ Signed PR Concurrence Sheet or,
☐ Signature of TR Reviewer(s) below	☐ Signature of PR Reviewer(s) below

Name and Signature of Reviewers

NOTE 1: *Appendix E should be filled out and submitted with the deliverable. Or, if the PICS:NE system permits, completely enter all applicable information in the PICS:NE Deliverable Form. The requirement is to ensure that all applicable information is entered either in the PICS:NE system or by using the FCT Document Cover Sheet.*

NOTE 2: *In some cases there may be a milestone where an item is being fabricated, maintenance is being performed on a facility, or a document is being issued through a formal document control process where it specifically calls out a formal review of the document. In these cases, documentation (e.g., inspection report, maintenance request, work planning package documentation or the documented review of the issued document through the document control process) of the completion of the activity along with the Document Cover Sheet is sufficient to demonstrate achieving the milestone. If QRL 1, 2, or 3 is not assigned, then the Lab/Participant QA Program (no additional FCT QA requirements box must be checked, and the work is understood to be performed, and any deliverable developed, in conformance with the respective National Laboratory/Participant, DOE- or NNSA-approved QA Program.*

This page is intentionally blank.

CONTENTS

FIGURES

TABLES

ACRONYMS

BBM	Barcelona Basic Model
BExM	Barcelona Expansive Model
DECOVALEX	Development of Coupled Models and their Validation against Experiments
DFN	Discrete Fracture Network
DOE	Department of Energy
DRZ	Disturbed Rock Zone
EBS	Engineered Barrier System
EDL	Electrical Double Layer
EDZ	Excavation Damaged Zone
ENRESA	Empresa Nacional de Residuos Radioactivos SA
EPCA	Elasto-Plastic Cellular Automata
FEBEX	Full-scale Engineered Barrier Experiment
FEPs	Features, Events and Processes
JAEA	Japan Atomic Energy Agency
JNC	Japan Nuclear Cycle Development Institute
LBNL	Lawrence Berkeley National Laboratory
LC	Load Collapse
MCC	Modified Cam Clay
NAGRA	Nationale Genossenschaft für die Lagerung radioaktiver Abfälle
NBS	Natural Barrier System
NS	Natural System
PB	Poisson-Boltzmann
PNP	Poisson-Nernst-Planck
PWR	Pressurized Water Reactor
RBSN	Rigid-Body-Spring Network
RH	Relative Humidity
T	Temperature
TCDP-A	Taiwan Chelungpu Fault Drilling Project
THM	Thermal-Hydrological-Mechanical
THMC	Thermo-Hydro-Mechanical-Chemical
TPHM	Two-Part Hooke’s Model
UFD	Used Fuel Disposition
UFDC	Used Fuel Disposition Campaign
UPC	University of Catalonia
URL	Underground Research Laboratories
XRD	X-Ray Diffraction

1. Introduction

Shale and clay-rich geological formations have been considered as potential host rock for geological disposal of high-level radioactive waste throughout the world, because of their low permeability, low diffusion coefficient, high retention capacity for radionuclides, and capability to self-seal fractures. Permeabilities arising from the primary porosity of these rock types are low because of the extremely fine-grained constituents and the very small pores associated with the fine-grained material. Permeability values are typically less than 10 microdarcies (10^{-17} m^2 or about 10^{-10} m/s equivalent hydraulic conductivity) and are often two to four orders of magnitude lower. While fractures can occur, clay and shale often demonstrate the tendency to self-seal fractures, which reduces the effects of fractures on bulk permeability. This occurs as a result of swelling from the increased water potential in fractures, the generation of fracture infilling materials and mineral precipitation, and plastic deformation of the rock (Mazurek et al., 2003). The low permeability of clay and shale rock are well-known in the hydrogeology community where these rock types represent aquitards that severely limit groundwater movement, and in petroleum geology, where they act as caprocks limiting the rise of buoyant petroleum fluids. Other favorable characteristics of clay/shale rock are the strong sorptive behavior for many radionuclides and (in saturated systems) the low flow rates, which typically lead to reducing conditions because of the lack of oxygen transport from the surface. Clay and shale rock also act to chemically buffer the effects of materials introduced through repository construction, operation, and emplaced materials (Arcos et al., 2008).

A large body of information concerning the behavior of clay/shale geologic environments using bentonite backfill/buffers for nuclear waste disposal has been developed through the repository programs with underground research laboratories in Switzerland, France, Belgium, and Japan. At Switzerland's Mont Terri underground rock laboratory, experiments are being carried out to investigate the geological, hydrogeological, geochemical and rock mechanical properties of the Opalinus Clay formation, an indurated clay (also referred to as shale) (Meier et al., 2000). Experimentation is ongoing in a variety of areas including hydrogeology, geomechanics, geochemistry, characterization of the excavation damaged zone (EDZ), heater testing, radionuclide diffusion and retention, cement-clay interactions, and self-sealing behavior. The Callovo-Oxfordian clay formation, an indurated clay at Bure in France, is used for research emphasizing reversible geologic disposal of high-level and long-term intermediate level radioactive waste (Fouche et al., 2004). The program is investigating the role of faults or fractures in hydrogeologic behavior, geochemical properties of water and gas and interpretations of system connectivity, geochemical properties affecting radionuclide mobility, and feasibility of excavation. The program is also addressing complex issues concerning bentonite backfill and material interactions with cement and metallic components. The Toracian clay at Tournemire, France, is an indurated clay that is used for scientific evaluation of argillaceous formations for nuclear waste disposal but is not a candidate disposal site (Patriarche et al., 2004). Investigations include the effects of hydro-geochemical properties, rheological properties, excavation effects, the role of fractures in argillaceous formations, and interactions with concrete. The underground laboratory at Mol in Belgium conducts experiments to investigate the geological, hydrogeological, geochemical, and rock mechanical properties of the Boom Clay formation (Barnichon and Volckaert, 2003). This is a softer clay than the Opalinus, Callovo-Oxfordian, or Toracian clays, and its geomechanical behavior is described as "plastic." Experiments include studies of the damage zone around drifts, thermal impact of the waste, radionuclide migration, and backfill characterization. The Koetoi and Wakkanai Formations at Horonobe, Japan, have been recently developed as a URL (Hama et al., 2007). The argillaceous rock at this location consists of mechanically soft to indurated, highly porous diatomaceous mudstone.

In addition to the favorable characteristics of and international interest in argillaceous rocks for nuclear waste disposal, another reason for considering this rock type for the U.S. nuclear waste disposal program is the abundance of clay/shale geologic resources in the United States. Recent work on the UFD

Campaign has updated shale resource estimates and identified extensive regions within sedimentary basins where shale formations are present, as shown in Figure 1.1.

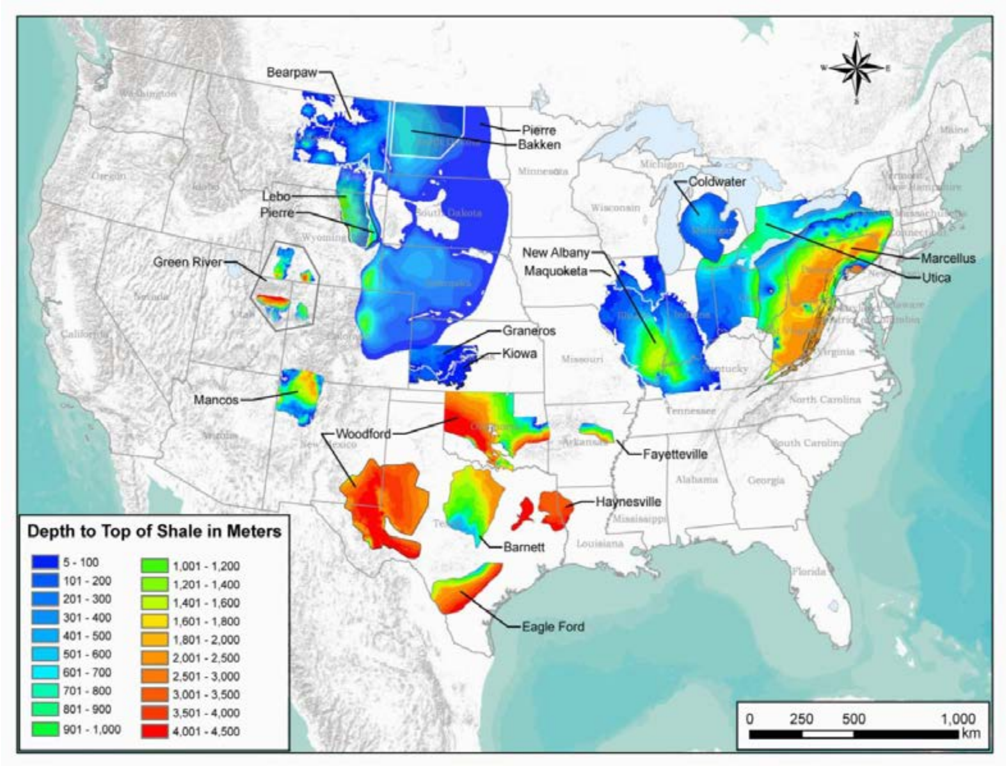

Figure 1.1. Summary of GIS data for depth to top of shale formations within major sedimentary basins in the US currently incorporated in the LANL GIS database. Figure produced by LANL from shale data populated into the GIS database. (Perry et al., 2014).

The focus of research within the UFD Campaign is on repository-induced interactions that may affect the key safety characteristics of an argillaceous rock. A nuclear-waste-repository excavation causes changes in mechanical stress and water saturation, and introduces air into the underground environment. These changes have been observed in URLs discussed above and have been found to lead to fracture formation around the drift in a region called the excavation damaged zone (EDZ). The formation of fractures and increased permeability of the EDZ needs to be evaluated for its potential effects on repository performance. The behavior of the EDZ has also been observed to change rapidly over time in response to changes in mechanical and hydrological conditions, including fracture self-sealing. Therefore, the formation and evolution of fractures in an argillaceous rock is a dynamic process.

Maximum allowable temperature is one of the most important design variables for a geological repository, because it determines waste-package spacing, distance between disposal galleries, and therefore the overall size (and cost) of the repository for a given amount of waste. This is especially important for a clay repository, because clay rock has relatively low thermal conductivity. However, data and knowledge gaps exist in establishing a scientific basis for determining this temperature for a clay repository.

Within the Natural Barrier System (NBS) group of the Used Fuel Disposition (UFD) Campaign at the Department of Energy's (DOE) Office of Nuclear Energy, LBNL's research activities have focused on understanding and modeling EDZ evolution and the associated coupled processes, and impacts of high temperature on parameters and processes relevant to performance of a clay repository to establish the technical base for the maximum allowable temperature. This report documents results from some of these activities. These activities address key Features, Events and Processes (FEPs), which have been ranked in importance from medium to high, as listed in Table 7 of the *Used Fuel Disposition Campaign Disposal Research and Development Roadmap* (FCR&D-USED-2011-000065 REV0) (Nutt, 2011). Specifically, they address FEP 2.2.01, Excavation Disturbed Zone, for clay/shale, by investigating how coupled processes affect EDZ evolution; FEP 2.2.05, Flow and Transport Pathways; and FEP 2.2.08, Hydrologic Processes, and FEP 2.2.07, Mechanical Processes and FEP 2.2.09, Chemical Process—Transport, by studying near-field coupled THMC processes in clay/shale repositories. The activities documented in this report also address a number of research topics identified in *Research & Development (R&D) Plan for Used Fuel Disposition Campaign (UFDC) Natural System Evaluation and Tool Development* (Wang, 2011), including Topics S3, Disposal system modeling – Natural system; P1, Development of discrete fracture network (DFN) model; P14, Technical basis for thermal loading limits; and P15 Modeling of disturbed rock zone (DRZ) evolution (clay repository).

This report documents progress made in LBNL’s FY14 research activities, including development and validation of rock stress-porosity and stress-permeability relationships based on the two-part Hooke’s model, a new constitutive relationship for coupled hydromechanical processes (Chapter 2), development of capabilities to treat anisotropic properties in a discrete-fracture network, a fracture-damage model for investigating coupled processes in the EDZ (Chapter 3), modeling of THM processes for the HE-E and FE heater tests at Mont Terri, Switzerland (Chapter 4), the effects of strongly elevated temperature on the bentonite backfill and near-field clay host rock (Chapter 5), and modeling of reactive diffusive transport with application to the DR-A test at Mont Terri, Switzerland (Chapter 6). A summary and discussion of future work activities are given in Chapter 7.

2. Relationships among Permeability, Porosity and Effective Stress for Low-Permeability Sedimentary Rock Based on the Two-Part Hooke’s Model

2.1 Introduction

One of the major concerns in post-closure safety evaluations of the repository system is the potential for hydromechanical perturbations caused by excavation, which is of particular importance for argillite repository. These perturbations are found within the excavation damaged zone (EDZ) around the repository drifts and access shaft. The EDZ is primarily caused by redistribution of *in situ* stresses and rearrangement of rock structures (Tsang et al., 2012). Field investigations conducted at underground laboratories such as at Mont Terri (Switzerland) and Bure (France) have shown that the permeability of the EDZ can be one or more orders of magnitude higher than the unaltered argillaceous rock. For these conditions, the EDZ could then act as a preferential flow path for advective transport and thereby speed up radionuclide migration toward the biosphere. The EDZ properties and their evolution over time have been analyzed in laboratory and field studies (Bossart et al., 2004; Baechler et al., 2011; Armand et al., 2013). These investigations suggest that a partial or complete self-sealing of fractures due to clay swelling and creep within the EDZ is possible after a certain amount of time. The self-sealing process can potentially decrease the EDZ permeability over time, which may eventually return to the values of the unaltered rock. Stress change during excavation is the mainly driving force for the changes in permeability in EDZ, and stress recovery is also one of the major causes for the self-healing, with the other one being chemical changes such as mineral precipitation. An accurate mathematical representation of the permeability-stress relationship is therefore critical for understanding the evolution of permeability and predicting the permeability changes during excavation and self-healing stages.

The changes in permeability with stress in EDZ is a phenomenon (so called “stress-dependence of permeability”) that is also widely observed for other low-permeability sedimentary rock and in other engineering applications, such as fossil-fuel exploitation (McLatchie et al., 1958; Vairogs et al., 1971; Jones and Owens, 1980; Walls et al., 1982; McKee et al., 1988; Brighenti, 1989; Spencer, 1989; Lei et al., 2008; Li et al., 2008), CO_2 geological sequestration (Rutqvist and Tsang, 2002; Cui et al., 2007), coal-mining safety (Somerton et al., 1975; Jasinge et al., 2011; Konecny and Kozusnikova, 2011), modeling fluid percolation and pore-pressure evolution in the crust (David et al., 1994; Wibberley and Shimamoto, 2005; Ghabezloo et al., 2009a; Dong et al., 2010). The low-permeability sedimentary rock typically refers to those with permeability less than 0.1 mD under reservoir conditions (Byrnes, 1996; Shanley et al., 2004; Holditch, 2006). Nowadays, hydraulic fracturing is widely used to extract oil and natural gas from tight sandstone and shale gas reservoirs, which usually show highly stress-sensitive mechanical and/or hydraulic properties. Knowledge of the dependence of such properties on stress is critical for productivity estimation and recovery-method design (Jones and Owens, 1980; Walls et al., 1982). The stress-dependence of porosity and permeability in argillite, especially in EDZ, as mentioned above, is of great importance for the performance assessment of the disposal site (Tsang et al., 2005), which motivate the study of an accurate mathematical representation of the permeability-stress, porosity-stress relationship as presented in this report.

The permeability and porosity change with effective stress are quite different for low-permeability rock. With an increase in effective stress, low-permeability rock undergoes fairly small porosity changes, typically less than 10% (Thomas and Ward, 1972; Jones and Owens, 1980; Byrnes, 1996; 1997; Byrnes and Castle, 2000). Some empirical relationships have been established between porosity and effective stress based on laboratory-measured data (Athy, 1930; Hoholick et al., 1984; Shi and Wang, 1986; Davies and Davies, 2001; Rutqvist et al., 2002). In contrast, significant permeability changes have been observed with relatively small increases in effective stress. For example, with the effective stress increases from zero to around 15 MPa (McLatchie et al., 1958; Thomas and Ward, 1972; Jones and Owens, 1980; Kilmer et al., 1987; David et al., 1994; Ghabezloo et al., 2009a; Dong et al., 2010; Metwally and Sondergeld, 2011), the permeability of this type of rock decreases more than one order of magnitude. Such a phenomenon is usually referred to as stress-sensitive rock permeability at low effective stress levels. Furthermore, as pointed out by McLatchie et al. (1958) and Vairogs et al. (1971), for tight sandstone, the lower the reference permeability (routinely tested permeability), the greater the permeability reduction under increasing effective stress. Some empirical relationships were established between permeability and effective stress based on laboratory-measured data. Representative relationships include exponential law (David et al., 1994; Evans et al., 1997; Mohiuddin et al., 2000; Jones, 2013) and power law (Shi and Wang, 1986; Lei et al., 2008; Ghabezloo et al., 2009a; Dong et al., 2010). However, the exponential law yields poor fitting in low effective-stress ranges, and the power law gives unreasonable predictions for certain effective-stress values. To describe the relationship between the significant permeability drop and the insignificant porosity reduction under effective stress has been a great challenge for scientists over a long period of time. Up to now, empirical relationships, usually in the form of a power law, were established based on laboratory-measured data to relate permeability and porosity. For example, Dong et al. (2010) systematically measured the porosity and permeability change with increasing effective stress. The relationship between permeability and porosity was represented by a power law, i.e. $k/k_0 = (\phi/\phi_0)^m$, where ϕ and ϕ_0 are the porosity under the current stress state and ambient conditions, respectively; k and k_0 are the permeability under the current stress state and ambient conditions, respectively; m is a material constant named porosity sensitivity exponent of permeability. The underlying assumption in relating permeability changes to the total porosity change is that the reduction of the total volume of pore space is the only driver for the permeability change—an assumption that leads to some problems with these relationships, one of which is the abnormally high m. If the flow path is largely controlled by slot-like micro-crack networks (as has been postulated by many researchers (Somerton et al., 1975; Jones and Owens, 1980; David and Darot 1989; David et al., 1994; Byrnes 1997; Evans et al., 1997; Byrnes and Castle 2000; Lei et al., 2008; Dong et al., 2010; Soeder and Randolph, 2013), the permeability change with the crack aperture reduction (reflected by porosity reduction) should obey the "cubic law"

(Witherspoon et al., 1980; Zimmerman and Bodvarsson, 1996) which implies that m should be around 3. However, the calculated values of m based on the experimental data for low-permeability samples were much higher than 3, with values up to 70 (David et al., 1994; Dong et al., 2010). The extremely high exponent in the current power law for the relationship between permeability and porosity suggests that relating permeability changes to the total porosity changes is not a valid assumption. In this report we therefore attempt to establish relationships that are more physically robust for low permeability rock.

This study is based on the concept of the two-part Hooke's model (TPHM). Natural rock, which contains different mineral compositions, pores, micro-cracks and fractures, are inherently heterogeneous and will experience non-uniform deformation under uniform stress. Based on this consideration, Liu et al. (2009; 2011) conceptually divided the rock body into "soft" and "hard" parts. As they pointed out, the natural strain (volume change divided by rock volume at the current stress state), rather than the engineering strain (volume change divided by the unstressed rock volume), should be employed in Hooke's law for accurately modeling the elastic deformation, unless the two strains are essentially identical (as they might be for small mechanical deformations in the "hard" part). Based on this concept, a series of constitutive relations between stress and a variety of hydromechanical rock properties can be derived, e.g., stress-dependent rock bulk compressibility, pore compressibility, rock porosity and fracture aperture (Liu et al., 2009; Zhao and Liu, 2012; Liu et al., 2013a). These theoretically derived relationships could represent the experimental data in literature very well. However, the TPHM based stress-dependent permeability relationship is not covered in the scientific literature. In this report, we will derive the stress-dependence of permeability based on the concept of TPHM. The derived relationships explain well the permeability stress-sensitive phenomena in the low effective-stress ranges. As demonstrated later in the report the soft part, while only a small portion of the low-permeability rock, plays a critical role in the stress-dependence of permeability.

In the next section (Section 2.2), the empirical relationships between porosity and stress and permeability and stress are reviewed and discussed. In Section 2.3, the theoretical development of the TPHM is provided for the sake of completeness. In Section 2.4, we derive the stress-dependence relationship for porosity and permeability based on the TPHM. In Section 2.5, the proposed relationships are used to match the experimental measured data.

2.2 Existing relationships for stress-dependent rock properties

The stress-dependent rock mechanical and/or hydraulic properties have been extensively studied, due to their importance in engineering applications (Walsh and Brace, 1984; McKee et al., 1988; Dewhurst et al., 1998; Louis et al., 2005; Sadhukhan et al., 2012; Wu and Dong, 2012). In this section, we discuss the existing empirical relationships for describing the stress-dependence of rock porosity and permeability. Also presented is the relationship between permeability and porosity as permeability changes occur via porosity changes with effective stress. Note that the effective stress refers to the confining pressure minus the pore pressure.

2.2.1 Relationship between porosity and effective stress

The influence of effective stress on porosity for low permeability rock is small, usually with less than 10 percent change of the total porosity (Byrnes, 1997; Byrnes and Castle, 2000). The relationship between porosity and effective stress, albeit in a slightly different form, can be described by exponential function, as shown in the following equations.

After studying the porosity of relatively pure shale samples from various depths, Athy (1930) presented the compaction induced porosity-depth relationship using an exponential equation:

$$\phi = \phi_0 \exp{(-bx)} \tag{2.1}$$

where ϕ is porosity at depth x, ϕ_0 is the porosity of surface sample, and b is a constant. This relationship could also be applied to sandstones (Hoholick et al., 1984). Because the equivalent effective stress can be deduced from burial depth, Shi and Wang (1986) reformat Equation (2.1) to relate the porosity to effective stress:

$$\phi = \phi_0 \exp(-\beta\sigma) \tag{2.2}$$

where σ is effective stress, and β is a material constant.

Based on laboratory experiments on sandstone by Davies and Davies (2001), Rutqvist et al. (2002) proposed a modified empirical stress-porosity expression that added an additional parameter called "residual porosity":

$$\phi = \phi_r + (\phi_0 - \phi_r)\exp(-\beta\sigma) \tag{2.3}$$

where ϕ_r is the residual porosity at high effective stress. With the presence of residual porosity, Equation (2.3) can better characterize the relatively large degree of stress dependency on porosity in the lower effective-stress ranges.

2.2.2 Relationship between permeability and effective stress

It has been well-recognized that the effective stress has a huge influence on rock permeability. Many empirical relationships have been put forward to describe permeability changes with effective stress. In general, these relationships can be divided into exponential law and power law.

2.2.2.1 Empirical exponential law for stress-dependency of permeability

Generally, the exponential law for describing stress-dependent permeability takes the form of (David et al., 1994):

$$\mathrm{k} = \mathrm{k}_0 \exp[-\gamma(\sigma - \sigma_0)] \tag{2.4}$$

where k is the permeability at the effective stress σ, k_0 is the permeability at ambient stress σ_0, and γ is the stress sensitivity coefficient.

In the study of generation and maintenance of pore-pressure excess in the crust, David et al. (1994) conducted stress-dependent permeability experiments for five sandstones with effective stress from 3 MPa to about 600 MPa, using water as the test fluid. The ambient porosities of these samples range from 14% to 35%. The steady-state method and transient pulse method were employed for permeabilities higher and lower than 10 µD, respectively. As indicated by David et al. (1994) a typical permeability-effective stress curve has a sigmoidal shape, with an inflection point called a "critical pressure" at which pore collapse occurs. The "critical pressures" for the five sandstones vary from 75 MPa to 380 MPa. As also noted in David et al. (1994), the permeability reduction caused by mechanical compaction (effective stress ranging from 3 MPa to the "critical pressure") could be approximated using Equation (2.4). This relationship was suitable for the relatively high-stress part of the focused effective stress range. However, the permeability of two out of five sandstones exhibits high stress-sensitivity at low effective-stress range, which as argued by David et al. (1994) was related to closure of the micro-cracks. Equation (2.4) cannot reflect the permeability change at this effective-stress range.

Evans et al. (1997) measured the stress-dependent permeability of intact core, fault core, and damaged zone core of granite rock collected from outcrops, with ambient porosity ranging from 0.143% to 3.706%. Four intact cores, three fault cores, and five damage-zone cores were subjected to a series of effective stresses ranging from 2.07–10.34 MPa, 2.07–33.10 MPa, and 2.07–46.89 MPa, respectively. The tests were conducted at room temperature using nitrogen and a transient pulse method. An exponential equation, similar to Equation (2.4), was used to fit the stress-dependency of permeability data. However, it should be noted that the data used in the curve-fitting for the intact rock was only in the relatively low effective-stress range, i.e., from 2.07 MPa to 10.34 MPa. The other two have wider ranges of effective stress data. However, the fitted curves underestimated the permeability in effective stresses lower than 5 MPa. The fitted stress-sensitive coefficient for intact core was much higher than the other two, which the authors speculated was due to the micro-crack closure in the intact rock.

The major caveat of the exponential law for permeability-effective stress is that it yields poor fittings in low effective-stress ranges. When the measured permeability spans large ranges of effective stress, it is very hard to find one permeability-stress function to fit all the data. Evans et al. (1997) seemed to be able to fit their data with one equation, but only because their data (for intact rock) is only for low effective stress.

2.2.2.2 Empirical power law for stress-dependent permeability

A simple power law described by Equation 2.5 has also been used to fit measured permeability with effective stress (Morrow et al., 1984; Shi and Wang 1986; Ghabezloo et al., 2009b):

$$\mathrm{k} = \mathrm{a}\sigma^{-b} \tag{2.5}$$

where *a* and *b* are material constants, σ is effective stress.

Ghabezloo et al. (2009b) studied the effective-stress law of permeability for limestone with effective porosity (connected porosity) between 13.4% and 17.6%. A series of steady-state permeability tests were performed for different combinations of pore pressure and confining pressure, using water as the test fluid. The authors used Equation (2.5) to describe the variation in permeability, with the effective stress ranging from ~1 MPa to ~ 8 MPa. However, as indicated by the authors, this power law cannot be accepted as a general stress-permeability relationship, due to the infinite permeability value at zero effective stress.

Shi and Wang (1986) also use Equation (2.5) to describe the relationship between effective stress and the permeability of fault gouge measured by Morrow et al. (1984). Morrow et al. (1984) studied the permeability changes in clay-rich, non-clay, and pure-clay artificial gouges under an effective stress ranging from 5 MPa to 200 MPa. The artificial fault gouge was comprised of two pieces of very permeable saw-cut Berea sandstone and 1-mm-thick-layer tested material. The tests were conducted at a temperature of 27 ± 0.5 ℃ , using distilled water and a steady-state method.

A slightly different form of power law, as shown in Equation 2.6, was employed by Kwon et al. (2001) to fit the measured permeability of illite-rich shale with different effective stresses ranging from 3 MPa to 12 MPa.

$$\mathrm{k} = \mathrm{k}_0[1 - (\sigma/\mathrm{P}_1)^{m}]^3 \tag{2.6}$$

where k_0 is the reference permeability at zero effective pressure, σ is effective stress, P_1 is the effective modulus of the equivalent asperities, and m is a constant between 0 and 1. Kwon et al. (2001) took samples from a depth around 3955 m in West Baton Rouge Parish, Louisiana, with effective porosities from 7% to 8%. The transient pulse method was employed in a permeability test using 1*M* NaCl solution as the test fluid. Equation (2.6) has the advantage that it relates permeability with the equivalent fracture aperture, which provided a possible explanation for the permeability change with effective stress through the “cubic law.” However, the flaw in the equation is also obvious, in that it gives negative k when σ is larger than P_1. The value of P_1 is only 19.3 ± 1.6 MPa for shale, based on the fitting of the measured data (Kwon et al., 2001). Jones and Owens (1980) also used a similar relationship to describe permeability reduction with increasing effective stress for tight sandstone. A comprehensive review of stress-dependent permeability based on the equivalent fracture models could be found in Ostensen (1983). The common flaw of this type of relationship is that above a certain effective stress, the predicted permeability gives negative values.

In summary, while the power law can provide a reasonable description of the permeability-stress relationship at relatively low effective stress ranges, its flaw is quite obvious—Equation (2.5) yields infinite permeability at zero effective stress, and Equation (2.6) yields negative permeability when effective stress is larger than a certain value.

2.3 Relationship between permeability and porosity

Porosity acts as a bridge between permeability changes and changes in effective stress when assuming the mechanical compaction of the flow path as the main factor in causing permeability reduction. Thus, researchers have tried to construct permeability-porosity relationships in describing mechanical compaction. It is generally believed that the relationship between permeability and porosity of a rock undergoing mechanical compaction could be expressed by a power law:

$$\mathrm{k}/\mathrm{k}_0 = (\phi/\phi_0)^{\alpha} \tag{2.7}$$

where k_0 and ϕ_0 are permeability and porosity under ambient stress state, and α is a material constant.

David et al. (1994) used Equation (2.7) to describe permeability and porosity data under different effective stress for five types of sandstones, with exponent value α ranging from 4.6 to 25.4. They also reviewed a batch of publish data on the permeability-porosity relationship for different geomaterials, and with α varying from 1.11 to 25.4.

Ghabezloo et al. (2009b) measured the permeability-porosity relationship for oil-well cement paste using a single transient method which allows the porosity and permeability data to be measured in a single test. The permeability-porosity relationships obeyed a power law identical with Equation (2.7), with α value equal to 11.

Dong et al. (2010) conducted a series of permeability and porosity tests under different effective stresses. Equation (2.7) was also employed in these tests to describe the permeability-porosity relationship, with exponent α value ranging from 2.04 to 5.04 for fine-grained sandstone, and from 9.92 to 70.17 for silty-shale samples.

As shown above, the value of exponent α for most low-permeability rock is very large, which means that a small change in porosity (due to the applied stress) causes a huge decrease in permeability. This was first noticed by David et al. (1994), who noted that the theoretical models that used low values of α would underestimate the permeability reduction induced by compaction. Dong et al. (2010) observed even higher values of α, and postulated that it was caused by the effect of micro-crack closure. It is known that permeability is largely determined by the pore throat, or the slot-like micro-cracks that connect large pores to form a flow network (Byrnes, 1996; Dewhurst et al., 1998). This supports the applicability of a "cubic law" (Zimmerman and Bodvarsson, 1996; Liu et al., 2013a) derived for a fractured medium. However, the fact that an exponent α up to 70 has to be used to fit the measured data suggests that relating permeability changes to total porosity is fundamentally flawed.

Using total porosity in Equation (2.7) is essentially assuming that all pores, both large pores and micro-cracks, have equal contribution to permeability, which runs contrary to the fact that micro-cracks actually control the connectivity of pores and subsequently control permeability. Another fact is that the micro-cracks are generally more deformable, which means that they experience relatively large deformation at low effective stress range. Thus, the impropriety of homogenizing the contribution of different types of pores to permeability is more pronounced for low-permeability rock under low effective stress. When the rock is subject to compaction, the deformation of micro-cracks, although insignificant in term of volume, is critical for permeability changes. It is therefore necessary to separate the contribution of micro-cracks and large pores, which can be done via the concept brought by TPHM, as described in detail in the following subsections.

2.4 A brief description of the TPHM

The TPHM proposed by Liu et al. (2009) is briefly described here for completeness. Liu et al. (2009) argued that the *true strain*, rather than the *engineering strain*, should be used in Hooke's law for accurately modeling elastic deformation of rock, unless the two strains are essentially identical (as they might be for small mechanical deformations). In terms of volumetric strain, the true strain refers to volume change divided by rock volume at the current stress state, and the engineering strain refers to volume change divided by the unstressed rock volume. (In the literature of rock mechanics and other related scientific fields, however, engineering strain is now used exclusively.) Liu et al. (2009) further argued that natural rocks are inherently heterogeneous, and thus different varieties of Hooke's law should be applied within ranges having significantly different stress–strain behavior. They conceptually divide the rock body into two parts, hard and soft, and hypothesize that the soft part obeys the true-strain-based Hooke's law, while the hard part approximately follows the engineering-strain based Hooke's law for mathematical convenience, because its deformation is small (true strain is practically identical to the engineering strain when the deformation is small). This conceptualization can be represented by the hypothesized composite spring system shown in Figure 2.1. These two springs are subject to the same stress, but follow different variations on Hooke's law. To be consistent with previous work, the subscripts $0, \mathrm{e}, \mathrm{and}\ \mathrm{t}$ denote the unstressed state, the hard part and the soft part, respectively. For the soft part, Hooke's law could be expressed using the true strain:

$$\mathrm{d}\sigma = \mathrm{K}_t \mathrm{d}\varepsilon_{V,t} = -\mathrm{K}_t \frac{\mathrm{dV}_t}{\mathrm{V}_t} \tag{2.8}$$

where K_t is the elastic modulus of the soft part, and V_t is the volume of the soft part. Integrating Equation (2.8) and the initial condition $\mathrm{V}_t = \mathrm{V}_{0,t}$ for $\sigma = 0$, we have:

$$\mathrm{V}_t = \mathrm{V}_{0,t} \exp\left(-\frac{\sigma}{\mathrm{K}_t}\right) \tag{2.9}$$

For the hard part, using the engineering strain, we have:

$$\mathrm{d}\sigma = \mathrm{K}_e \mathrm{d}\varepsilon_{V,e} = -\mathrm{K}_e \frac{\mathrm{dV}_e}{\mathrm{V}_{0,e}} \tag{2.10}$$

where K_e is the elastic modulus of the hard part, and V_e is the volume of the hard part. Integrating Equation (2.9) and the initial condition $\mathrm{V}_e = \mathrm{V}_{0,\mathrm{e}}$ for $\sigma = 0$, we have:

$$\mathrm{V}_e = \mathrm{V}_{0,e}\left(1 - \frac{\sigma}{\mathrm{K}_e}\right) \tag{2.11}$$

By combining Equations (2.9) and (2.11), the TPHM-based stress-strain relationship under a hydrostatic state can be expressed by:

$$\varepsilon = -\frac{\mathrm{dV}}{\mathrm{V}_0} = -\frac{\mathrm{dV}_e + \mathrm{dV}_t}{\mathrm{V}_0} = \gamma_e \frac{\mathrm{d}\sigma}{\mathrm{K}_e} + \gamma_t \exp\left(-\frac{\sigma}{\mathrm{K}_t}\right)\frac{\mathrm{d}\sigma}{\mathrm{K}_t} \tag{2.12}$$

$$\gamma_t = \frac{V_{0,t}}{V_0} \tag{2.13}$$

$$\gamma_e = 1 - \gamma_t \tag{2.14}$$

where V_0 is the rock bulk volume under an unstressed state. Equation (2.12)-(2.14) together comprise the basic stress–strain relationship.

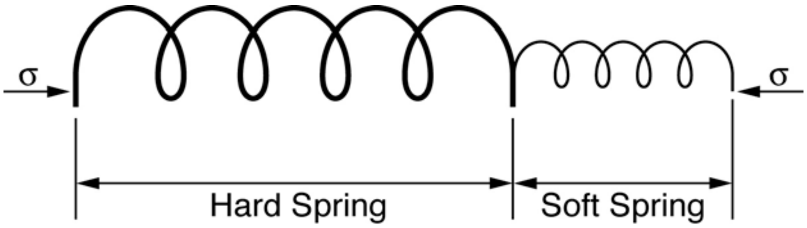

Figure 2.1. A composite spring system consisting of two springs. The hard and soft springs follow engineering-strain-based and natural-strain-based Hooke’s law, respectively.

With the basic stress-strain relationship available, a number of rock mechanical and/or hydraulic properties subjected to elastic deformation can be developed. For example, Liu et al. (2009) derived the stress-dependent bulk rock compressibility, pore compressibility, rock porosity, and fracture aperture based on the TPHM. The derived relationships were compared with a variety of laboratory experimental data, which showed a great consistency. Furthermore, they argued that the proposed relationships are robust for engineering applications, because the parameter values estimated from different types of data are quite consistent for similar types of rocks. Zhao and Liu (2012) extended the stress-dependent relationships for porous rock under elastic and anisotropic conditions by assuming that the principal strain resulting from the soft part is a function of principal stress along the same direction only. These relationships also showed great consistency with the data gathered from the literature. Liu et al. (2013a) focused on the normal-stress dependent fracture hydraulic properties. The derived relationship between stress and fracture permeability (or related aperture and closure) based on the TPHM showed a satisfactory agreement with the datasets obtained from the literature. Li et al. (2014) incorporated the TPHM-based relationships into a geomechanical simulator to study the coupled hydromechanical behavior of the Opalinus Clay in responding to tunnel excavations. The simulation results obtained using the TPHM-based constitutive relationships are more consistent with the field observations than the results using the traditional constitutive relationships.

2.5 Stress-dependent relationships for rock porosity and permeability based on the TPHM

It is clear that the permeability changes in the low stress range is mainly due to the compaction of micro-cracks that experienced relatively large deformation. As pointed out by Liu et al. (2009; 2013a), some portion of the pores and microfractures in a rock body could be subjected to significant deformation due to their geometrical heterogeneity. Byrnes et al. (1997; 2000) found that the average pore-throat size in low-permeability sandstones under *in situ* stress decreased by as much as 50 to 70% (e.g., from 1 μm to 0.5–0.3 μm) compared with that under no confining stress, whereas, the porosity under in-situ stress were just several percent less than that under no confining stress. As indicated by Byrnes et al., the thin and sheet-like interconnecting throats, although constituting only a small portion of the porosity, make a significant contribution to permeability reduction. More attention should be paid to the deformation of the more compliant part of the rock body (e.g., micro-cracks), since they act as critical fluid-flow paths that determine hydraulic properties. However, most previous studies (Gangi, 1978; Shi and Wang, 1986; Ghabezloo et al., 2009a; Dong et al., 2010) assumed homogeneity of the rock sample and ignored the likelihood that the different parts of the rock have different mechanical responses under stress and thus affect permeability differently. The division of hard and soft parts in THPM provides us with a framework to consider such heterogeneity development of stress-dependent permeability-porosity relationships. The derivations based on the TPHM are given below.

2.5.1 Stress-dependence of porosity

As discussed above, we conceptualize the pore structures into two parts. The hard part experiences small deformation, whereas the soft part undergoes relatively large deformation. The aforementioned micro-cracks correspond to the soft part, while the rest of the pores and solids belong to the hard part. Using the same notations as in Section 2.4, the porosity change could be defined as:

$$d\phi \approx \frac{dV^p}{V_0} = \frac{dV_t^p + dV_e^p}{V_0} = \frac{dV_t + dV_e^p}{V_0} \tag{2.15}$$

where the superscript p refers to pore space. The soft part of rock body V_t is considered to be a portion of pore volume, which leads to $V_t = V_t^p$. Liu et al. (2009) indicated that, for the purpose of calculating porosity, the changes in total rock volume V could be ignored, and its value could be approximated with the unstressed volume V_0. With this assumption, and following the same procedure used to derive Equation (2.12), we obtained:

$$d\phi = -\phi_{e,0} C_e d\sigma - \frac{\gamma_t}{K_t} \exp\left(-\frac{\sigma}{K_t}\right) d\sigma \tag{2.16}$$

$$\phi_{e,0} = \phi_0 - \gamma_t \tag{2.17}$$

where C_e is the compressibility for the hard fraction of pore volume.

Integrating Equation (2.16) and using $\phi = \phi_0$ for $\sigma = 0$ gives

$$\phi = \phi_{e,0}(1 - C_e\sigma) + \gamma_t \exp\left(-\frac{\sigma}{K_t}\right) \tag{2.18}$$

$$\phi_e = \phi_{e,0}(1 - C_e\sigma) \tag{2.19}$$

$$\phi_t = \gamma_t \exp\left(-\frac{\sigma}{K_t}\right) \tag{2.20}$$

As expressed by Equations (2.18)–(2.20), the porosity of a rock sample is divided into two parts. The hard-part porosity, i.e., $\phi_e = \phi_{e,0}(1 - C_e\sigma)$, has a linear relationship with the effective stress. The soft-part porosity, i.e., $\phi_t = \gamma_t \exp\left(-\frac{\sigma}{K_t}\right)$, changes exponentially with effective stress. The soft-part porosity corresponds to those more compliant, slot-like micro-cracks, which experience relatively large deformation under low effective stress. The two porosities experience different types of reduction with increasing effective stress. Specifically, the soft part is important in the low-stress range while negligible in the high stress range because K_t is relatively small (i.e., $\exp\left(-\frac{\sigma}{K_t}\right) \approx 0$ when $\sigma \gg K_t$).

2.5.2 Stress-dependence of permeability

The division of total porosity into a soft part and a hard part, which obey different relationships for effective stress, allows us to consider their respective effect on the total permeability.

The permeability changes in relatively high effective-stress ranges is controlled by the hard part with the consideration that the soft-part porosity could be neglected in this stress range (micro-crack closure). Mathematically, the stress-dependent permeability contributed by the hard part (referred to as "hard-part permeability" hereafter) could be written as:

$$\mathrm{k}_e = \mathrm{k}_{e,0}\exp\left[\beta\left(\phi_e - \phi_{e,0}\right)\right] = \mathrm{k}_{e,0}\exp\left[-\beta \mathrm{C}_e\phi_{e,0}\sigma\right] \tag{2.21}$$

where ϕ_e and k_e are the stress-dependent hard-part porosity and permeability, β is a constant that represents a stress-sensitive coefficient. Equation 2.21 is consistent with most of the experimental observations (David et al., 1994; Evans et al., 1997; David et al., 2001; Kwon et al., 2001), such that permeability changes linearly with the logarithm of effective stress within the relatively high effective stress range, as discussed in Section 2.2.2.1.

The stress-sensitive permeability changes in the low effective-stress range are mainly due to the deformation of the soft part (micro-cracks) porosity, which experienced relatively large deformation, despite the fact that the soft-part porosity makes up only a small portion of the total pore volume. The permeability contributed by the soft part, referred to as the "soft-part permeability" hereafter, could be considered as the total permeability minus the hard-part permeability:

$$\mathrm{k}_t = \mathrm{k} - \mathrm{k}_e \tag{2.22}$$

where k is the total permeability and k_t is the soft-part permeability.

Mathematically, we postulate the relationship between soft-part porosity and soft-part permeability as:

$$\mathrm{k}_t = \alpha\phi_t^{\mathrm{m}} \tag{2.23}$$

where ϕ_t, k_t are the soft-part porosity and permeability, respectively**;** and α and m are constants.

Combining Equations (2.20)-(2.23) yields the total permeability as:

$$k = \mathrm{k}_{e,0}\exp\left[-\beta \mathrm{C}_e\phi_{e,0}\sigma\right] + \alpha\left[\gamma_t \exp\left(-\frac{\sigma}{\mathrm{K}_t}\right)\right]^{\mathrm{m}} \tag{2.24}$$

In this report the soft part corresponds to those thin, slot-like micro-cracks. If such a hypothesis holds, the permeability change caused by the soft-part deformation should obey the "cubic law" (Witherspoon et al., 1980; Zimmerman and Bodvarsson, 1996; Kwon et al., 2001). In other words, the soft-part permeability should be well related with the soft-part porosity through a relationship similar to the "cubic law," i.e., m in Equation (2.23) should be around 3. In the next section, we will evaluate the equations proposed here using the experimental observations collected from the literature.

2.6 Verification of the proposed stress-dependent relationships for rock porosity and permeability based on the TPHM

Here we evaluate the proposed relationships using the experimental observations provided by Dong et al. (2010). Actually, there are a number of stress-dependent permeability data for low-permeability rock in the literature (McLatchie et al., 1958; Vairogs et al., 1971; Thomas and Ward, 1972; Walls et al., 1982; Wei et al., 1986; Kilmer et al., 1987; Brighenti, 1989; Spencer, 1989; Kwon et al., 2001; Lei et al., 2008; Jasinge et al., 2011; Konecny and Kozusnikova, 2011; Metwally and Sondergeld, 2011). However, those that include stress-dependent porosity data are few. To the best of our knowledge, these data sets can be found in Wyble (1958), Jones and Owens (1980), Yale and Nur (1985), David et al. (1994), Mohiuddin et al. (2000); and Dong et al. (2010). In the selection of the experimental data sets we used to evaluate the proposed relationships, several criteria were considered. First of all, the samples and the measurement procedures had to be well documented. Second, we preferred that the permeability be measured by gas rather than liquid, because gas (e.g., nitrogen and helium) is more chemically inert than liquid (e.g., pure water and NaCl solution). Third, the samples collected from wells were preferred over outcrop rock samples, since the relationships of interest are mostly for underground engineering applications. Other selection considerations include sufficient data density and microscopic pore structure analysis. Given these considerations, we chose the data sets provided by Dong et al. (2010) to evaluate the proposed relationships.

2.6.1 Experiments description

Rock samples from depths of 900–1235 m were collected from a deep drilling project (Taiwan Chelungpu Fault Drilling Project, TCDP-A) in the Western Foothills of Taiwan. Only the relatively homogeneous cores were selected; cores with interbedded layers were discarded. The samples were carefully prepared to reduce the occurrence of micro-cracks during sample preparation. A series of stress-dependent porosity and permeability of dry rock samples were measured on an integrated porosity/permeability measurement system, i.e. YOYK2. A steady-state flow method was employed to assess the stress-dependent permeability, while stress-dependent porosity was measured by a gas-expansion method. Nitrogen was used as the test fluid for both tests. The experiments were conducted by first gradually increasing (loading) the confining pressure P_c from 3 to 5 MPa, then to 20 MPa (in 5 MPa increments), and finally to 120 MPa (in 10 MPa increments). P_c was then gradually reduced (unloaded) back to 3 MPa in the reverse order. The average pore pressures P_p were relatively low, i.e., 0.13–1.40 MPa for the permeability measurement and 0.3–1.41 MPa for the porosity measurement. The effective stress is defined as the difference between the P_c and P_p. Tested samples included Pliocene to Pleistocene fine-grained sandstone and silty-shale. The sandstone samples had relatively high permeability, exceeding the definition of low-permeability rock. In this study, we focused on the stress-dependent hydraulic properties of the silty-shale. The basic geophysical properties of the samples are listed in Table 2.1.

Table 2.1. Basic geophysical properties of silty-shale samples for permeability and porosity measurements

Sample name	Depth(m)	Dry density (g/cm3)	Rock type
R255_sec2	902.68	2.59	Silty-shale
R287_sec1	972.42	2.58	Silty-shale
R351_sec2	1114.33	2.59	Silty-shale
R390_sec3	1174.24	2.66	Silty-shale

2.6.2 Matching experiment data using TPHM based relationships

Since the porosity under zero effective stress ($\phi_{e,0}$) was not given due to the limitation of the experimental method, we simply used the porosity at lowest effective stress $\phi_{e,1}$ to substitute $\phi_{e,0}$. The subscript 1 hereafter refers to the lowest effective stress state. Equation (2.18) is therefore revised as:

$$\phi = \phi_{e,1}(1 - \mathrm{C}_e\Delta\sigma) + \gamma_{t,1}\exp\left(-\frac{\Delta\sigma}{\mathrm{K}_t}\right) \tag{2.25}$$

where $\Delta\sigma = \sigma - \sigma_1$, and $\gamma_{t,1}$ was the soft-part fraction at the lowest effective stress.

Similarly, the Equation (2.24) was revised as:

$$k = \mathrm{k}_{e,1}\exp\left[-\beta \mathrm{C}_e\phi_{e,1}\Delta\sigma\right] + \alpha\left[\gamma_{t,1}\exp\left(-\frac{\Delta\sigma}{\mathrm{K}_t}\right)\right]^{\mathrm{m}} \tag{2.26}$$

The matching process of stress-dependent porosity and permeability for the loading part of sample R255_sec2 was used to illustrate the determination of parameters in Equations (2.25) and (2.26). As shown in Figure 2.2(a), the porosity-effective stress relationship can be well represented by a straight line for the relatively high effective-stress range. In this study, we chose the effective-stress range 35 MPa–120 MPa as the relatively high effective stress range. The slope of the straight line was used to determine $(-\phi_{e,1}\mathrm{C}_e)$, because the second term on the right hand side of Equation (2.25) is negligible for high effective stress values. The value of $\phi_{e,1}$ was determined by extrapolating the straight line to σ_1, as illustrated by the intersection of the red line and Y axis in Figure 2.2(a). The measured porosity ϕ_1 was equal to $\phi_{e,1} + \gamma_{t,1}$ as implied by Equation (2.25). The above procedure allowed for direct determination of values for $\phi_{e,1}$, C_e, and $\gamma_{t,1}$. The remaining parameter K_t could be estimated using the porosity data at relatively low effective stress, based on Equation (2.25). The effective stress range 3 MPa–15 MPa was chosen as the relatively low effective-stress range.

Figure 2.2(b) shows the permeability-effective stress relationship with permeability plotted in logarithm. A linear relationship exists for $log(K_e)$ versus σ, as shown by the red straight line for the relatively high effective-stress range. In this effective-stress range, the contribution of the soft part to permeability is neglected, because the second term on the right-hand side of Equation (2.26) is negligible. The slope of the straight line in the relatively high effective-stress range yields the value of $(-\beta\mathrm{C}_e\phi_{e,1})$, which leads to the determination of β as $\phi_{e,1}$ and C_e is known by fitting the porosity-stress data. $\mathrm{k}_{e,1}$, the hard-part permeability at σ_1, is given by the intersection of the straight line with Y axis.

Once the hard-part permeability is known, the soft-part permeability is calculated by the total permeability minus the hard-part permeability. Then, the soft-part permeability is related to the soft-part porosity at corresponding stress with $k_t = \alpha\phi_t{}^{\mathrm{m}}$, which yields the exponent m. The m value is marked out on the stress-permeability figure.

Experimental data matched with Equations 2.25 and 2.26 are shown in Figures 2.2–2.5. A close match between Equation (2.25) and (2.26) and the experimental data confirms the validity of these TPHM-based porosity-stress and permeability-stress relationships. As shown in the porosity- stress figures, the soft part mainly accounts for the nonlinear porosity reduction with effective stress in the low stress range. The porosity reduction in this range resulted mainly from the deformation of slot-like micro-cracks. In addition, as shown in the permeability-stress figures, the soft part accounts for most of the permeability reduction in the low effective-stress range. The soft-part porosity, which occupied only a small portion of the total pore volume, acted as critical flow paths that connected the hard-part porosity. Thus, its deformation significantly affected the permeability. Using the concept of dividing the rock body into hard and soft parts, the stress-dependent rock porosity and permeability have a reasonable explanation.

The determined value of $\phi_{e,1}$, C_e, $\gamma_{t,1}$, K_t, $\mathrm{k}_{e,1}$, β, α, m and its coefficient of determination R^2 are listed in Table 2.2. As listed, the soft-part porosity at lowest effective stress $\gamma_{t,1}$ was only a small portion of the total porosity (from 0.07% to 0.77%). The elastic modulus of the soft part (from 2.83 to 14.81 MPa) was significantly smaller than the general rock bulk modulus. The values of $\mathrm{k}_{e,1}$ were significantly smaller than the total permeability, suggesting that the soft part makes the major contribution to the total permeability at low effective-stress range. In addition, the soft-part permeability is nicely correlated to the soft-part porosity by a power law with exponent m from 1.62 to 3.03, which validates our hypothesis that the soft-part permeability is controlled by the slot-like micro-cracks.

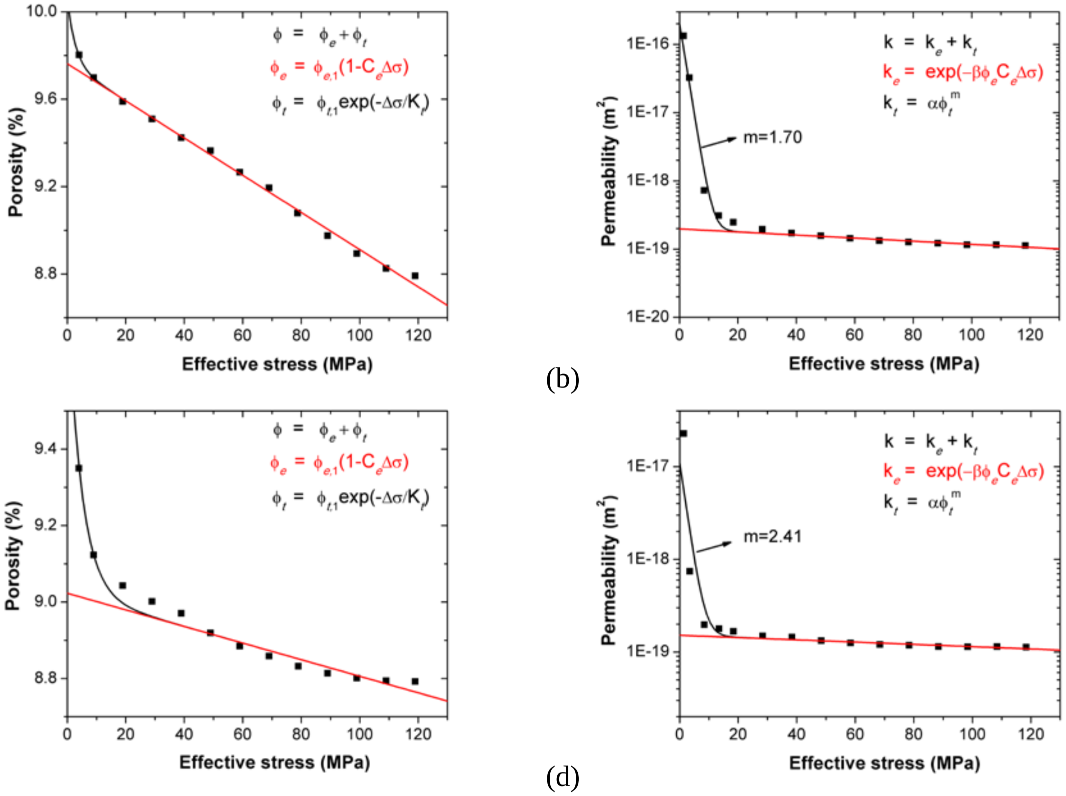

(a) (b)

(c) (d)

Figure 2.2. The matching result of the proposed relationships and the experimental test data for sample R255_sec2. (a) porosity-stress on loading stage. (b) permeability-stress permeability on loading stage. (c) porosity-stress on unloading stage. (d) permeability-stress permeability on unloading stage.

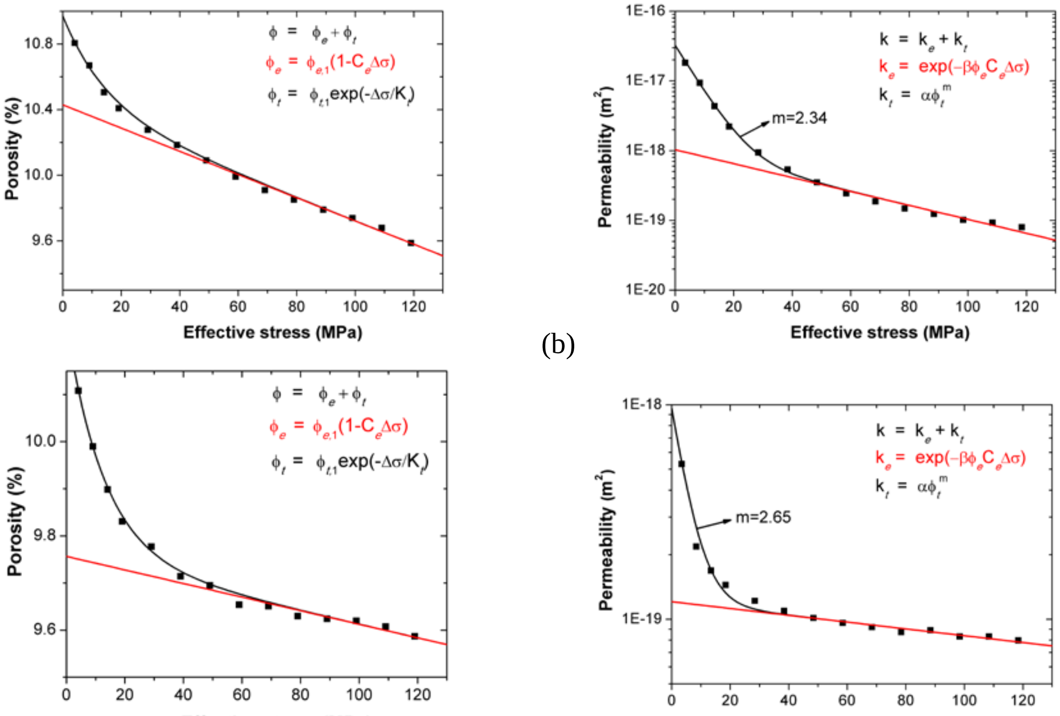

(a) (b)

(c) (d)

Figure 2.3. The matching result of the proposed relationships and the experimental test data for sample R287_sec1. (a) Stress-dependent porosity on loading stage. (b) Stress-dependent permeability on loading stage. (c) Stress-dependent porosity on unloading stage. (d) Stress-dependent permeability on unloading stage.

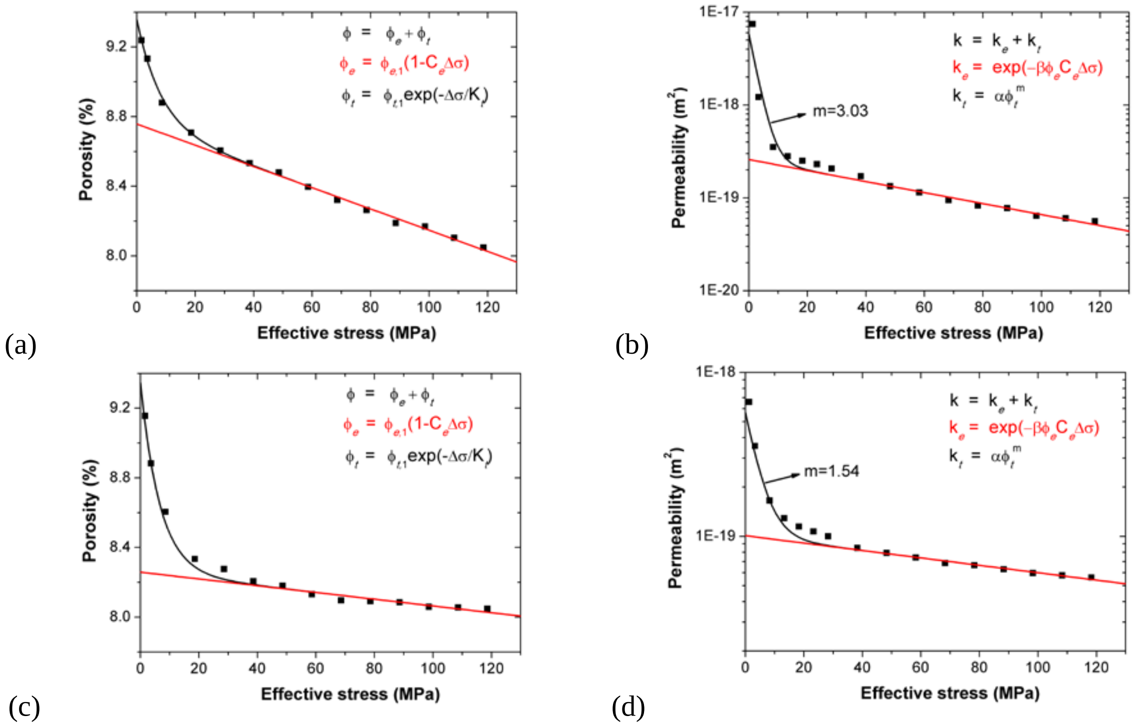

Figure 2.4. The matching result of the proposed relationships and the experimental test data for sample R351_sec2. (a) porosity-stress on loading stage. (b) permeability-stress permeability on loading stage. (c) porosity-stress on unloading stage. (d) permeability-stress permeability on unloading stage.

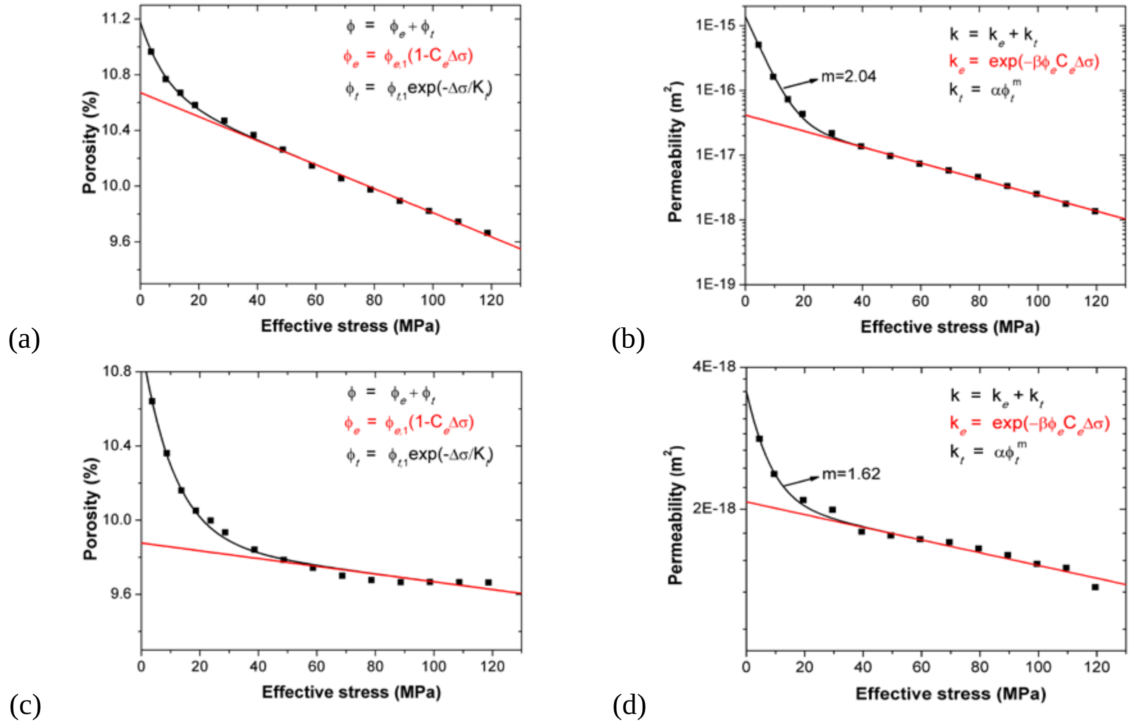

Figure 2.5. The matching result of the proposed relationships and the experimental test data for sample R351_sec3. (a) porosity-stress on loading stage. (b) permeability-stress permeability on loading stage. (c) porosity-stress on unloading stage. (d) permeability-stress permeability on unloading stage.

Table 2.2. Fitted parameter values from the experimental data of Dong et al. (2010).

Sample		$\phi_{e,1}$ (%)	$\gamma_{t,1}$ (%)	C_e (MPa^{-1})	K_t (MPa)	$k_{e,1}$ (m^2)	β	α (m^2)	m	R^2
R255_sec2	Loading	9.73	0.07	8.75×10^{-4}	2.83	1.97×10^{-19}	0.61	1.66×10^{-15}	1.70	0.94
	Unloading	9.01	0.34	2.41×10^{-4}	4.84	1.51×10^{-19}	1.30	1.99×10^{-17}	2.41	0.69
R287_sec1	Loading	10.40	0.41	6.81×10^{-4}	14.81	9.54×10^{-19}	3.25	1.32×10^{-16}	2.34	0.99
	Unloading	9.75	0.36	1.48×10^{-4}	13.04	1.19×10^{-19}	2.53	5.53×10^{-18}	2.65	0.91
R351_sec2	Loading	8.75	0.49	6.97×10^{-4}	8.09	2.54×10^{-19}	2.24	2.61×10^{-17}	3.03	0.83
	Unloading	8.26	0.90	2.35×10^{-4}	6.67	1.01×10^{-19}	2.68	4.12×10^{-19}	1.54	0.95
R390_sec3	Loading	10.64	0.33	8.11×10^{-4}	8.74	3.66×10^{-17}	3.30	5.42×10^{-15}	2.04	0.99
	Unloading	9.87	0.77	2.12×10^{-4}	11.30	2.04×10^{-18}	1.49	1.33×10^{-18}	1.62	0.95

2.6.3 Match of Klinkenberg corrected permeability data using TPHM based relationships

The permeability measured using gas as the test fluid is generally higher than when using water, due to the Klinkenberg gas slippage effect (Klinkenberg 1941). As discussed in Tanikawa and Shimamoto (2009), the Klinkenberg effect is important when the permeability is lower than 10^{-18} m^2 and when there is little pore-pressure difference on the different sides of the test sample. The following equations, suggested by Tanikawa and Shimamoto (2009) and Dong et al. (2010), are used in this study to correct the measured permeability data.

$$k_g = k_l[1 + (b/P_{av})] \tag{2.27}$$

where k_g is the measured gas permeability, k_l is the corrected permeability using Klinkenberg correction, and P_{av} is the average pore pressure, which could be calculated using Dong et al. (2010):

$$P_{av} = 2(P_u^2 + P_u P_d + P_u^2)/3(P_u + P_d) \tag{2.28}$$

where P_u denotes upper-end pore pressure, P_d denotes the lower-end pore pressure, assumed at atmospheric pressure. b is the Klinkenberg slip factor and can be obtained using the following equation, based on the experimental data (Tanikawa and Shimamoto, 2009):

$$b = 0.15 \times k_l^{-0.37} \tag{2.29}$$

The same procedure is used to determine the parameters in the permeability-stress relationship for Klinkenberg corrected permeability. The matching results for the Klinkenberg corrected permeability are shown in Figures 2.6-2.9. The determined value of $k_{e,1}$, α, β, m and the coefficient of determination R^2 are listed in Table 2.3.

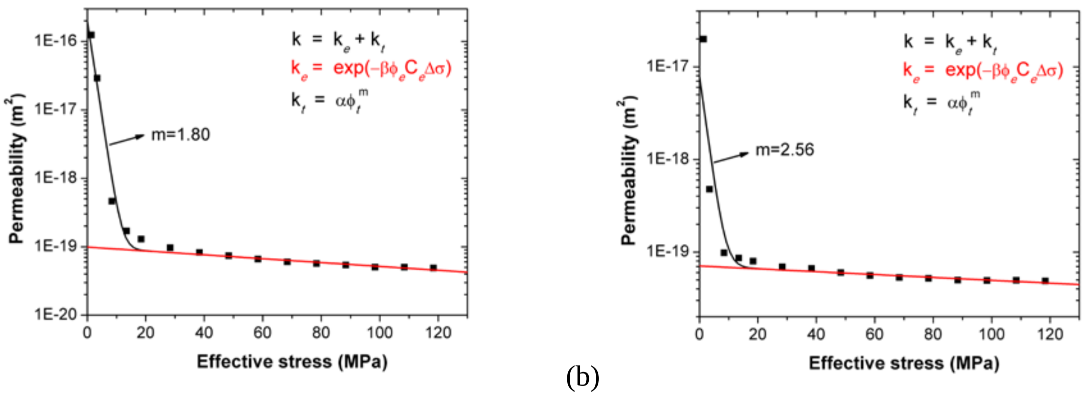

(a) (b)

Figure 2.6. The Klinkenberg corrected permeability matching result of the proposed relationships and the experimental test data for sample R255_sec2. (a) Stress-dependent permeability on loading stage. (b) Stress-dependent permeability on unloading stage.

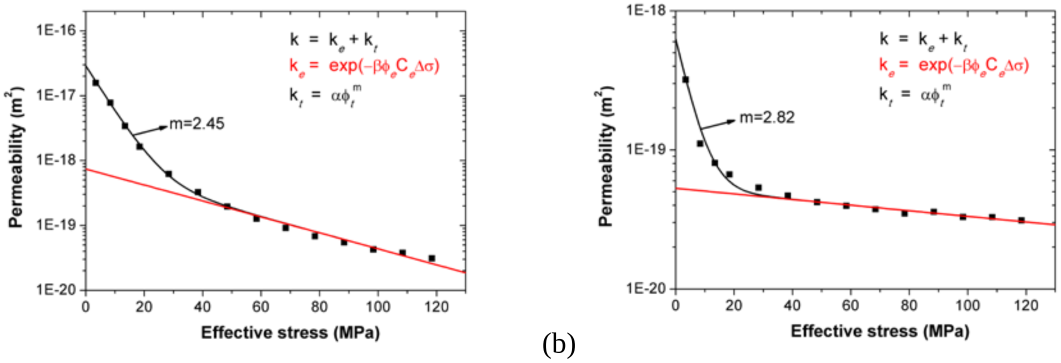

(a) (b)

Figure 2.7. The Klinkenberg corrected permeability matching result of the proposed relationships and the experimental test data for sample R287_sec1. (a) Stress-dependent permeability on loading stage. (b) Stress-dependent permeability on unloading stage.

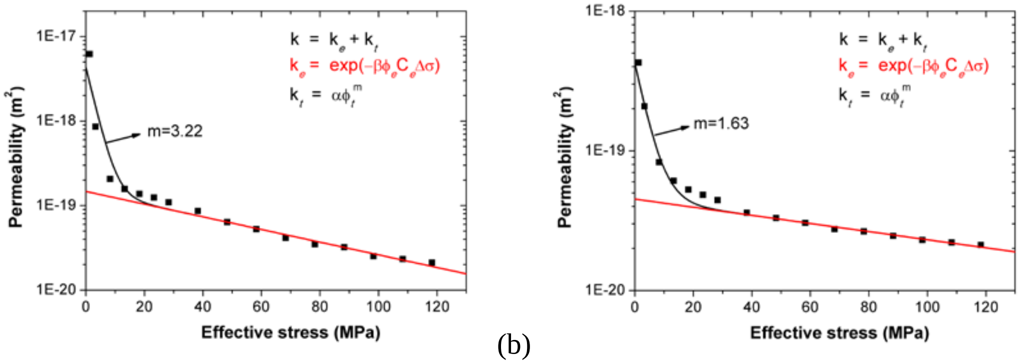

(a) (b)

Figure 2.8. The Klinkenberg corrected permeability matching result of the proposed relationships and the experimental test data for sample R351_sec2. (a) Stress-dependent permeability on loading stage. (b) Stress-dependent permeability on unloading stage.

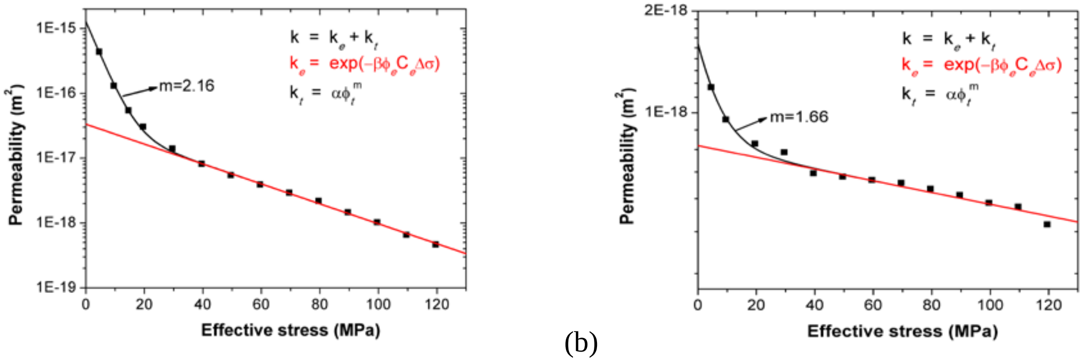

(a) (b)

Figure 2.9. The Klinkenberg corrected permeability matching result of the proposed relationships and the experimental test data for sample R390_sec3. (a) Stress-dependent permeability on loading stage. (b) Stress-dependent permeability on unloading stage.

Table 2.3. Fitted parameter values for stress-dependent relationship of Klinkenberg corrected permeability.

Sample		$k_{e,1}$ (m^2)	β	α (m^2)	m	R^2
R255_sec2	Loading	9.80×10^{-20}	0.76	1.82×10^{-15}	1.80	0.94
	Unloading	7.05×10^{-20}	1.64	1.70×10^{-17}	2.56	0.68
R287_sec1	Loading	6.75×10^{-19}	4.00	1.28×10^{-16}	2.45	0.99
	Unloading	5.22×10^{-20}	3.23	4.24×10^{-18}	2.82	0.91
R351_sec2	Loading	1.44×10^{-19}	2.83	2.39×10^{-17}	3.22	0.82
	Unloading	4.48×10^{-20}	3.45	3.30×10^{-19}	1.63	0.94
R390_sec3	Loading	2.85×10^{-17}	4.10	5.46×10^{-15}	2.16	0.99
	Unloading	7.85×10^{-19}	1.92	7.20×10^{-19}	1.66	0.95

In general, the Klinkenberg corrected permeability k_l is smaller than the gas-measured permeability k_g. After the Klinkenberg correction, the $k_{e,1}$ value decreases, and the stress sensitivity coefficient β for the hard part increases. In addition, the porosity sensitivity parameter for soft part m increases slightly, which means that the Klinkenberg corrected permeability drops quicker with the porosity decrease at low stress range. The coefficient of determination R^2 remains almost the same.

2.7 Concluding remarks

Redistribution of *in situ* stresses and rearrangement of rock structures leads to development of EDZ. In the one hand, field investigations conducted at underground laboratories have shown that the permeability of the EDZ can be one or more orders of magnitude higher than the unaltered argillaceous rock. For these conditions, the EDZ could then act as a preferential flow path for advective transport and thereby speed up radionuclide migration toward the biosphere. On the other hand, laboratory and field studies (Bossart et al., 2004; Baechler et al., 2011; Armand et al., 2013) suggest that a partial or complete self-sealing of fractures due to clay swelling and creep within the EDZ is possible after a certain amount of time. The self-sealing process can potentially decrease the EDZ permeability over time, which may eventually return to the values of the unaltered rock. In either case, permeability in EDZ shows strong stress-dependence. An accurate mathematical representation of the permeability-stress relationship is therefore critical for understanding the evolution of permeability and predicting the permeability changes during excavation and self-healing stages.

Because of its importance in other engineering applications such as fossil-fuel exploitation and CO_2 geological sequestration, the stress-dependence of permeability and porosity has been widely studied. The permeability and porosity change with effective stress for argillite is featured with significant permeability changes with relatively small changes in effective stress and porosity. Some empirical relationships were established between permeability and effective stress based on laboratory-measured data. Representative relationships include exponential law and power law. However, the exponential law yields poor fitting in low effective-stress ranges, and the power law gives unreasonable predictions for certain effective-stress values. Moreover, to describe the relationship between the significant permeability change and the insignificant porosity change has been a great challenge for scientists over a long period of time. Up to now, empirical relationships, usually in the form of a power law, were established based on laboratory-measured data to relate permeability and porosity. The underlying assumption in relating permeability changes to the total porosity change is that the reduction of the total volume of pore space is the only driver for the permeability change—an assumption that leads to some problems with these relationships, one of which is the abnormally high value for the exponent, which is up to 70 in some studies (David et al., 1994; Dong et al., 2010). The extremely high exponent in the current power law for the relationship between permeability and porosity suggests that relating permeability changes to the total porosity changes is not a valid assumption. In this report we established relationships that are more physically robust for low permeability rock.

Based on the concept of the two-part Hooke's model Liu et al. (2009; 2011), in which rock body is conceptually divided into "soft" and "hard" parts, we derived a series of stress-porosity, stress-permeability and permeability-porosity relationships. The derived relationships explain well the stress-dependence of permeability and porosity in the low effective-stress ranges for low-permeability rock such as argillite, and they have been validated by the published data. These relationships provide a critical link between hydrological to mechanical properties and will greatly improve our capability of modeling the coupled processes for a radioactive waste repository.

In the future, we hope to further validate the derived constitutive relationships with more comprehensive experimental data. Then these relationships will be implemented in our simulator TOUGHREACT-FLAC3D to evaluate the evolution of the EDZ for an argillite repository.

3. Discrete Fracture Network (DFN) Approach for Fractures in Argillaceous Rock

Although clay-rich formations are usually characterized by low intrinsic rock permeability and very limited fracture permeability, observations indicate that permeable fracture networks can form for limited times (e.g., Bossart et al., 2004; Cosgrove, 2001). There are two classes of fracturing that require investigation: (1) fracturing around an excavation in the excavation damaged zone (EDZ) and (2) natural fracturing.

Fractures in the EDZ have been routinely observed in clay-rock underground research laboratories (URL) in Europe, including the Opalinus Clay in Switzerland, Boom Clay in Belgium, and the Callovo-Oxfordian Clay in France (Volckaert et al., 2004). These fractures form as a consequence of tectonic disturbance by excavation, shrinkage caused by ventilation dry-out, and other conditions that are expected during the pre-closure phase of a repository. However, post-closure effects, such as thermal pressuring and gas evolution may also result in fracturing (Blümling et al., 2007). The EDZ not only exhibits fracturing along tunnel surfaces, but can contain fracture damage in thin zones (<~1 m) around drifts, which has been verified from measurements of permeability in that area (Bossart et al., 2004). Finally, fractures in clay-rich formations also show significant self-sealing over a three-year period (Bossart et al., 2004). The connectivity of fractures along a tunnel has been observed in the HG-A test at Mont Terri, Switzerland, where a test tunnel section, sealed by a packer, was injected with fluid that showed preferential pressure increases along the packer where the most severe EDZ damage was observed (Lanyon et al., 2009).

Fracturing has also been observed in clay-rich formations as a result of natural processes, often associated with abnormal pore-pressure conditions. These can lead to fault reactivation and hydraulic fracturing. Geologic evidence suggests that the Mercia Mudstone within the Bristol Channel Basin in the UK was subject to repeated episodes of natural hydraulic fracturing over its 250 million year history (Cosgrove, 2001). This mudstone underwent 150 M years of burial followed by 100 million years of uplift. Outcrop evidence shows that natural fractures formed, conducted fluids, and then sealed at various points in time both during burial and uplift.

The main inference to be drawn from the observations is that fractures in argillaceous rocks are transient features that require a dynamic modeling approach. In this chapter, we mainly focus on the first case of fracturing process, which undergoes relatively in a short period, such as the excavation damage fracturing. The TOUGH-RBSN model is applied to simulate coupled thermal-hydrological-mechanical (THM) processes including fracture initiation, propagation, and evolution in rock formations.

3.1 Overview of the RBSN Approach for Mechanical Damage Modeling of Geomaterials

Discrete models have been used to study the heterogeneous characteristics of geological systems, with advantages in modeling mechanical behavior accompanied by discontinuities, such as fracture processes. The Rigid-Body-Spring Network (RBSN) approach, as a kind of discrete model, represents the system behavior by simple two-node elements interconnected on a set of nodal points. The RBSN formulation is based on the concept of the Rigid-Body-Spring Model (RBSM), first introduced by Kawai (1978), in which the material constitution is represented as a collection of rigid bodies connected by spring sets.

The RBSN model adopts the Voronoi diagram for partitioning the domain and the dual Delaunay tessellation for constructing the assembly of lattice elements. A lattice element is formed from a spring set, which is connected to neighboring nodes *i* and *j* via rigid-body constraints (Figure 3.1). The spring set has zero size since the rigid arm constraints relate to the same position, *C* (the centroid of the common Voronoi cell boundary). For the case of 3-D modeling, three displacements and three rotations are defined at each node, and the rigid-body constraints link these nodal degrees of freedom to the generalized relative displacements of the spring set. The spring set consists of three axial springs and three rotational springs acting independently, with stiffnesses $\mathbf{D} = \mathrm{diag}[k_n, k_s, k_t, k_{\phi n}, k_{\phi s}, k_{\phi t}]$ in local *n*-*s*-*t* coordinates. The local spring coefficients are defined according to the geometrical features of Voronoi diagram:

$$k_s = k_t = \alpha_1 k_n = \alpha_1 \alpha_2 E \frac{A_{ij}}{h_{ij}}, \quad k_{\phi n} = E \frac{J_p}{h_{ij}}, \quad k_{\phi s} = E \frac{I_{ss}}{h_{ij}}, \quad k_{\phi t} = E \frac{I_{tt}}{h_{ij}} \tag{3.1}$$

in which E is the elastic modulus, J_p, I_{ss}, and I_{tt} are the polar and two principal moments of inertia of the Voronoi cell boundary with respect to the centroid, respectively. The axial and rotational springs are scaled in proportion to the lattice element length h_{ij}, and the area of the Voronoi cell boundary A_{ij}. Effective (i.e., macroscopic) Poisson ratio can be adjusted by setting α_1 and α_2 for the axial spring coefficients, but a local description of Poisson effect is not realized. For the special case of $\alpha_1 = \alpha_2 = 1$, the Voronoi scaling of the spring coefficients enables the model to be elastically homogeneous under uniform modes of straining, albeit with zero effective Poisson ratio (Bolander and Saito, 1998; Asahina et al., 2011).

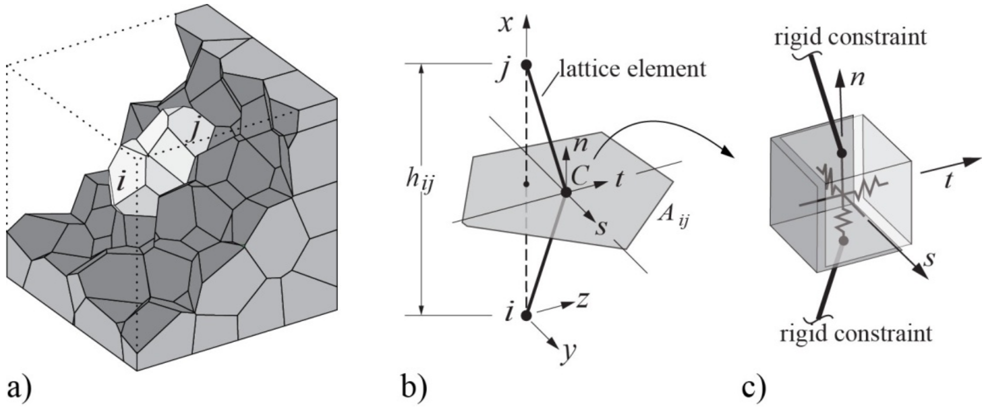

Figure 3.1. Typical RBSN element *ij*: a) within a Voronoi grid; b) isolated from the network; and c) a zero-size spring set located at centroid *C* of Voronoi cell boundary area A_{ij} (rotational springs have been omitted for clarity).

The RBSN model provides a discrete representation of fracture in the matrix material. Crack movement is constrained to occur along cell boundaries; therefore, the lattice orientation is important for the fracture representation. The random lattice geometry based on the Delaunay-Voronoi discretization reduces mesh bias on the cracking directions (Bolander and Saito, 1998).

Fracture is represented by the damage/breakage of the springs. For the damaged spring set, the local stiffness matrix is

$$\mathbf{D}' = (1 - \omega)\mathbf{D} \tag{3.2}$$

where ω is a scalar damage index with a range from 0 (undamaged) to 1 (completely damaged). In the modeling of brittle fracturing, which is applied to the cases presented in this report, ω is either 0 or 1. Fracture may initiate within a lattice element when the applied stress exceeds the given material strength. To determine the stress state, a stress ratio is calculated for each lattice element:

$$R_f = \sigma_e / \hat{\sigma} \tag{3.3}$$

where σ_e is the measure of the element stress and $\hat{\sigma}$ is the material strength. During iterative calculations, only one element, with the most critical stress state (i.e., the largest $R_f \geq 1$), is allowed to break per iteration, and the fracture event entails a reduction of spring stiffnesses (Equation (3.2)) and a release of the associated elemental forces.

In this study, a Mohr-Coulomb criterion is used to determine the fracture event. Figure 3.2 shows the fracture surface defined by three parameters: the angle of internal friction ψ (surface inclination with respect to σ_n-axis); cohesive strength c (surface intersection with the shear axes); and the tensile strength f_n (tension cut-off). Nodal displacements produce forces F_n, F_s, and F_t in the respective axial springs, and dividing these spring forces by the cell boundary area A_{ij} yields measures of stress $P(\sigma_n, \sigma_s, \sigma_t)$. The criticality of the stress state is assessed as $R_f = \overline{OP}/\overline{OP_O}$, where P_O is the point at which $\overline{OP}$ intersects the fracture surface.

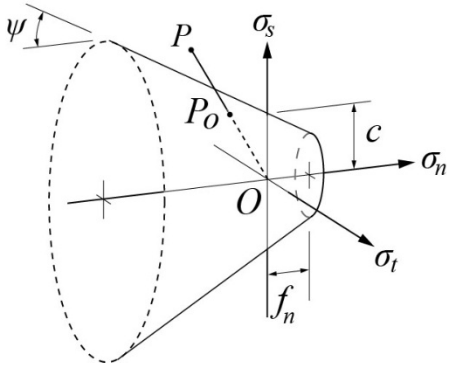

Figure 3.2. Mohr-Coulomb fracture surface with tension cut-off.

3.2 Representation of Anisotropy

Most sedimentary and metamorphic rocks (e.g., shales and slates) have directional features such as bedding, foliation, and flow structures that result in anisotropic mechanical behavior. These types of rocks usually exhibit transversely isotropic elastic properties in macro-scale. For example, Young's modulus parallel to bedding of the Opalinus Clay has been observed to be greater than normal to the bedding (Bossart, 2012). Anisotropic features may also be found in strength properties. In this section, a new scheme is proposed to represent the anisotropic rock properties in the RBSN model. The novelty of the new modeling scheme is the use of unstructured Voronoi grids without manipulating the mesh geometry, and straightforward formulations to construct the local stiffness matrix reflecting the anisotropy.

3.2.1 Anisotropic elastic properties

Figure 3.3 shows the arrangements of spring sets within a Voronoi grid and the corresponding lattice elements. A 2-D modeling case is illustrated to simplify visualization of the geometry, but the method is applicable to 3-D. In the ordinary RBSN model, the spring sets are oriented to their individual local coordinates defined by the Voronoi diagram (Figure 3.3a, and refer to Figure 3.1 for 3-D formations). In the new scheme, by comparison, all the spring sets are aligned to the principal bedding direction. The spring coefficients are defined in global fabric coordinates, where two orthogonal *N*- and *P*-axes are normal and parallel to bedding, respectively (Figure 3.3b). The formulation of the spring coefficients is based on the local geometry of the Voronoi diagram and a logical extension to Equation (3.1) for anisotropic materials. Transversely isotropic elastic properties are calculated by using two different Young's moduli related to the bedding direction:

$$k_N = E_N \frac{A_{ij}}{h_{ij}}, \quad k_P = E_P \frac{A_{ij}}{h_{ij}}, \quad k_\phi = E_N \frac{I_\phi}{h_{ij}} \tag{3.4}$$

where E_N and E_P are Young's moduli normal and parallel to bedding, respectively, which can be directly determined from laboratory measurements.

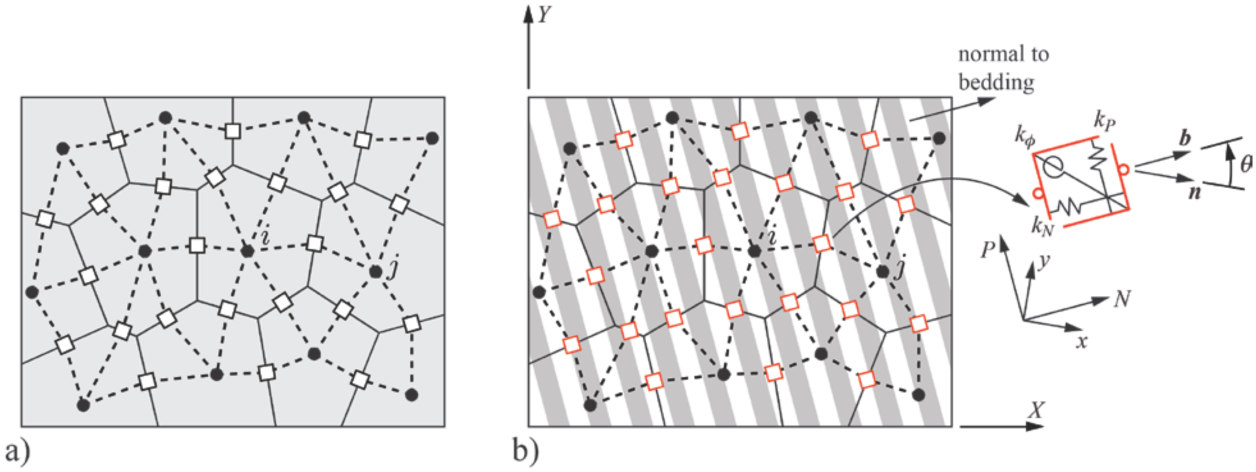

Figure 3.3. Arrangements of the spring sets in the identical lattice structure: a) the ordinary RBSN approach representing isotropic materials; and b) modified orientation of spring components with transversely isotropic elastic properties.

As seen in Figure 3.3b, three distinct coordinate systems are considered for representation of kinematic quantities: global *X*-*Y* coordinates based on domain construction; local *x*-*y* coordinates for individual elements; and global *N*-*P* coordinates related to the orientation of fabric. For each spring set, the spring stiffness matrix is established in *N*-*P* coordinates:

$$\mathbf{k}_b = \begin{bmatrix} k_N & & \\ & k_P & \\ & & k_\phi \end{bmatrix} \tag{3.5}$$

Although the derivation is invariant to coordinate systems, it is more convenient for matrix formulation to represent and manipulate the stiffness quantities in local *x*-*y* coordinates rather than in global *N*-*P* coordinates. Thus the spring stiffness matrix, $\mathbf{k}_b$, is transformed to local *x*-*y* coordinates using following coordinate transformation (McGuire and Gallagher, 1979):

$$\mathbf{k}_s = \boldsymbol{\gamma}^T\, \mathbf{k}_b\, \boldsymbol{\gamma} \tag{3.6}$$

where $\boldsymbol{\gamma}$ is the 3×3 coordinate transformation matrix from local (*x*-*y*) to global fabric (*N*-*P*) coordinates:

$$\boldsymbol{\gamma} = \begin{bmatrix} Nx & Ny & 0 \\ Px & Py & 0 \\ 0 & 0 & 1 \end{bmatrix} \tag{3.7}$$

The first 2×2 entries in $\boldsymbol{\gamma}$ are the direction cosines between the bedding direction and the local coordinate axes.

The element stiffness matrix, $\mathbf{k}_e$ (with respect to local *x*-*y* coordinates), is obtained by post- and pre-multiplication of $\mathbf{k}_s$ by the geometric transformation matrix that relates the generalized relative displacements at the spring set to the nodal displacements. Detailed formulation is presented elsewhere (Bolander and Saito, 1998; Berton and Bolander, 2006).

Finally, the element stiffness matrix is transformed to global coordinates in a similar way to Equation (3.6):

$$\mathbf{K}_e = \boldsymbol{\Gamma}^T\, \mathbf{k}_e\, \boldsymbol{\Gamma} \tag{3.8}$$

where $\mathbf{\Gamma}$ is the coordinate transformation matrix from global domain (X-Y) to local (x-y) coordinates. The transformed element stiffness matrices, $\mathbf{K}_e$, for individual lattice elements are assembled into the system stiffness matrix.

3.2.2 Anisotropic failure properties

Anisotropic strength in failure behavior is represented in the RBSN with an anisotropic version of the Mohr-Coulomb criterion. On the notion of microstructure of the RBSN model, the anisotropy of the strength parameters is represented based on the relative rotation θ, between normal to bedding and normal to the Voronoi cell boundary (Figure 3.3b). The dot product of the unit vectors in these two directions gives

$$\cos\theta = \boldsymbol{b} \cdot \boldsymbol{n} \tag{3.9}$$

Spatial variations of the strength parameters are calculated as linear scalar functions of the fabric tensors. The concept of the fabric tensor is introduced by Pietruszczak and Mroz (2001). The diagonal entries of the fabric tensor, representing the spatial bias of the strength parameters, are summed to be zero. For the Mohr-Coulomb fracture criterion, the friction angle, cohesion, and tensile strength can be calculated respectively as

$$\psi = \psi_0[1 + \Omega^{\psi}(1 - 3\cos^2\theta)] \tag{3.10}$$

$$c = c_0[1 + \Omega^{c}(1 - 3\cos^2\theta)] \tag{3.11}$$

$$\sigma = \sigma_0[1 + \Omega^{\sigma}(1 - 3\cos^2\theta)] \tag{3.12}$$

where ψ_0, c_0, and σ_0 are constant coefficients; and Ω^{ψ}, Ω^{c}, and Ω^{σ} are the intensities of anisotropy. Equations (3.10), (3.11), and (3.12) can be written in a generalized form as

$$s = s_0[1 + \Omega(1 - 3\cos^2\theta)] \tag{3.13}$$

The strength parameter becomes the minimum $s_{min} = s_0(1 - 2\Omega)$ when the Voronoi cell boundary is parallel to the bedding plane (i.e., $\theta = 0^{\circ}$), and the maximum $s_{max} = s_0(1 + \Omega)$ when the Voronoi cell boundary and the bedding plane are orthogonal (i.e., $\theta = 90^{\circ}$). Then, Equation (3.13) can be rewritten as

$$s = s_{min}\cos^2\theta + s_{max}(1 - \cos^2\theta) \tag{3.14}$$

This spatial correlation function serves the local failure with some preferred characteristics in accordance with the orientation of fabric. By virtue of the random geometry of the Voronoi grid, the model can inherently represent heterogeneity as well as anisotropy in the failure behavior of geomaterials.

3.3 Coupled THM Models using TOUGH-RBSN Simulator

3.3.1 Coupling procedure

This section describes the linkage between the multiphase flow simulator TOUGH2 and the RSBN model. Several advantages of the coupled TOUGH-RBSN simulator stem from the availability of sharing the same geometrical mesh structure based on the Voronoi discretization techniques (Okabe et al., 2000), which allow representation of dynamically forming discrete fracture networks (DFNs) within a rock matrix in a simple and straightforward manner.

Rutqvist et al. (2002) have developed the TOUGH-FLAC software, which is based on linking TOUGH2 with FLAC3D, a continuum geomechanical modeling code. The general coupling procedure of TOUGH-RBSN is basically similar to that of the TOUGH-FLAC simulator, but the coupling modules to handle the thermal-hydrological and mechanical quantities are substantially modified and extended for modeling the existence of the DFNs. TOUGH2 is used to simulate scalar quantities (e.g., temperature, pressure, and degree of saturation) associated with fluid flow and heat transport, whereas RBSN accounts for mechanical quantities (e.g., displacement, strain, and stress) of interest. Such primary variables are coupled through simplified linear relationships or through nonlinear empirical expressions, which could be estimated by laboratory experiments with appropriate calibration. As previously noted, both models share the same unstructured, 3-D Voronoi grid and the same nodal information, which simplifies their data exchange.

Figure 3.4 shows a schematic flow diagram of the coupling procedure between TOUGH2 and RBSN, which are currently linked through external modules that handle two-way coupling of the relevant quantities at each time step. First, the TOUGH2 to RBSN link, shown on the left side of Figure 3.4, supplies multiphase pressure, temperature, and degree of saturation to update the mechanical quantities. For multiphase liquid, the choice of the definition of pore pressure is problem-specific and depends on the target materials. Various approaches to determine the pore pressure have been exampled elsewhere (Rutqvist et al., 2001a; 2011; Vilarrasa et al., 2010).

The stress applied to the lattice element is modified by the general conventional effective stress law of Biot's theory (Biot and Willis, 1957):

$$\sigma' = \sigma + \alpha_p P \tag{3.15}$$

where σ is the total stress obtained from overall loading, including external loads; σ' is the effective (grain-to-grain) stress; α_p is the Biot effective stress parameter; and P is the pore pressure. Note that the effective stress concept is valid only for the normal stress terms, and tensile stress is taken to be positive. In incremental form, Equation (3.15) becomes

$$\Delta\sigma' = \Delta\sigma + \alpha_p(\Delta P_i + \Delta P_j)/2 \tag{3.16}$$

where ΔP_i and ΔP_j are the changes in pore pressures over the time step at neighboring nodes *i* and *j*.

It is assumed that the local changes in temperature and liquid saturation induce strain as follows:

$$\Delta\varepsilon_T = \alpha_T(\Delta T_i + \Delta T_j)/2 \tag{3.17}$$

$$\Delta\varepsilon_s = \alpha_s(\Delta S_i + \Delta S_j)/2 \tag{3.18}$$

where ε_T is thermal strain; ε_s is shrinkage/swelling strain; α_T is the coefficient of linear thermal expansion; and α_s is the hydraulic shrinkage coefficient. The changes in temperature and saturation are averaged from the variables at nodes *i* and *j*. If an expansible soil material is subjected to constant stress conditions in an elastic region, the effective stress due to thermal and swelling/shrinking strains can be calculated as

$$\Delta\sigma' = (\Delta\varepsilon_T + \Delta\varepsilon_s)E \tag{3.19}$$

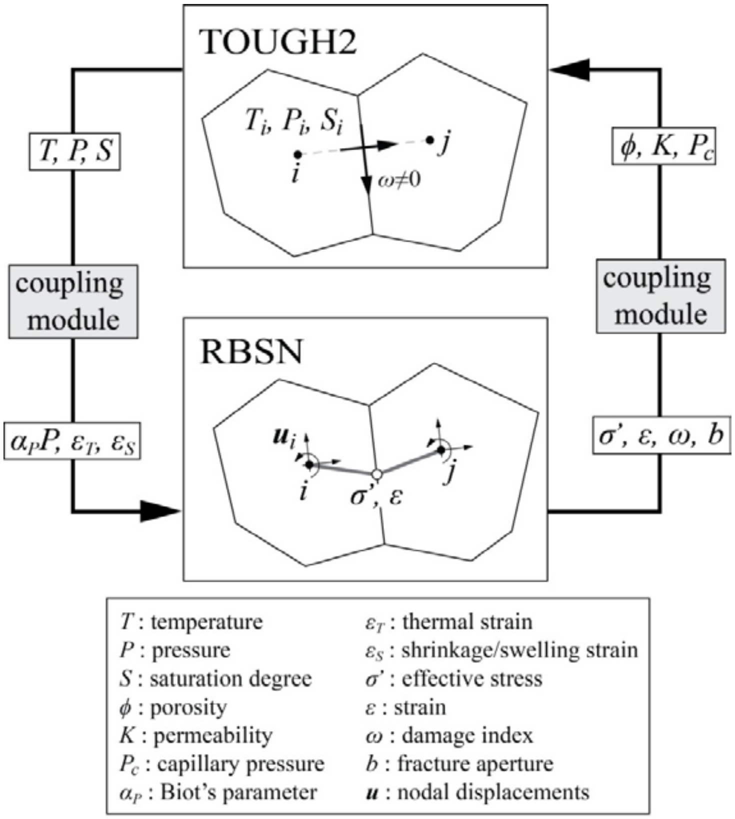

Figure 3.4. Flow diagram of the linkage between the TOUGH2 and the RBSN for coupled THM simulations.

Thereafter, the RBSN to TOUGH2 link, shown on the right side of Figure 3.4, supplies vectorial variables for the effective stress and the strain calculated at the lattice element to update the hydrogeological properties of the corresponding Voronoi cells i and j in the TOUGH2 model. The following general relations are considered (Rutqvist and Tsang, 2002):

$$\phi = \phi(\boldsymbol{\sigma}', \boldsymbol{\varepsilon}) \tag{3.20}$$

$$K = K(\boldsymbol{\sigma}', \boldsymbol{\varepsilon}) \tag{3.21}$$

$$P_c = P_c(\boldsymbol{\sigma}', \boldsymbol{\varepsilon}) \tag{3.22}$$

where ϕ is porosity, K is permeability, and P_c is capillary pressure.

In the TOUGH2 model using an ordinary Voronoi grid to represent an intact rock matrix, flow and mass transport are enacted only between nodes i and j, across the Voronoi cell boundary. However, if a fracture occurs within the matrix, substantial flow and mass transport may happen along the fracture length. As an integrated finite volume method, TOUGH2 allows for flexible gridding that can accommodate representation of fractures or fracture networks embedded within the matrix (Zhang et al., 2004; Rutqvist et al., 2013a). By utilizing a discrete fracture approach, continuity of the fracture is not assumed but rather explicitly modeled. A flow through the discrete fracture is activated in response to the damage/breakage of the lattice element from the RBSN simulation (i.e., $\omega \neq 0$). Following Darcy's law, the intrinsic permeability of an individual fracture can be based on a parallel-plate model which relates fracture permeability to fracture aperture b (Bear, 1972). Details about forming fractures and their interconnections within Voronoi grids are presented in the next section.

3.3.2 Discrete representation of flow and mass transport in fractured media

In this study, a fracture is considered to be a discrete feature that facilitates flow and mass transport. Such crack-assisted flow and its permeation into the surrounding matrix are explicitly represented. Pre-existing or newly generated fractures are directly mapped onto the Voronoi grid representing the spatial domain of the geomaterial system. Descriptors of the fracture geometry (e.g., fracture orientation, length, width, shape) can be obtained by field mapping, computer-generated statistical representations, or the simulation outcomes of mechanical models. With reference to the 2-D case, a straight-lined fracture is discretized as follows (Figure 3.5):

- Discretize the spatial domain with an irregular Voronoi grid.
- Overlay the reference fracture onto the Voronoi grid.
- Select node-node (natural neighbor) connections that cross the reference fracture. The corresponding Voronoi cell boundaries of such nodal connections represent the reference fracture.

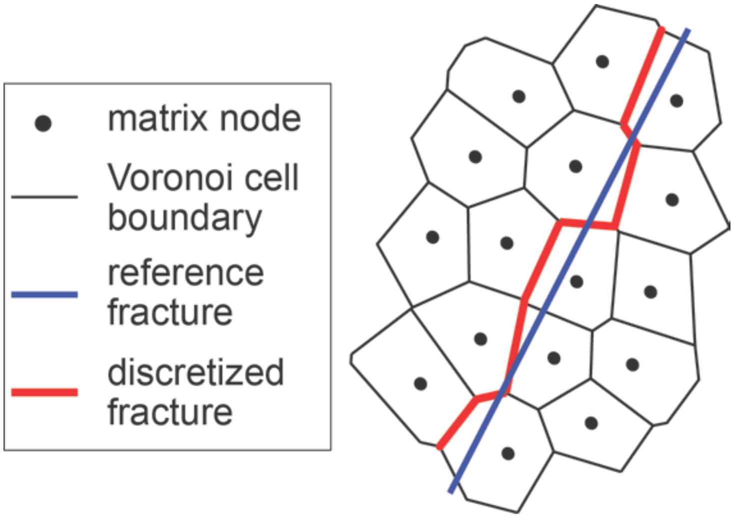

Figure 3.5. Mapping of a fracture geometry onto an irregular Voronoi grid.

The grid size should be selected to obtain a sufficiently accurate representation of the fracture line. As the density of nodal points increases, the discretized fracture path more closely resembles the reference line. By repeating the above process for multiple fractures, a network of discrete fractures can be generated. The advantages of this DFN generation approach include the abilities to: (1) simply activate and connect new discrete fractures; (2) automatically handle discrete fracture intersections; (3) control mesh size with a graded nodal density, which can be advantageous for reducing computational expense; and (4) straightforwardly extend to more complicated 3-D geometries.

Dynamically forming flow channels (i.e., discrete fractures) are implemented by introducing fracture nodes and the associated connections in addition to matrix nodes and connections within the Voronoi grid (Figure 3.6). A fracture node is inserted at the intersection of a Voronoi cell boundary and a connection between two adjacent matrix nodes. The original matrix-matrix connection is divided into two matrix-fracture (and vice versa) connections by the newly generated fracture node. In addition, the connections between the fracture nodes are established to represent flow channels through the fracture networks. The hydrological properties of an individual fracture can be based on the grid geometry and the local fracture aperture computed by a mechanical-damage model. In the following simulations, however, the fracture permeability is simply assigned to be constant and very high relative to the permeability of the rock matrix.

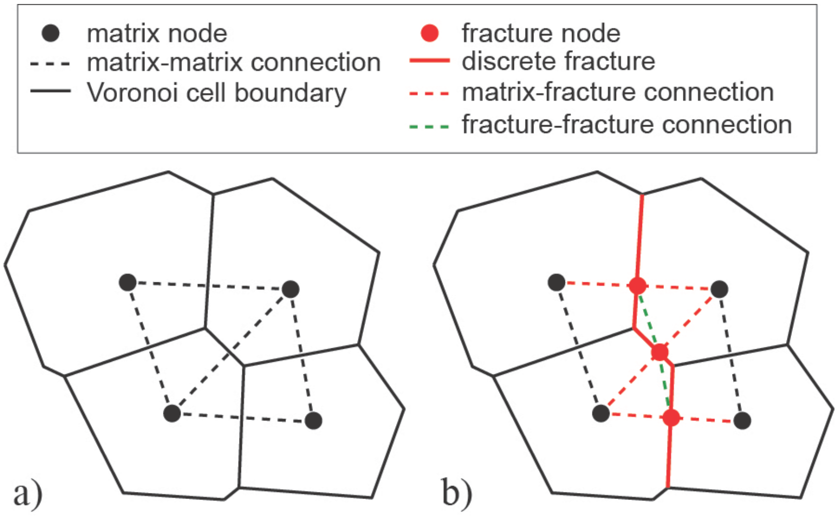

Figure 3.6. Nodal connectivity in the DFN approach for flow simulations: a) ordinary matrix nodes and connections; and b) additional fracture nodes and connections.

3.4 Mechanical Simulations of Transversely Isotropic Rock Formations

3.4.1 Uniaxial compression tests

The modeling scheme proposed in Section 3.2 is validated through uniaxial compression tests for transversely isotropic rock specimens. Consider 2-D configurations of a cylindrical core sample subjected to unconfined uniaxial compression, in which the loading direction forms an angle relative to the bedding plane, β (see Figure 3.7a). In laboratory experiments, the drilling direction for core sampling determines the angle between the axial loading direction and the bedding direction. The simulations consider seven cases of the orientation of fabric: $\beta = 0^\circ, 15^\circ, 30^\circ, 45^\circ, 60^\circ, 75^\circ, 90^\circ$. The model is discretized with about 3,800 nodal points and 10,000 elements. Boundary conditions are assigned at top and bottom layers of cells. Incremental loading is applied at the top layers by displacement control and the bottom layers are fixed. Herein the anisotropic mechanical properties of the rock material are adopted from the experimental results for the Opalinus Clay (Bossart, 2012), which are arranged in Table 3.1.

Table 3.1. Anisotropic mechanical properties of the Opalinus Clay (Bossart, 2012).

Rock mechanical properties	Parallel to bedding	Normal to bedding
Young’s modulus [GPa]	15.5	9.5
Uniaxial tensile strength [MPa]	2.0	1.0
Cohesion (shear strength) [MPa]	5.5	2.2
Internal friction angle [°]	25	

Note: In Bossart (2012), the experiments on cohesion or shear strength are reported for three different parameters: minimum value of 2.2 MPa (normal bedding), maximum value of 5.5 MPa (parallel bedding), and the third value of 1 MPa (shear strength of bedding planes). In this study, 2.2 MPa is taken as cohesion normal to bedding as stated.

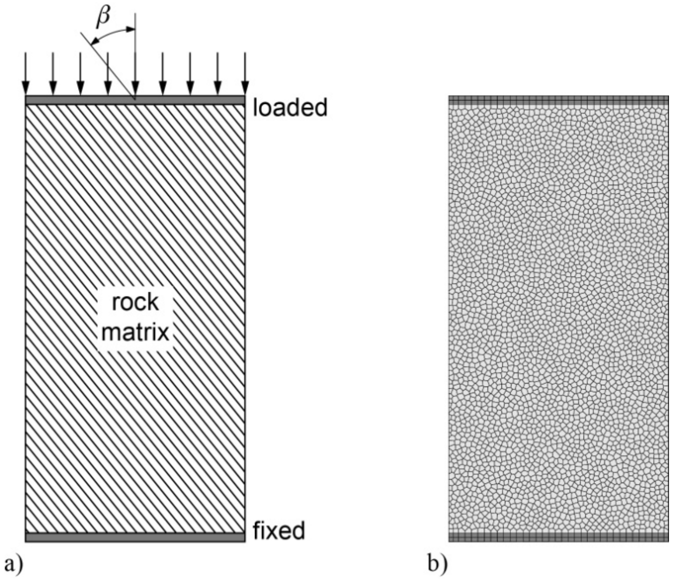

Figure 3.7. 2-D specimen for uniaxial compression test: a) schematic drawing of the test program; and b) model discretization.

The resulting stress-strain curves are plotted in Figure 3.8. The stress response is calculated by dividing the sum of reaction measured at the fixed layers of cells by the cross sectional area of the specimen. In the elastic region, the stress response linearly increases with strain. In the post-peak region, the models exhibit brittle behavior. Once the first breakage (i.e., fracture initiation) occurs at the most critical element, the neighboring elements undergo knock-on breakage even without increasing load/displacement. After sufficient elements have broken to release the energy in the fracture process, the fracture becomes stable in the sense that small load increments no longer produce bursts of elemental breakages. The unstable fracture process can be controlled by introducing softening/energy release rate of fracture in the post-peak behavior.

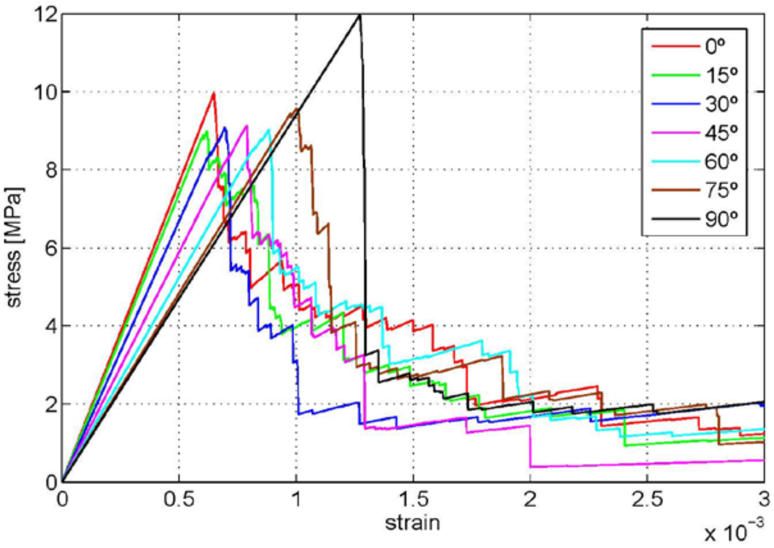

Figure 3.8. Stress-strain curves of transversely isotropic rock specimens with various orientations of bedding with regard to the loading direction.

The anisotropy of the elastic properties can be found in bulk Young's moduli, the slopes of linearly ascending branches in the stress-strain curves of Figure 3.8. Theoretically, the bulk Young's modulus at angle to bedding β can be obtained by (Pariseau, 2006):

$$\frac{1}{E} = \frac{\cos^4\beta}{E_P} + \left(\frac{1}{G_{12}} - \frac{2\nu_{12}}{E_P}\right)\sin^2\beta\ \cos^2\beta + \frac{\sin^4\beta}{E_N} \tag{3.23}$$

where G_{12} is shear modulus and ν_{12} is Poisson ratio. Equation (3.23) shows that the shear modulus greatly influences the variation in Young's modulus, so the shear modulus of anisotropic rock should be measured rather than estimated (Pariseau, 2006). However, the shear modulus can only be approximated in the RBSN model.

For an isotropic material, the shear modulus is derived from elasticity theory, which shows that

$$G = E/2(1+\nu) \tag{3.24}$$

For $\nu = 0$, $G = E/2$. An approximation of this relationship between shear modulus and Young's moduli for an anisotropic system with $\nu = 0$ is given as

$$G_{12} = 1/(\frac{1}{E_P} + \frac{1}{E_N}) \tag{3.25}$$

With this assumption for Equation (3.23), the variation in Young's modulus is depicted in Figure 3.9 and compared with the simulated bulk Young's moduli, where the two curves show a good agreement.

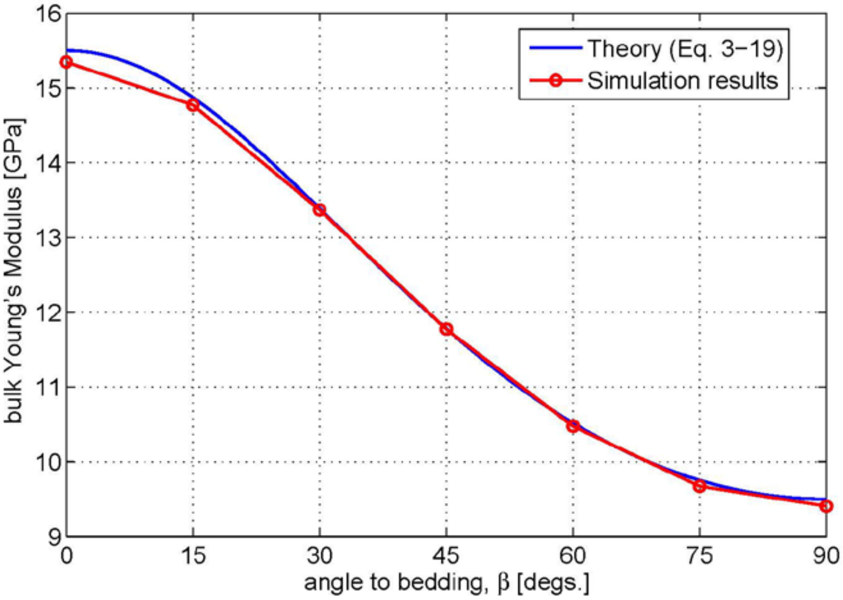

Figure 3.9. Variation of bulk Young's modulus of a transversely isotropic rock.

The peak stress values of the stress-strain curves, plotted in Figure 3.8, can be regarded as uniaxial compressive strengths. A comparison of the peak stresses indicates that the rock exhibits the maximum strength when the bedding is perpendicular to the axial loading (i.e., $\beta = 90^\circ$) and the minimum level of strength in cases of the bedding inclined to the loading direction. Similar interpretations of the compression failure of anisotropic rocks have been presented in other studies (Jaeger, 1960; McLamore and Gray, 1967; Kwaśniewski and Mogi, 2000). Quantitatively, however, the strength values are not accurately simulated. In the experiments, the compressive strengths parallel and normal to bedding are measured as 10.5 MPa and 25.6 MPa, respectively (Bossart, 2012). This discrepancy for the compressive strengths might result from the vague choice for the anisotropic shear strength parameters. Also, the RBSN model has been originally developed for simulating tension-dominated behavior, and the proposed fracture criteria generally account for tension failure, which could lead to some shortcomings in modeling of compression or multi-axial failure behavior (Bolander and Saito, 1998; Berton and Bolander, 2006). Currently, the failure is modeled to be brittle, which means the entire strength is lost at immediate failure. However, a more realistic failure response may result in gradual loss of strength during failure. In addition, contacts between fracture surfaces under compressive loads lead to friction along the fracture surface, which is not appropriately represented in the current model. This problem will be addressed in future studies.

Figure 3.10 shows deformed shapes and fracture patterns of the specimens at the final loading stage with the global strain of 0.003. The specimens with the bedding parallel and perpendicular to the loading direction do not demonstrate apparent directivity of the fracture patterns (Figure 3.10a and g). On the contrary, in the cases of the inclined orientations of fabric, the direction of fracturing appears biased towards the bedding direction (Figure 3.10b to f). This directivity of fracture pattern gets stronger with the bedding angle nearing 45°, in which the inclined major cracks are connected across the specimen. An additional case of the bedding angle $\beta = -15^\circ$ is considered (Figure 3.10h), in which the orientation of fabric has the same amount but the opposite direction of rotation from the vertical axis. As expected, a symmetrical fracture pattern with respect to the vertical axis is presented, in comparison to the case of bedding angle $\beta = 15^\circ$ (Figure 3.10b).

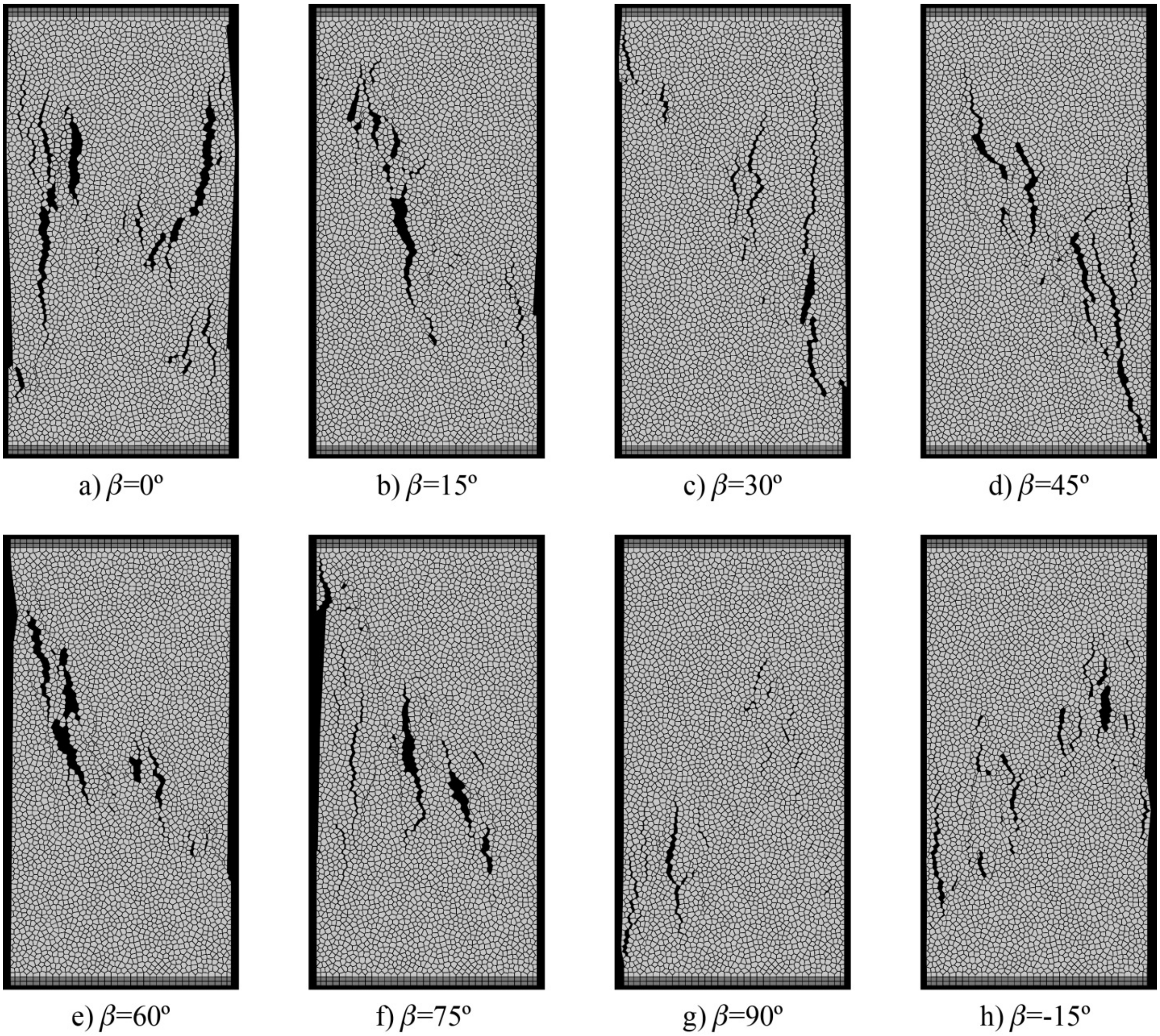

Figure 3.10. Fracture patterns of the specimens with various orientations of fabric forming the angle of β with the loading axis. Note that the positive angle indicates counter-clockwise rotation from the vertical orientation.

In the set of simulations for uniaxial compression tests, the anisotropic characteristics in elastic properties and failure properties are realistically demonstrated. Various bedding angles with respect to the axis of loading are represented by assigning global coordinates related to the orientations of fabric within the same Voronoi grid. By utilizing the proposed modeling scheme, rock materials are represented as macroscopically homogeneous, whereas microscopically, the anisotropic strength parameters, formulated by random local orientations of lattice elements, give intrinsic heterogeneity in failure behavior. This modeling scheme is applied to simulate fracture processes in the excavation damage zone (EDZ) of the HG-A microtunnel, which is presented in the next section.

3.4.2 Fracture damage modeling of the HG-A test

The HG-A test is being conducted on a 13-m long microtunnel of 1 m diameter, located at the Mont Terri underground research laboratory (URL) near Saint-Ursanne, Switzerland. One main purpose of the HG-A test is to provide data on the geomechanical and hydrogeologic effects of the excavation damage zone (EDZ). The test is specifically targeted to observe how fluids injected into a test section sealed by a packer penetrate both into the rock and within the EDZ (Marschall et al., 2006). Although the long-term physical features observed in the test are related to coupled hydro-mechanical processes, as an initial study, herein the problem is simplified by assuming a constant uniform pore pressure such that fracture damage is simulated using the mechanical modeling of the RBSN approach exclusively. This assumption is valid up until the point at which mechanical deformation occurs much more quickly than water flow processes in the rock formation, where mechanical equilibrium is held within a rapid (undrained) excavation (Liu et al., 2013b).

The rock of the test site is relatively homogeneous in meter-scale, but pronounced bedding was discovered at finer scales (Marschall et al., 2006). The rock formation is highly fractured with frequencies of 0.3 to 1 m, although the fracture permeability is not significant, which indicates that fractures are mostly closed under natural stress conditions (Marschall et al., 2006; 2008).

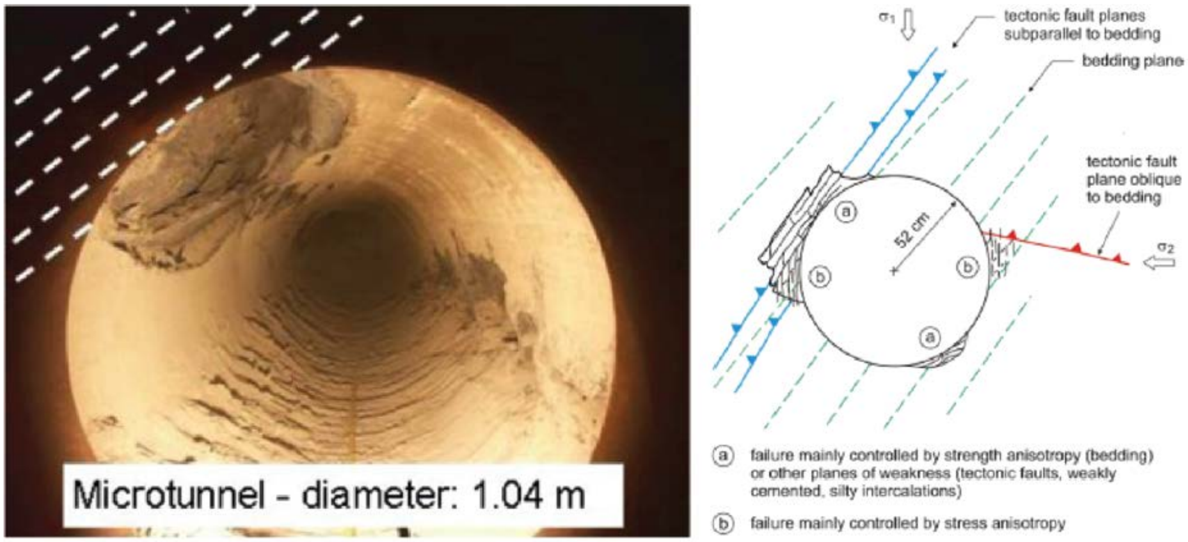

a) b)

Figure 3.11. a) Excavation damage viewing from the HG-A Niche towards back end (Marschall et al., 2006); and b) Conceptual diagram of the damage zone (Lanyon et al., 2009; Marschall et al., 2006).

Figure 3.11 shows excavation damage of the microtunnel. Partial damage and exfoliations have occurred along the microtunnel wall (Figure 3.11a), which are mainly attributed to the anisotropic strength characteristics of the rock. Strength of an anisotropic rock is found to be a function of orientation relative to the bedding plane (Bock, 2001). The relative weakness orthogonal to the bedding and the weakness near faults intercepting the tunnel, as depicted in Figure 3.11b, result in the nonuniform damage around the excavation wall.

The analyses start with the simulation of the elastic stress profiles around the microtunnel under compression condition. Figure 3.12a shows a 2-D square domain with a 10-m long side, where a circular opening with a radius of 0.5 m is placed at the center. The computational domain is discretized with 2044 nodes, and the nodal density is graded for computational efficiency. Far-field compressive stresses are 4.5 MPa in the horizontal direction and 6.5 MPa in the vertical direction (Martin and Lanyon, 2003). First, a homogeneous and isotropic material is considered in order that the simulation results can be verified with analytical solutions (Kirsch, 1898). Young’s modulus and Poisson ratio are 15.5 GPa and 0.3, respectively. In Kirsch's solutions, the stress profiles are expressed as a function of the distance from the center, r and the normal angle, θ. Figure 3.12b compares the simulation results and the analytical solutions of stress profiles for $\theta = 0°$, which shows a good agreement between the two types of solutions.

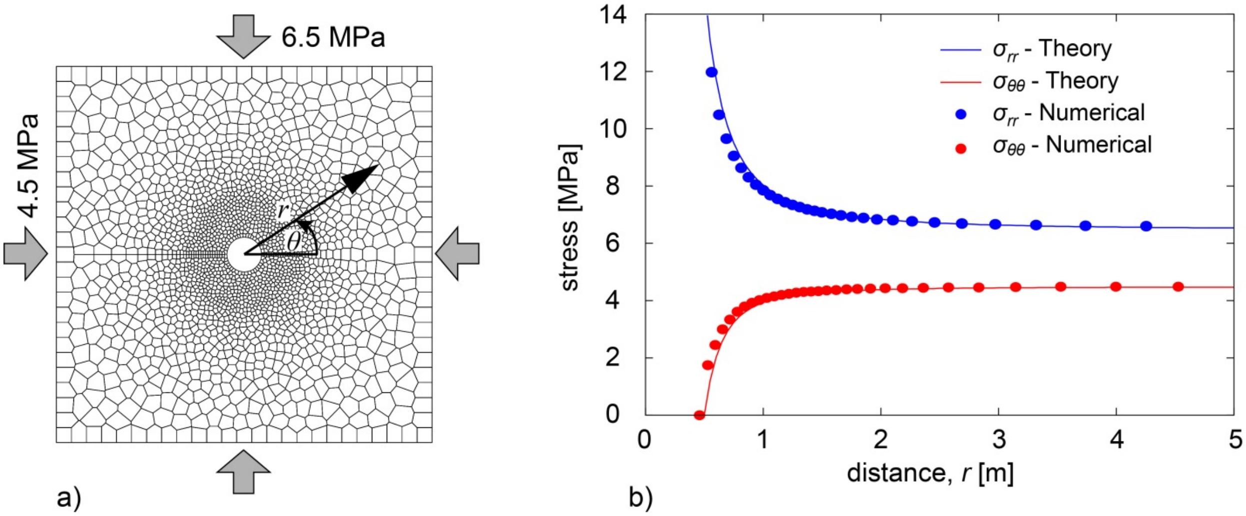

Figure 3.12. a) Discretization of the computational domain and loading configurations; and b) radial and tangential stress values versus the radial distance.

Next, the excavation damage of the HG-A microtunnel is simulated. In Figure 3.12b, we see that the asymptotic stress profiles approach sufficiently close to the far-field stresses at $r = 4$ m. For that reason, the dimension of the computational domain is reduced. Figure 3.13a shows the discretization of the reduced 8×8 m computational domain using a finer Voronoi grid (4042 nodes). External loading configurations are the same as in the previous simulation, and additionally, an internal pore pressure of 1.5 MPa is applied to the matrix volume. Mechanical properties of the Opalinus Clay, summarized in Table 3.1, are used to represent anisotropy of the on-site rock formation. The bedding planes are aligned at 45° from the horizontal axis, which is similar to the orientation of fabric shown in Figure 3.11. Figure 3.13b illustrates the fracture pattern, where the damage occurs mainly around the tunnel. Damaged zones are more prominent at the tunneling wall tangential to the bedding planes, similarly to the failure characteristics seen in Figure 3.11. For identification of failure modes, individual fracture segments are drawn in different colors: blue and red segments represent tensile and shear failure modes, respectively. Tension fracturing is concentrated at the borehole boundary, due to the lack of constraints against the pore pressure acting towards the center of the tunnel. This failure feature can be supported by observation of the deformation around the borehole. Figure 3.13c depicts the deformed shape of the tunnel, in which the deformation is exaggerated for better visibility. Voronoi cells adjacent to the borehole come off the body, which indicates the tensile failure.

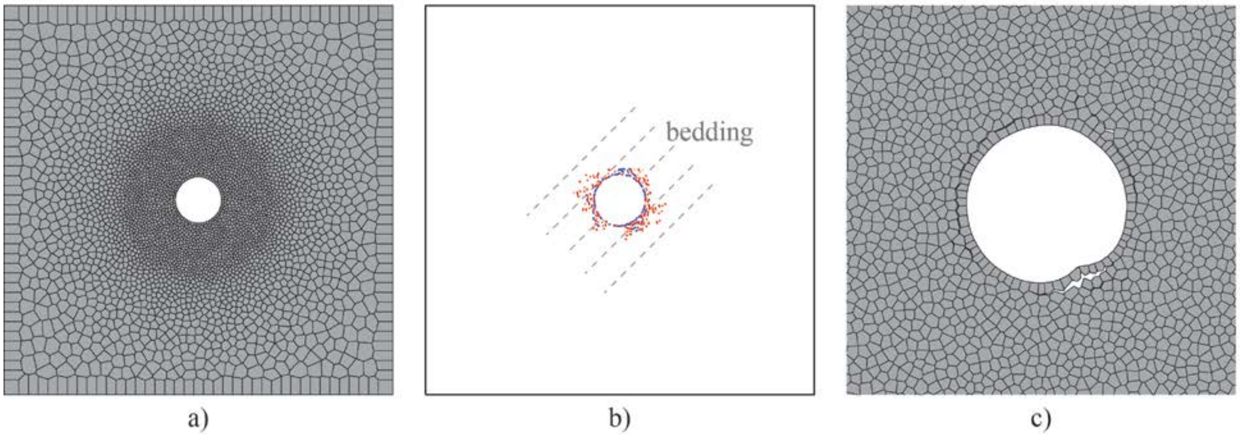

Figure 3.13. a) Discretization of the computational domain for the HG-A test simulation; b) nonuniform fracture pattern around the tunnel; and c) deformed shape of the borehole.

Although the tectonic faults around the tunnel are not modeled in this study, fracture damage process is in qualitative agreement with observations. In future study, the fracture damage process will be quantitatively analyzed along with long-term hydro-mechanical behavior, which is simulated by a coupled THM modeling approach, i.e. the TOUGH-RBSN simulator.

3.5 THM Simulations of Hydraulic Fracturing

This section provides an example application of the TOUGH-RBSN simulator for coupled THM processes, including hydraulic fracturing behavior within a geological system. Consider a 30×30 m domain with a relatively small borehole of 0.15 m diameter, subjected to respective far-field stresses of 45.5 MPa vertically and 34.5 MPa horizontally (Figure 3.14a). The Voronoi grid is generated with a graded nodal density, in which the mesh size around the expected fracturing path is controlled to be much finer (Figure 3.14b). The rock material is assumed to be homogeneous and isotropic with the following mechanical properties: Young’s modulus $E = 11.0$ GPa; tensile strength $f_t = 15.0$ MPa; cohesion $\mathrm{c} = 22.5$ MPa; and internal friction angle $\psi = 45°$. The hydrological properties are as follows: matrix density $\rho = 2{,}500$ kg/m^3; porosity $\phi = 0.06$; and permeability $K = 10^{-15}$ m^2. A pore pressure of 31.0 MPa is used throughout the matrix as the initial condition, and injection of water is conducted at a constant rate 0.18 kg/s per unit thickness.

If a fracture event occurs at a lattice element of the RBSN model, a fracture node and the connections to the surrounding nodes for the TOUGH2 simulation are activated as described in Section 3.3.2, and the porosity and permeability for the fracture node are drastically increased (e.g., $\phi_f = 1.0$ and $K_f = 10^{-6}$ m^2). These hydrological properties for individual fractures can be calculated as a function of fracture aperture; however, for simplicity, herein they are set to be constant, irrespective of the fracture geometries.

Two cases of rock formations are considered for simulations: (1) an intact medium without any pre-existing fracture or damage within the rock matrix, and (2) a fractured medium, in which a 3-m long inclined fracture is included (see Figure 3.14a), so that a newly generated fracture path will meet the pre-existing fracture during the hydraulic fracturing process. The pre-existing fracture retains high porosity and permeability from the initial stage of the simulation. The simulations are performed for a 600 s duration, when the steady-state pressure evolutions at the borehole are attained.

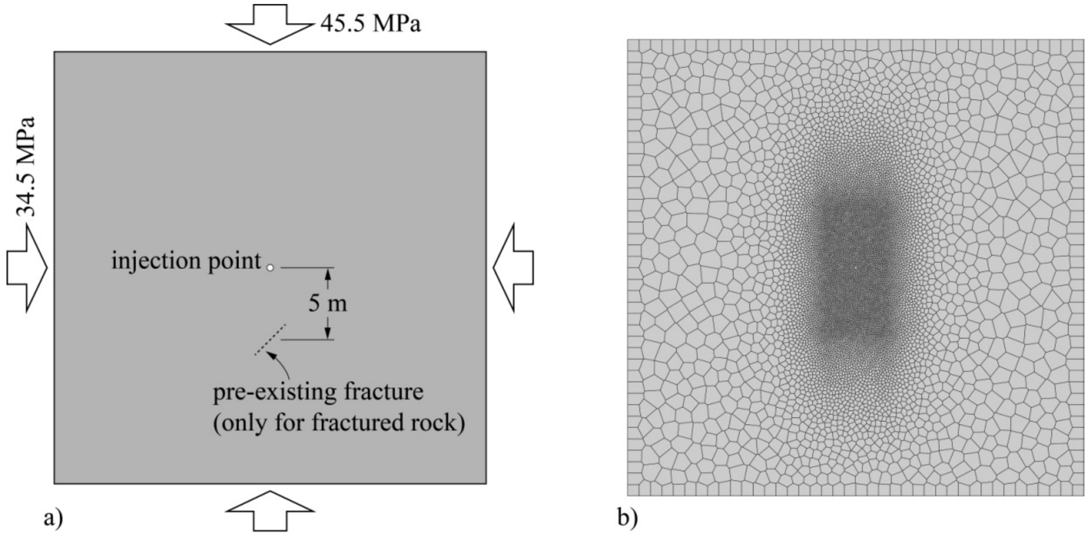

Figure 3.14. Hydraulic fracturing simulation: a) simulation configurations; and b) discretization of the computational domain.

Figure 3.15 compares the resulting fracture developments at the final stage for the two cases of simulations. In both cases, a single major crack stretching out from the borehole forms in the direction of maximum compressive stress, which represents tensile failure. As shown in Figure 3.15b, a distinctive bend in the fracture is observed near the inclined pre-existing fracture. The opening of the pre-existing fracture is not pronounced due to the shear movement along the fracture path.

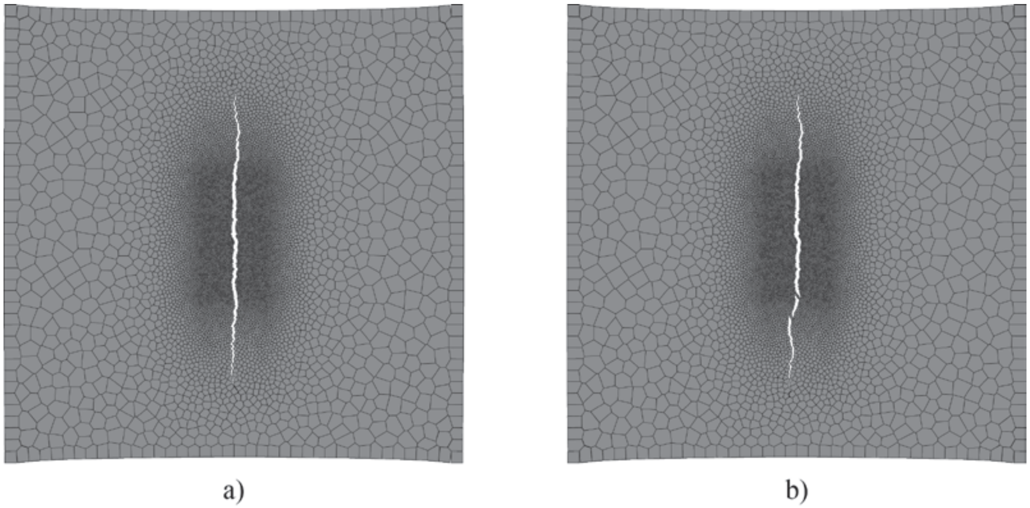

Figure 3.15. Comparison of fracture paths in deformed shapes of the domain: a) intact rock matrix; and b) fractured rock matrix.

Figure 3.16 arranges snapshots of pressure distributions, captured at the point of fracture initiation, at the early and the latter stages of fracture propagation, based on the length of the fracture, and at the final stage of the simulation, where the real time is specified in seconds. Up until fracture initiation, local pressure at the borehole increases due to the water injection (Figure 3.16a). The intact rock exhibits fracture initiation 16 s sooner than the fractured rock. The delayed fracture initiation results in greater energy stored in the matrix around the borehole for the case of the fractured rock. Therefore the fracture develops more rapidly after initiation. As the fracture propagates, the pressure at the borehole is directly transferred into the fracture path (Figure 3.16b). Figure 3.16c describes the effect of the pre-existing fracture on the hydraulic fracturing process. Hydraulic fracturing keeps proceeding through the intact rock matrix, whereas in the fractured rock, the propagation of downward fracture hitting the pre-existing fracture is arrested. The flow channels along the discrete fractures are connected to reduce the pressure gradient that promotes the fracturing process at the crack tip, thus the fracture development is slowed down. Figure 3.16d shows pressure contours in the shape of the final fracture path, in which the percolating water flow, from the fracture surface towards surrounding matrix, diffuses the concentrated pressure.

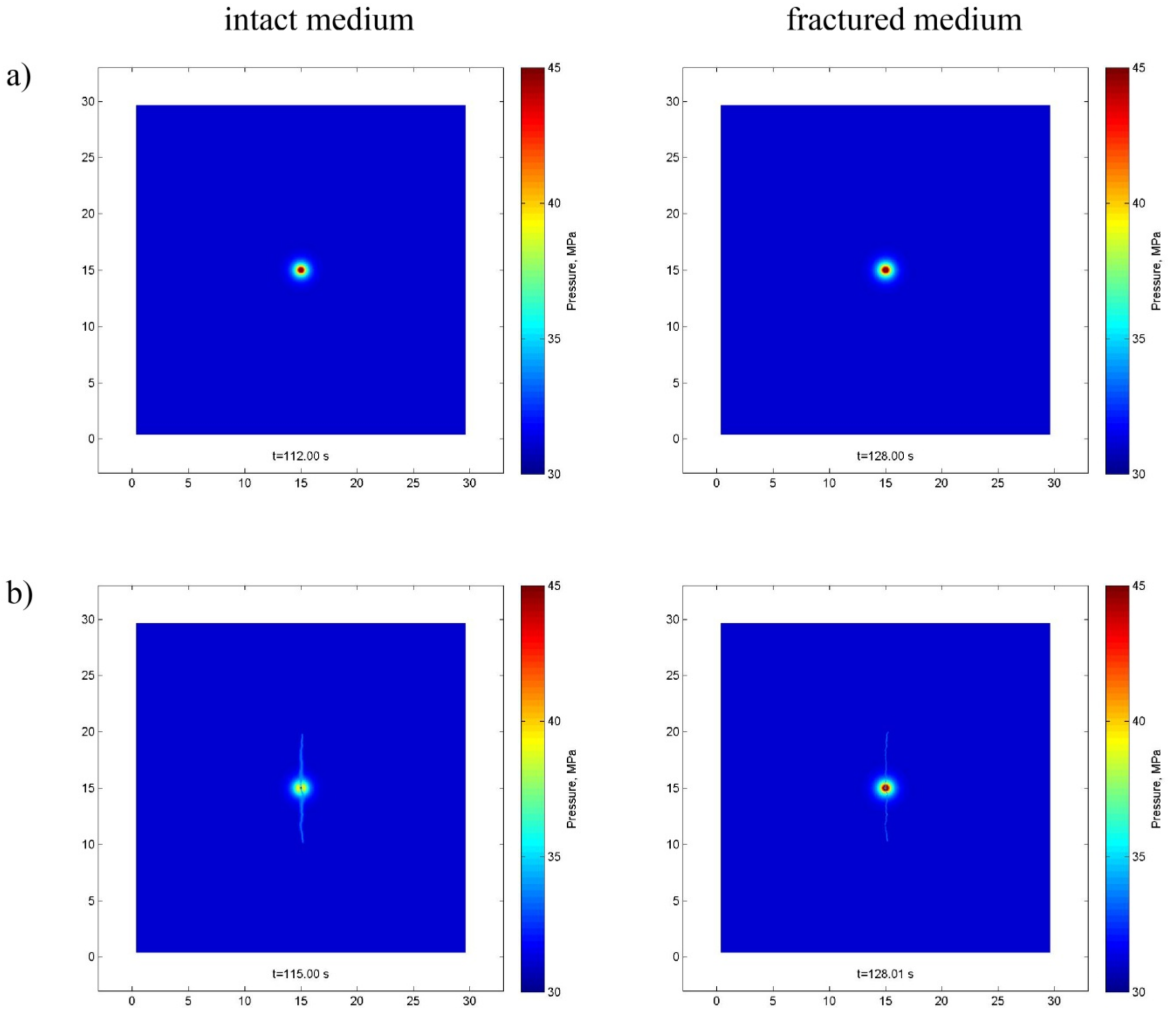

Figure 3.16. Pressure contour evolutions for intact and fractured rock formations: a) at the point of fracture initiation; and b) at the early stage of fracture propagation.

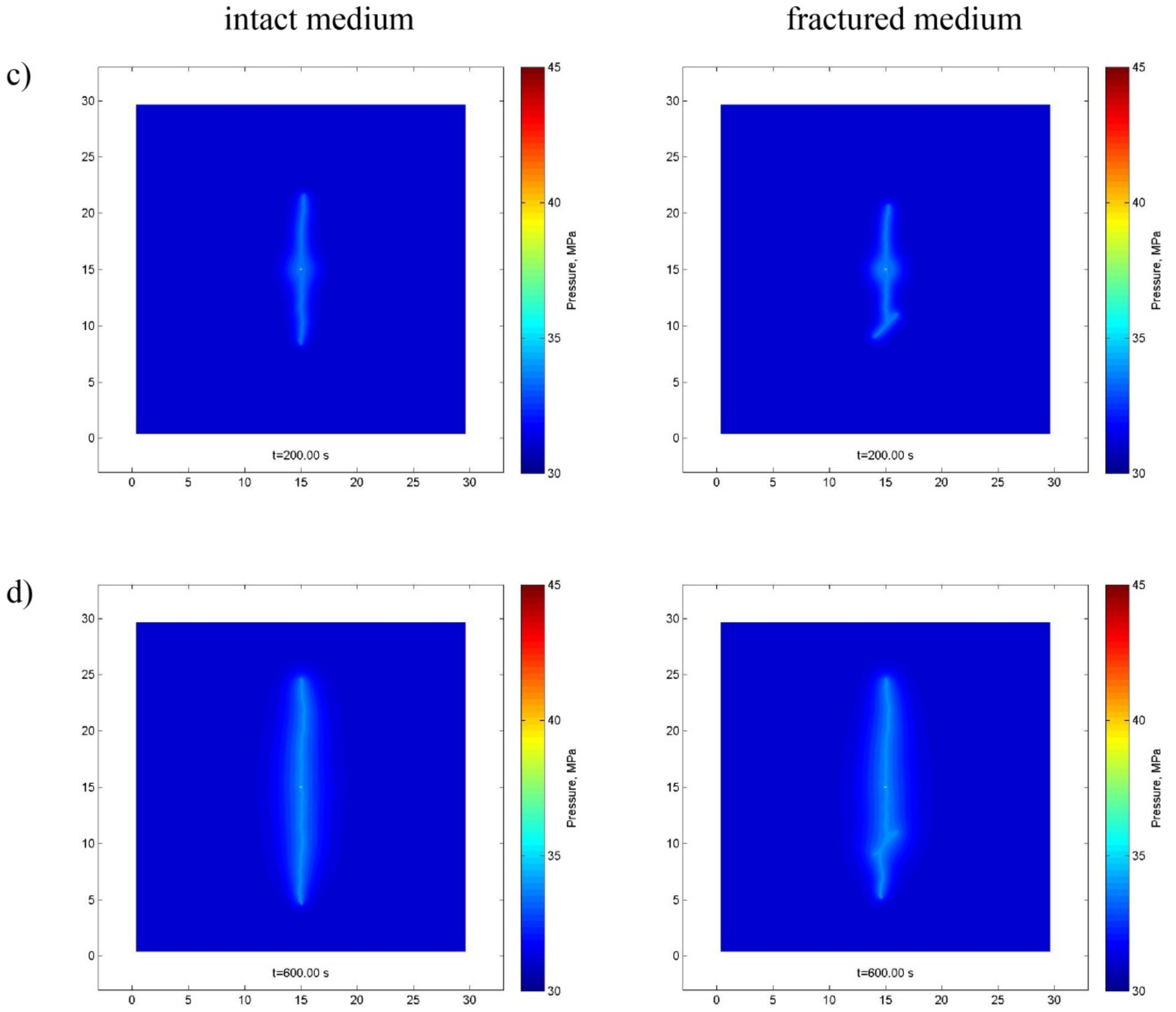

Figure 3.16. (continued). Pressure contour evolutions for intact and fractured rock formations: c) at the latter stage of fracture propagation; and d) at the final stage of the simulation.

This simulation example demonstrates the capabilities of the developed modeling approach for the coupled THM processes in geological systems. The mechanical effect of the excessive pressure produced by water injection (i.e., induced hydraulic fracturing) and the preferential flow features through the newly generated fracture path are realistically represented. As seen in the case of the fractured medium, the pre-existing fracture exerts a considerable influence on the flow behavior as well as on the mechanical behavior of the system, such that the fracturing process is disturbed. In the future, parametric studies on the hydro-mechanical effects of fracture networks can be done for various sizes, shapes, locations, and orientations of the fractures.

3.6 Conclusions

This study uses the RBSN approach to model geomechanical behavior including fracturing. The model provides a discrete representation of material elasticity and fracture development, and in that respect, it is considered to be suitable for the DFN approach to investigating fracturing processes. However, the original RBSN is limited to macroscopically modeling isotropic materials, or requires additional treatments in partitioning the domain (e.g., layering of individually isotropic materials) for introducing anisotropic mechanical properties.

To extend the applicability of the model to general anisotropic geomaterials, we propose a new modeling scheme. Elastic spring coefficients and strength parameters are systematically formulated for individual lattice elements based on the principal bedding direction, which facilitate a straightforward representation of anisotropy. Uniaxial compression tests are simulated for a transversely anisotropic material, the Opalinus Clay, to demonstrate the validity of the new modeling scheme. Thereafter, a simulation of fracture damage around the EDZ of the HG-A microtunnel is conducted. Qualitatively the simulation results closely match the physical observations, in which nonuniform damage, due to the anisotropic mechanical characteristics, forms around the excavation wall.

The behavior of strongly coupled THM processes has also been investigated using the TOUGH-RBSN simulator. We have established an effective linkage between the TOUGH2 code based on the finite volume method for simulating heat and mass transport within porous rock formations, and the RBSN method for simulating mechanical responses and fracture initiation and propagation. One main advantage of linking TOUGH2 and the RBSN is that both models utilize the same set of nodal points, along with the natural neighboring connections and the volume rendering definitions, according to the unstructured Voronoi discretization. The capabilities of the TOUGH-RBSN simulator are shown through simulation of hydraulic fracturing. In the simulations, two-way coupling of the THM variables produces realistic hydro-mechanical behavior in the fracturing process.

4. THM Modeling of Underground Heater Experiments

In this section, we present LBNL’s activities related to THM modeling of underground heater experiments in clay formations, including studies related to the Development of Coupled Models and their Validation against Experiments (DECOVALEX)-2015 project and the Mont Terri FE (Full-scale Emplacement) Experiment.

DECOVALEX-2015 is an acronym for the 6th and current phase of the “Development of Coupled Models and their Validation against Experiments” project, ongoing from 2012 to 2015. In DECOVALEX-2015, LBNL participates in Task B, which includes:

Subtask B1—Mont Terri HE-E Experiment: A heating experiment to evaluate sealing and clay-barrier performance, in a micro-tunnel at the Mont Terri URL in Switzerland; and

Subtask B2—Horonobe Engineered Barrier System (EBS) Experiment: A heating experiment to study the thermo-hydro-mechanical-chemical (THMC) behavior of the EBS and its interaction with the mudstone host rock, in a vertical emplacement hole at the Horonobe URL in Japan

In addition to the modeling work in these two DECOVALEX tasks, LBNL participates in the Mont Terri FE Experiment as one of the participating modeling teams. The FE Experiment is undertaken as an ultimate test for the performance of geologic disposal in Opalinus Clay, with focuses on both the EBS components and the host-rock behavior; it will be one of the largest and longest running heater tests worldwide.

UFD objectives for participating in these international activities are to develop expertise and test advanced models on coupled processes in clay-based backfill in interaction with clay host rock. Through participation in modeling these field experiment, the models will be developed and experience will be gained for a range of different backfill materials (e.g., bentonite pellets and sand/bentonite mixture), as well as different host rocks (e.g., Opalinus clay and mudstone).

In the following Subsection 4.1, the modeling approach and the status of model development will be summarized. Then the modeling work conducted associated with field experiments are presented in Subsections 4.2 through 4.4. Finally, in Subsection 4.5, the current status and future plans for THM m modeling are summarized.

4.1 Modeling approach

LBNL uses two independent numerical simulators (TOUGH-FLAC and ROCMAS) for modeling of coupled THM processes associated with nuclear waste disposal and for modeling of the aforementioned heater experiments. The TOUGH-FLAC simulator developed at LBNL is the primary analysis tool, because this simulator has the required capabilities to model a large variety of problems associated with nuclear waste disposal for various engineering and natural systems. The ROCMAS code, also developed at LBNL, will in this project be used for confidence building through code-to-code verification. That is, models of a particular problem might be built in both TOUGH-FLAC and ROCMAS, and if the simulation results agree, that provides confidence in the models. Both the TOUGH-FLAC and ROCMAS codes solve THM coupled problems, but are two different codes with different characteristics. TOUGH-FLAC can simulate coupled THM processes under multiphase flow conditions through a sequential coupling of the TOUGH2 multiphase flow simulator with the FLAC3D geomechanical code (Rutqvist et al., 2002; Rutqvist 2011). TOUGH-FLAC has recently been modified for applications related with to bentonite-backfilled repositories in clay host formations (Rutqvist et al., 2014). ROCMAS simulates coupled THM processes in unsaturated media, including single-phase liquid flow and vapor diffusion in a static gas phase (Rutqvist et al., 2001a). The code has been extensively applied in earlier phases of the DECOVALEX project for THM analysis in bentonite-rock systems (Rutqvist et al., 2001b, 2005, 2009). In the following, the TOUGH-FLAC simulator (primary analysis tool) is described in more detail.

The TOUGH-FLAC simulator (Rutqvist 2011), is based on linking the TOUGH2 multiphase flow and heat transport simulator (Pruess et al., 2011) with the FLAC3D geomechanical simulator (Itasca 2011). In this approach, TOUGH2 (Pruess et al., 2011) is used for solving multiphase flow and heat transport equations, whereas FLAC3D (Itasca 2011) is used for solving geomechanical stress-strain equations. The two codes are sequentially coupled, but a TOUGH-FLAC simulation runs seamlessly. For analysis of coupled THM problems, the TOUGH2 and FLAC3D are executed on compatible numerical grids and linked through a coupled thermal-hydrological-mechanical (THM) model (Figure 4.1) with coupling functions to pass relevant information between the field equations that are solved in respective code. Depending on the problem and specific porous media (e.g., fractured rock, unsaturated clay, or hydrate-bearing sediments), a number of coupling functions have been developed.

In the coupling scheme between TOUGH2 and FLAC3D, the TOUGH2 multiphase pressures, saturation, and temperature are provided to update temperature, and pore pressure to FLAC3D (Figure 4.1). After data transfer, FLAC3D internally calculates thermal expansion, swelling, and effective stress. Conversely, element stress or deformation from FLA3D are supplied to TOUGH2 for correcting element porosity, permeability, and capillary pressure for the fluid-flow simulation in TOUGH2. The corrections of hydraulic properties are based on material-specific functions.

In a TOUGH-FLAC simulation, the calculation is stepped forward in time with the transient multiphase fluid flow analysis in TOUGH2, and at each time step or at the TOUGH2 Newton iteration level, a quasi-static mechanical analysis is conducted with FLAC3D to calculate stress-induced changes in porosity and intrinsic permeability. In this scheme, the fluid-flow sequence is solved first under fixed stress, and the resulting pressure and temperature are prescribed in the mechanical sequence. This corresponds to so-called stress fixed iterations in the sequential scheme, in which the solution becomes unconditionally stable. The resulting THM analysis may be *explicit sequential*, meaning that the porosity and permeability is evaluated only at the beginning of each time step, or the analysis may be implicit sequential, with permeability and porosity updated on the Newton iteration level towards the end of the time step using an iterative process.

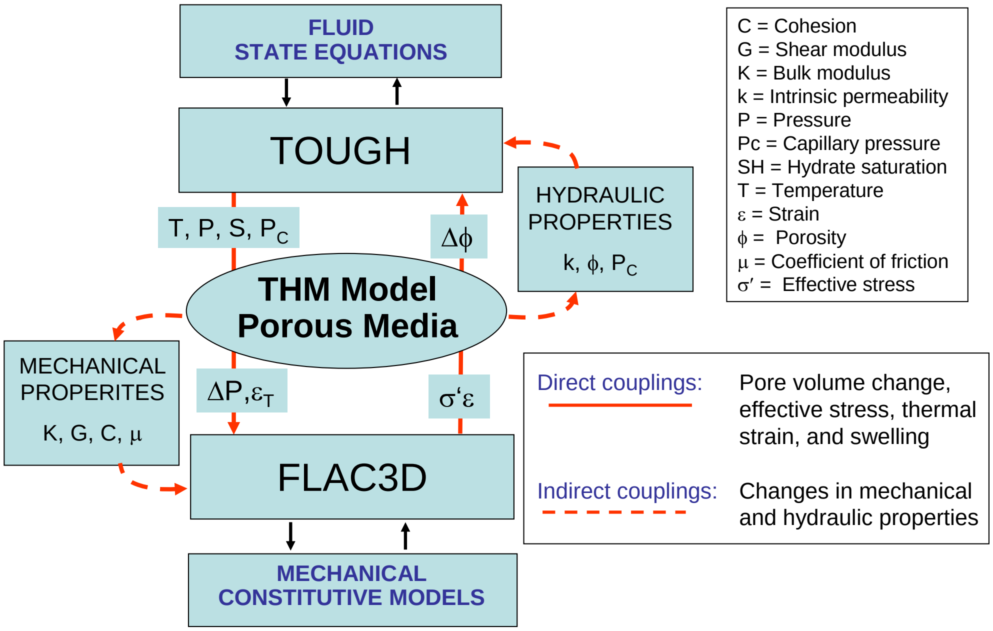

Figure 4.1. Schematic of linking of TOUGH2 and FLAC3D in a coupled TOUGH-FLAC simulation.

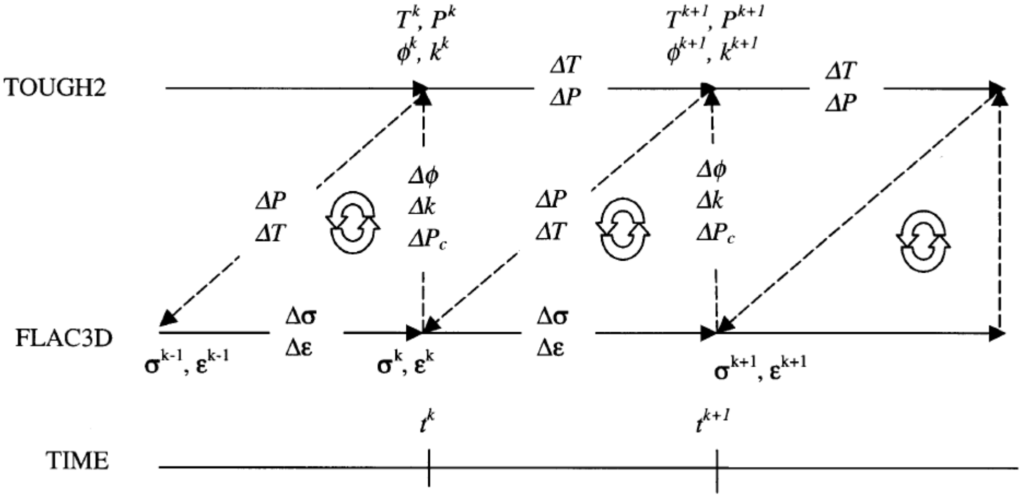

Figure 4.2. Numerical procedure of a linked TOUGH2 and FLAC3D simulation.

A great advantage with this adopted approach is that both codes are continuously developed and widely used in both academia and industry. In TOUGH2, a large number of fluid equation-of-state modules are available, while in FLAC3D, a large number of geomechanical constitutive models are available. This means that the simulator can be relatively easily extended to new application areas.

The TOUGH-FLAC simulator has in recent years been extended and applied to issues related to nuclear waste disposal with bentonite backfilled tunnels (Rutqvist et al., 2011; 2014). This includes implementation of the Barcelona Basic Model (BBM) (Alonso et al., 1990), for the mechanical behavior of unsaturated soils and applied for modeling of bentonite backfill behavior (Rutqvist et al., 2011). The BBM was first developed and presented in the early 1990s as an extension of the Modified Cam Clay (MCC) model to unsaturated soil conditions (Alonso et al., 1990). The model can describe many typical features of unsaturated-soil mechanical behavior, including wetting-induced swelling or collapse strains, depending on the magnitude of applied stress, as well as the increase in shear strength and apparent preconsolidation stress with suction (Gens et al., 2006). Figure 4.3 presents the yield surface of the BBM model in q-p-s space. The shaded surface corresponds to the elastic region at fully water-saturated conditions, which is equivalent to the modified MCC model. The figure also shows how the yield surface expands at unsaturated and dryer conditions when suction increases. There is an increase in both the apparent pre-consolidation pressure along the load collapse (LC) yield surface and by the increasing tensile strength, which in turn leads to an increased cohesion and shear strength.

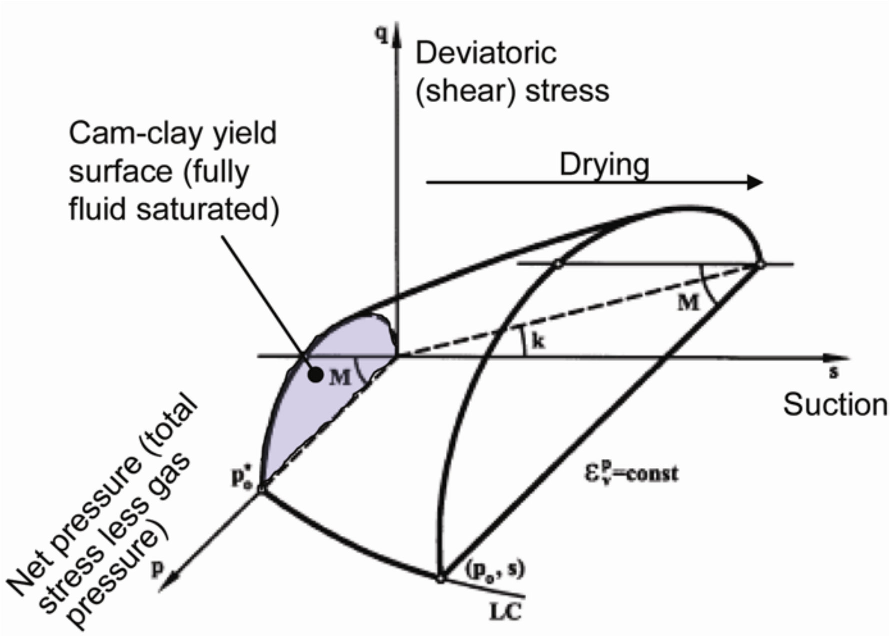

Figure 4.3. BBM constitutive model showing the yield surface in q-p-s space.

The BBM has been used for modeling of bentonite-buffer behavior in various national nuclear waste programs in Europe and Japan. For example, the BBM was successfully applied to model the coupled THM behavior of unsaturated bentonite clay associated with the FEBEX *in situ* heater test at the Grimsel Test Site, Switzerland (Gens et al., 2009). The BBM has also been applied to other types of bentonite-sand mixtures based on MX-80, considered as an option for an isolating buffer in the Swedish KBS-3 repository concept (Kristensson and Åkesson 2008). As part of the UFD program, the BBM was also used by Rutqvist et al. (2014), for the modeling of coupled THM processes around a generic repository in a clay host formation.

Recently, as part of the UFD EBS program, the BBM has been extended to a dual structure model, corresponding to the Barcelona Expansive Model (BExM). In a dual-structure model, the material consists of two structural levels: a microstructure in which the interactions occur at the particle level, and a macrostructure that accounts for the overall fabric arrangement of the material comprising aggregates and macropores (Figure 4.4) (Gens et al., 2006, Sánchez et al., 2005, Gens and Alonso 1992). A dual-structure model has important features for modeling the mechanical behavior of a bentonite buffer, such as irreversible strain during suction cycles. However, most importantly, a dual-structure model provides the necessary link between chemistry and mechanics, enabling us to develop a coupled THMC model for the analysis of long-term EBS behavior. This approach enables mechanistic modeling of processes important for long-term buffer stability, including effects of pore-water salinity on swelling (loss of swelling), conversion of smectite to nonexpansive mineral forms (loss of swelling), and swelling pressure versus exchangeable cations. The recent developments, testing and applications of the dual structure model, are presented in the upcoming FY2014 milestone report entitled "Investigation of coupled THMC process and reactive transport", as well as in a new scientific article submitted to a journal (Vilarrasa et al., 2014)

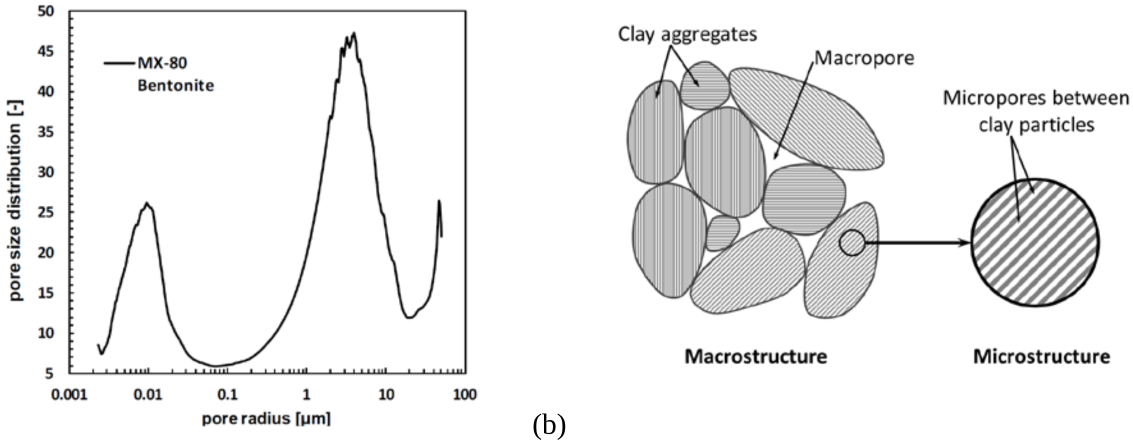

(a) (b)

Figure 4.4. (a) Pore size distribution and (b) schematic representation of the two structural levels considered in the dual structure model. Clay particles are represented by the gray lines.

4.2 Mont Terri HE-E Experiment (DECOVALEX)

The Mont Terri HE-E Experiment focuses on the THM behavior of bentonite barriers in the early nonisothermal resaturation stage and their THM interaction with Opalinus Clay (Figure 4.5). The objective is to better understand the evolution of a disposal system of high level waste in the early post-closure period, with emphasis on the thermal evolution, buffer resaturation (*in situ* determination of the thermal conductivity of bentonite and its dependency on saturation), pore-water pressure in the near field, and the evolution of swelling pressures in the buffer. Because the test is conducted in a micro-tunnel (at 1:2 scale), it is considered a validation, not a demonstration experiment. The heating test involves two types of bentonite buffer materials (Figure 4.5, left). The heater-buffer interface is heated to a maximum temperature of 135°C and a temperature of 60–70°C is expected at the buffer-rock interface. A dense instrumentation network was in place in the host rock surrounding the micro-tunnel from a previous experiment testing the impact of ventilation on the clay host rock, and has been improved for the purpose of the HE-E Heater Test (up to 40 piezometers in total); various sensors have also been placed in the buffer material. The heating phase started in the late summer of 2011 and is being continued for at least three years.

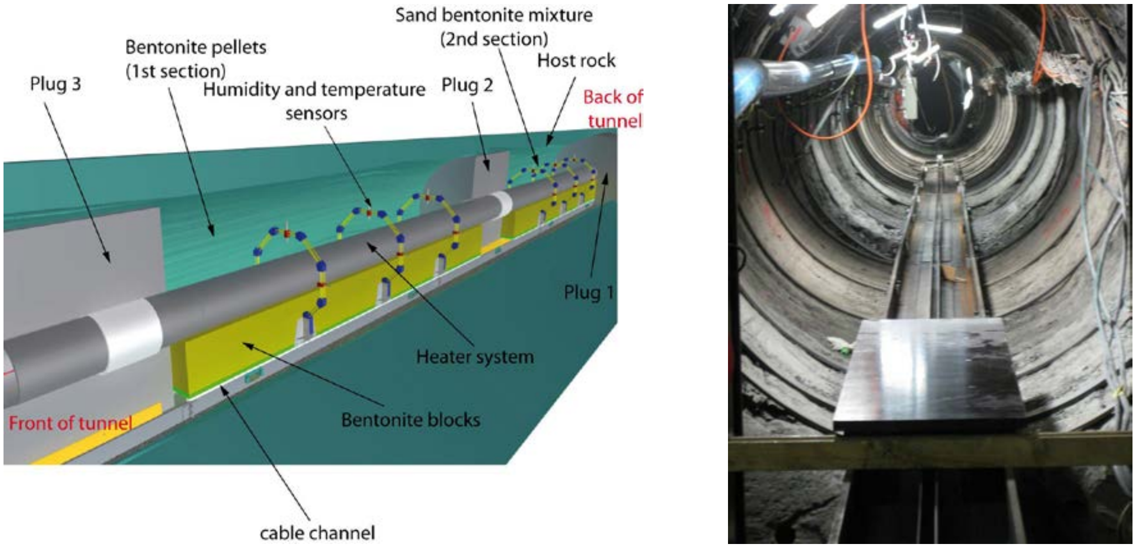

Figure 4.5. Schematic setup of HE-E experiment at Mont Terri and photo of micro-tunnel (Garritte, 2012).

In DECOVALEX-2015 (Task B1), eight international research teams are participating in the modeling of the HE-E experiment. Task B1, which is running over 3 years, is divided into the following steps:

- Step 1a: Opalinus Clay study including HE-D experiment, literature study, processes understanding and parameter determination.
- Step 1b: Buffer material study including CIEMAT column cells, literature study, processes understanding and parameter determination.
- Step 2: HE-E predictive modeling using as-built characteristics and true power load. Modeling is 2D (axisymmetric, plane strain or combination) and 3D.
- Step 3: HE-E interpretative modeling when data are made available.

Step 1a started in 2012 with the modeling of the previous HE-D experiment for *in situ* characterization of THM material parameters for the Opalinus Clay and was completed in November 2013. The HE-D experiment involved 1 year of heating of the Opalinus Clay without any bentonite buffer. The modeling of the HE-D experiment and comparison of the TOUGH-FLAC modeling results to the results of other modeling teams were reported in the FY2013 milestone report entitled “Report on THMC modeling of the near field evolution of a generic clay repository: Model validation and demonstration” (Liu et al., 2013b). Step 1b, which is a study of buffer material properties through modeling of laboratory experiments on buffer material samples, has recently been completed by all the modeling teams in DECOVALEX-2015, although the final comparison of the results between different teams is still ongoing. In this report, we present LBNL’s final analysis of the CIEMAT column experiments, which has been substantially updated from last year. This update includes a more detailed analysis of transient temperature evolution, the heat loss through the experimental equipment, and more detailed consideration of the retention properties, including their temperature dependency. This also resulted in a much improved agreement between simulated and observed THM responses. We have also begun Step 2 of Task B1, which is the HE-E predictive analysis, planned to be completed by October 2014.

4.3 Buffer characterization using CIEMAT column experiments

In this subsection, we present updated modeling of the CIEMAT column experiments (Villar 2012). The modeling of the CIEMAT column experiments are being done as part of DECOVALEX-2015 Task B1 for characterization of the buffer material associated with the Mont Terri HE-E experiment. However, the CIEMAT column experiments are also critical for the modeling of the Mont Terri FE experiment, because one of the bentonite materials studied in the column experiments will also be used for backfill at the FE experiment. In CIEMAT column experiments, two buffer materials, granular bentonite (or bentonite pellets) and sand/bentonite mixture, were tested (Figure 4.6). The design of the column experiments mimicked the HE-E conditions, with the height of the column equal to the thickness of the buffer filled between the canister and host rock. A heater was placed at the bottom and a cooler at the top of each column, so that the column was heated while the top remained at an ambient temperature of ~21.5°C. During the experiments, temperature and relative humidity were measured at three points along the axis of the column. The power input was monitored as well. In this study, our objectives are to model the fluid-flow and heat-transfer processes that occur in the experiment, and to calibrate the flow and thermal properties of the two buffer materials against the experimental measurements. In DECOVALEX-2015, only the granular bentonite experiment was required to be modeled by the research teams, whereas it was optional to model the sand/bentonite experiment.

The modeling of this experiment in the DECOVALEX-2015 project has revealed substantial heat loss through the equipment, such that it was decided at the last DECOVALEX-2015 workshop (in April 2014) that each research team should carefully look at both the heat power and temperature evolution, to properly consider the heat loss from the equipment. It is particularly important to quantify the heat loss if using this experimental data to determine the thermal conductivity of the tested bentonite material. LBNL has conducted model simulations of both experiments (both granular bentonite and sand/bentonite mixture). However, the main emphasis was placed on the modeling of the granular bentonite, because this was the main task in DECOVALEX-2015, and granular bentonite is the buffer material that will be used in the Mont Terri FE experiment.

4.3.1 Model setup of column experiment on granular bentonite

In the experiment, bentonite pellets were poured into a Teflon column without extra packing (Villar, 2012). A heater was placed at the bottom and a cooler at the top of the column (Figure 4.6). Sensors were installed at distances of 10 m, 22 m, and 40 cm from the heater to measure temperature and relative humidity. The Teflon column was wrapped with a layer of foam, which was later replaced with rock wool and another insulating material denoted in Villar (2012) as BT-LV.

After the system was assembled, the relative humidity and temperature were measured without heating the system. The measured initial relative humidity was uniformly 40% within the column. It remained unchanged until the start of heating, which was set to be the reference time (t=0). After the heater was turned on, the surface temperature of the heater reached the target temperature of 100°C within 33 minutes. By automatically adjusting the power into the heater, the surface temperature of the heater remained at 100°C. By 1566 hours, the foam layer was replaced with a rock wool of 30 mm thickness, covering the entire column length, and a BT-LV of 25 mm thickness, covering the bottom 5 cm of the column (Figure 4.6). At 3527 hours, an adjustment of the target temperature was made for the heater, and its surface temperature increased to 140°C about 17 minutes after the adjustment. A hydration valve was opened by 5015 hours. Water flowed into the column from the top while the surface temperature of the heater remained at 140°C. During the hydration process, the changes in relative humidity and temperature along the column and the power input of the heater were monitored.

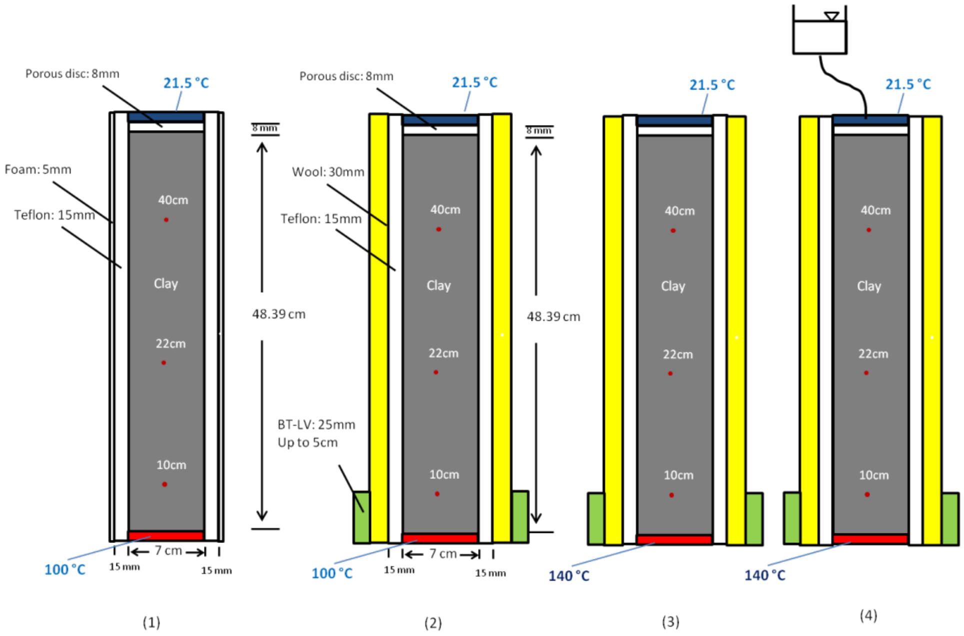

Figure 4.6. Schematic of experimental setups of column experiment in sequential steps: (1) Heating at temperature of 100 ˚C from 0 to 1566 hours, (2) heating with new insulation layer from 1566 to 3527 hours, (3) heating at 140 ˚C from 3527 to 5015 hours, (4) heating with hydration valve open after 5015 hours.

A 2D radial symmetric mesh of 9×28 elements was created for the modeling of this column experiment (Figure 4.7). Bentonite is represented in a zone of 4×25 elements (grey zone in Figure 4.7). The multiple stages of the experiment were simulated sequentially, and the boundary conditions of each step were adjusted according to the experiment. During the experiment, the hydration valve was closed, and therefore no water flowed into the column before the start of heating. Fixed temperature conditions at the heaters were simulated by assigning a large heat capacity to the heater elements. To simulate the temperature increase at the heater element, e.g., from 21.5 to 100°C, and from 100 to 140°C, a heating rate was applied to the heater element, such that the heating rate equal to the experiment. Hydration was simulated by assigning a constant absolute pressure of 1.1×10^4 Pa at the top boundary.

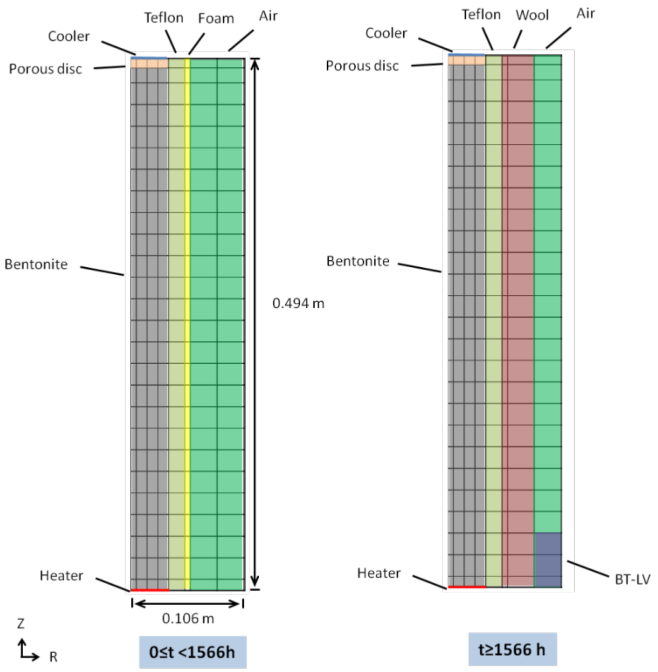

Figure 4.7. Model mesh and the materials represented in the model at different steps for column experiment on bentonite pellets. The reference time (t = 0) is the start of heating.

For assigning the initial properties we resorted to literature data of granular MX-80 bentonite or other similar bentonite materials. For example, properties for granular bentonite was defined by Nationale Genossenschaft für die Lagerung radioaktiver Abfälle (NAGRA) for a benchmark model problem associated with the Mont Terri FE experiment. These properties are listed Table 4.9 and an estimate of the properties. Here we complement these with new data from Villar, (2012) and Rizzi et al, (2011). The basic physical properties of the granular bentonite are presented in Table 4.1, including a solid grain density of 2700 kg/m^3 and a porosity of 0.46 (Villar, 2012). The specific heat of the bentonite is 950 J/kg°C (NAGRA best estimate, Table 4.9). The initial water saturation is 22% and the measured initial relative humidity was 40% uniformly along the column.

Table 4.1. Properties of bentonite pellets used in the modeling of the column experiment.

Properties	Values
Solid grain density	2700 kg/m^3
Porosity	0.46
Specific heat	950 J/kg^{o}C
Tortuosity	0.67

Transport of vapor in tight formation is enhanced by diffusion and Klinkenberg effects. Olivella and Gens (2000) reported that the measured permeabilities of FEBEX and Boom Clay samples to gas are about 6–7 orders of magnitude higher than those to liquid. To account for the increased gas permeability, we considered vapor and air diffusion and the Klinkenberg effect in the model. A diffusion coefficient of 2.13×10^{5} m^2/s was used for both vapor and air, and a tortuosity factor of 0.67 was used in the model. A Klinkenberg parameter of 2.5×10^{11} Pa was used.

Gas phase is assumed to be perfectly mobile, and the relative permeability of liquid water is a power function of the degree of water saturation (NAGRA best estimate, Table 4.9).

$$k_{rl} = s_l^{\ 5} \tag{4.1}$$

$$k_{rg} = 1 \tag{4.2}$$

Typical values (Table 4.2) were used for the thermal conductivities of the Teflon wall and insulation layers, as described in Villar (2012).

Table 4.2. Properties of other materials used in the model for column experiment on bentonite pellets.

Materials	Thermal conductivity
Porous disc	3.5 W/mºC (wet and dry)
Teflon	0.25 W/mºC (wet and dry)
Foam	0.04 W/mºC (wet and dry)
Wool	0.03 W/mºC (wet and dry)
BT-LV	0.03 W/mºC (wet and dry)
Air	0.032 W/mºC (wet and dry)

4.3.2 Analysis of thermal conductivity of the granular bentonite

The analysis of the thermal conductivity of the granular bentonite was challenging, because the substantial heat loss from the test equipment affected the experimental results. We first investigated the possibility of calibrating the thermal conductivity of the granular bentonite using the temperature profile at steady-state conditions at the end of each heating step. The model for this analysis considered an insulation layer of 0.45 m in thickness (equals to the sum of Teflon and wool layers). The temperature was fixed at 140°C at the bottom, 21.5°C at the top, and 21.5°C at the sides. Both thermal conductivities of bentonite (λ) and insulation layer (h) were calibrated against the temperature profile at steady-state conditions.

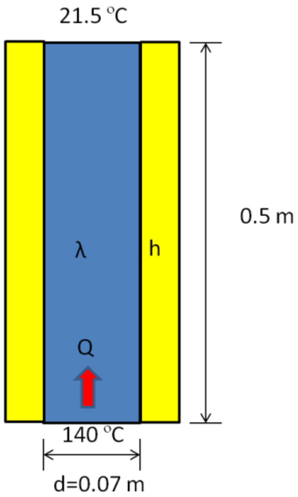

Figure 4.8. Schematic of the model for the calibration of thermal conductivity.

The analysis showed that steady-state temperature data alone do not contain enough information to calibrate the thermal conductivity of the benotonite. Different combinations of bentonite and insulation thermal conductivities can equally match the temperature profile measured at steady state (Figure 4.9). A thermal conductivity of 0.4 W/mK for bentonite and 0.032 W/mK for insulation layer produces the same temperature profile at λ=0.2 W/mK and h=0.016 W/mK or at λ=0.75 W/mK and h=0.06 W/mK. A thermal conductivity ratio (λ/h) of 12.5 is critical for matching the steady-state temperature data.

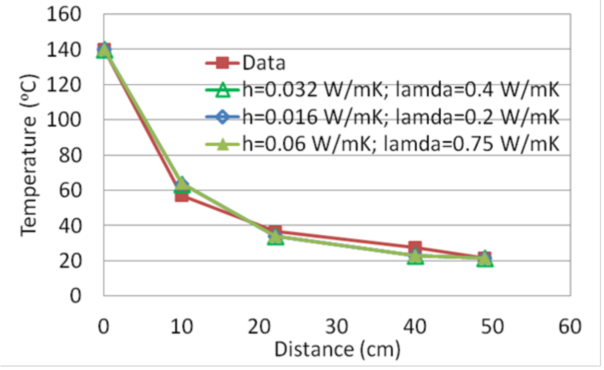

Figure 4.9. Simulated temperature profiles using different combinations of bentonite and insulation thermal conductivities and the measured temperature profile.

We then investigated the possibility of analyzing the transient temperature evolution in each step to calibrate the model for thermal conductivity of the bentonite. We found that when the temperature of heater is increased, the transient temperature data measured in the bentonite column contain information needed for the calibration of thermal conductivity of the bentonite and insulation layer, because the sensitivity of temperature response over thermal conductivities of the bentonite and insulation layer is time-dependent. When temperature at the heater is changed, the temperature evolution at the early stage is more sensitive to the thermal conductivity of the bentonite, while the impact of thermal conductivity of the insulation will show up at later. As shown in Figure 4.10, thermal conductivities of 0.4 W/mK for bentonite and 0.04 W/mK for the insulation layer produce a temperature response that matches the transient temperature data well. Although changing the thermal conductivity of the insulation layer leads to a misfit in the temperature 2 hours after the start of heating, the match before that remains essentially the same. A change in thermal conductivity of the bentonite, however, results in a significant mismatch at the early time (Figure 4.11). Therefore, we conclude that the thermal conductivity of the granular bentonite in this experiment is 0.4 W/mK.

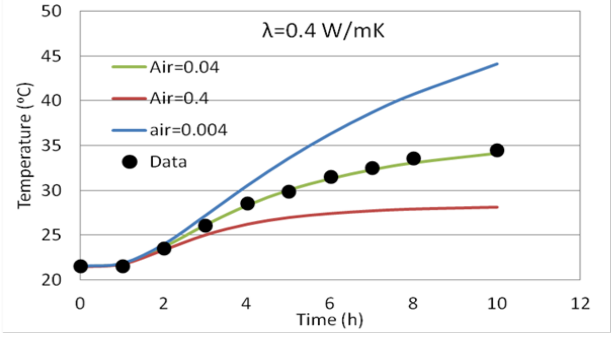

Figure 4.10. Sensitivity analysis over the amount of lateral heat loss on transient temperature data at t=0, where temperature increased from 21.5 to 100 ˚C at the surface of heater.

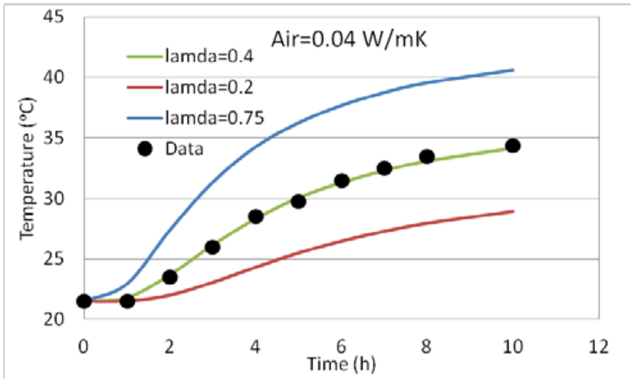

Figure 4.11. Sensitivity analysis over the thermal conductivity of bentonite on transient temperature data at t=0, where temperature increased from 21.5 to 100 ˚C at the surface of heater.

4.3.3 Dependency of thermal conductivity on water saturation

It is well known that thermal conductivity is a function of water saturation in porous soil. In this experiment, water saturation near the heater decreases with time as more water vaporized. A decrease in temperature in the first plateau (dashed box in Figure 4.12) was observed in the experiment. This phenomenon can be explained by the fact that even though the temperature at the heater surface remained unchanged, a sharper temperature gradient occurred near the heater, as the thermal conductivity in the region decreased with time. Using a constant thermal conductivity of 0.4 W/mK, the model failed to produce the decrease in temperature in the first plateau.

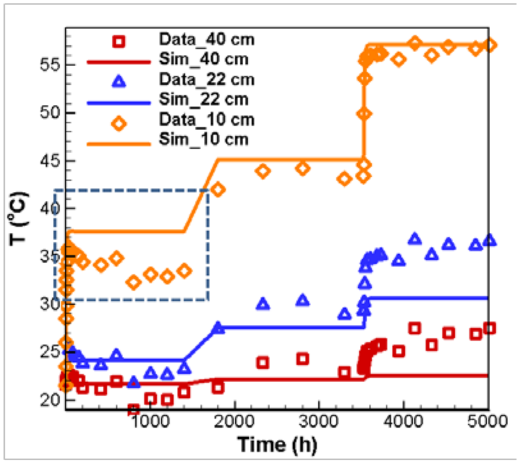

Figure 4.12. Simulated temperatures using constant thermal conductivity of 0.4 W/mK and measured temperatures.

The analysis showed that the match in temperature could be improved when the thermal conductivity varies as a function of water saturation (Figures 4.13 and 4.14). A linear function was used to describe the dependency of thermal conductivity on water saturation. With thermal conductivities of 0.28 W/mK under dry conditions and 0.825 W/mK under wet conditions, the initial thermal conductivity is still 0.4 W/mK (initial water saturation is 0.22). Considering the dependency of thermal conductivity on water saturation, the model not only reproduced the declining temperature in the first plateau (Figure 4.13), but also the transient temperature responses of two increases in temperature of the heater surface (Figure 4.14).

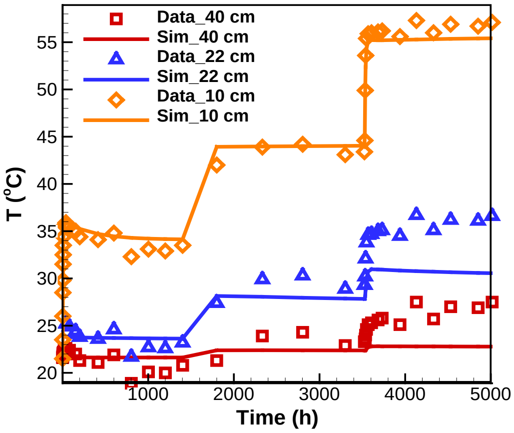

Figure 4.13. Measured temperatures and simulated temperatures with the thermal conductivity as a function of water saturation.

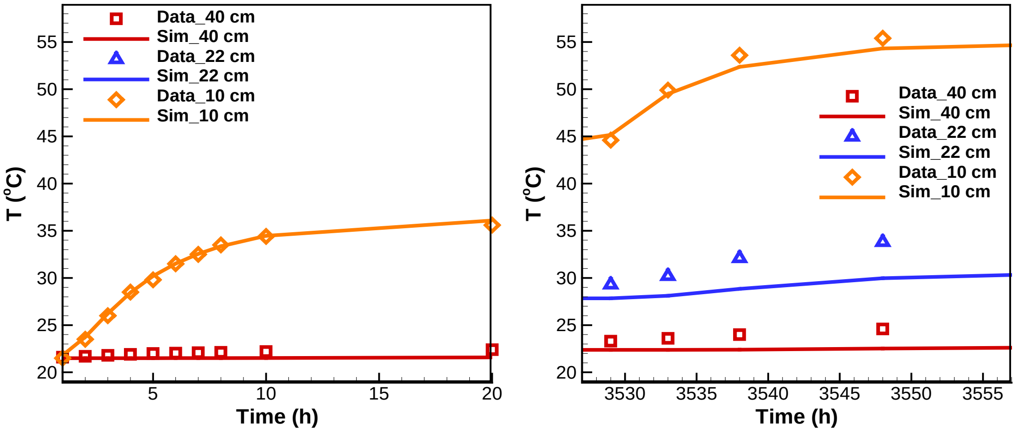

Figure 4.14. Simulated temperatures compared with the transient temperature data at t=0 and t=3527 h, when the temperature at heater surface was increased from 21.5°C to 100°C, and from 100°C to 140°C, respectively.

The calibration efforts show that the thermal conductivity of granular bentonite in this experiment is 0.28 W/mK under dry conditions and 0.825 W/mK under wet conditions. With an initial water saturation of 0.22, the bentonite in column B has an initial thermal conductivity of 0.4 W/mK. The calibrated value is consistent with the measured value by Wieczorek et al. (2013). These values were then used for the following simulations when calibrating the capillary pressure curve and analyzing the heat loss.

4.3.4 Calibration of Capillary Pressure Curve

The capillary pressure curve was described using the van Genuchten formula (van Genuchten 1980):

$$P_c = -P_0\left[(s^*)^{-1/\lambda} - 1\right]^{(1-\lambda)} \tag{4.3}$$

$$s^* = \frac{(s_l - s_{lr})}{(s_{ls} - s_{lr})} \tag{4.4}$$

where the curve fitting parameter, λ, is 0.55 (Table 4.3), residual water saturation, s_{lr}, is 0, reciprocal of entry pressure, $1/P_0$, is 2.7×10^{-8} 1/Pa, full saturation is 1.0.

The parameters were obtained by fitting the curve to the initial state (water saturation of 0.22 and capillary pressure of 1.06×10^{8} Pa) and the measurements at ambient temperature (Figure 4.15) (Rizzi et al. 2011), while matching the evolution in relative humidity in the column experiment (Figure 4.16). Note that in the column experiment, the relative humidity varies between 25 to 60%, which with the matched retention curve correspond to a saturation ranging from about 10 to 30%. Thus, we are only able to calibrate the dry end of the retention curve and this is also the range were the assumed retention curve matches the data the best in Figure 4.15.

According to the report by Rizzi et al. (2011), the capillary pressure of the bentonite sample was significantly lowered at 80°C. This temperature dependency of capillary pressure was taken into account using a simple square root function:

$$P_c(t) = P_c(t_0)\sqrt{t_0/t}, \tag{4.5}$$

where $P_c(t)$ is the capillary pressure at temperature, t; $P_c(t_0)$ is the capillary pressure at temperature, t_0.

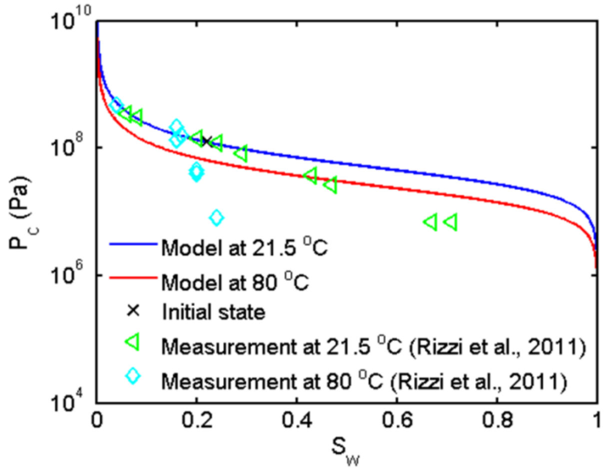

Figure 4.15. Capillary pressure curves in the model and measured capillary pressures at 21.5 and 80 ºC (Rizzi et al., 2011) for granular bentonite.

Assuming local thermodynamic equilibrium, we calculated the vapor pressure in the gas phase using the Kelvin's relationship, and the relative humidity (R_H) is therefore obtained as follows (e.g., Rutqvist et al., 2001a):

$$\ln(R_H) = \frac{P_c m^w}{\rho_l R T} \tag{4.6}$$

where P_c is the capillary pressure, ρ_l is the density of liquid water, e.g., $998.2\frac{kg}{m^3}\ at\ 20°C$ and $971.8\frac{kg}{m^3}\ at\ 80°C$, m_w is the molar mass of water, $18\times10^{-3}\ kg/mol$, R is the universal gas constant, which is $8.314\ J/(mol\ K)$, and T is the absolute temperature.

Table 4.3. Capillary pressure of granular bentonite used in the model.

Parameters	Values
λ	0.55
s_{lr}	0
$1/P_0$ (1/Pa)	2.7×10^{-8}
P_{max} (Pa)	3×10^{13}
s_{ls}	1.0

The simulated relative humidity is in good agreement with the measured relative humidity (Figure 4.16). After the heater was turned on, the simulated relative humidity increased rapidly at 10 cm. This is partially caused by the upward-flowing vapor from the heated zone beneath the sensor. The other factor that contributes to increased relative humidity is the increased local temperature. At a higher temperature, the capillary pressure of the granular bentonite tends to be lower, even though the water saturation is the same. Such a phenomenon was evidenced by the measured capillary pressure at increased temperature by Rizzi et al. (2011). A lower capillary pressure, therefore, corresponds to a higher relative humidity. Over time, the relative humidity decreases at the 10 cm location, as a result of drying that occurred at the 10 cm location caused by continued heating. A discrepancy between the simulated and measured relative humidity appears after 3527 h, when insulation was improved. This is because the van Genuchten function overestimates the increase in capillary pressure at low water saturations, causing the underestimation of relative humidity at the 10 cm location. The upflow of vapor is evidenced by the continuous increases in relative humidity at the 22 cm and 40 cm locations. Overall, the simulated relative humidity is in good agreement with the measured ones at three locations.

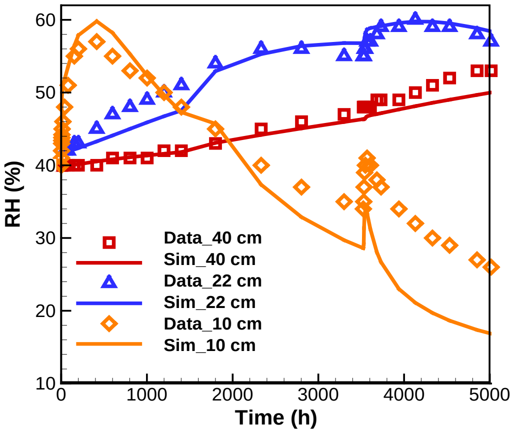

Figure 4.16. Simulated and measured relative humidity and temperature at 10, 22, and 40 cm from the heater in column experiment B.

4.3.5 Calibration of Intrinsic Permeability

Intrinsic permeability of bentonite was calibrated against the water-intake data of the hydration test. The amount of water flowing into the column was measured with time (Villar et al., 2014). Calibration results show that an intrinsic permeability of 5.5×10^{-21} m^2 produces a water intake consistent with the experiment (Figure 4.17).

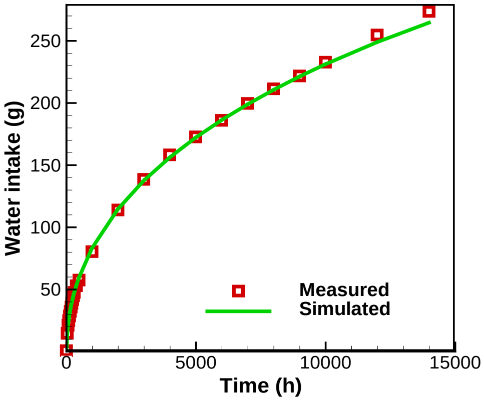

Figure 4.17. Simulated and measured water intake.

4.3.6 Analysis of Power Entering the Column

Power input was logged in the experiment to be 12 W at the end of heating (Villar et al., 2014). Our calibrated model shows that the power entering into the column at the end of heating is ~2.4 W, which is about 20% of the power input (Figure 4.18). During the experiment, heat loss occurred by means of thermal conduction through the lateral insulation layers and the bottom side of the heater and radiation.

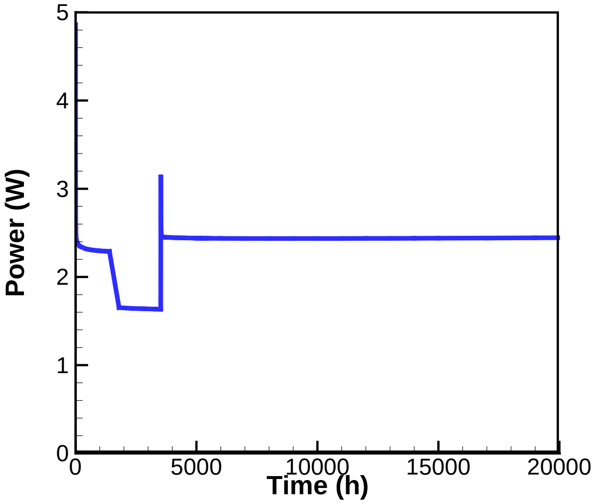

Figure 4.18. Calculated power entering the column during the heating test.

4.3.7 Model setup of column experiment on sand/bentonite mixture

For modeling of the column experiment with a sand/bentonite mixture, the same modeling approach was used. The experimental setup was also similar, but the insulation was different. In this case, the column was initially not wrapped with any insulation layers (Figure 4.19), but rather with a layer of foam 7 hours after the heater was turned on. The foam layer was later replaced with wool and BT-LV materials.

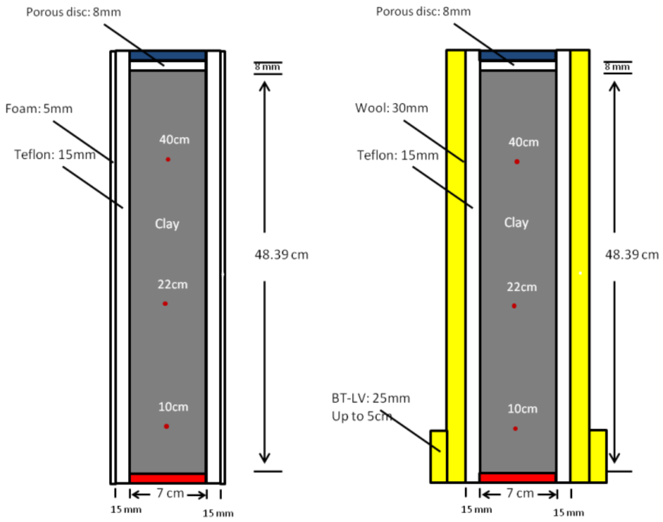

Figure 4.19. Schematic of the experimental setups before and after changing insulation.

The data acquisition system was turned on right after the system was assembled. Relative humidity and temperature were monitored for 260 hours without heating the system. The initial relative humidity is 0.46 uniformly within the column. After 95 hours, the hydration valve was accidentally opened, and water was flowing into the column until the valve was shut off ~5 minutes later. The measured relative humidity showed a steady increase from 0.46 to 0.52 at 40 cm, and an increase of 0.5% at the other two locations by 260 hours (Villar, 2012).

The heater was turned on at 260 hours and the target temperature was set at 100°C (t=0 in the simulation and the following experiment). The target temperature was reached after 25 minutes. The top of the column remained at 22.5°C. A foam layer was wrapped around the column 7 hours after the start of heating. After 1566 hours, the foam layer was replaced with wool of 30 mm thickness covering the entire column length and BT-LV of 25 mm thickness covering the bottom 8 cm. After 2498 hours, the target temperature of the heater was adjusted to 140°C. The temperature increased to 140°C 17 minutes after the adjustment was made. The experiment stopped after 3692 hours.

A 2D radial symmetric mesh was created to simulate the column experiment. The mesh has 9 columns and 28 rows (Figure 4.20). Materials used in the model include sand/bentonite mixture, porous disc, heater, cooler, Teflon, foam, wool, BT-LV, and air. The sand/bentonite mixture is represented by 4×25 elements (grey zone in Figure 4.20). Multiple steps were involved to simulate the experiment. Similar to the experimental procedure, we simulated the hydration process by assigning a slight overpressure (10^4 Pa, gauge pressure) to the cooler element. The duration of the hydration process was 5 min, as reported in the experiment. The calculated state variables (Pg, Sg, and Pa) of the system were used as the initial condition for the next step. We then simulated the heating experiment. Increasing temperature at the surface of heater was simulated by applying time-dependent heating rates to the “heater” element, with the heating rates being consistent with the experiment. During the experiment, the insulation around the column was changed. The change of insulation is considered in the model by assigning corresponding rock properties to the insulation elements.

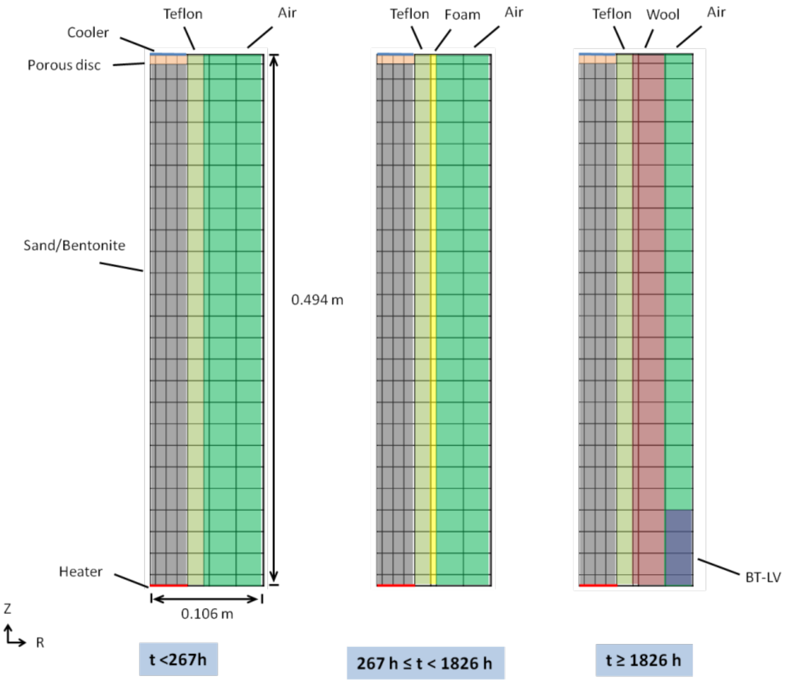

Figure 4.20. Model mesh and the materials represented in the model at different steps for column experiment A. The reference time (t = 0) is the start of heating.

The sand/bentonite mixture properties used in the model are as shown in Table 4.4. The sand/bentonite mixture has a solid grain density of 2700 kg/m^3. Its intrinsic permeability is 1.2×10^{-20} m^2, which is consistent with the measured permeability by Wieczorek et al. (2013). The porosity is 0.46. It has a wet thermal conductivity of 0.8 W/mºC and a dry thermal conductivity of 0.29 W/mºC. Thermal conductivity in between was interpolated linearly as a function of water saturation. The value of thermal conductivity is close to the measured values by Wieczorek et al. (2013), where the thermal conductivity of sand/bentonite mixture was measured to be 0.305 W/ mºC at a water saturation of 2.78%. The specific heat of the sand/bentonite mixture is 950 J/kgºC. Before the experiment started, the pores of the sand/bentonite mixture were initially saturated with 11% of water.

Table 4.4. Properties of sand/bentonite mixture used in the model.

Solid grain density	2700 kg/m^3
Porosity	0.46
Intrinsic permeability	1.2×10^{-20} m^2
Saturated thermal conductivity	0.8 W/ mºC
Unsaturated thermal conductivity	0.29 W/mºC
Specific heat	950 J/kgºC
Tortuosity	0.67

Similarly to the modeling of the granular bentonite, for the sand/bentonite mixture a diffusion coefficient of 2.13×10^{5} m^2/s was used for both vapor and air, and a tortuosity factor of 0.67 was used in the model. A high Klinkenberg parameter of 2.5×10^{11} Pa was used to simulate high gas intrinsic permeability.

Transport of vapor in a tight formation is enhanced by diffusion and Klinkenberg effects. Olivella and Gens (2000) reported that the measured permeabilities of Full-scale Engineered Barrier Experiment (FEBEX) and Boom Clay samples to gas are about 6–7 orders of magnitude higher than those to liquid. To account for the increased gas permeability, we considered vapor and air diffusion and Klinkenberg effect in the model. A diffusion coefficient of 2.13×10^{5} m^2/s was used for both vapor and air, and a tortuosity factor of 0.67 was used in the model. A Klinkenberg parameter of 2.5×10^{11} Pa was used.

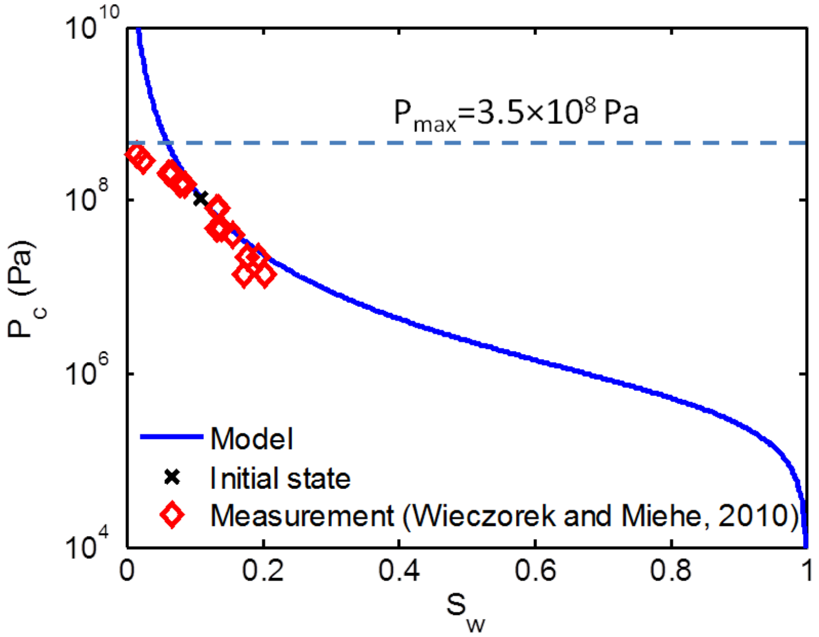

Figure 4.21. Capillary pressure curve used in the model and measured capillary pressures by Wieczorek and Miehe (2010) for sand/bentonite mixture.

Again, we used the van Genuchten formula (Equations (4.3) and (4.4)) to describe the water-retention curve (van Genuchten, 1980), where λ is the curve fitting parameter, P_0 is the entry pressure, and s_{ls} and s_{lr} are the full and residual water saturations, respectively. The variables λ and P_0 were adjusted to fit the capillary pressure curve over the capillary pressures measured with sand/bentonite mixture at varied water saturations (Wieczorek et al., 2013) and the measured initial state of the sand/bentonite mixture (Figure 4.21). The sand/bentonite mixture in column has an initial relative humidity of 46% (capillary pressure of 1.06×10^{8} Pa) at a water saturation of 11% (Figure 4.22). To better represent the capillary pressures at low water saturations, a cut-off upper limit of 3.5×10^{8} Pa was used for the capillary pressure curve in the model. Values for the parameters in the van Genuchten model are presented in Table 4.5. Temperature dependency of capillary pressure was considered using the simple square root function in Equation (4.5).

Table 4.5. Capillary pressure of the sand/bentonite mixture.

Parameters	Values
λ	0.29
s_{lr}	0
$1/P_0$ (1/Pa)	2.1×10^{-6}
P_{max} (Pa)	3.5×10^{8}
s_{ls}	1.0

The relative permeability used for liquid water is described as a power function of the degree of water saturation, and the gas phase was assumed to be perfectly mobile, with a relative permeability of 1 (Equations (4.1) and (4.2)).

Other materials in the model use values close to typical values of the materials and those measured by Villar (2012). The porous disc has a high permeability of 1.2×10^{-12} m^2. Teflon, heater, cooler, foam, wool, and BT-LV were assigned with an extremely low permeability (1.0×10^{-24} m^2). The thermal conductivities of other materials are shown in Table 4.6. The thermal conductivity values were close to the measured ones by Villar (2012) and typical thermal conductivity of the materials. Only slight adjustments were made to better match the temperature profile.

Table 4.6. Properties of other materials used in the model.

Materials	Permeability	Thermal conductivity
Porous disc	1.2×10^{-12} m^2	3.5 W/m°C (wet), 0.5 W/m°C (dry)
Teflon	1.0×10^{-24} m^2	0.4 W/m°C (wet and dry)
Foam	1.0×10^{-24} m^2	0.08 W/m°C (wet and dry)
Wool	1.0×10^{-24} m^2	0.06 W/m°C (wet and dry)
BT-LV	1.0×10^{-24} m^2	0.054 W/m°C (wet and dry)
Air	1.0×10^{-24} m^2	0.06 W/m°C (wet and dry)

4.3.8 Sand/bentonite mixture simulation results and discussion

The simulated results agree with the experimental measurements well during the hydration (Figure 4.22). Relative humidity at 40 cm increased from 46% to 52%, during which the hydration valve was opened, while at other locations it remained unchanged. Temperature for all sensors remained at 22.5°C, because the heater has yet to be turned on.

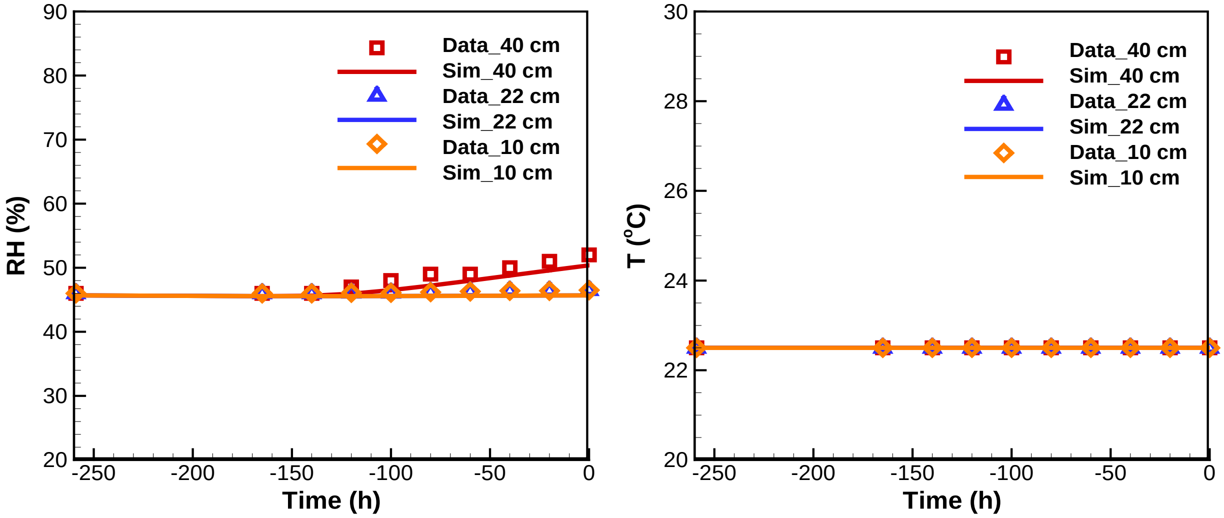

Figure 4.22. Simulated and measured relative humidity (RH) and temperature (T) during hydration.

After the heater was turned on, the simulated relative humidity increases rapidly at 10 cm (Figure 4.23), due to the increase in temperature and the vapor flowing up. When temperature increases at the 10 cm location, relative humidity increases as the capillary pressure drops, even if the water saturation remains unchanged. However, heating also causes the vapor pressure to increase near the heater, which drives vapor flowing up and contributes to the increased relative humidity at the 10 cm location during the early stage of heating. Over time, the relative humidity decreases at the 10 cm location. This is because further heating causes the drying at the 10 cm location with the vapor flowing further up. This upflow of vapor is evidenced by the continuous increases in relative humidity at the 22 cm and 40 cm locations. In addition to the upflow of vapor, the large increase in relative humidity at the 40 cm location is also contributed by the hydration process. As water flowed into the column before the start of heating, the water saturation at the 40 cm location gradually increases as a result of liquid water flowing downward via gravity and capillary forces. Overall, the simulated relative humidity at three locations is in a good agreement with the measured ones.

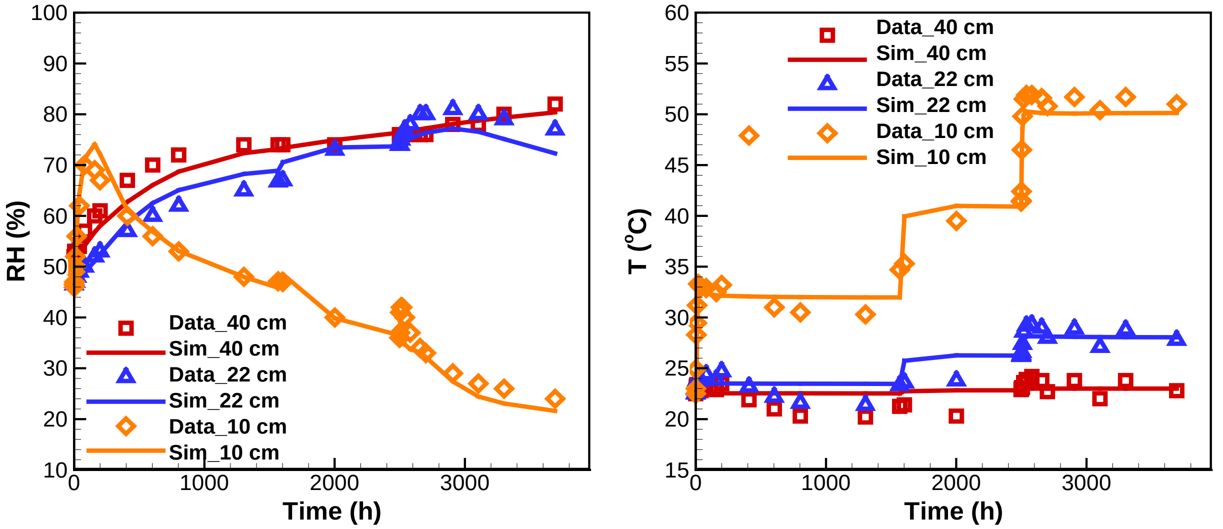

Figure 4.23. Simulated and measured relative humidity (RH) and temperature (T) after heater was turned on.

Simulated temperature profiles agree well with the measured data. As expected, the temperature at the 10 cm location increases rapidly to ~30°C after the start of heating. It then increases to 41°C when the heater temperature was increased to 140°C. Further increase to 50°C occurs as insulation was improved. The temperature at the 40 cm location only increases slightly, due to the heat loss along the column, suggesting that the increase in relative humidity at this location is primarily caused by the transport of vapor and liquid water.

4.3.9 Concluding remarks on CIEMAT column experiments

We have conducted very detailed model simulations of CIEMAT column experiments for the characterization of buffer properties used in the Mont Terri *in situ* heating experiments. The simulation of the CIEMAT turned out to be more cumbersome than expected, because of a substantial heat loss from the equipment that has to be considered in order to characterize the thermal properties of the buffer material. We learned that by looking at the transient temperature and moisture responses in addition to steady-state profiles, we could obtain a unique solution for back-calculating the thermal and hydraulic properties of the buffer material. Calibration against transient temperature data showed that the thermal conductivity of the granular bentonite is 0.4 W/mK at a water saturation of 22%, which is in agreement with other independent measurements on this type of bentonite. Moreover, we found that a gradual decrease in temperature during the first month could be used for validating the dependency of thermal conductivity on water saturation. The capillary-pressure curves for the buffer materials were adjusted to fit the measured data and initial state of the bentonite in the experiments. Temperature dependency of capillary pressure was considered using a square root function. By accounting for the enhanced permeability of gas and temperature dependency of the capillary pressure, the model can reasonably reproduce the evolution of relative humidity along the column in the experiments. Intrinsic permeability was calibrated against the water intake data when available. The calibrated model for the granular bentonite experiment showed that the heat flow entering the column was ~2.4 W, about 20% of the total power input.

4.4 Horonobe EBS Experiment (DECOVALEX)

This task focuses on coupled THMC modeling of a planned full-scale EBS experiment conducted by the Japan Atomic Energy Agency (JAEA) at the Horonobe URL, Hokkaido, Japan (Figure 4.24). The EBS experiment will be carried out at a depth of 350 m in a very porous and soft, siliceous mudstone with the following basic properties:

- Porosity 35-60%
- Permeability $10^{-20} – 10^{-18}$ m^2
- UCS (Strength) 5-25 MPa
- Young’s Modulus 1-4 GPa
- Thermal Conductivity 1.34-1.53 W/mK

Figure 4.25 show the experimental layout with a vertical heater emplacement installed in a test pit at the bottom of an experimental drift. The experimental drift will be backfilled after the installation of the heater and bentonite buffer into the test pit. Backfill and buffer materials will be based on the Japanese Kunigel V1 bentonite. The experimental area will then be isolated by a concrete plug.

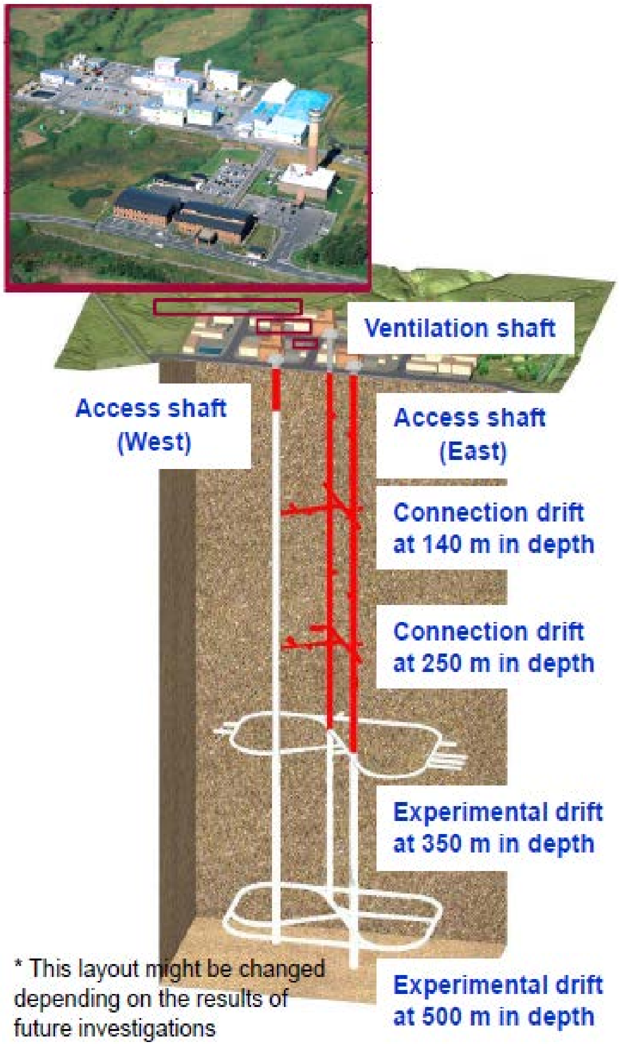

Figure 4.24. Layout of the Horonobe URL in Hokkaido, Japan.

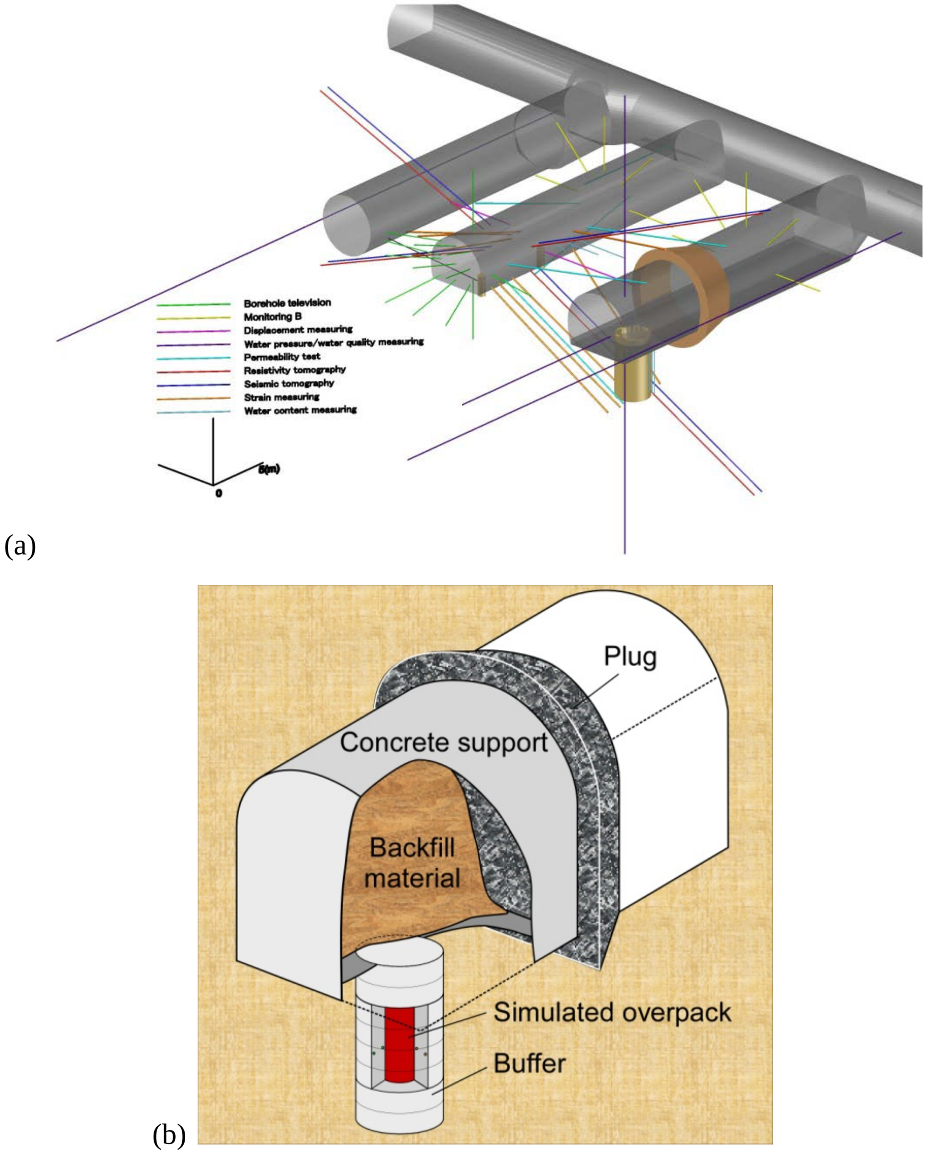

Figure 4.25. General description of the EBS experiment at the Horonobe URL Project in Japan.

Sensors will be installed in buffer, backfill, and rock to monitor temperature, stress, strain, pore pressure, humidity, displacement, pH, resistivity, electric potential, and seismic velocity. The detailed layout is not yet fixed and may be changed, depending on the initial modeling results.

The DECOVALEX Task B2 related to the Horonobe EBS experiment is divided into the following steps;

- Step 1 (1D benchmark test with comparison of numerical models)
- Step 2 (Prediction analysis and proposal of the sensors layout)
- Step 3 (Calibration analysis)

The 1D benchmark test (Step 1) was defined with exact properties and boundary conditions given by the JAEA. The benchmark test was conducted for the teams to familiarize themselves with the problem and for precise comparison of computer codes before going into the more complex full-scale case. Thereafter, in Step 2, a model of the real experimental design should be constructed and a first predictive analysis should be performed for several years from the start of the heating. The results will then be used to guide the installation of sensors, which began in April 2014. The heating is planned to start in November 2014, and in April 2015, JAEA will provide the monitored data for the first six months of heating to the research teams. The research teams will calibrate their models against this first 6 months of field data and then carry out coupled numerical analysis for long-term predictions (100–1,000 years) using the test conditions of the EBS experiment.

JAEA provides reports from the investigations at the Horonobe URL for input parameters related to the mudstone host rock and buffer material properties for the Kunigel V1 bentonite from the previous H12 project, whereas properties for the backfill are being investigated along with this project.

Task B2 started in May 2013 with Step 1, which has been completed. In the next section, we present the final LBNL results and comparison to the simulation results of other research teams. Step 2 has begun and should be completed before the next DECOVALEX workshop, to be held in November 2014. In this report, we present the model setup and preliminary model prediction for this case.

4.4.1 Final 1D Benchmark Modeling and Comparison to Other Models

The initial modeling of the 1D benchmark modeling associated with the Horonobe EBS experiment was presented in the FY2013 milestone report entitled “THM and Reactive Transport Model Development and Evaluation: International Activities” (Rutqvist et al., 2013b). The results are to be presented at DECOVALEX-2015 workshops and compared with the results of other modeling teams. Here, we present the final results of this benchmark, as well as a comparison to the final results of other modeling teams. We used TOUGH-FLAC for modeling of this benchmark and comparison to the other modeling teams. We also used the ROCMAS code, which was beneficial for understanding input parameters given by the JAEA related to the diffusion properties of the bentonite. The material properties used for the overpack, buffer and rock used in the LBNL simulation are listed in Table 4.7.

Table 4.7. Material parameters for TOUGH-FLAC.

	Overpack	Buffer	Rock
Solids density (kg/m^3)	10,000.	2680.	2454.
Porosity	0.403	0.403	0.4482
Permeability (m^2)	5 x 10^{-51}	4 x 10^{-20}	1.33 x 10^{-15}
Thermal conductivity (saturated) (W/m°C)	20	1.986	1.231
Specific heat (solids) (J/kg°C)	10,000	341	626
Thermal conductivity (desaturated) (W/m°C)	20	0.444	0.579
Klinkenberg parameter (Pa)	8.47 x 10^{-10}	8.47 x 10^{-10}	8.47 x 10^{-10}
Water relative permeability parameter A, (Equation (4.7))	1.3	1.3	NA
Water relative permeability residual saturation, S_r (Equation (4.7))	0	0	NA
Water relative permeability maximum saturation, S_m (Equation (4.7))	1	1	NA
Water relative permeability parameter *m*, (Equation (4.8))	NA	NA	0.503
Water relative permeability residual saturation, S_r (Equation (4.8))	NA	NA	0
Water relative permeability maximum saturation, S_m (Equation (4.8))	NA	NA	1
Capillary pressure parameter, α (m^{-1}) (Equation (4.11))	8 x 10^{-3}	8 x 10^{-3}	9.928 x 10^{-3}
Capillary pressure parameter, *m*, (Equation (4.11))	0.375	0.375	0.503
Capillary pressure residual saturation, S_r (Equation (4.11))	0	0	0
Capillary pressure maximum saturation, S_r (Equation (4.11))	1	1	1
Vapor diffusion coefficients (m^2/s)	3.5 x 10^{-6}	3.5 x 10^{-6}	3.5 x 10^{-6}
Klinkenberg parameter (Equation (4.12))	-	2.5 x 10^{11}	-
Young's modulus E, (MPa)	200.000	37	1820.0
Poisson's ratio, ν (-)	0.3	0.3	0.21
Linear thermal expansion coefficient (C^{-1})	1 x 10^{-6}	1 x 10^{-6}	1.33 x 10^{-5}
Moisture swelling coefficient, β_{sw} (Equation (7.24))	0	0.0108	0

The water relative permeability in the buffer (and overpack) is a power-law relationship given by

$$k_{rw}(S_w) = \left(\frac{S_w - S_r}{S_m - S_r}\right)^A \qquad (4.7)$$

The water relative permeability in the rock is given by the van Genuchten relationship:

$$k_{rw}(S_w) = \left(\frac{S_w - S_r}{S_m - S_r}\right)^{1/2} \left[1 - \left\{1 - \left(\frac{S_w - S_r}{S_m - S_r}\right)^{1/m}\right\}^m\right]^2 \tag{4.8}$$

In the buffer (and overpack), the gas relative permeability is the Corey model,

$$k_{rg}(S_w) = \left\{1 - \left(\frac{S_w - S_r}{1 - S_r - S_{gr}}\right)^2\right\} \left\{1 - \left(\frac{S_w - S_r}{1 - S_r - S_{gr}}\right)\right\}^2 \tag{4.9}$$

In the rock, the gas relative permeability is

$$k_{rg}(S_w) = 1 - k_{rw}(S_w) \tag{4.10}$$

Capillary pressure in the buffer (and overpack) and rock is given by the van Genuchten relationship:

$$\psi(S_w) = \frac{1}{\alpha}\left\{\left(\frac{S_w - S_r}{S_m - S_r}\right)^{-1/m} - 1\right\}^{1-m} \tag{4.11}$$

Variations in thermal conductivity and specific heat with water saturation are assumed to be linear between the defined end points. The vapor diffusion coefficient is constant; there is no temperature dependence.

For the multiphase flow simulation using TOUGH2 we found that gas permeability has an important effect. Indeed, laboratory data on bentonite and clay rocks have shown that the intrinsic permeability for air is up to six orders of magnitude higher than the intrinsic permeability for water flow (Olivella and Gens, 2000). A high value of gas permeability was also inferred by Xu et al. (unpublished) from modeling of a salt-imbibition experiment using a mixture of the Kunigel V1 bentonite. In order to match the saturation profile observed in the experiment, the gas permeability had to be increased to five-orders-of-magnitude larger than that of liquid. In TOUGH2, this was accomplished by specifying a large Klinkenberg parameter, which is used to account for the increase in gas-phase permeability at low pressures:

$$K_g = K_l(1 + b/P) \tag{4.12}$$

Xu et al. (unpublished) inverted the Klinkenberg parameter to 2.5×10^{11} Pa^{-1}. Using this parameter, the intrinsic permeability for air will be about 5 orders of magnitude higher than the intrinsic permeability for water.

In Figure 4.26, results are presented with and without high gas permeability. If the intrinsic permeability for the gas phase is similar to that of the liquid, the gas pressure will increase, and this will suppress the vapor diffusion. In such a case, no drying occurs near the heat source, and the evolution of saturation is completely different for that with high gas permeability.

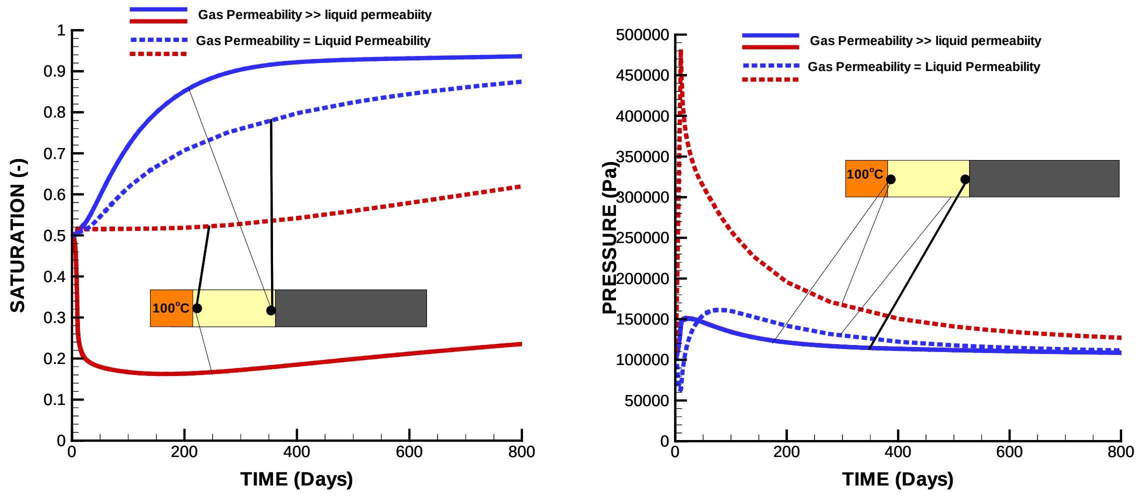

(a) (b)

Figure 4.26. Simulation results with and without high gas permeability: (a) saturation and (b) pressure evolution.

The selection of the diffusivity has a pronounced impact on the simulation results. In the task definition, a constant thermal diffusivity is given as $D_T = 1.5 \times 10^{-11}$ m^2/sK. This is a parameter input to the THAMES code used by the JAEA. In TOUGH2, the basic diffusion coefficient should be given as an input, but it is not straightforward to know what basic diffusion coefficient would correspond to $D_T = 1.5 \times 10^{-11}$ m^2/sK. In this case, the basic diffusion coefficient was estimated using the ROCMAS code, in which either the basic diffusion coefficient or the thermal diffusivity can be given as an input. By model calibration using ROCMAS, it was found that a good value for the basic diffusion coefficient would be $D_{Vo} \approx 3.5 \times 10^{-6}$ m^2/s.

$$\mathbf{i}_{\psi}^{\kappa} = -\rho_{\psi} D_{v0} \phi S_g \mathbf{I} \nabla X_{\psi}^{\kappa} \tag{4.13}$$

Finally, a linear elastic swelling model was used to model the evolution of swelling stress, and the model input parameters can be determined analytically to achieve a desired maximum swelling stress of 0.5 MPa. In such a case, the bentonite is assumed to behave elastically, with a volumetric swelling and a swelling stress that depends on the changes in water saturation, ΔS_l, according to:

$$\Delta\sigma'_{sw} = 3K\Delta\varepsilon_{sw} = K\Delta S_l \beta_{sw} \tag{4.14}$$

where $\Delta\sigma'_{sw}$ is the induced swelling stress (an effective stress), K is the bulk modulus, and β_{sw} is a moisture swelling coefficient. For an average bulk modulus of 30.83 MPa, the appropriate moisture swelling coefficient can be calculated using Equation (4.14) as:

$$\beta_{sw} = \frac{\Delta\sigma'_{sw}}{3K\Delta S_l} = \frac{0.5\cdot 10^6}{3\cdot 30.83\cdot 10^6\cdot (1.0-0.5)} = 0.0108 \qquad (4.15)$$

Thus a moisture swelling coefficient of $\beta_{sw} = 0.0108$ was applied in this case.

In Figure 4.27, results are presented for the thermal hydrological behavior using TOUGH2 and ROCMAS. In both simulations, a basic diffusion coefficient of 3.5×10^{-6} m^2/s was used. The results are almost identical, although it appears that the water infiltration from the rock is slightly faster in the TOUGH2 simulation.

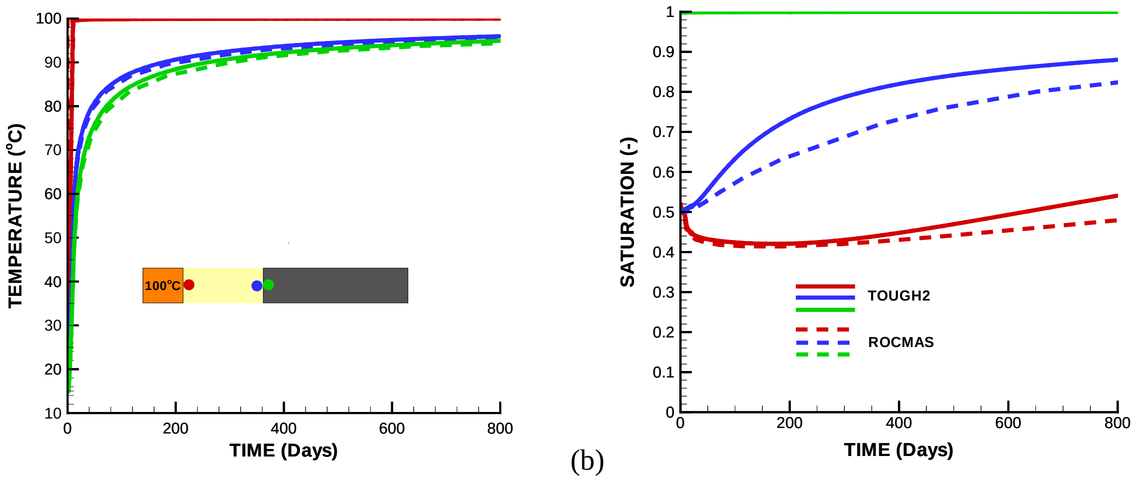

(a) (b)

Figure 4.27. (a) Temperature and (b) saturation evolution for simulations using TOUGH2 and ROCMAS.

Figure 4.28 shows the x-stress evolution in the buffer. The simulation results are shown for two simulations, with and without consideration of thermal expansion. The results show that over the 800 days, thermal stresses dominate. This is actually caused by thermal expansion of the rock, which in this 1D model expands inwards towards the bentonite buffer. The buffer is therefore compressed and compressive stress increases.

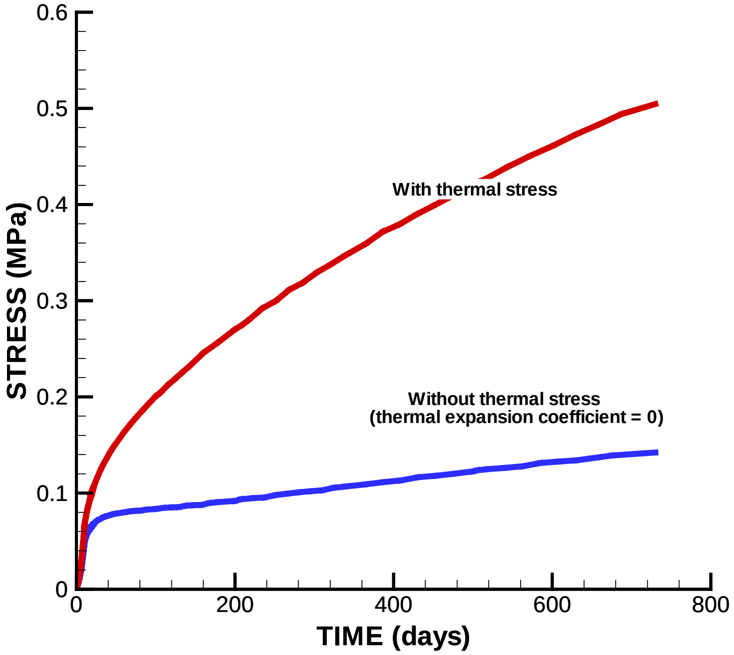

Figure 4.28. Buffer stress evolution with/without thermal expansion.

In DECOVALEX-2015, five research teams are participating in the modeling of the Horonobe EBS experiment with the models listed in Table 4.8. Some of the models listed in Table 4.10 have been extensively applied in previous DEOCOVALEX project phases, whereas some are new and being developed. Figures 4.29 to 4.33 show comparisons of the simulation results regarding temperature, saturation, and stress. A very good agreement between different models is achieved for temperature and saturation, whereas the results of stress show some differences. Heat conduction dominates the temperature evolution, though the buffer saturation can have a significant impact on thermal conductivity. There is good agreement in the wetting of the bentonite from the surrounding rock, whereas there is some difference in the saturation evolution near the heat source. At the point next to the heater, a slight drying occurs in the results of DOE, BGR and JAEA, whereas no drying occurs in the results of CAS and KAERI. This is most probably related to the modeling of diffusion of vapor in the gas phase, which was not considered by CAS and KAERI. The calculated stress evolution in the buffer is very similar for DOE, KAERI, and JAEA, whereas BGR and CAS obtained somewhat lower stress. However, considering all the complex THM processes that affect the stress evolution, the agreement between the different teams is acceptable.

Table 4.8. Research teams and numerical simulators applied in this study.

Research Team	Numerical Simulator	Brief Description of Numerical Simulator
DOE U.S. Department of Energy's Research Team: Lawrence Berkeley National Laboratory (LBNL)	TOUGH-FLAC	TOUGH-FLAC is a simulator for analysis of coupled THM processes under multiphase fluid flow conditions being developed at the LBNL (Rutqvist et al., 2002). The simulator is based on linking of the existing computer codes TOUGH2 and FLAC3D, and has been extended for modeling of coupled THM and THMC processes associated with nuclear waste disposal with backfilled emplacement tunnels in clay formations (Rutqvist et al., 2014).
	ROCMAS	ROCMAS is a finite element program for analysis of coupled THM processes in porous and fractured rock developed at LBNL (Rutqvist et al., 2001a). It can model unsaturated media with single-phase liquid flow and vapor diffusion in a static gas phase The code has been extensively applied in earlier phases of the DECOVALEX project for THM analysis in bentonite-rock systems (Rutqvist et al., 2001b; 2005).
BGR Bundesanstalt für Geowissenschaften und Rohstoffe's Research Team: University of Tübingen	GeoSys/ Rockflow	GeoSys/Rockflow is based on object-oriented programming (Kolditz et al., 2003). It was first applied in previous DECOVALEX phases for analysis of thermal-hydrological and thermal-mechanical processes and has been extended to THM (Wang et al., 2006). For the present study, an unsaturated single-phase liquid flow and vapor diffusion is considered.
CAS Chinese Academy of Sciences' Research Team	EPCA3D	The EPCA code (Elasto-Plastic Cellular Automata) uses the concept of cellular automata inspired by the self-organizing theory in biology. This code has been successfully used to simulate the failure process of heterogeneous rocks with and without consideration of hydro-mechanical coupling (Feng et al., 2006; Pan et al., 2008).
JAEA Japan Atomic Energy Agency's Research Team, including Hazama Cooperation	THAMES	THAMES is a finite element program for analyzing coupled THM processes in porous and fractured rock developed at the Kyoto University (Ohnishi and Kobayashi, 1996). The code has been extended to unsaturated media with single-phase liquid flow and vapor diffusion in a static gas phase (Chijimatsu et al., 2005).
KAERI Korean Atomic Energy Research Institute	FLAC/ FLAC3D/ Tough2	Simulation tools being developed along with the DECOVALEX-2015 project based on FLAC and FLAC3D linked with TOUGH2.

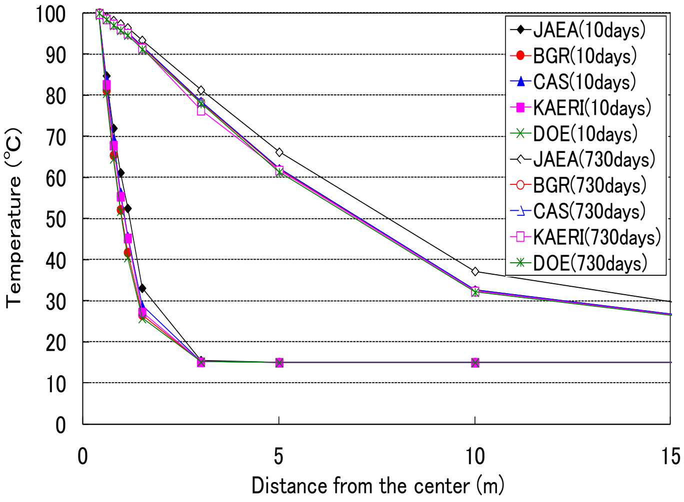

Figure 4.29. Comparison of the analytical results on distribution of temperature.

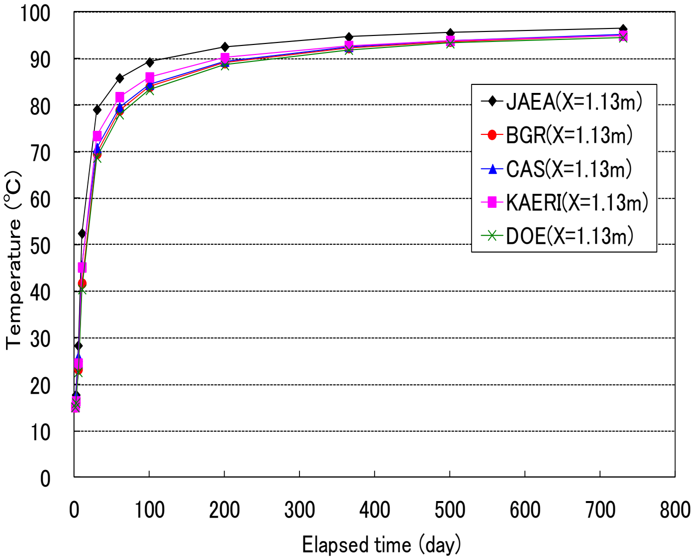

Figure 4.30. Comparison of the analytical results on variation of temperature at the output point (*X*=1.13m).

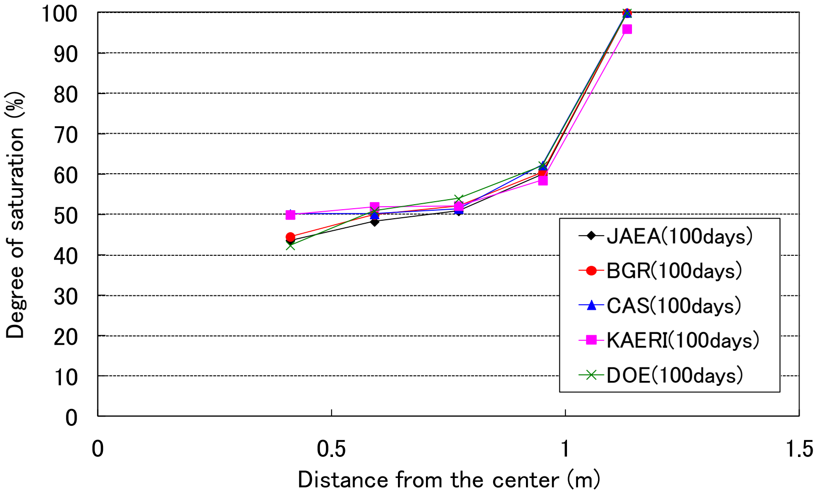

Figure 4.31. Comparison of the analytical results on degree of saturation in the buffer after 100 days.

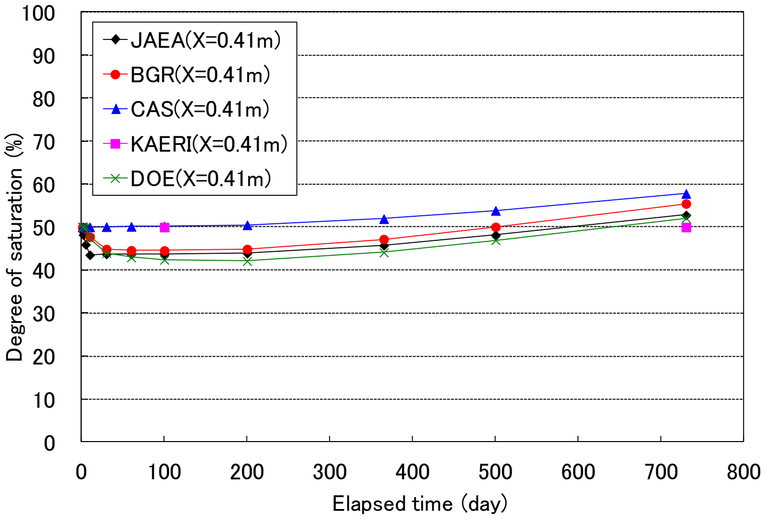

Figure 4.32. Comparison of the analytical results on variation of degree of saturation at the output point (X=0.41m).

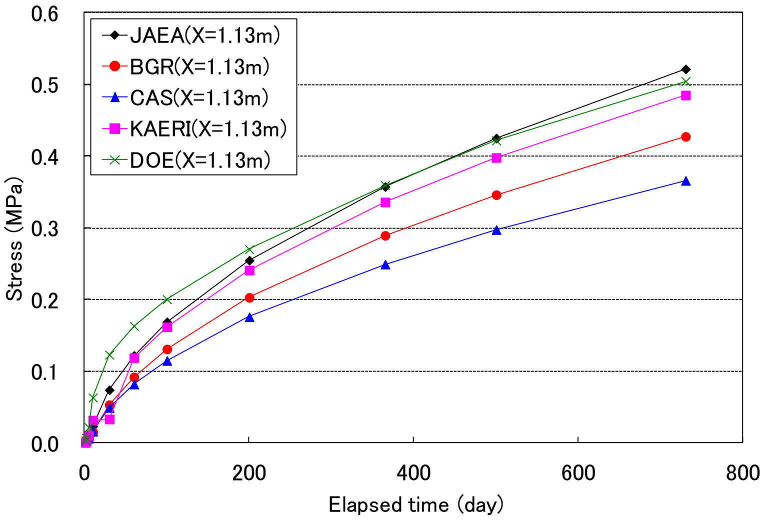

Figure 4.33. Comparison of the analytical results on vartiation of stress at the output point (*X*=1.13m).

4.4.2 Initial model prediction of the full scale Horonobe EBS experiment

We have recently developed a 3D model and made an initial prediction of the THM responses at the Horonobe EBS experiment. The model is half symmetric, including half of the tunnel and half of the deposition hole (Figure 4.34). It contains all relevant materials, including mudstone rock, buffer, backfill, a sand layer at the rock/buffer interface, concrete lining and plug. In this model prediction, we use the properties of the buffer and rock developed associated with the 1D benchmark calculation (Table 4.11). However, additional properties are needed for the backfill, sand layers, concrete lining and plug. At the moment, material properties for the backfill, which consists of bentonite mixed with sand and rocks, has not been completely characterized and provided to the DECOVALEX research teams.

The only parameters we currently have for the backfill is a dry density of 1300 kg/m^3, a porosity of 0.5, and an initial degree of liquid saturation of 0.7. Our approach is to use backfill properties determined in the Swedish nuclear waste program for a backfill consisting of a mixture of bentonite and crushed rock with a weight ratio of 30/70. The 30/70 backfill material was used in Rutqvist and Tsang (2008) for modeling of proposed Swedish nuclear waste disposal sites. Here we consider the 30/70 bentonite properties for estimating the properties of the backfill material to be used in the Horonobe EBS experiment. In general, the backfill will be emplaced at lower dry density having a higher porosity than the compacted bentonite buffer material. Therefore, we expect smaller stiffness (Young's modulus) and swelling stress, a higher intrinsic permeability, and a lower capillary pressure. The greatest difference is expected for the intrinsic permeability and water-retention curve. For estimating the intrinsic permeability, we used an empirical relation between dry density and intrinsic permeability provided by JAEA. According to this relation, for a backfill dry density of 1300 kg/m^3, the intrinsic permeability would be 0.64×10^{-19} m^2. We used the water-retention curve from the abovementioned 30/70 backfill material (Rutqvist and Tsang, 2008).

In addition, we have to assign properties for the concrete plug, concrete lining, and the sand layer at the rock-buffer interface. For the concrete material, we assigned typical properties including a permeability of 1×10^{-19} m^2, Young's modulus of 23 GPa. For simplicity, we assumed a water-retention curve equivalent to that of the mudstone rock. For the sand layer, because of its expected high porosity and permeability, we used the same properties as for the surrounding mudstone rock.

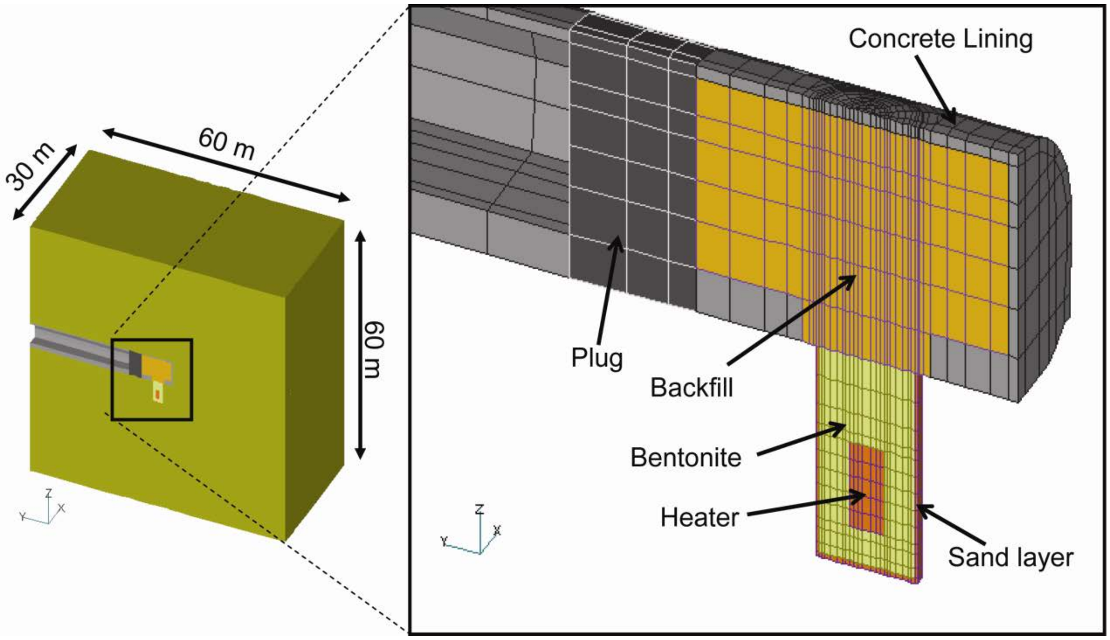

Figure 4.34. TOUGH-FLAC 3D numerical grid of the Horonobe EBS experiment.

We simulated the experiment in 3 steps:

1) Excavations are open for 3 months.
2) Excavations are filled with backfill and the heater, buffer and plug are all installed for 6 months.
3) Then heating starts.

In this preliminary study, we simulated heating for about 2 years. The results of temperature and saturation evolution for points located in the buffer and near-field rock are shown in Figures 4.36 and 4.37. When keeping the heater temperature constant at 100°C, the simulation shows that the temperature at the buffer-rock interface (P3, P4 in Figure 4.35) increases to about 60°C after 2 years. The liquid saturation in the buffer increases slowly by water infiltration from the surrounding rock (Figure 4.36). However, after 2 years, the liquid saturation at the inner parts of the buffer has not changed significantly (P1 in Figure 4.36). The calculated results in Figures 4.36 and 4.37 are sensible and show that we are able to use this full 3D TOUGH-FLAC model of the Horonobe EBS experiment for making a model prediction of the THM responses during the heating. Our next step will be to make a careful prediction of all the required output considering new material-property data for the backfill and concrete that will be distributed to the research teams by JAEA. The results will be presented at the next DECOVALEX-2015 workshop in November 2014 and then compared to initial monitoring results.

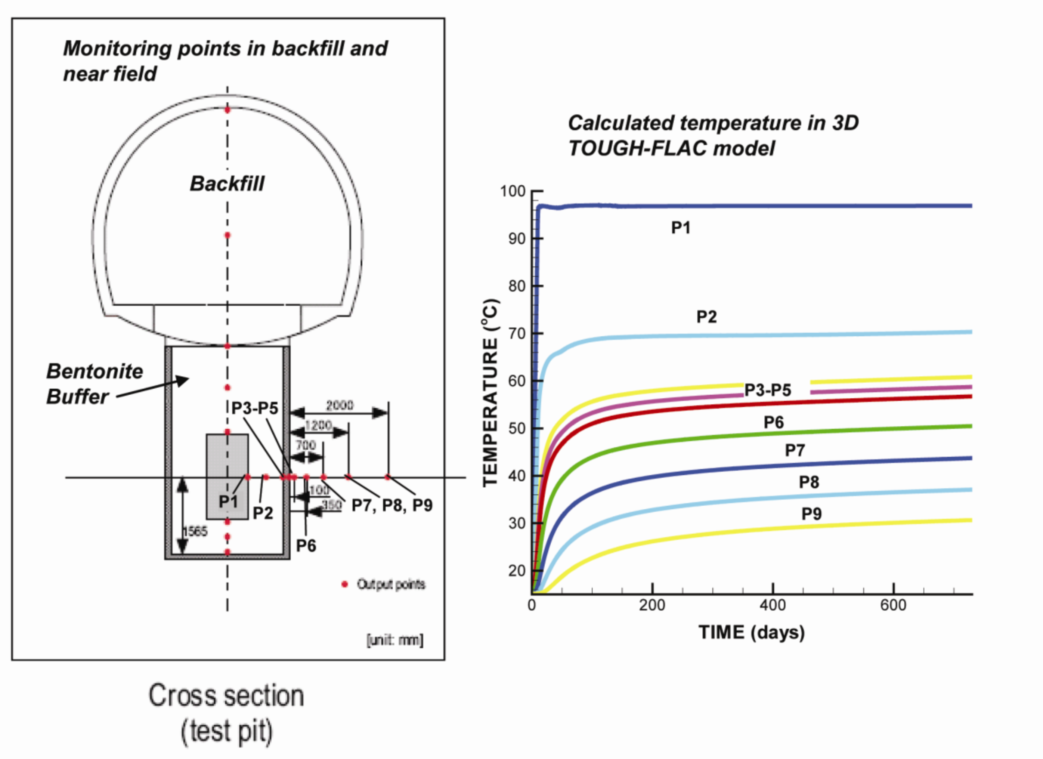

Figure 4.35. TOUGH-FLAC simulation results of temperature in the buffer and rock.

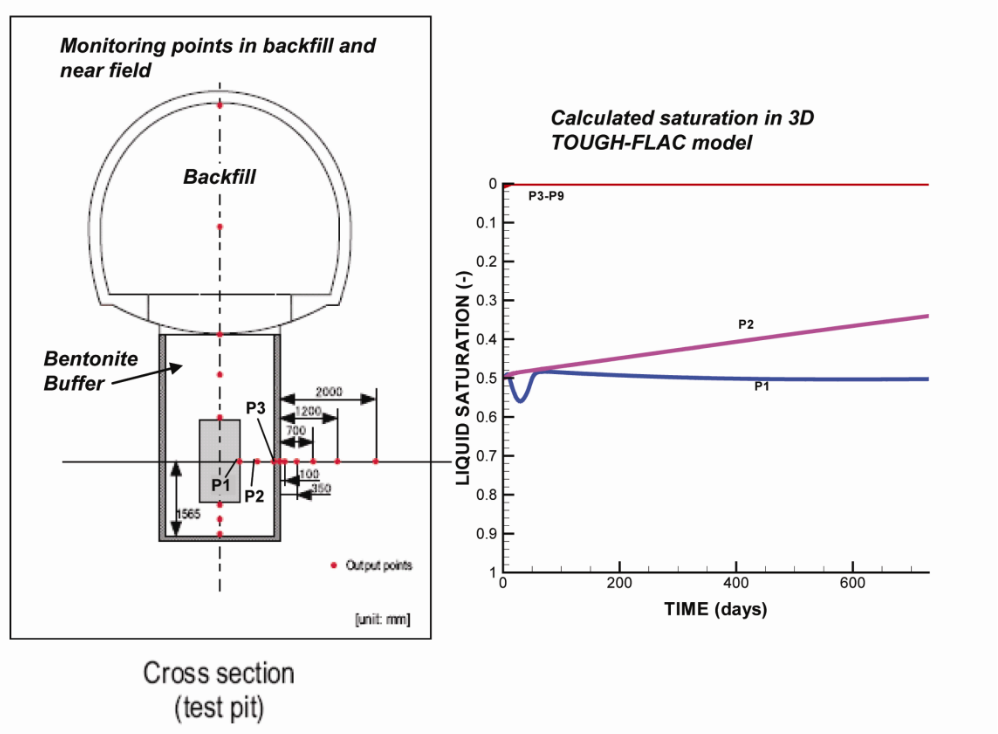

Figure 4.36. TOUGH-FLAC simulation results of liquid saturation in the buffer and rock.

4.5 FE Experiment at the Mont Terri Site

In this section, we present the FE Experiment and the current status of the modeling efforts, which are currently focused on the prediction of the temperature evolution as part of the experimental field test design. Moreover, we are actively working on defining the material properties for the granular bentonite and bentonite blocks that will be emplaced into the experimental tunnel. This includes the characterization of the bentonite in the CIEMAT column experiment, which was presented in Section 4.3 above.

As mentioned, the Mont Terri FE Experiment will be one of the largest and longest-duration heater tests worldwide, with focus on both the EBS components and the host-rock behavior. The FE experiment will be conducted in a side tunnel at Mont Terri, excavated along the claystone bedding planes for this purpose, extending 50 m in length and about 2.8 m in diameter (Figure 4.37). Heating from emplaced waste will be simulated by three heat-producing canisters of 1500 W maximum power. The temperature is expected to exceed 100°C, with a target temperature125 to 135°C at the inner parts of the buffer. A sophisticated monitoring program is planned, including dense pre-instrumentation of the site for *in situ* characterization, dense instrumentation of the bentonite buffer and host rock, and extensive geophysical monitoring (seismic and electric tomography).

The experiment will provide data useful for the validation of THM coupling effects regarding the processes in the host rock, while correctly accounting for (and examining) the conditions in the emplacement tunnel (temperature, saturation, and swelling pressure). Due to the 1:1 scale of the experiment, it will be possible to achieve realistic temperature, saturation, and stress gradients. It will also be possible to test backfilling technology with granular bentonite, as well as lining technology with shotcrete, anchors, and steel rips. Processes examined in the test cover many aspects of repository evolution, such as EDZ creation and desaturation of the EDZ during tunnel excavation and operation (including ventilation for about one year), as well as reconsolidation of the EDZ, resaturation, thermal stresses, and thermal pore-pressure increase after backfilling and heating (heating and monitoring period > 10 years).

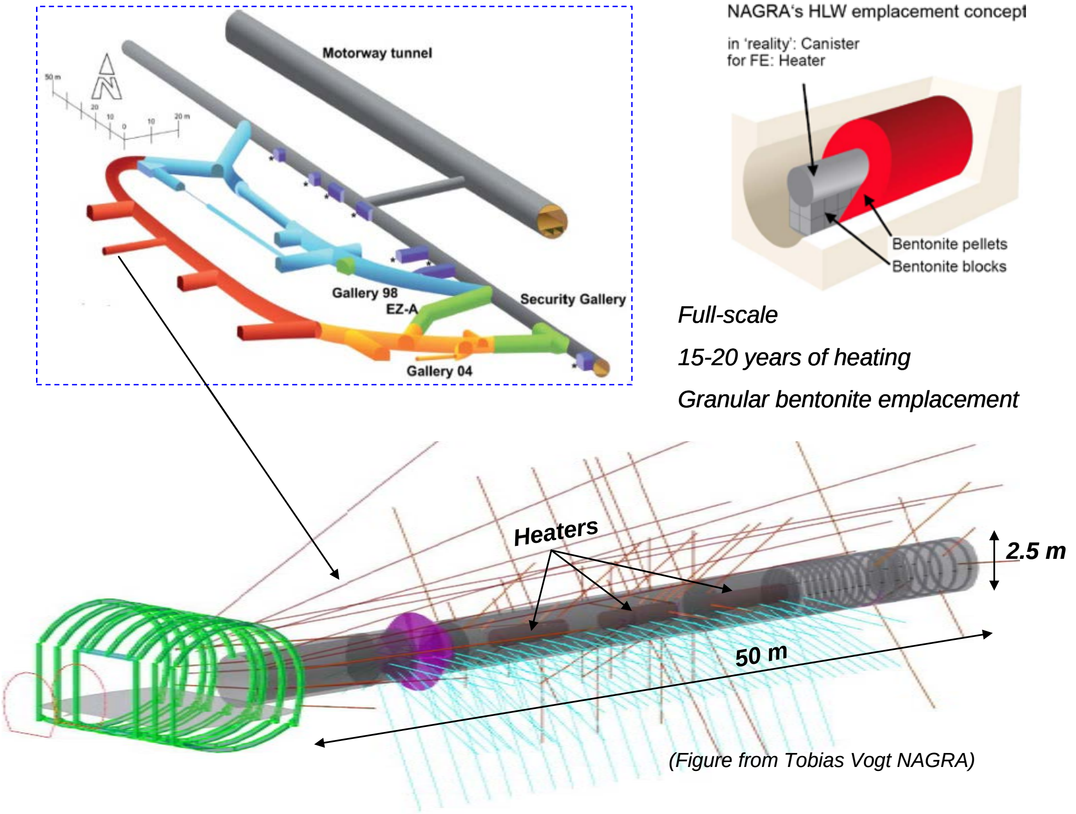

Full-scale

15-20 years of heating

Granular bentonite emplacement

(Figure from Tobias Vogt NAGRA)

Figure 4.37. Plan view of experiment setup and borehole layout.

In 2011, a niche in front of the FE tunnel was constructed followed by a first phase of instrumentation of the rock mass surrounding the tunnel, using boreholes from the niche. The FE tunnel was then excavated by road-header in 2012; this was followed by another phase of instrumentation. The tunnel is currently open for a 1-year ventilation period. This will be followed by the emplacement of the heaters, bentonite buffer, and a concrete plug, after which the heating is expected to start at the end of 2014. The heating is then expected to go on for at least 15 years, with continuous monitoring of THM processes in both the bentonite buffer and surrounding rock.

DOE is one of the experimental partners for the FE heater experiment, and LBNL is one of the modeling teams. In addition to LBNL, there are currently six other modeling teams involved in the Mont Terri FE experiment from Germany (2 teams), U.K., Spain, Switzerland, and Canada.

The plans for the THM modeling program are discussed and updated at regular meetings and include three types of computations:

1) Scoping computations
2) Bench Marking
3) Predictive computations

The scoping computations include brainstorming on potential ongoing processes, evaluating their significance and parameter range, comparing simulation results and input parameters derived by each team, and lessons learned (parameter range, importance, expected response). The benchmarking uses well-defined geometry problems with exact parameter values given to the teams, focusing on process modeling with precise comparison of codes. In the predictive calculations, likely parameters values and the as-built information of the experiment will be frozen.

The modeling will be used to predict the behavior of the system, and this should be reported prior to heating start (in 2014). Currently, each modeling team develops their conceptual models and material properties using available literature (papers and reports) on lab experiments and previous Mont Terri *in situ* tests, etc. Moreover, this is complemented with a restricted benchmark test for code comparison, in which properties and model geometry are set by NAGRA. In the FY2013 UFD milestone report entitled "Report on International Collaboration Involving the FE Heater and HG-A Tests at Mont Terri" (Houseworth et al., 2013), we presented results on the scoping calculations and the benchmarking which was completed in April 2014. We also made a first full THM 3D simulation of the FE heater test, including the BBM model for calculating the mechanical responses. These were scoping and preliminary predictions with the material properties available at the time, though in some cases including a different kind of bentonite.

In this report, we focus on the current task of predicting the temperature evolution and peak temperature, since this will be important for the design of the heat load of the experiment. Thus, in the following, we present the current LBNL model of the Mont Terri FE experiment, including numerical grid and thermal and hydraulic material properties. Finally, we present some simulation results related to the thermal evolution for different heat power schemes. This includes a staged heating during the first few months of the experiment, perhaps using only one of the three heaters. The staged heating schedule will be conducted to be able to make an early model calibration of the *in situ* thermal properties that can then be used to make a more reliable prediction of the peak temperature, once the full thermal power is applied. This will be done to assure that the temperature will not be so high that damage would happen to the monitoring system.

4.6 3D Model setup of the Mont Terri FE Experiment

For the modeling of the FE experiment, we have developed a conceptual model and modeling approach based on experience from previous design scoping calculations conducted by teams contracted by NAGRA, to help with the experimental design:

1) Pöyry (Engineering and Consulting): Modeling for excavation design using FLAC3D with ubiquitous joint model (anisotropic plasticity with different shear strength along bedding planes). This modeling approach was used to analyze the ground support design (Nater, 2012).

2) CINEMAT and UPC of Spain conducted scoping calculations for thermal and monitoring design using the CODE-Bright FEM code, and they used the BBM for modeling bentonite mechanical behavior (Garitte and Gens 2012).

3) The Interra Swiss Branch performed 3D TOUGH2 model simulations with anisotropic properties and inclined mesh. Their modeling was limited to thermal-hydrological processes (no mechanics) and done for thermal and monitoring design (Ewing and Senger, 2011).

LBNL's modeling approach contains important components from these three models. The host rock is modeled using TOUGH-FLAC with anisotropic properties considering bedding planes of the Opalinus Clay. The bedding planes across the FE tunnel are inclined, as can be seen in Figure 4.38. To accurately model anisotropic thermal and hydrological behavior, we created an inclined TOUGH2 mesh. Anisotropic mechanical material behavior is simulated using the FLAC3D ubiquitous joint model, with initial properties of those derived from the excavation design analysis by the Pöyry team (Nater 2012). In the ubiquitous joint model weak planes are assumed along the bedding planes of the Opalinus Clay in which the shear strength properties are different along bedding versus across bedding. The mechanical used for the Opalinus Clay were presented in Houseworth et al. (2013), but are not used in this study of peak temperature. For the bentonite, we started with the BBM model as applied by the CINEMAT and UPC (Garitte and Gens, 2012), and derived specific input material parameters for the MX-80 bentonite pellets that will be used as emplaced bentonite buffer around the heaters. With this modeling approach, we are able to simulate THM processes in both the bentonite and host rock, as well as their interactions.

Figure 4.38. View of FE tunnel face from the FE niche showing beddings dipping 45° (Vietor, 2012).

Figure 4.39 presents the 3D TOUGH-FLAC numerical grid of the FE experiment. This model grid includes all vital material components for the modeling of the FE experiment, including layered Opalinus Clay host rock, excavation disturbed zone, tunnel, 3 heaters, bentonite buffer, concrete liner, and concrete plug. The initial conditions for the model simulation are 2 MPa in pore-fluid pressure and 15°C in temperature for the host rock. The 2 MPa of pore pressure is not under hydrostatic conditions, and the process is affected by the existing tunnel system at the site. In our simulations, we first run a simulation with an open tunnel at atmospheric pressure for 1 year, creating a pressure drop and hydraulic gradient around the tunnel. Thereafter, we assume instantaneous emplacement of the heater and buffer, and start our heating simulation.

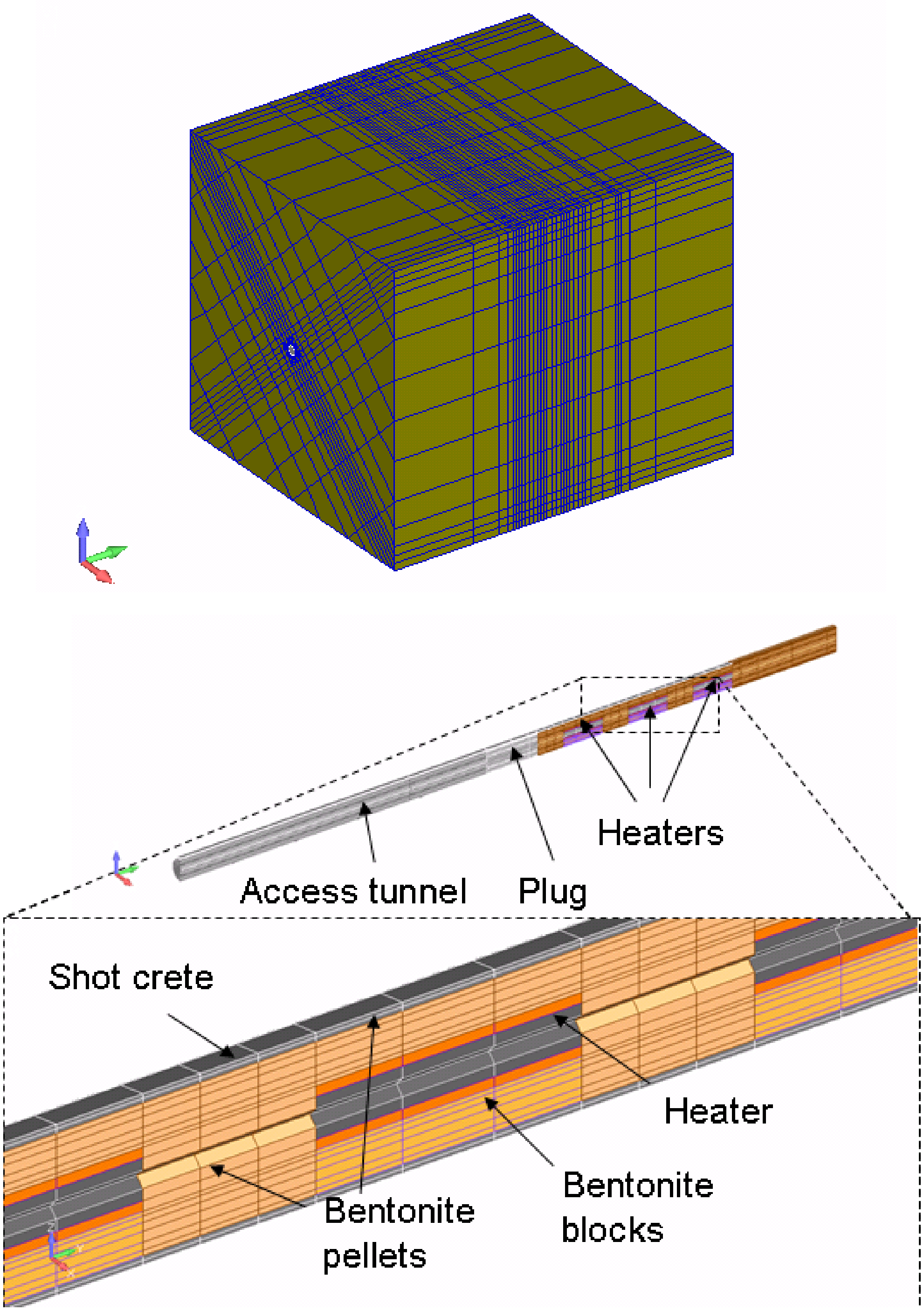

Figure 4.39. TOUGH-FLAC 3D numerical grid of the FE experiment.

The thermal and hydraulic material properties for modeling the FE experiment are given in Table 4.9. These include properties defined by NAGRA and used for the 1-D benchmarking exercise and reported in FY2013 milestone report “Report on International Collaboration Involving the FE Heater and HG-A

Tests at Mont Terri” (Houseworth et al., 2013), and is considered the current best estimate of the properties.

Table 4.9. Parameters for the Opalinus and Bentonite clay used in the modeling of the FE experiment.

Properties	Parameters	Symbol	Opalinus Clay	Bentonite	Concrete (shotcrete and plug)	Unit
Physical	Grain density	ρ_g	2.7×10^3	2.7×10^3	2.7×10^3	kg/m^3
	Porosity	Ø	0.15	0.46	0.15	-
Hydraulic	Intrinsic permeability	K	5.0×10^{-20}	2.0×10^{-21}	3.5 x 10^{-21}	M^2
	Liquid relative permeability (Eq. 4.16)	A	-	5	-	-
	Liquid relative permeability (Eq. 4.17)	m	0.52	-	0.52	-
	Capillary curve (Eq. 4.18)	P_0	1.09×10^7	1.00×10^7	1.09×10^7	Pa
	Capillary curve (Eq. 4.18)	m	0.29	0.4	0.29	-
	Capillary curve (Eq. 4.18)	S_{ls}	1.0	1.0	1.0	-
	Capillary curve (Eq. 4.18)	S_{lr}	0.01	0.0	0.01	-
Thermal	Thermal conductivity (wet)	λ_{sat}	1.7	1.0	1.7	W/m/K
	Thermal conductivity (dry)	λ_{dry}	1.06	0.3	1.06	W/m/K
	Grain specific heat	C	800	950	800	J/kg/K

The water relative permeability in the buffer is a power-law relationship given by

$$k_{rw}(S_w) = \left(\frac{S_w - S_r}{S_m - S_r}\right)^A \tag{4.16}$$

The water relative permeability in the concrete and rock is given by the van Genuchten relationship,

$$k_{rw}(S_w) = \left(\frac{S_w - S_r}{S_m - S_r}\right)^{1/2} \left[1 - \left\{1 - \left(\frac{S_w - S_r}{S_m - S_r}\right)^{1/m}\right\}^m\right]^2 \tag{4.17}$$

Capillary pressure in the buffer, concrete, and rock are given by the van Genuchten relationship:

$$\psi(S_w) = \frac{1}{\alpha}\left\{\left(\frac{S_w - S_r}{S_m - S_r}\right)^{-1/m} - 1\right\}^{1-m} \tag{4.18}$$

The relative permeability to gas for the buffer is set to a constant value of 1. The relative permeability to gas in the shotcrete and rock is

$$k_{rg}(S_w) = 1 - k_{rw}(S_w). \tag{4.19}$$

Variations in thermal conductivity and specific heat with water saturation are assumed to be linear between the defined end points. The vapor- and air-diffusion coefficients are a function of temperature and gas saturation defined by:

$$D_g^w = \tau S_g D \frac{P_{g0}(273.15+T)^n}{P_g(273.15)^n} \tag{4.20}$$

The problem was solved using TOUGH2 with the EOS4 equation of state module. We simulated high intrinsic gas permeability in the bentonite through the Klinkenberg parameter according to:

$$K_g = K_l(1+b/P) \tag{4.21}$$

where K_g is intrinsic permeability for gas flow, K_l is intrinsic permeability of water flow, b is the Klinkenberg parameter, and P is pressure. In this case, we assigned a high value of the Klinkenberg parameter of 2.5×10^{11} Pa^{-1}, which means that the intrinsic permeability for gas flow would be about 6 orders of magnitude higher than the intrinsic permeability for water flow.

The simulation of the heating is conducted with the initial saturation in the bentonite equal to 20% in the bentonite. Although the bentonite pellets when emplaced will be very dry, with a saturation of a few percent, experience and monitoring in the Mont Terri HE-E experiment shows that moisture is quickly taken up by the pellets from the surrounding humid air. This means that an initial saturation of 20% is realistic. In our modeling, we assign an initial capillary pressure, which corresponds to an initial saturation of 20% (Figure 4.40).

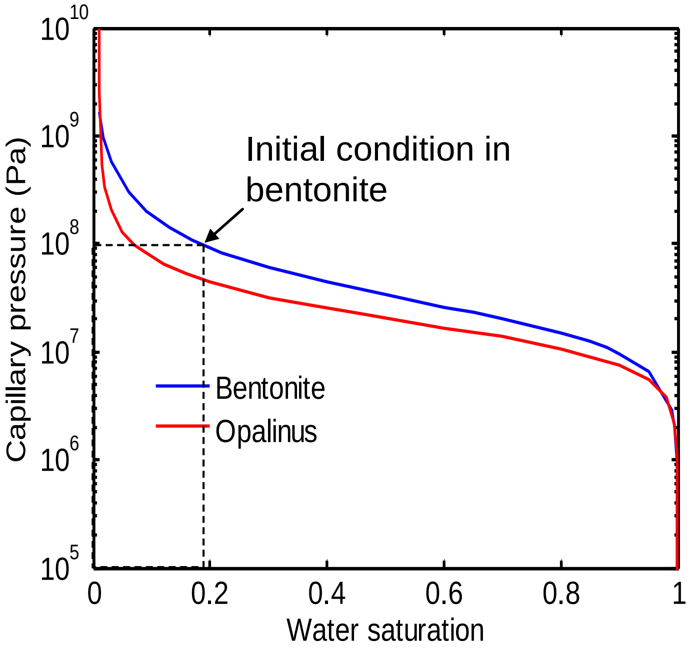

Figure 4.40. Capillary curves for Bentonite and Opalinus clays.

4.7 Model Prediction of Temperature and Saturation Evolution for Heat Power Design

Figure 4.41 shows our prediction of temperature and saturation evolution, assuming the full 1500 W power in each heater. In this case, the peak temperature at the buffer is as high as 160°C, i.e., considerably higher than the targeted 125 to 135°C. In the experiment, the temperature should not exceed 150°C, because this could be damaging for some of the monitoring sensors. The high peak temperature at the canister surface is caused by the combined effects of low thermal conductivity of the buffer and the rock, as well as the high diffusion coefficient that keeps the buffer dry around the heater. We consider these modeling results to be an initial predictive modeling, as there are still uncertainties related to the thermal conductivity and diffusion coefficient to be applied for this type of bentonite material.

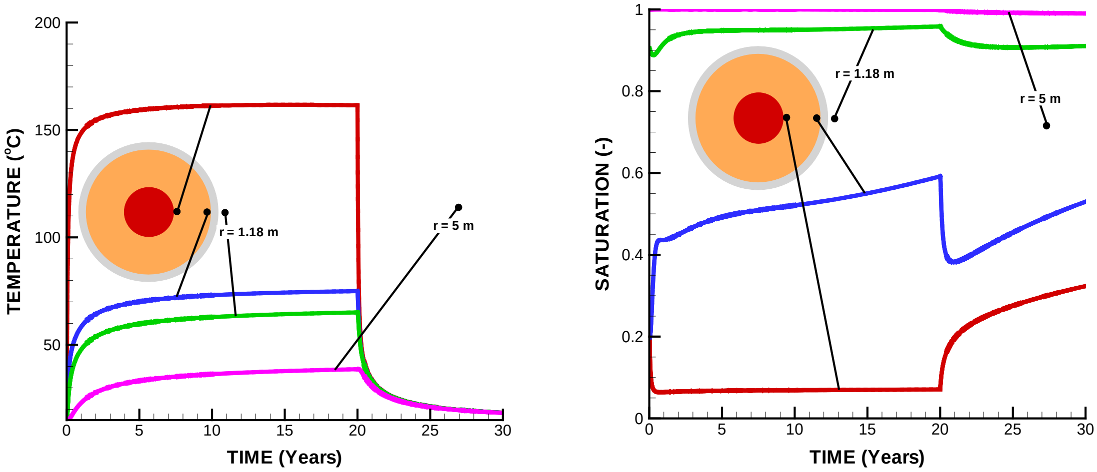

(a) (b)

Figure 4.41. Model prediction of (a) temperature and (b) liquid saturation for full power of 1500 W at each heater.

Figure 4.42 presents the results considering a staged heat power schedule the first few months. In this case, we assume that all 3 heaters are turned on and set at a constant power of 500 w for 30 days and then set to 1000 w for another 30 days. We then assume that full power of 1500 W is applied after 60 days. The simulation results in Figure 4.42 show that during the first 30 days, almost no drying occurs in the buffer. This means that a model calibration on this initial step can give a value of the initial thermal conductivity of the bentonite at 20% saturation (Figure 4.43c). During the next few months, there are some changes in saturation in the buffer, with some wetting from the rock and some drying near the heater. After turning on the full power at 60 days, the temperature increases and, finally at 1000 days, it has reached over 150°C at the heater surfaces. At this stage, the buffer has been substantially dried near the heater, and this drying has a significant impact on the peak temperature.

Figure 4.43 presents the results considering a staged heating only in the heater that is emplaced first, i.e., the one placed farthest into the tunnel. Included in Figure 4.43 are the temperature and saturation evolution at all three heaters, although heating is turned on only at one heater. By comparing Figures 4.43 and 4.42, we can conclude that during the first 100 days, the temperature and saturation evolution is identical at heaters that are turned on (solid lines). That is, the temperature and saturation evolution at one heater is not affected by the heating, temperature, saturation at the other two heaters. Figure 4.44 also shows the difference in temperature and saturation evolution between heaters that are turned on or off. At heaters that are turned off, there is no drying near the heater (red dashed line) and there is some slow infiltration from the rock, causing some slow increase in saturation (blue dashed line). The results indicate that for the heating design it is possible to first turn on only one heater with the staged heating test to calibrate the THM models. It might be possible to turn on the heater emplaced first and make this initial heating test before the entire test tunnel is completely backfilled.

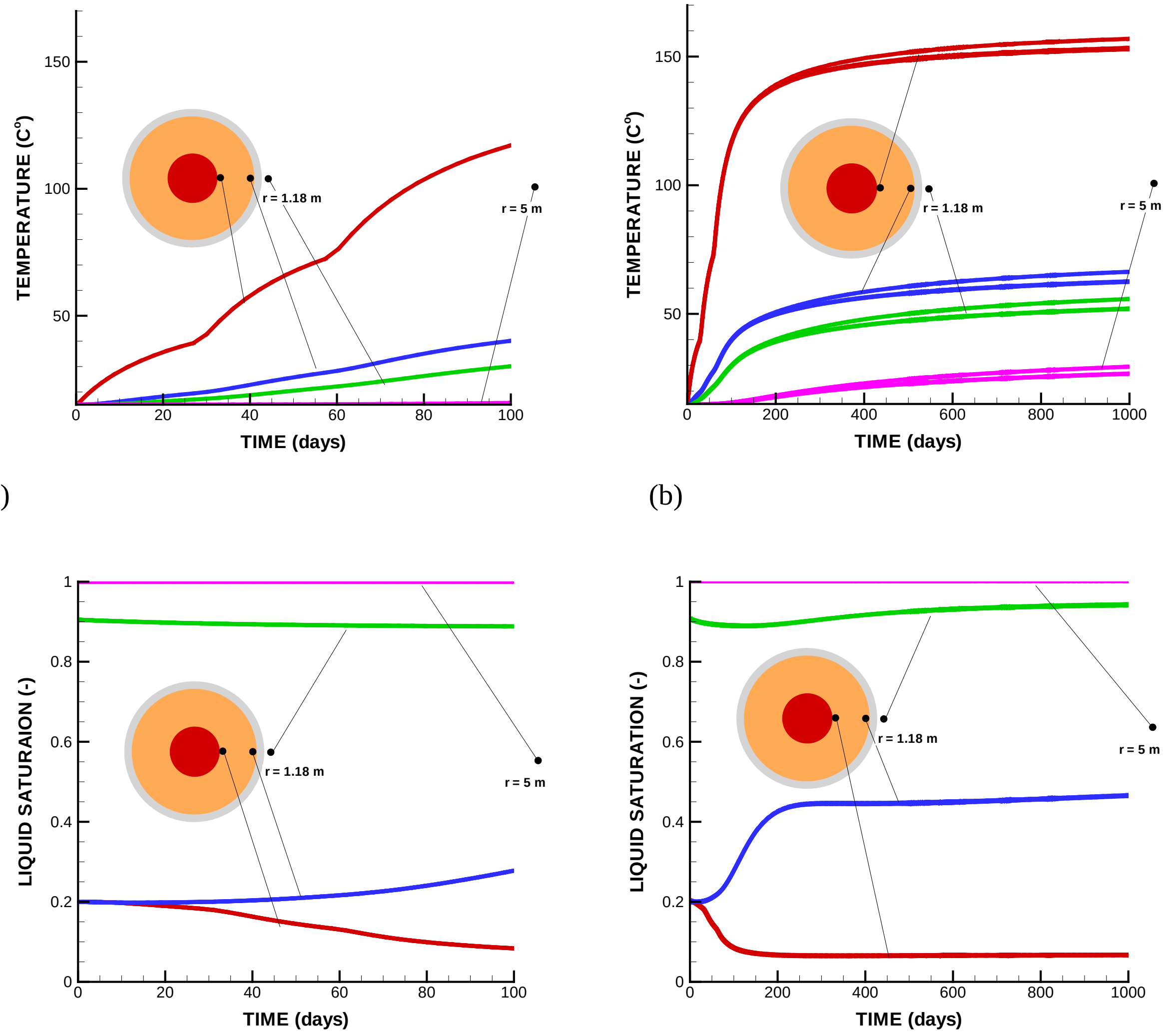

(a) (b)

(c) (d)

Figure 4.42. Model prediction of (a, b) temperature and (c, d) liquid saturation for staged power in 3 heaters.

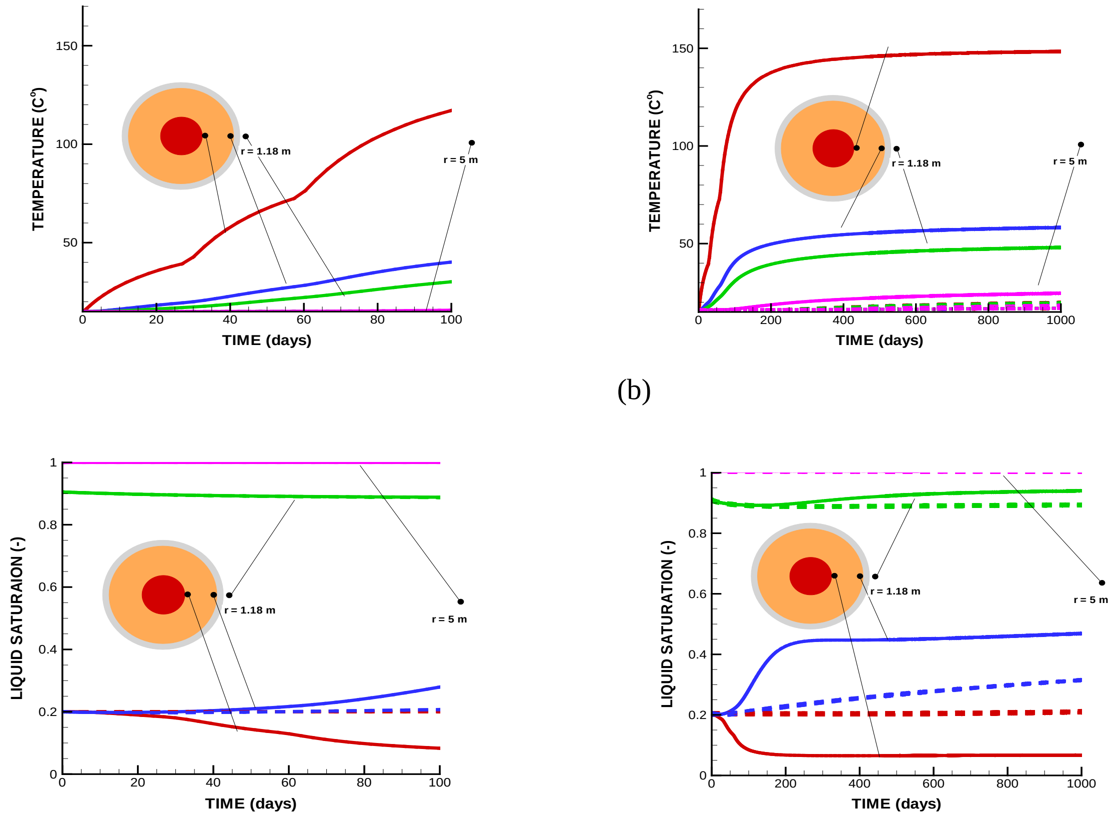

(a) (b)

(c) (d)

Figure 4.43. Model prediction of (a, b) temperature and (c, d) liquid saturation for staged power in first emplaced heater. Solid lines refers to evolution at the heater that is turned on, whereas dashed lines refers to evolution at heater that are turned off.

4.8 Status of THM Modeling of Heater Experiments and Plans

UFD and LBNL greatly benefit from participating in these international activities for developing expertise and testing advanced models for coupled THM processes. LBNL is leveraging on previous experience and existing models (TOUGH-FLAC and ROCMAS) that are extended to meet technical requirements for being able to predict the long-term THM and THMC evolution of a multibarrier nuclear waste repository system, involving backfilled emplacement tunnels in argillite host formations. FY2014 accomplishments include:

- Completed implementation of constitutive models for the coupled geomechanical behavior of bentonite-based buffer material, including most recently the advanced dual-structure model.
- Verification and testing of the implemented geomechanical constitutive models for bentonite-based buffer material by modeling laboratory experiments and long-term behavior of a generic repository.
- Validation of TOUGH-FLAC and characterization of THM properties for two types of bentonite-based buffer materials through modeling of CIEMAT laboratory column experiments.

- Development of full-scale 3D TOUGH-FLAC models of the Horonobe EBS experiment and Mont Terri FE experiment and initial model predictions of temperature and saturation evolutions.
- Benchmarking associated with the Horonobe EBS experiment achieving good agreement with the results of other international modeling teams, providing code-to-code verification of TOUGH-FLAC.
- Published one journal paper (Rutqvist et al., 2014) on THM modeling of nuclear waste disposal in argillite and submitted one journal paper on the use of the dual-structure model for modeling long-term behavior of a nuclear waste repository (Vilarrasa et al., 2014).

The implemented constitutive models have been verified and tested by modeling laboratory experiments and generic repository, but the dual-structure model has not yet been applied in the modeling of the large-scale field experiments. Although a number of features in the dual-structure model are important for evaluating the long-term performance of a buffer-rock system, there is still a lack of experimental data and experience to apply such a model. It is only LBNL’s TOUGH-FLAC simulator and the Code-bright simulator at University of Catalonia (UPC) in Barcelona that have the full capabilities of such a dual-structure model in a THM simulator. In this context, participation as a modeling team in the FE Experiment will be particularly beneficial, as one of the other modeling teams participating is the UPC, who are planning to apply the dual-structure model in their modeling of the experiment. We note that UPC is one of the world leaders in unsaturated soil mechanics and the original developer of the dual-structure constitutive model for expansive clay that we have implemented into TOUGH-FLAC. Thus, participating in the Mont Terri FE experiment provides an important opportunity for collaboration and model comparison and comparison to field data using this advanced constitutive model. Likewise, the participation in the DECOVALEX-2015 provides the opportunity to gain experience and test our models for a range of different backfill materials (e.g., bentonite pellets and sand/bentonite mixture), as well as different host rocks (Opalinus Clay and mudstone).

Our work in the remaining months of FY2014 and beginning of FY2015 will be focused on the model predictions to be performed for the three *in situ* heater experiments; the Mont Terri HE-E experiment, the Horonobe EBS experiment, and the Mont Terri FE experiment. We have already developed full 3D models and made preliminary predictions for the Horonobe EBS Experiment and the Mont Terri FE experiment. Next, we will develop the 3D mesh for the Mont Terri HE-E experiment, with the prediction to be presented at the next DECOVALEX-2015 workshop in November 2014. By participating as a DECOVALEX research team for modeling the Mont Terri HE-E experiment, we will be able to compare the results with experimental data already at the November workshop— this will be an important model validation test and provide experience on modeling a buffer consisting of granular bentonite, which is also the buffer material that will be used at the Mont Terri FE experiment. Our work for FY2015 will then be very much focused on validation of our models against these field experiments, as well as characterization of parameters for BBM and dual-structure constitutive models from laboratory data that are now becoming available in the various projects. In summary, proposed work for FY2015 related to these international activities include,

- Full-scale 3D model predictions for the three *in situ* heater experiments; the Mont Terri HE-E experiment, the Horonobe EBS experiment, and the Mont Terri FE experiment, and compare with data and with the results of other international modeling teams in the DECOVALEX and Mont Terri projects
- Collaborate with the UPC (Barcelona) modeling team in application of the BBM and dual-structure models to the Mont Terri FE experiment.
- Validation of models against these field experiments as well as characterization of parameters for BBM and dual-structure constitutive models from laboratory data that are now becoming available in the various projects.

- Review of THM properties of bentonite-based buffer and backfill materials in these field experiments (and in nuclear waste isolation in general) and identify critical parameters and experimental data needs.
- Participated and presenedt simulation results at DECOVALEX and Mont Terri workshops.

Finally, we note that by participating in these international activities we are making significant progress toward achieving UFD goals to fill data needs and confirm advanced modeling approaches (by 2015), and to have a robust modeling and experimental basis for evaluation of multiple disposal system options (by 2020).

5. Investigation of the Impacts of High Temperature Limits with THMC modeling

5.1 Introduction

Radioactive waste from spent fuel emanates a significant amount of thermal energy, due to decay processes, which cause temperature increases in the surrounding environment, particularly in the early stages of waste emplacement. The temperature to which the EBS and natural rock can be exposed is one of the most important design variables for a geological repository, because it determines waste package spacing, distance between disposal galleries, and therefore the overall size (and cost) of a repository for a given amount of heat-emanating waste (Horseman and McEwen, 1996). This is especially important for a clay repository, because argillaceous rocks have relatively small heat conductivity. A thermal limit of about 100°C is imposed unanimously in all disposal concepts throughout the world, despite their differences in design concepts (Hicks et al., 2009). Chemical alteration and the subsequent changes in mechanical properties are among the determining factors. A high temperature could result in chemical alteration of buffer and backfill materials (bentonite) within the EBS through illitization and cementation, which compromise the function of these EBS components by reducing their plasticity and capability to swell when wetting (Pusch and Karnland, 1996; Pusch et al., 2010; Wersin et al., 2007). The swelling capability of clay minerals within the bentonite is important for sealing gaps between bentonite blocks, between bentonite and other EBS components, and between the EBS and the surrounding host rock. Chemical alteration may also occur in the near-field host rock, which could reduce the clay capability for self-sealing within the excavation damaged zone (EDZ). As a result of the low permeability of clay rock, a high temperature may induce significant pore-pressure buildup (through pore-water expansion and vaporization) in the near field, which could generate adverse mechanical deformation (such as fracturing), damaging the integrity of the host rock (Horseman and McEwen, 1996).

Regarding the concern of chemical alteration and the associated mechanical changes, Wersin et al. (2007), after reviewing a number of data sets, concluded that the criterion of 100°C for the maximum temperature within the bentonite buffer is overly conservative. Their conclusion was based on their findings that no significant changes in bentonite hydraulic properties occur at temperatures of at least 120°C under wet conditions and that bentonite is chemically stable to much higher temperatures under dry conditions. The impact of a high temperature on bentonite and clay host rock behavior, and the consequences on repository performance, are largely open questions for a clay repository system. While various studies shed light on certain aspects of this question, there is a lack of studies that integrate the relevant THMC processes and consider the interaction between the EBS and the host rock.

Since FY13, in UFDC, LBNL has used coupled THMC modeling to evaluate the chemical alteration and mechanical changes in EBS bentonite and the natural system (NS) clay formation under various scenarios, attempting to provide necessary information for decisions on temperature limits. In the FY13 report (Liu et al., 2013b), after an extensive review of the THMC alteration of EBS and clay formation (argillite) under various temperature conditions, fully coupled THMC simulations were developed for a nuclear waste repository in a clay formation with a bentonite-backfilled EBS. Two scenarios were simulated for comparison: a case in which the temperature in the bentonite near the waste canister can reach about 200°C, and a case in which the temperature in the bentonite near the waste canister peaks at about 100°C. In these simulations, it was assumed that the EBS bentonite was Kunigel-V1 bentonite (Ochs et al., 2004) and that the host rock properties were representative of Opalinus Clay (Bossart, 2011; Lauber et al., 2000). Simulations showed that the decrease in smectite volume fraction in bentonite ranges from 0.004 to a maximum of 0.085, or up to about 27% of the initial volume fraction of smectite for the 200°C scenario, and decrease in smectite volume fraction leads to a reduction in swelling stress around 16–27%, subject to a great deal of variation in terms of the decrease in smectite volume fraction and swelling pressure under different chemical conditions. In FY14, we first continued to analyze the sensitivity of calculated swelling pressure for Kunigel-V1 bentonite to critical parameters. Second, we replace Kunigel-V1 bentonite with FEBEX bentonite in the THMC model to evaluate potential chemical change in FEBEX bentonite and its effect on the swelling pressure. Kunigel-VI bentonite (Ochs et al., 2004) has low smectite content and relatively low swelling capacity, whereas FEBEX bentonite (ENRESA, 2000) has a high fraction of smectite and high swelling capacity. Modeling results showed that FEBEX bentonite undergoes less degree of illitization and smaller swelling pressure reduction that is very minimal comparing with the swelling capacity of FEBEX bentonite.

5.2 Modeling Study

5.2.1 Model Development

Because the model used in this report is the same as that of last year (Liu et al., 2013b), we only briefly describe each element of the THMC model here, referring the reader to Liu et al. (2013b) for details.

5.2.1.1 Simulator

Numerical simulations are conducted with TOUGHREACT-FLAC, which sequentially couples the multiphase fluid flow and reactive transport simulator, TOUGHREACT (Xu et al., 2011), with the finite-difference geomechanical code FLAC3D (Itasca, 2009). The coupling of TOUGHREACT and FLAC was initially developed in Zheng et al. (2011) to provide the necessary numerical framework for modeling fully coupled THMC processes. It was equipped with a linear elastic swelling model (Zheng et al., 2012; Rutqvist et al., 2013c) to account for swelling as a result of changes in saturation and pore-water composition and the abundance of swelling clay (Liu et al., 2013b).

5.2.1.2 Modeling scenario

The model is applied to a hypothetical bentonite-backfilled nuclear waste repository in clay rock, a repository example that involves a horizontal nuclear waste emplacement tunnel at 500 m depth (Figure 5.1) (Rutqvist et al., 2013c). The Z-axis is set as vertical in the model, while the horizontal Y- and X-axes are aligned parallel and perpendicular to the emplacement tunnel, respectively (Figure 5.1). An initial stress field is subjected to the self-weight of the rock mass. Zero normal displacements are prescribed on the lateral boundaries of the model. Vertical displacements are prevented at the bottom. The model simulation was conducted in a nonisothermal mode with a time-dependent heat power input (Rutqvist et al., 2013c), adopted from the heat load developed within the U.S. DOE's Used Fuel Disposition campaign as a generic disposal system environment for Pressurized Water Reactor (PWR) used nuclear fuel. This heat load is then scaled in the 2D model to represent a certain line load, which depends on the assumed spacing between individual waste packages along an emplacement tunnel. Initially, the EBS bentonite has a water saturation of 65% and the clay formation is fully saturated. From time zero, the EBS bentonite simultaneously undergoes resaturation, heating, chemical alteration, and stress changes.

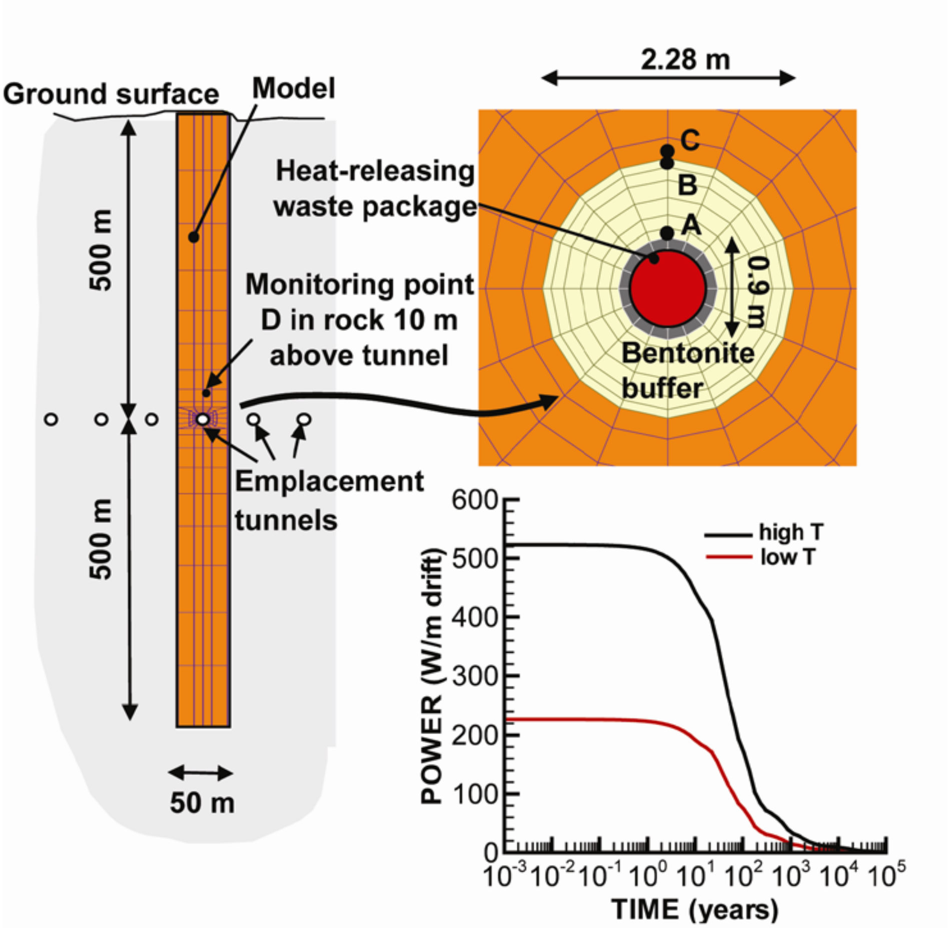

Figure 5.1. Domain for the test example of a bentonite back-filled horizontal emplacement drift at 500 m (Rutqvist et al., 2013c).

5.2.1.3 Mechanical Model

To consider the swelling due to both moisture and chemical concentration changes, we include the stress due to changes in chemical concentration and abundance of swelling clay:

$$d\sigma_s = 3K\beta_{sw}ds_l - A_n dC + A_{sc}dm_s \tag{5.1}$$

where K is the bulk modulus and β_{sw} is a moisture swelling coefficient. In this report, β_{sw} is 0.048, which is calibrated for the swelling pressure of 1 MPa (Börgesson et al., 2001) the swelling pressure measured for Kunigel-V1 bentonite (which was used in current models as the EBS material) under the condition that bentonite is saturated with dilute solution (e.g., deionized water), and K is 20 MPa (Rutqvist et al., 2011). A_n is a constant that linearly relates chemical concentration (C) variation and the corresponding stress change. A_n is typically calculated from swelling pressures measured using different solutions (e.g. deionized water versus 1 M NaCl solution) than are used to saturate the bentonite. Laredj et al. (2010) proposed the following expression for A_n:

$$A_n = \frac{(5.312 \ln C - 23.596)}{\sqrt{C}} - \frac{7.252 \times 10^{-4}}{C^2} \tag{5.2}$$

A_{sc} is a constant that relates the change in mass fraction of swelling clay, m_s, to change in stress. An empirical value is derived from measured swelling pressure for bentonite materials of different smectite mass fraction (Liu et al., 2013b), which is 2.5×10^6 Pa^{-1}.

5.2.1.4 Chemical Model

In these generic cases, it is assumed that the host-rock properties are representative of Opalinus Clay (Bossart, 2011; Lauber et al., 2000), and two cases for the EBS backfill, one composed of Kunigel-V1 bentonite (Ochs et al., 2004) and the other FEBEX bentonite (ENRESA, 2000). The mineral composition of the bentonite and clay formation is listed in Table 5.1. The pore-water composition of the Kunigel-V1 bentonite (Sonnenthal et al., 2008), FEBEX bentonite (Fernández et al., 2001) and the clay formation (Fernández et al., 2007) are listed in Table 5.2. Table 5.3 lists the thermal and hydrodynamic parameters used in the model. The majority of these parameters for the EBS bentonite are based on the properties of Kunigel-VI bentonite (Sonnenthal et al., 2008), and those for the NS clay formation are from Thury (2002). Permeability for the clay formation is from Soler (2001), and that for the bentonite is from Japan Nuclear Cycle Development Institute (JNC) (2000).

FEBEX and Kunigel-VI bentonite also have distinct hydrological and thermal parameters, with the most relevant ones being thermal conductivity and permeability. However, in this report, we keep them the same thermal conductivity and permeability, which are actually fairly similar for both bentonite — thermal conductivity for saturated Kunigel-VI bentonite is 1.5W/m°C (see Table 5.2)—and for FEBEX bentonite is 1.3 W/m°C (Empresa Nacional de Residuos Radioactivos SA (ENRESA), 2000). Permeability for Kunigel-VI bentonite is 2E-21 m^2 and that for FEBEX ranges from 3.75E-21 to 1E-21 m^2 (ENRESA, 2000; Zheng et al., 2011; Chen et al., 2009). Moreover, by keeping thermal conductivity and permeability the same, we can isolate the effect of variation in chemical and CM coupling parameters on stress changes.

Table 5.1. Mineral volume fraction (dimensionless, ratio of the volume for a mineral to the total volume of medium) of the Kunigel-V1bentonite (Ochs et al., 2004), FEBEX bentonite (ENRESA, 2000; Fernández et al., 2004; Ramírez et al., 2002) and Opalinus Clay (Bossart 2011; Lauber et al., 2000).

Mineral	EBS Bentonite: Kunigel-V1	EBS Bentonite: FEBEX	Clay formation: Opalinus Clay
Calcite	0.016	0.0065	0.093
Dolomite	0.018	0.0	0.050
Illite	0.000	0.0	0.273
Kaolinite	0.000	0.0	0.186
Smectite	0.314	0.6	0.035
Chlorite	0.000	0.0	0.076
Quartz	0.228	0.026	0.111
K-Feldspar	0.029	0.0065	0.015
Siderite	0.000	0.0	0.020
Ankerite	0.000	0.0	0.045

Table 5.2. Pore-water composition of Kunigel-V1bentonite (Sonnenthal et al., 2008), FEBEX bentonite (Fernández et al., 2001) and Opalinus Clay (Fernández et al., 2007).

	EBS Bentonite: Kunigel-V1	**EBS Bentonite: FEBEX**	**Clay formation: Opalinus Clay**
pH	8.40	7.72	7.40
Cl	1.50E-05	1.60E-01	3.32E-01
SO_4^{-2}	1.10E-04	3.20E-02	1.86E-02
HCO_3^-	3.49E-03	4.1E-04	5.18E-03
Ca^{+2}	1.37E-04	2.2E-02	2.26E-02
Mg^{+2}	1.77E-05	2.3E-02	2.09E-02
Na^+	3.60E-03	1.3E-01	2.76E-01
K^+	6.14E-05	1.7E-03	2.16E-03
Fe^{+2}	2.06E-08	2.06E-08	3.46E-06
SiO_2(aq)	3.38E-04	1.1E-04	1.10E-04
AlO_2^-	1.91E-09	1.91E-09	3.89E-08

Table 5.3. Thermal and hydrodynamic parameters.

Parameter	**Clay formation : Opalinus Clay**	**EBS Bentonite**
Grain density [kg/m^3]	2700	2700
Porosity ϕ	0.162	0.33
Saturated permeability [m^2]	2.0×10^{-20}	2.0×10^{-21}
Relative permeability, k_{rl}	$m = 0.6$, $S_{rl} = 0.01$	$K_{rl} = S^3$
Van Genuchten α [1/Pa]	6.8×10^{-7}	3.3×10^{-8}
Van Genuchten m	0.6	0.3
Compressibility, β [1/Pa]	3.2×10^{-9}	5.0×10^{-8}
Thermal expansion coeff., [1/^{o}C]	1.0×10^{-5}	1.5×10^{-4}
Dry specific heat, [J/kg ^{o}C]	860	800
Thermal conductivity [W/m ^{o}C] dry/wet	1.48*/1.7$	1.1/1.5
Tortuosity for vapor phase	$\phi^{1/3} S_g^{10/3}$	$\phi^{1/3} S_g^{10/3}$
Bulk modulus, (GPa)	4.17	0.02
Shear modulus, (GPa)	1.92	0.0067

from http://www.mont-terri.ch/internet/mont-terri/en/home/geology/key_characteristics.html

The kinetic rates and surface areas for the minerals considered in current model are taken mostly from Xu et al. (2006). However, the illitization rate (the rate of illite precipitation and smectite dissolution) was calibrated (Liu et al., 2013) based on the measured illite percentage in an illite/smectite (I/S) mixed layer from Kinnekulle bentonite, Sweden (Pusch and Madsen, 1995). The thermodynamic data are from the Data0.dat.YMPv4.0, a EQ3/6 (Wolery, 1993) database qualified by the U.S. Department of Energy for the Yucca Mountain project.

5.2.2 Model Results

5.2.2.1 Cases for Kunigel Bentonite

The model results for the base case, expressed as the evolution of temperature, pore pressure, water saturation, concentration, and stress, were discussed in detail in Liu et al. (2013b). In this report, the evolution of stress in EBS bentonite is further analyzed to study the contributions of different processes to total stress. We first briefly discuss the change in temperature, water saturation, and the volume fraction of smectite, because their changes essentially determine the evolution of stress. Then we discuss the changes in stress.

5.2.2.1.1 THC Evolution

The evolution of heat release from decaying waste is shown in Figure 5.1. The heat release rates have been adjusted to make two cases for comparison: a “high T” case, in which the temperature near the canister can reach 200°C; and a “low T” case, in which the temperature near the canister peaks at about 100°C. In this paper, the temporal evolution at four monitoring points (see Figure 5.1 for their positions) is used to present thermal, hydrological, chemical, and mechanical results: point A is inside the bentonite near the canister, point B is inside the bentonite and near the EBS-NS interface, point C is inside the clay formation and near the EBS-NS interface, and point D is inside the clay formation at a distance from canister of 10 m. The temperature evolution at the four monitoring points A, B, C, and D is shown in Figure 5.3. Pore pressure increases as a result of resaturation and heating. The “high T” case exhibit much higher pore pressure than the “low T,” with a difference of about 5 MPa after 1000 years (Figure 5.5). The clay formation near the EBS-NS interface goes through desaturation (Figure 5.4), which interestingly lasts much longer for the “low T” case than the “high T” case. The higher temperature leads to a higher pore pressure (Figure 5.5) in the EBS bentonite, which reduces desaturation in the clay formation because higher pore pressure in the EBS bentonite lowers the hydraulic pressure gradient and therefore the flow of water towards the EBS bentonite.

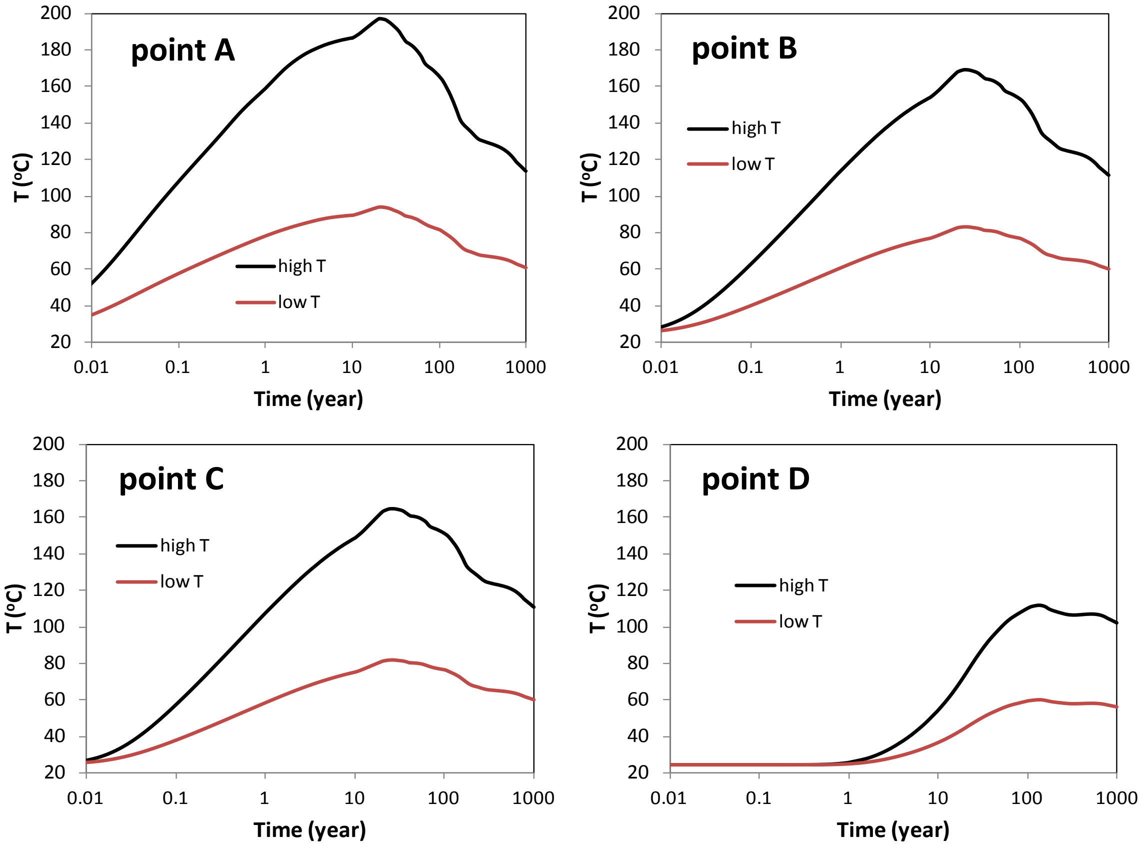

Figure 5.2. Temperature evolution at points A, B, C, and D.

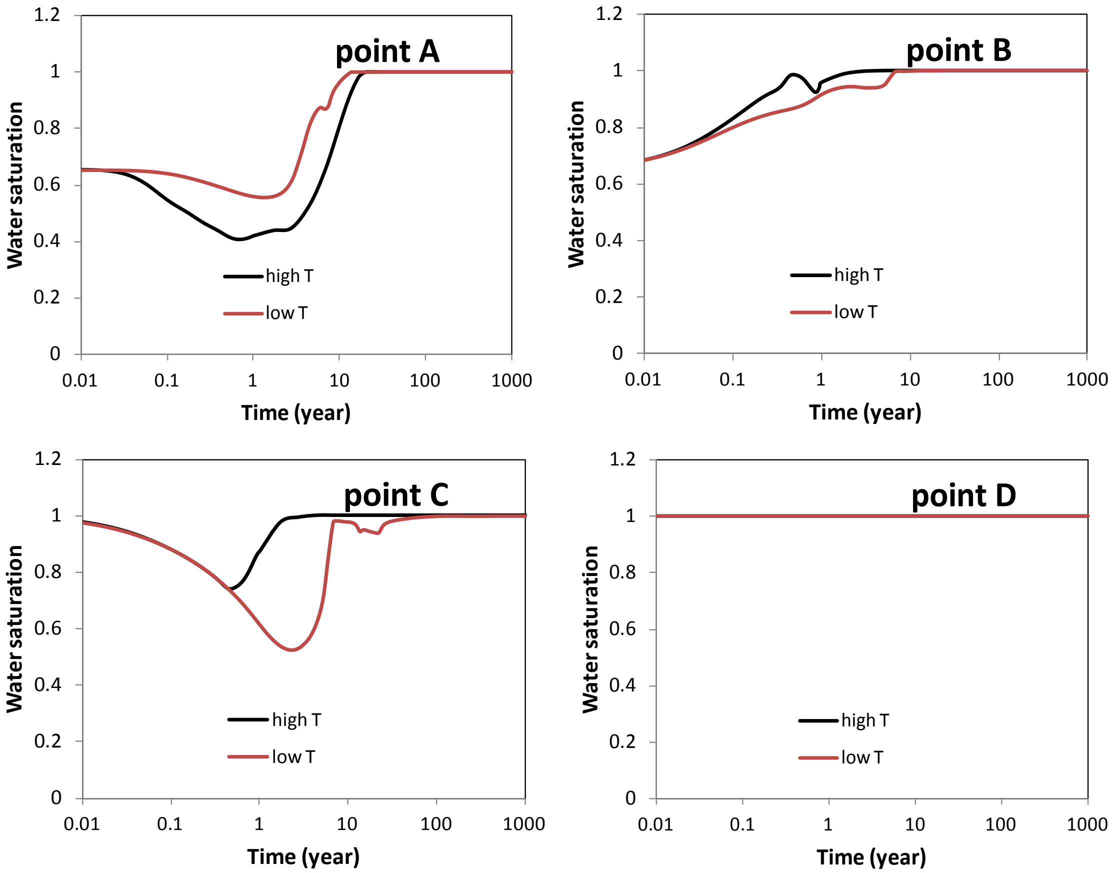

Figure 5.3. The temporal evolution of water saturation at points A, B, C, and D.

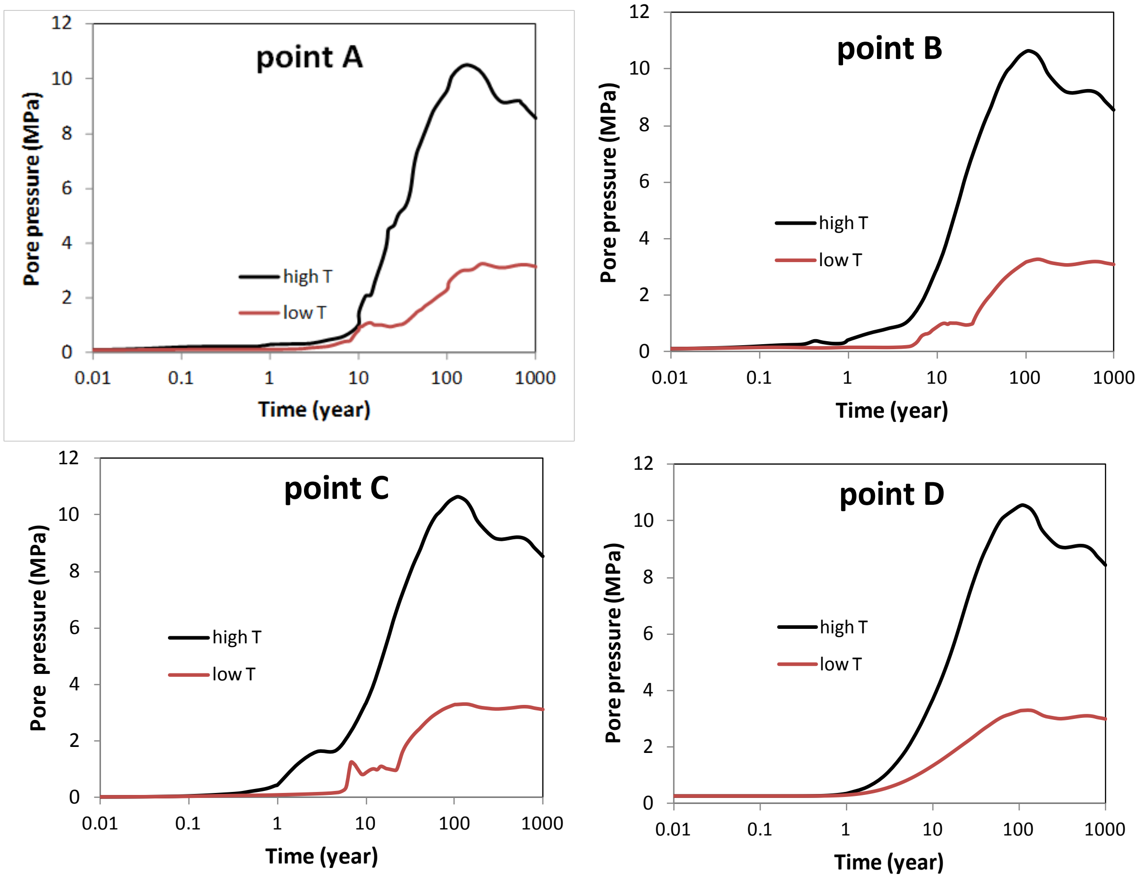

Figure 5.4. The temporal evolution of pore pressure at points A, B, C, and D.

Illitization is modeled as the dissolution of smectite and precipitation of illite. The overall reaction can be written as:

$$\text{Smectite} + 0.52\text{H}^{+} + 0.63\text{AlO}_2^{-} + 0.6\text{K} = \text{illite} + 0.26\text{H}_2\text{O} + 0.08\text{Mg}^{+2} + 0.33\text{Na}^{+} + 0.5\text{SiO}_2(aq) \qquad 5.3$$

Based on the database used in the model, this reaction yields a volume change of -4.9 ml/mol. Note that H_2O is not considered in the reaction.

Many factors can affect the chemical reactions, such as the initial water-mineral disequilibrium in bentonite (since the water used for making bentonite blocks is not necessarily in equilibrium with the mineral phase in bentonite, and it takes time to reach that equilibrium), as well as the thermal and hydrological disturbances in response to emplacement.

Results from the base case confirm that the clay host rock undergoes a small degree of illitization similar to the process widely observed in geological systems (e.g., Wersin et al., 2007; Pusch and Madsen 1995), as illustrated by the smectite dissolution at point C and D in Figure 5.5 and illite precipitation at point C and D in Figure 5.6. The volume fraction of smectite decreases by only about 0.002 (or 6% of the initial amount) in 1000 years. When the temperature is higher (“high T” case), illitization at point D in the clay rock is clearly accelerated, resulting in a decrease of 0.015 (or 43% of the initial amount) in the smectite volume fraction after 1,000 years. At point C, located near the EBS-NS interface, more hydrological and chemical interactions take place between the bentonite and the clay formation. Subsequently, more smectite dissolves and more illite precipitates. For the "high T" case, the smectite volume fraction decreases by 0.035, a 100% loss of smectite.

Illitization also occurs in the EBS bentonite, as shown by the smectite and illite volume fraction changes at points A and B in Figures 5.5 and 5.6. In addition to temperature effects, illitization is affected by the initial disequilibrium between the pore-water solution and the mineral phase. Initially, the pore water in the bentonite buffer is oversaturated with respect to illite and undersaturated with respect to smectite. In addition, the pore water in the clay formation contains a much higher concentration of K and Al, and thus provides a source of Al and K for the EBS bentonite alteration through diffusion and advection. Note that the increase in Al and K concentrations in bentonite is caused not only by diffusion and advection, but also by the dissolution of other minerals, such as K-feldspar and quartz. The pore water in the clay formation also has a higher concentration of Mg and Na, which inhibits illitization. But it seems that the factors in favor of illitization outpace those against illitization. At the end of 1,000 years, the smectite volume fraction in the bentonite decreases by 0.035 (or 11%) for the "high T" case and 0.006 (or 2%) for the "low T" case, which corresponds to an illite volume fraction increase of similar magnitude. Clearly, the "high T" case demonstrates stronger illitization than the "low T" case. In "high T" case, at point A near the canister, bentonite undergoes desaturation in short term, the evaporation of pore water therefore results in the precipitation of smectite. The smectite start to dissolve (Figure 5.5) and illite starts to precipitate (Figure 5.6) after about 20-30 years. After that, the dissolution of smectite and precipitation of illite proceed rapidly.

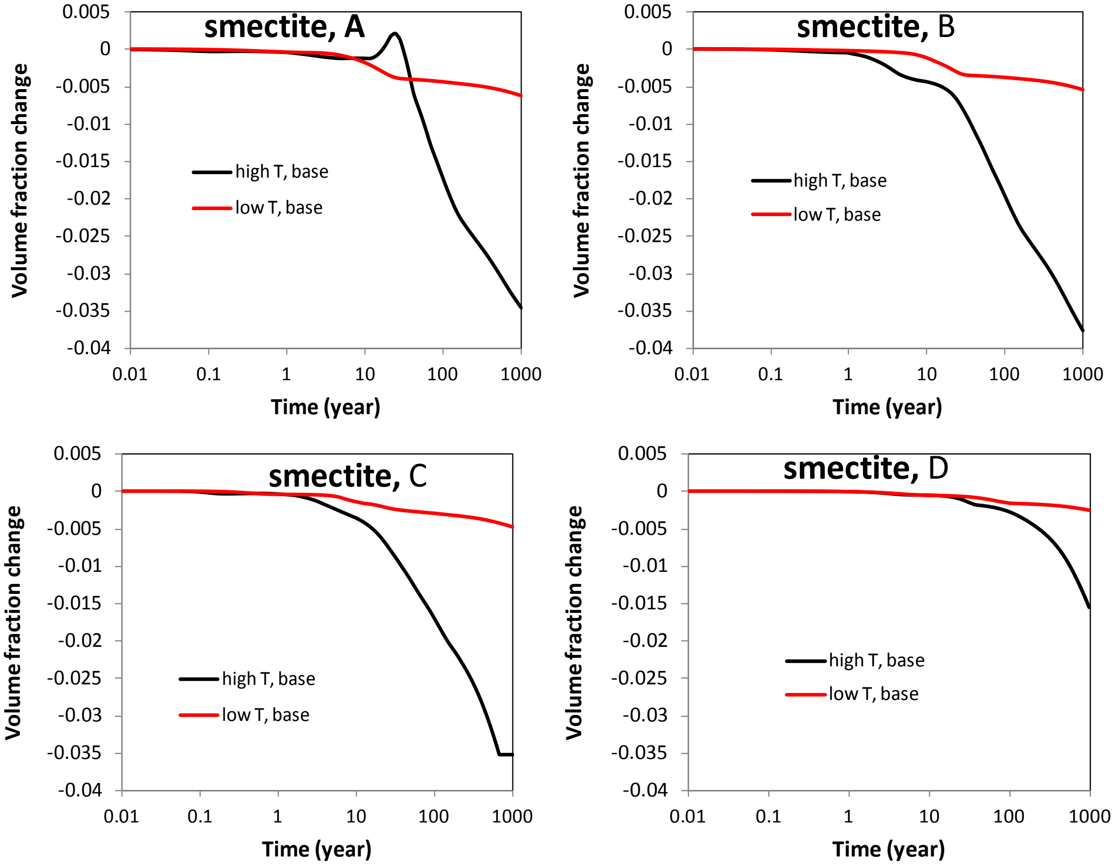

Figure 5.5. The temporal evolution of smectite volume fraction at points A, B, C, and D. Volume fraction change shown in the Y-axis is equal to the volume fraction of smectite at a given time minus the initial volume fraction (see Table 5.1), so negative value means dissolution.

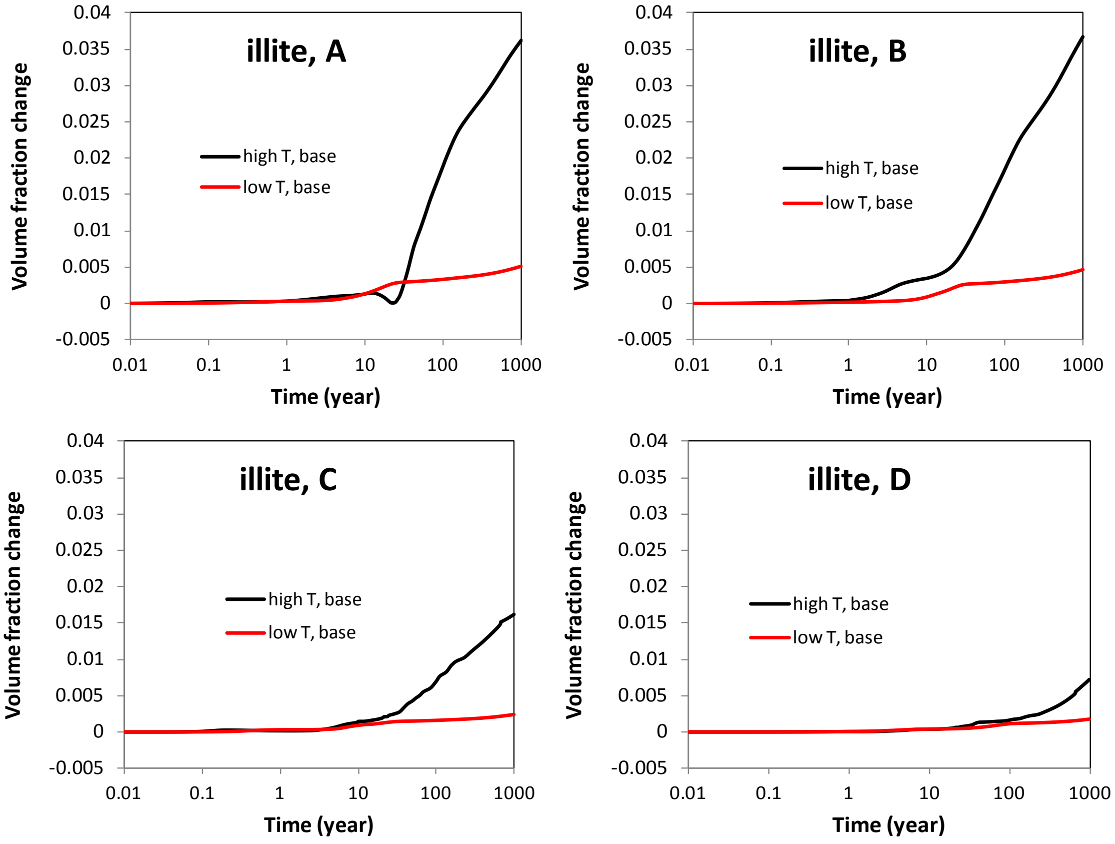

Figure 5.6. The temporal evolution of illite volume fraction at points A, B, C, and D. Volume fraction change shown in the Y-axis is equal to the volume fraction of smectite at a given time minus the initial volume fraction (see Table 5.1), so positive value means precipitation.

5.2.2.1.2 Stress Evolution

In this section, we estimate how the chemical changes observed above may affect the mechanical behavior of the EBS bentonite related to the evolution of swelling and total stress. We limit our analysis to the effects of ion concentration and illitization on swelling, and do not include other potential effects of chemical changes on mechanics, such as changes in mechanical properties due to cementation.

Figures 5.7 and 5.8 show the stress changes at points A and B for both “low T” and “high T” cases. Several processes combine to drive the stress in bentonite up to around 5.1 MPa for the “low T” and 11.5 MPa for the “high T” case after 1,000 years, including the increase in pore pressure due to hydration and thermal pressurization (a processes caused by the difference in thermal expansion of the fluid and solid host rock), bentonite swelling, and thermal expansion. In comparison with the “low T” case, clearly the stronger thermal pressurization in the “high T” case leads to much higher stress in the bentonite. For both the “high T” and “low T” case, the total stress within the buffer has the major contribution from pore pressure, with minor contributions from swelling and thermal stress.

The constitutive relationship described by Equation (5.1) provides an opportunity to evaluate the effect of chemical changes on swelling stress. The mechanical results presented in this section are based on the chemical results in the previous section. In order to isolate the contributions of ion concentration changes versus smectite changes to swelling stress changes, we present three sets of calculated swelling stress. In the first set, denoted in Figures 5.9 and 5.10 as “S=f(Sl,C,Sc)”, the swelling stress is calculated according to Equation (5.1) as a function of liquid saturation changes (Sl), ion concentration (C) changes, and smectite (Sc) changes. In the second set, denoted as “S=f(Sl,C)”, the contribution from smectite changes in Equation (5.1) is disregarded, and the swelling stress is only a function of liquid saturation and ion concentration. In the third set, denoted as “S=f(Sl)”, all chemical effects are neglected, and the swelling stress is only a function of liquid saturation changes.

At early time (< 20 years), the fact that results for “S=f(Sl,C,Sc)” and “S=f(Sl,C)” cases are indistinguishable (Figures 5.9 and 5.10) indicates that smectite changes have not yet contributed to the stress change, because the volume fraction of smectite shows significant changes only after about 20 years (see Figure 5.5). Ion concentration changes start to affect stress at early times (< 20 years) and maintain such effect afterwards. Initially, bentonite near the canister undergoes desaturation and therefore negative swelling stress (see Figure 5.9 for changes at point A). At point A, for the “low T” case, at the end of the 1,000-year simulation period, the ion concentration increase leads to a drop in swelling stress of about 0.14 MPa, and the dissolution of smectite reduces the swelling stress a little further, by about 0.003 MPa. For the “high T” case, after 1000 years, ion concentration changes cause about a 0.1 MPa decrease in swelling stress, and the loss of smectite due to dissolution results in about a 0.05 MPa reduction in swelling stress at the end of the 1000-year simulation (see Figure 5.9). In general, the chemical changes in bentonite have a fairly moderate effect on swelling stress, about 14% swelling stress reduction due to chemical change for the “low T” case and 15% swelling stress reduction for the “high T” case at point A (Figure 5.9). The stress changes near the EBS-NS (point B) interface behave similarly to those near the canister, except the stress starts to increase earlier; the stress after 1000 years is similar as well. The chemical changes in bentonite lead to about 15% swelling stress reduction for the “low T” case and 18% swelling stress reduction for the “high T” case (see Figure 5.10). In terms of the total stress, the decrease in swelling stress accounts for about a 1.4–1.7% reduction in the total stress.

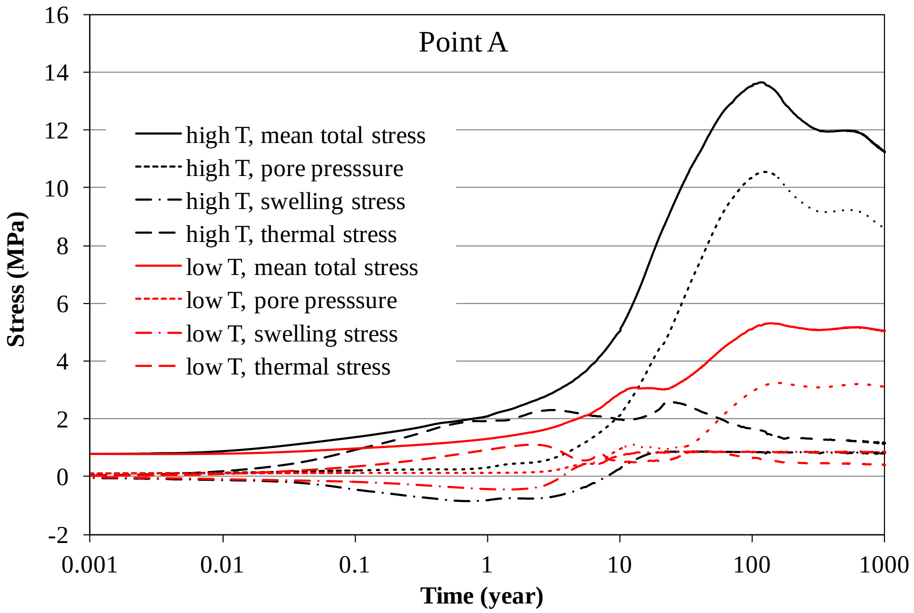

Figure 5.7. Simulation results of mean total stress, pore pressure, and thermal stress at point A for the “low T” and “high T” scenario, respectively.

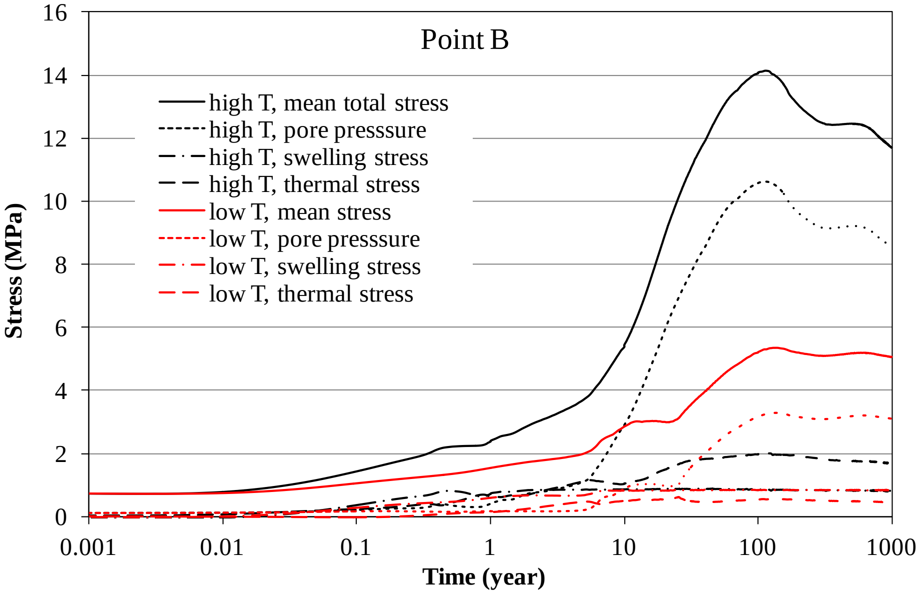

Figure 5.8. Simulation results of mean total stress, pore pressure, and thermal stress at point B for the "low T" and "high T" scenario, respectively.

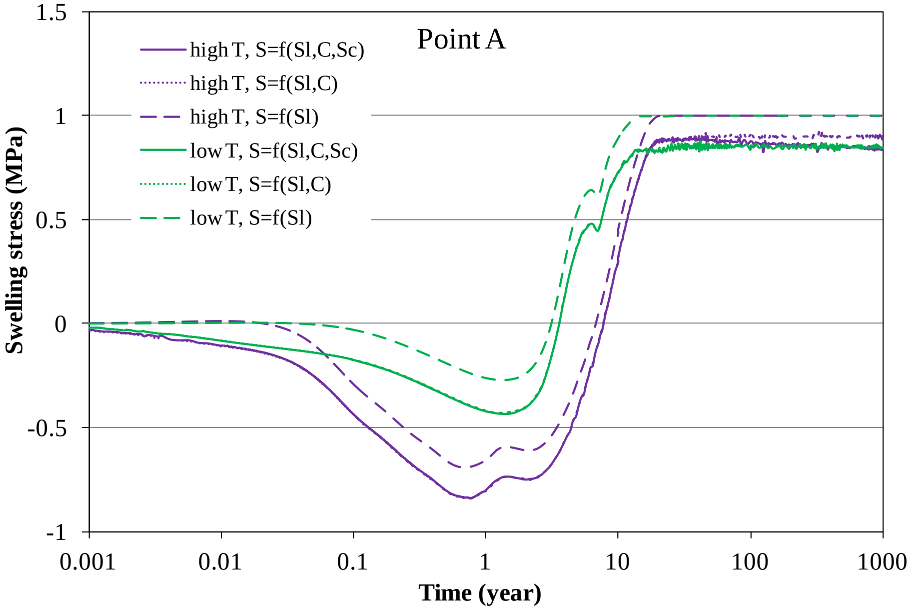

Figure 5.9. Simulation results of swelling stress at point A and B for the "low T" and "high T" scenarios, respectively.

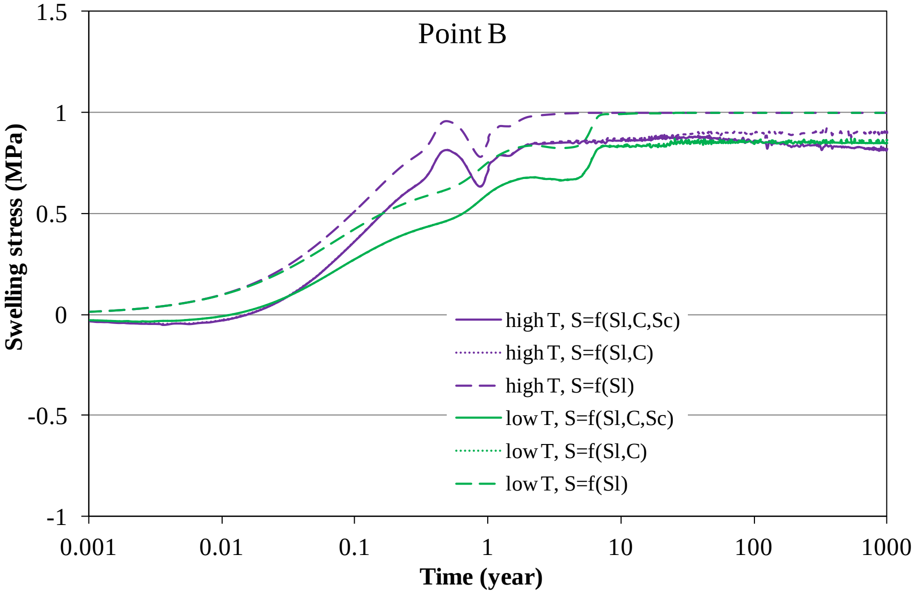

Figure 5.10. Simulation results of swelling stress at point A and B for the “low T” and “high T” scenarios, respectively.

5.2.2.1.3 The Effect of Mechanical Parameters

As shown by Equation (5.1), the reduction of swelling stress by the dissolution of smectite is dependent on the values of A_{sc}, an empirical constant that relates the swelling stress with the abundance of smectite. The value of A_{sc} is derived from measured swelling pressure for bentonite materials with different smectite mass fractions, as shown in Figure 5.11. However, probably because these bentonite materials differ not only in the mass fraction of smectite, but also in other properties, these data points are fairly scattered, which makes it hard to establish one linear correlation between swelling-pressure change and mass fraction change in smectite. We therefore chose a line cross the measured swelling pressure for Kunigel VI bentonite and use the slope of this line as the value of A_{sc} which is 2.5×10^6 Pa^{-1} for the base case. A sensitivity run with a A_{sc} of 9.3×10^6 Pa^{-1} was also conducted to illustrate how the different behavior of other bentonites may affect the calculated swelling pressure, although an A_{sc} of 9.3×10^6 Pa^{-1} is less likely for Kunigel VI bentonite.

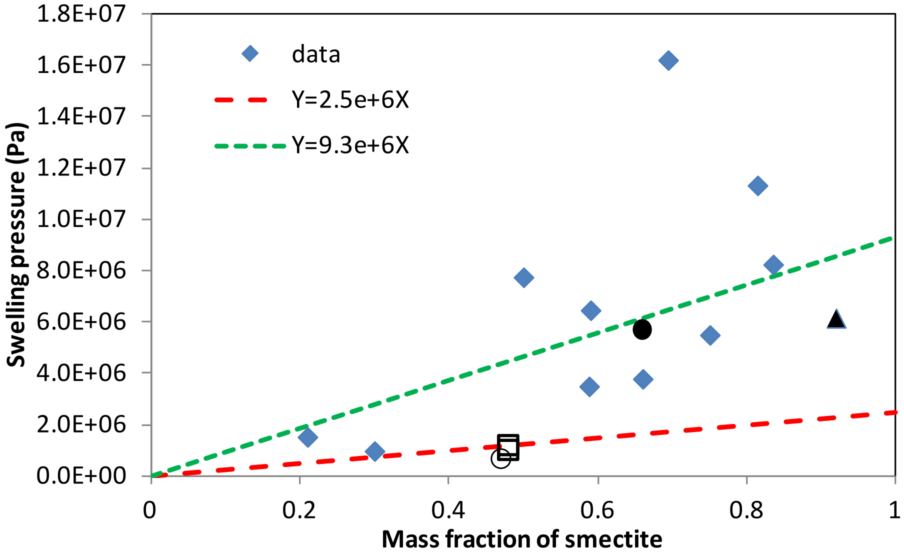

Figure 5.11. Swelling pressure versus mass fraction of smectite for various bentonites. ▲, FEBEX bentonite (ENRESA, 2000); ●, Montigel bentonite (Bucher and Muller-Vonmoos, 1989); □, Kunigel VI bentonite (JNC, 1999); ○, Kunigel bentonite (Konime and Ogata, 1996), ♦ are data for reference material from Czech, Danish, Friedland, Milos Deponit CA-N, Kutch (Indian) and Wyoming MX-80 (Karnland et al., 2006).

In the "high T" base case in which A_{sc} is 2.5×10^6 Pa^{-1}, the calculated swelling pressure after 1000 years is around 1 MPa without considering any chemical effects. Ion concentration changes cause about a 0.1 MPa decrease in swelling stress, and the loss of smectite results in about an additional 0.05 MPa reduction of swelling stress. In contrast, an additional reduction in swelling pressure of about 0.21 MPa at point A (Figure 5.12) is observed in sensitivity runs with A_{sc} of 9.3×10^6 Pa^{-1}. At point B, the swelling stress reduction caused by the dissolution of smectite in the sensitivity run is 0.31 MPa (Figure 5.13), which is higher than the 0.05 MPa in the base case. In total, chemical changes lead to about a 15–18% reduction in swelling stress (see Figures 5.10 and 5.11) in the base case, whereas chemical changes cause about a 32–40% decrease in swelling stress (see Figures 5.12 and 5.13). For the "low T" cases, because the dissolution of smectite is fairly moderate, the increase in A_{sc} has a less pronounced effect than that for "high T" cases.

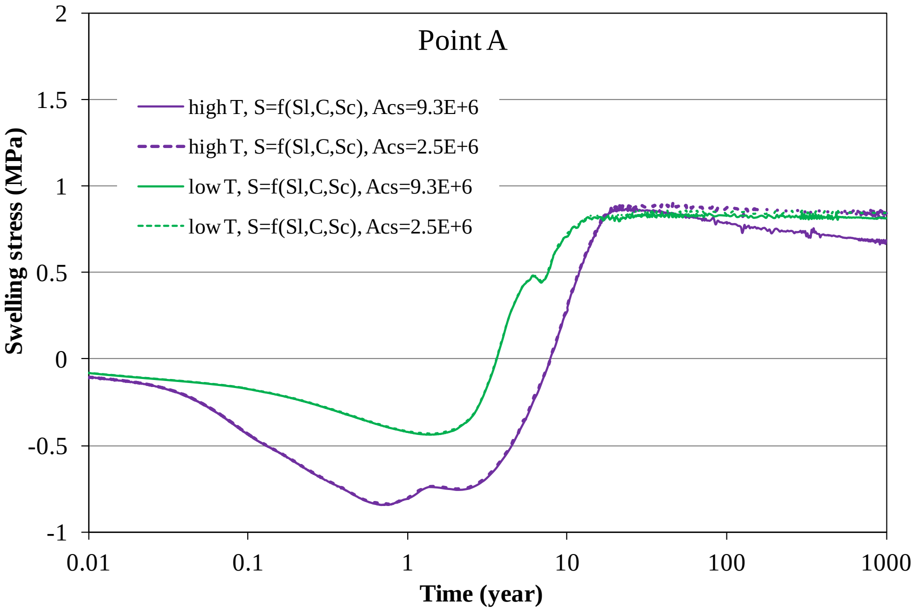

Figure 5.12. Simulation results of swelling stress at point A for the base case (A_{sc} is 2.5×10^6 Pa^{-1}) and sensitivity cases with A_{sc} values of 9.3×10^6 Pa^{-1}.

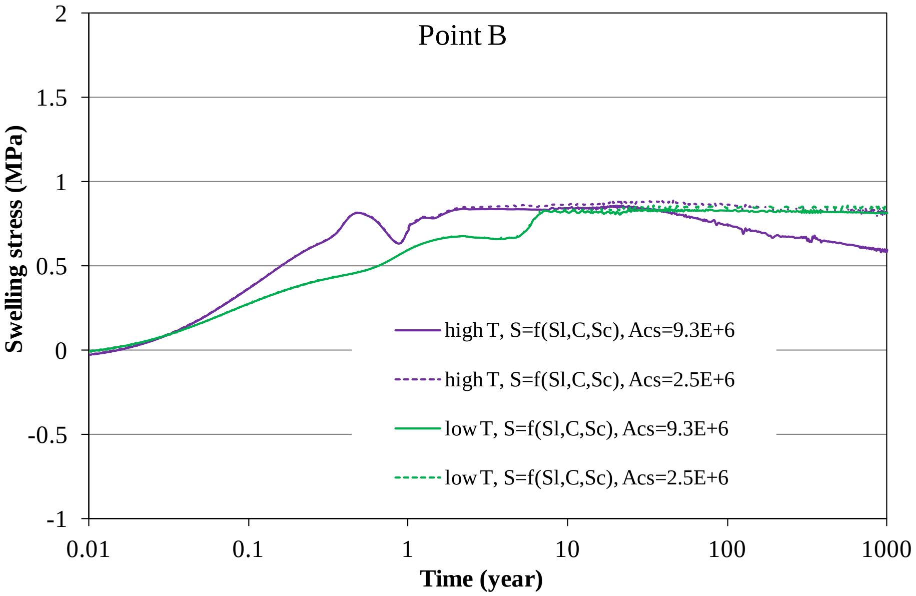

Figure 5.13. Simulation results of swelling stress at point B for the base case (A_{sc} is 2.5×10^6 Pa^{-1}) and sensitivity cases with A_{sc} values of 9.3×10^6 Pa^{-1}.

The more smectite dissolves, the larger the impact of A_{sc} values on the calculated swelling stress. Liu et al. (2013b) showed that among the many factors that affect the dissolution of smectite, the dissolution of K-feldspar plays a key role, and a maximum dissolution of smectite was observed if the dissolution of K-feldspar increased by two orders of magnitude. In Figures 5.15 and 5.16, we compare model results with A_{sc} values of 2.5×10^6 Pa^{-1} to that with A_{sc} values of 9.3×10^6 Pa^{-1}, for the case in which dissolution of K-feldspar increased by two orders of magnitude, the case "r(feldspar)*100". A further decrease in swelling stress of 0.26 MPa at point A and 0.44 MPa at point B is observed if A_{sc} values of 9.3×10^6 Pa^{-1} are used in the model.

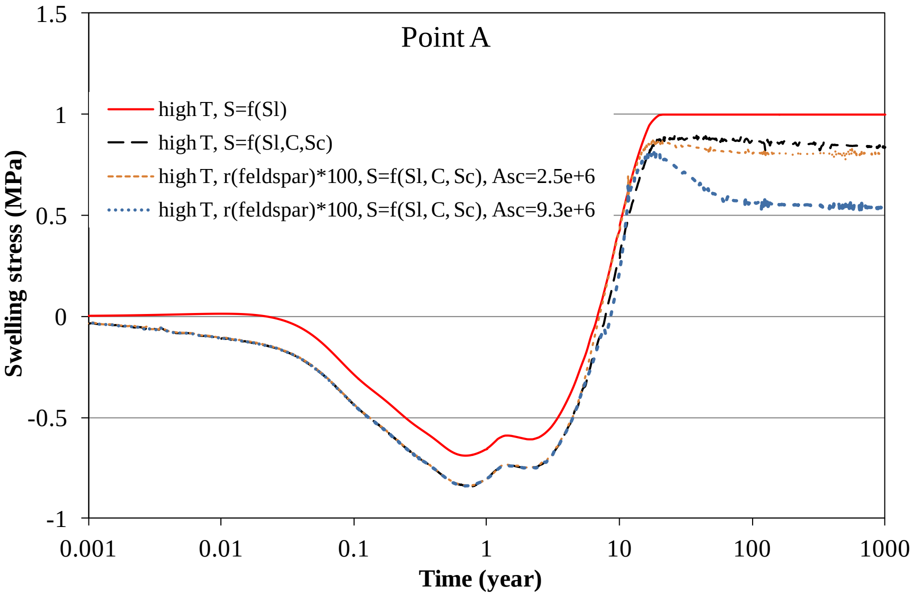

Figure 5.14. Simulation results of swelling stress at point A for the base case and two sensitivity cases for "r(feldspar)*100" with different A_{sc} values.

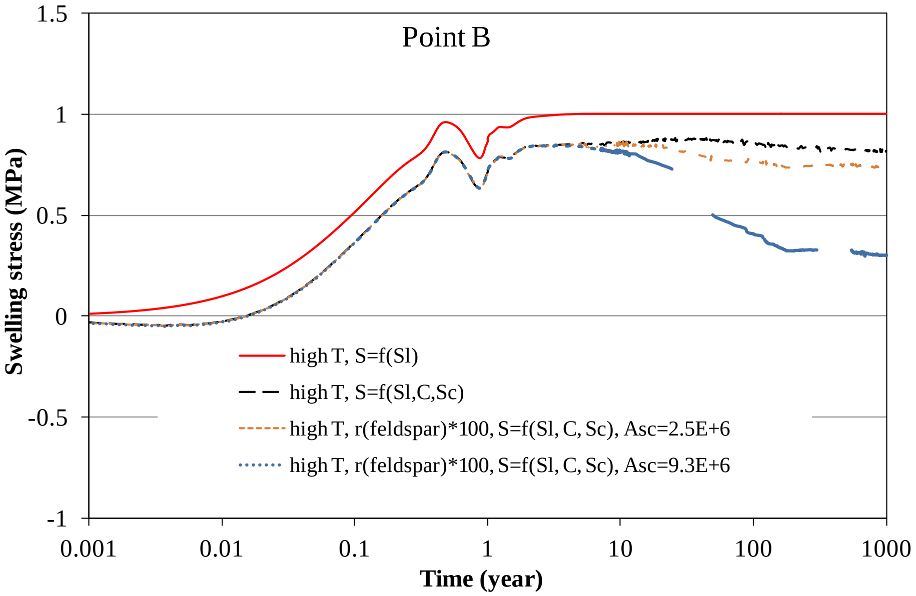

Figure 5.15. Simulation results of swelling stress at point B for the base case and two sensitivity cases for "r(feldspar)*100" with different A_{sc} values.

Our mechanical model for the clay formation is equivalent to that of Rutqvist et al. (2013c), and therefore the stress response in the clay formation is the same. Except for swelling, the mechanical model for the clay formation is not tied to chemical variables, which prevents further analysis of the effects of chemical changes on mechanical behavior in clay formations. In the future, a constitutive relation that incorporates the chemical component within the mechanical model for the clay formation will be implemented. Based on this development, we will be able to analyze the effects of chemical changes on mechanical behavior in a clay formation.

5.2.2.2 Cases for FEBEX Bentonite

A variety of type of bentonite has been studied as the EBS material throughout the world. Kunigel-VI bentonite (Ochs et al., 2004) is one of those that have low smectite content and relative low swelling capacity, whereas FEBEX bentonite (ENRESA, 2000) represents a type of bentonite that has high fraction of smectite and high swelling capacity. MX-80 bentonite (Herbert et al., 2008) is somewhere in between in term of the smectite content and swelling capacity. In the base case, the EBS bentonite is assumed to be Kunigel-VI bentonite (Ochs et al., 2004). In this section, we present model results using FEBEX bentonite as the EBS. Kunigel-VI bentonite differs from the FEBEX bentonite in the following aspects:

1. In terms of aqueous chemistry, FEBEX bentonite has higher ion concentration in pore water than Kunigel-VI bentonite, as shown in Table 5.2 in Section 5.2.1.4. The concentration of major cations, i.e., Ca, Mg, Na, K for FEBEX bentonite is about 2 orders of magnitude higher than that for Kunigel-VI bentonite, which could affect the illitization over the course of heating and hydration.
2. In terms of mineralogical composition, the most pronounced and relevant difference between FEBEX and Kunigel-VI bentonite is the content of smectite, with FEBEX bentonite containing about 60 vol% smectite and Kunigel-VI bentonite having only about 31 vol% smectite (see Table 5.1 in Section 5.2.1.4). FEBEX bentonite has also less K-feldspar, which could affect illitization. The published mineralogical compositions vary slightly, as shown in Table 5.4, and here we take

the average. Note that Table 5.1 lists the volume fraction, whereas Table 5.4 lists the mass fraction; the numbers are therefore different.

3. FEBEX bentonite also has higher swelling pressure, ranging from 4.5 MPa (Castellanos et al., 2008) to 7 MPa (ENRESA 2000), than Kunigel-VI bentonite, which has swelling pressure of around 1 MPa (Börgesson et al., 2001; Konime and Ogata 1996) measured using distilled water. Therefore, the β_{SW} in Equation (5.1) for FEBEX bentonite is 0.238 (Rutqvist et al., 2011), which is higher than that used for Kunigel-VI bentonite (0.048).

4. Another difference between FEBEX and Kunigel-VI bentonite is the parameter A_{sc} that relates swelling stress to the abundance of smectite. For FEBEX bentonite, as shown in Figure 5.16, a linear regression curve is taken across the FEBEX bentonite, which give us a slope (A_{sc}) of 6.5E+6 Pa^{-1} that is higher than the 2.5E+6 Pa^{-1} used for Kunigel-VI bentonite.

Table 5.4. Mass fraction of minerals (%) for FEBEX bentonite from different publications.

Mineral	ENRESA (2000), Fernández et al. (2004)	Ramírez et al. (2002)
Calcite	trace	1 ± 0.7
Dolomite	0.0	0
Illite	0.0	0
Kaolinite	0.0	0
Smectite	92 ± 3	93 ± 3
Chlorite	0.8	-
Quartz	2 ± 1	2 ± 0.5
K-Feldspar	trace	2 ± 1
Siderite	0.0	0
Ankerite	0.0	0

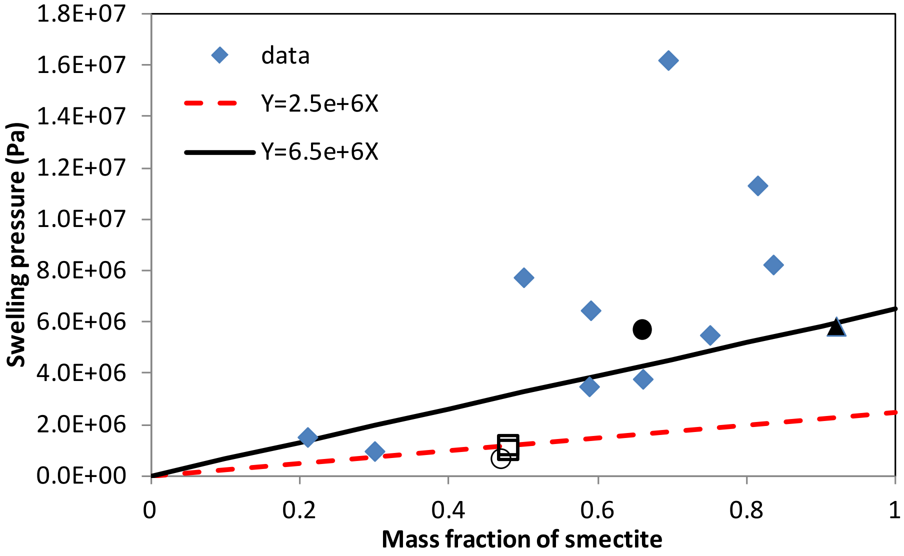

Figure 5.16. Swelling pressure versus mass fraction of smectite for various bentonites. ▲, FEBEX bentonite (ENRESA, 2000); ●, Montigel bentonite (Bucher and Muller-Vonmoos, 1989); □, Kunigel VI bentonite (JNC, 1999); ○, Kunigel bentonite (Konime and Ogata, 1996), ♦ are data for reference material from Czech, Danish, Friedland, Milos Deponit CA-N, Kutch (Indian) and Wyoming MX-80 (Karnland et al., 2006).

5.2.2.2.1 Chemical Evolution

As mentioned above, the thermal conductivity and permeability remain the same for the sensitivity run using FEBEX bentonite as the EBS. The temperature, water saturation, and pore pressure for the sensitivity run are therefore the same, as shown in Figures 5.2-5.4. Changes in smectite and illite volume fractions are shown in Figures 5.17 and 5.18. Model results from the sensitivity case confirm the occurrence of illitization (dissolution of smectite and precipitation of illite), and illitization is enhanced at higher temperature for FEBEX bentonite, just as what were observed for the base case for Kunigel bentonite. However, in comparison with the model results for the base case with Kunigel bentonite, several distinct features have been observed for the FEBEX bentonite. First, for the “high T” scenario, there is less smectite dissolution in the FEBEX bentonite. Smectite volume fraction decreases about 0.01 at point A and 0.018 at point B, about 1.6% and 3% of the initial smectite volume fraction, respectively, significantly lower than the decrease of 0.035 (11% of the initial amount) in Kunigel bentonite. Second, the enhancement of illitization (expressed as smectite dissolution and illite dissolution) is less pronounced for FEBEX, because while the amount of smectite dissolving for the “low T” scenario is similar for both FEBEX and Kunigel bentonite, the amount of smectite dissolving for the “high T” scenario is much less for FEBEX bentonite. The differences in dissolved smectite between “high T” and “low T” scenarios for FEBEX bentonite are smaller than that for Kunigel bentonite. Third, although different types of EBS bentonite have almost no impact on the chemical changes in the clay rock away from the EBS-NS interface (illustrated by the results at point D, Figures 5.17 and 5.18), such differences have a moderate impact on the clay rock near the interface. As shown by the results at point C in Figures 5.17 and 5.18, within the FEBEX bentonite, smectite dissolution occurs earlier. The reason for this earlier dissolution is that FEBEX bentonite has a higher K concentration (see Table 5.4), so that diffusion of K from clay rock to bentonite occurs at a lower rate, and subsequently more K is available within the clay rock for illitization.

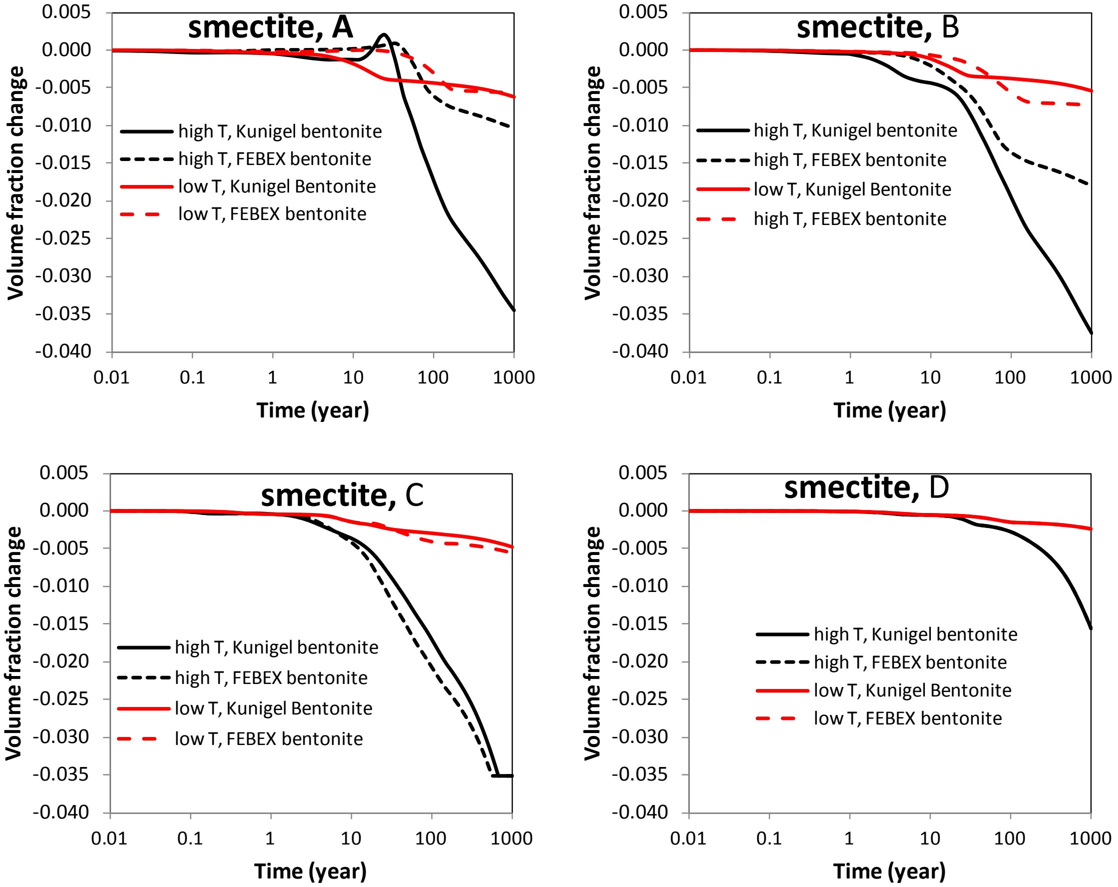

Figure 5.17. The temporal evolution of smectite volume fraction at points A, B, C, and D in the base case with Kunigel bentonite and a sensitivity case with FEBEX bentonite.

The sensitivity of illitization in EBS bentonite to key chemical parameters was investigated in Liu et al. (2013b), which confirmed the importance of available K as widely observed in geological formations (e.g., Cuadros 2006), but demonstrated that the source K is actually the dissolution of K-feldspar. When FEBEX bentonite is used as the EBS material, K-feldspar dissolves much less compared with the base case, which uses Kunigel bentonite, as illustrated in Figure 5.19. This is the reason why in Figure 5.17, smectite dissolves less in FEBEX bentonite than in Kunigel bentonite. Less dissolution of K-feldspar in FEBEX bentonite can be attributed to two factors: a lower volume of K-feldspar and a higher K concentration in pore water for FEBEX bentonite.

One of the byproducts of illitization is the precipitation of quartz, as shown in Equation 5.3. The cementation by quartz (or amorphous SiO_2 minerals) might lower the swelling of bentonite and increase the brittleness of the bentonite. In comparison with the base case using Kunigel bentonite, less quartz precipitates for the sensitivity case with FEBEX bentonite. For the "high T" scenario, the amount of quartz formed for FEBEX bentonite is only about 1/10 of that for kunigel bentonite.

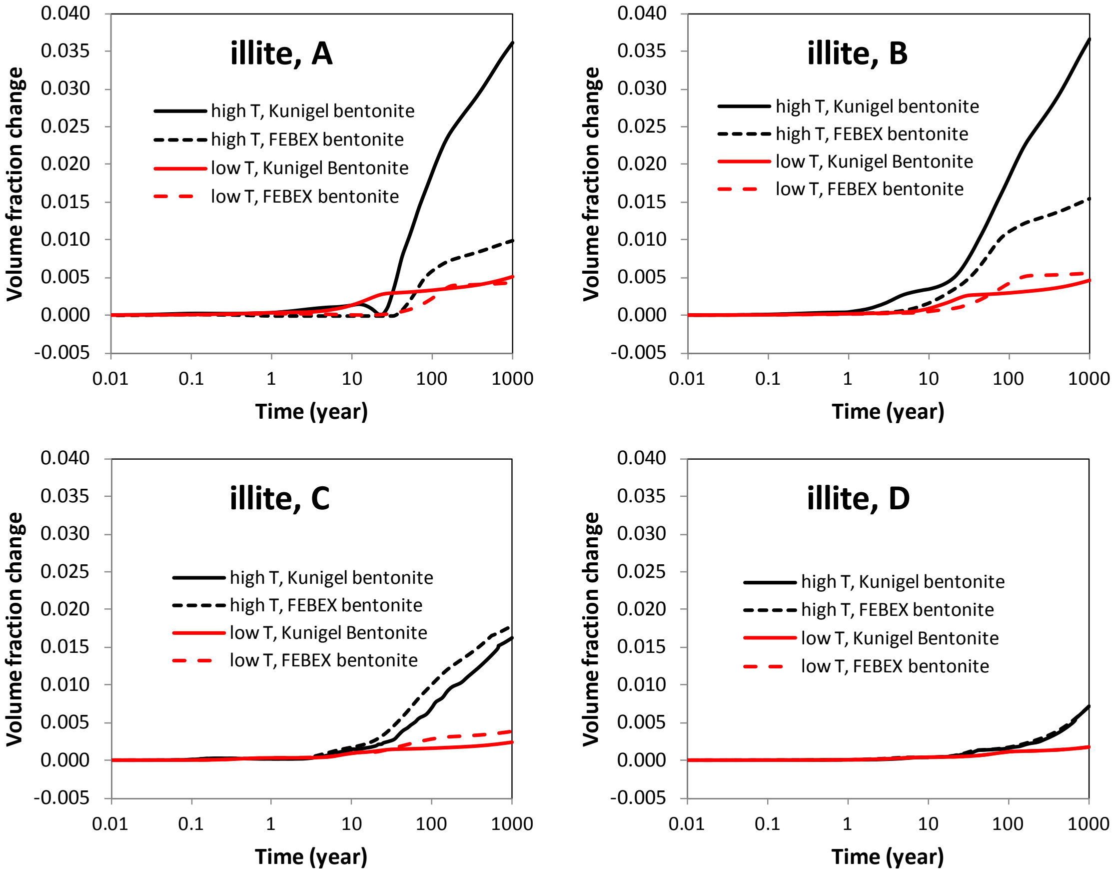

Figure 5.18. The temporal evolution of illite volume fraction at points A, B, C, and D in the base case with Kunigel bentonite and a sensitivity case with FEBEX bentonite.

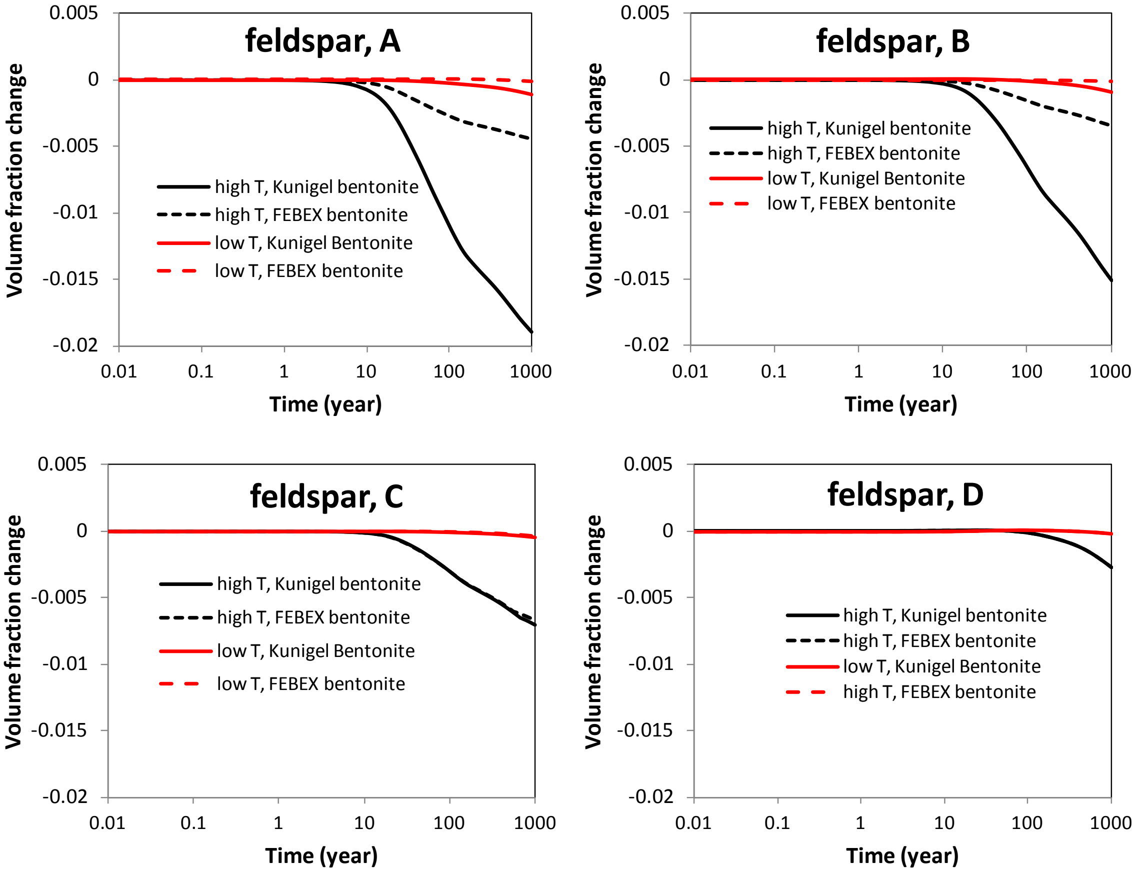

Figure 5.19. The temporal evolution of K-feldspar volume fraction at points A, B, C, and D in the base case with Kunigel bentonite and a sensitivity case with FEBEX bentonite.

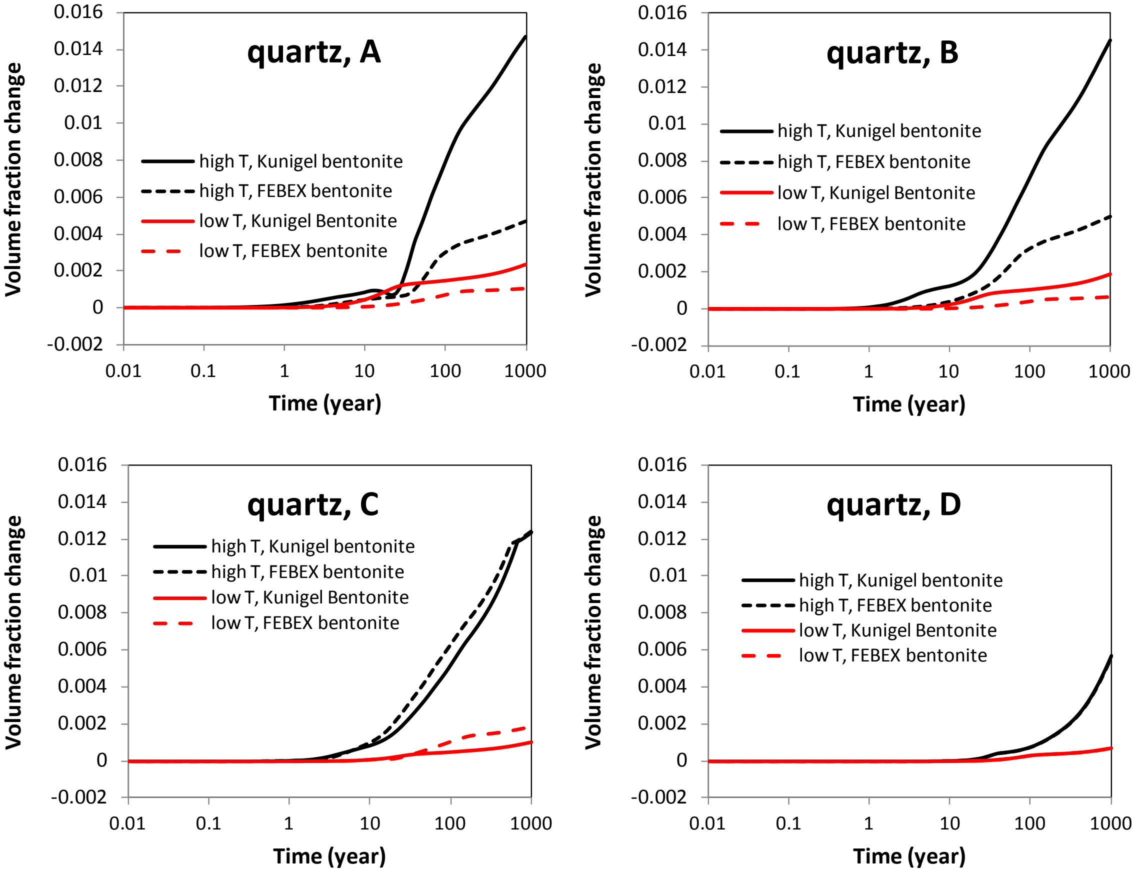

Figure 5.20. The temporal evolution of quartz volume fraction at points A, B, C, and D in the base case with Kunigel bentonite and a sensitivity case with FEBEX bentonite.

5.2.2.2.2 Stress Evolution

As discussed in Section 1.3.1, the increase in pore pressure due to hydration and thermal pressurization (processes caused by the difference in thermal expansion of the fluid and solid host rock), bentonite swelling, and thermal expansion are the main driving force for the increase in total stress in bentonite. In comparison with the “low T” case, clearly the stronger thermal pressurization in the “high T” case leads to much higher stress in the bentonite. For both the “high T” and “low T” case, the total stress within the buffer has the major contribution from pore pressure, with minor contributions from swelling and thermal stress.

Figures 5.21 and 5.22 compares the total stress calculated for the Kunigel (the base case) and FEBEX bentonite (the sensitivity case). Because FEBEX bentonite has higher swelling pressure, the total stress for FEBEX bentonite at point A and B are 3–4 MPa higher than that for Kunigel bentonite after 1000 years.

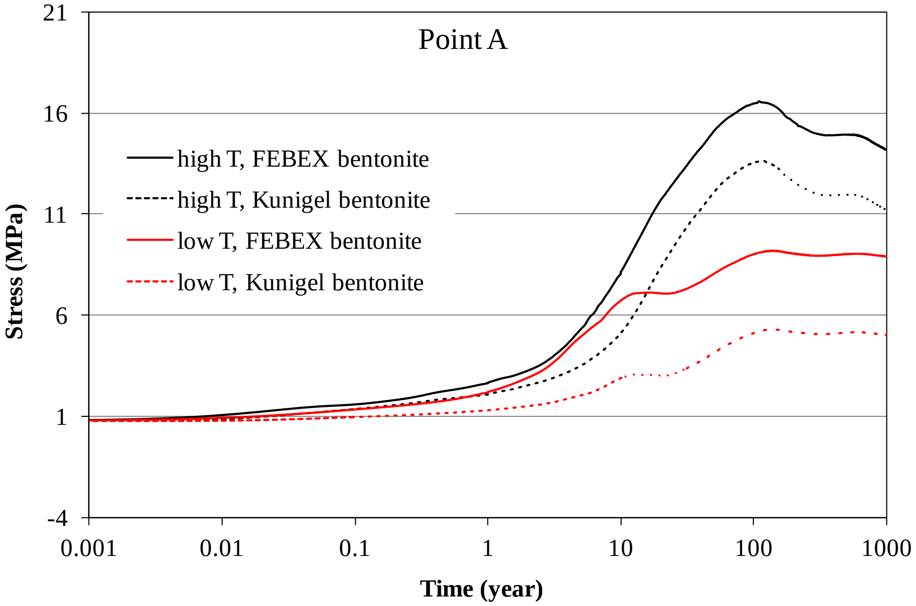

Figure 5.21. Simulation results for mean total stress at point A in the base case with Kunigel bentonite and the sensitivity case with FEBEX bentonite for the "low T" and "high T" scenarios, respectively.

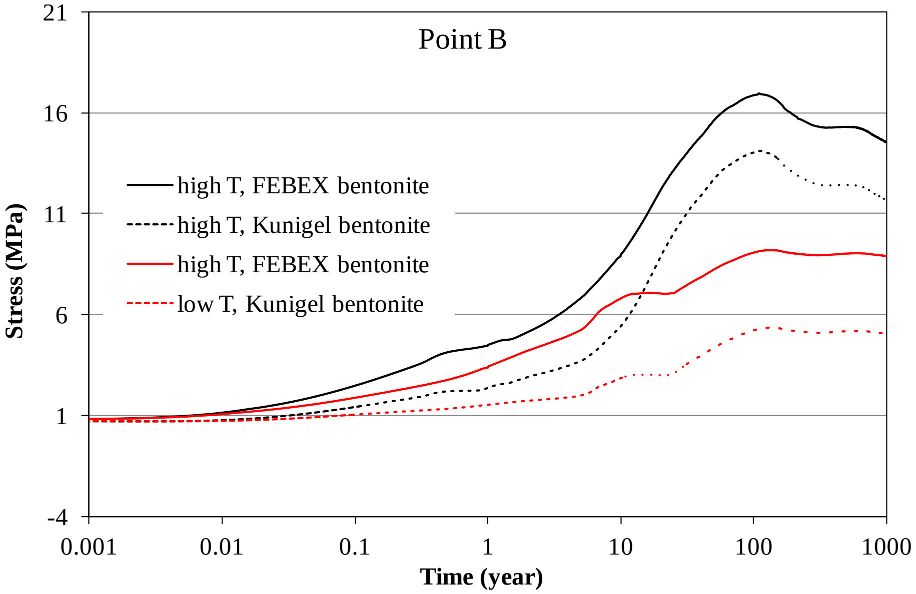

Figure 5.22. Simulation results of mean total stress at point B in the base case with Kunigel bentonite and the sensitivity case with FEBEX bentonite for the "low T" and "high T" scenarios, respectively.

The constitutive relationship described by Equation (5.1) shows that the swelling stress changes receive contributions from moisture, ion concentration, and smectite changes. Just as what has been done for the base case, we also present three sets of calculated swelling stresses for FEBEX bentonite to delineate the contribution from each process.

In the first set, denoted in Figures 5.23 to 5.26 as “S=f(Sl,C,Sc)”, the swelling stress is calculated according to Equation (5.1) as a function of liquid saturation changes (Sl), ion concentration (C) changes, and smectite (Sc) changes. In the second set, denoted as “S=f(Sl,C)”, the contribution from smectite changes in Equation (5.1) is disregarded, and the swelling stress is exclusively a function of liquid saturation and ion concentration. In the third set, denoted as “S=f(Sl)”, all chemical effects are neglected, and the swelling stress is exclusively a function of liquid saturation changes. At point A near the canister, bentonite undergoes evaporation and liquid saturation decrease, which results in a decrease in swelling stress (shrinkage) for about 4 years for the “low T” scenario and about 8 years for the “high T” scenario (Figure 5.23). After that, the increase in liquid saturation induces swelling, and swelling stress keeps increasing, reaching the swelling capacity of 5 MPa. Figure 5.24 zooms in to the stress range from 4.5 to 5 MPa to illustrate the contribution from ion concentration and smectite changes.

Compared to the swelling stress for Kunigel bentonite presented in Section 5.2.2.1, the swelling stress for FEBEX bentonite has two distinct features. First, change in ion concentration has a minimal effect on the swelling stress, because the ion concentration of the pore water in FEBEX bentonite is fairly close to that for clay rock. Initially, pore water in clay rock, FEBEX bentonite, and Kunigel bentonite has an ionic strength of 0.38 M, 0.25 M, and 0.004 M, respectively. Clearly the concentration gradient between clay rock and FEBEX bentonite is smaller and therefore diffusion occurs at a lower rate. As a result, the ion concentration in pore water for FEBEX bentonite increases only moderately, which changes the swelling stress noticeably. Note that about 0.1 MPa swelling stress reduction due to ion concentration has been observed for Kunigel bentonite. Second, more stress reduction due to smectite dissolution has been observed for FEBEX bentonite. Despite the fact that less smectite dissolution has been observed for FEBEX bentonite (Figure 5.17), higher A_{sc} (a parameter that relates swelling stress to the abundance of smectite) for FEBEX bentonite leads to a slightly higher reduction in swelling stress.

Table 5.5 lists the stress reduction by ion concentration and smectite dissolution at point A for Kunigel and FEBEX bentonite. In total, chemical changes lead to about a 0.15 MPa stress change for Kunigel bentonite and 0.08 MPa for FEBEX bentonite. Relative to the swelling stress obtained with “S=f(Sl)”, chemical change causes about a 15% reduction in swelling stress for Kunigel bentonite, but only 1.6% for FEBEX bentonite. Model results at point B (Figures 5.27 and 5.28) lead to the same observation in terms of the difference between Kunigel and FEBEX bentonite, although the specific values differ slightly from those at point A.

Table 5.5. The geochemically induced swelling stress for Kunigel and FEBEX bentonite at point A for “high T” scenario. Stress reduction by ion concentration is the difference between the swelling stress obtained with “S=f(Sl)” and “S=f(Sl,C)”, and the stress reduction by smectite dissolution is the difference between the swelling stress obtained with “S=f(Sl,C)” and “S=f(Sl,C,Sc)” (see Figure 5.26), the relative amount (%) use the results from “S=f(Sl)” as the basis.

Kunigel bentonite				FEBEX bentonite			
Stress reduction by ion concentration, MPa	Stress reduction by ion concentration, (%)	Stress reduction by smectite dissolution MPa	Stress reduction by smectite dissolution (%)	Stress reduction by ion concentration, MPa	Stress reduction by ion concentration, (%)	Stress reduction by smectite dissolution, MPa	Stress reduction by smectite dissolution (%)
0.1	10%	0.05	5%	0.006	0.1%	0.076	1.5%

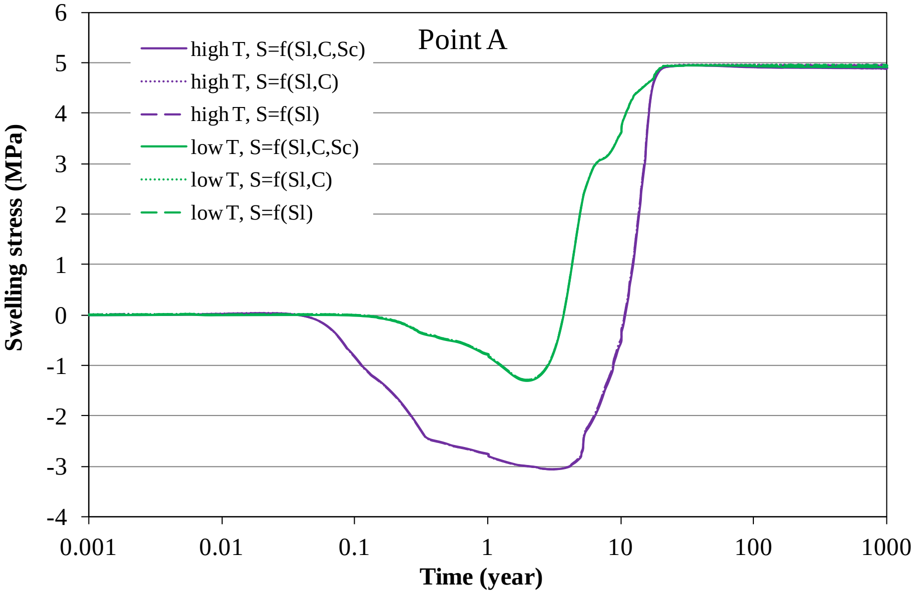

Figure 5.23. Simulation results of swelling stress at point A for the FEBEX bentonite for the “low T” and “high T” scenarios, respectively, focusing on the stress range from 4.5 to 5 MPa.

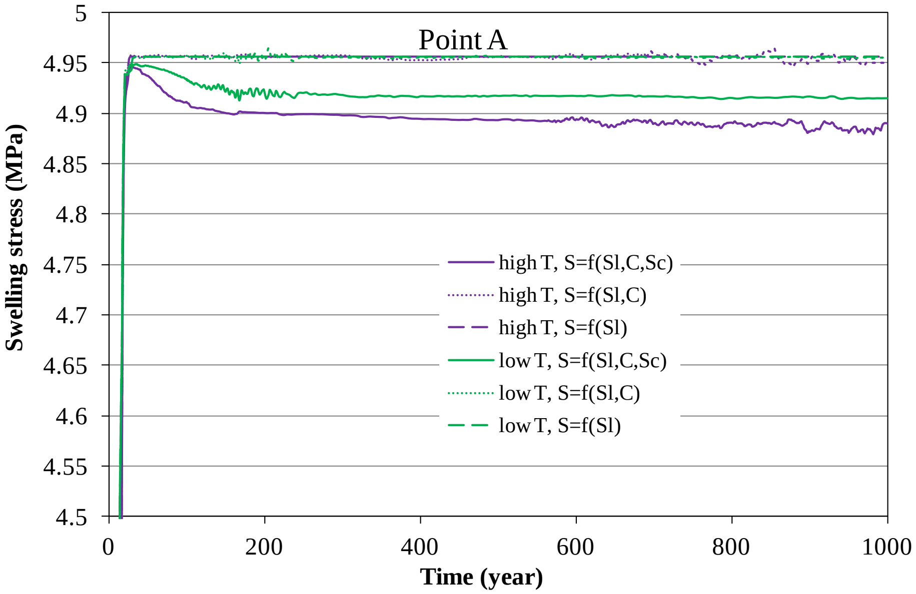

Figure 5.24. Simulation results of swelling stress at point A for the FEBEX bentonite for the “low T” and “high T” scenarios, respectively, focusing on the stress range from 4.5 to 5 MPa.

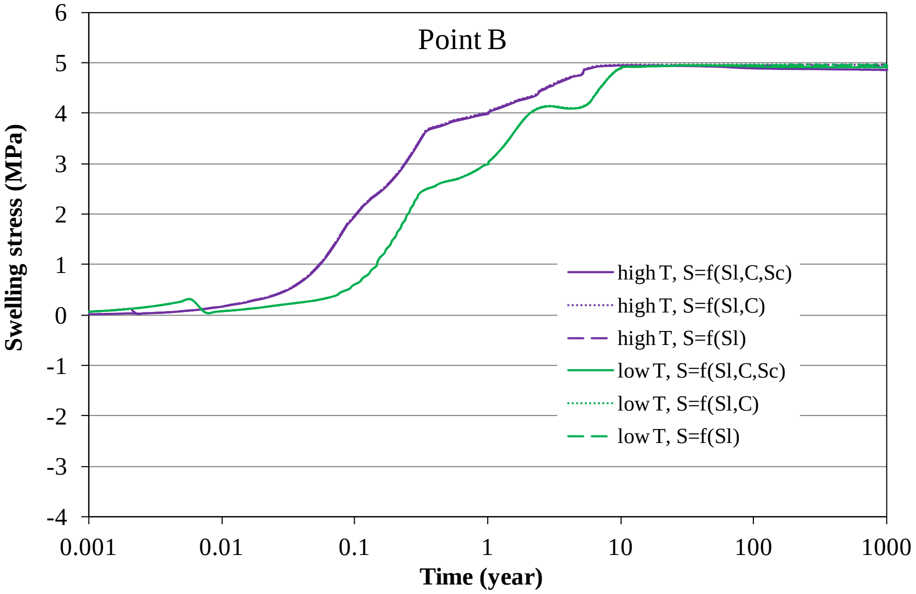

Figure 5.25. Simulation results of swelling stress at point B for the FEBEX bentonite for the "low T" and "high T" scenarios, respectively, focusing on the stress range from 4.5 to 5 MPa.

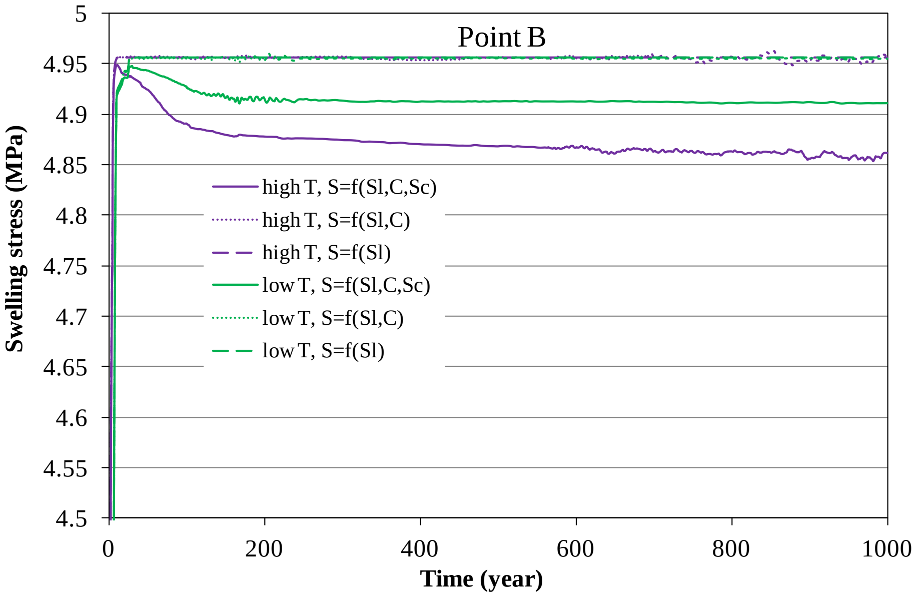

Figure 5.26. Simulation results of swelling stress at point B for the FEBEX bentonite for the "low T" and "high T" scenarios, respectively, focusing on the stress range from 4.5 to 5 MPa.

5.2.2.2.3 Effect of K-Feldspar Dissolution Rate on Illitization and Swelling Stress for FEBEX Bentonite

Sensitivity analyses conducted by Liu et al. (2013b) for the Kunigel bentonite showed that the pore-water concentration of K in the bentonite is critical for the illitization, with the dissolution of K-feldspar being the major source of K needed for illitization. The maximum dissolution of smectite for Kunigel bentonite is achieved in a run that has a K-feldspar dissolution rate two orders of magnitude higher than the base case. Here we conduct the same type of simulation for FEBEX bentonite, i.e. increasing the dissolution rate of K-feldspar by two orders of magnitude, to evaluate the quantity of smectite dissolution and the subsequent swelling stress reduction. As expected, a higher K-feldspar dissolution rate leads to more dissolution of feldspar (Figure 5.27) and eventually depletes the initially presented K-feldspar, so that the volume fraction of K-feldspar does not decrease any more after about 100 years. More smectite dissolves and illite precipitates when the dissolution rate of K-feldspar increases (Figures 5.28 and 5.29). Note that dissolution rate of K-feldspar in current model is taken from Xu et al. (2006) and it is know there is large uncertainty associated with this rate due to various reasons (e.g., Zhu 2005). At point A near the canister, because the dissolution of K-feldspar is the dominant source of K, no further dissolution of smectite is observed as K-feldspar is depleted; the smectite volume fraction decreases about 0.017 (about 3% of the initial amount) and remains at such a value from 100 to 1000 years. At point B near the EBS-NS interface, because the host clay can supply K through diffusion and advection, even local K-feldspar is depleted, dissolution of smectite continues, and at the end of 1000 years, the volume fraction decreases about 0.04 (about 7% of the initial amount).

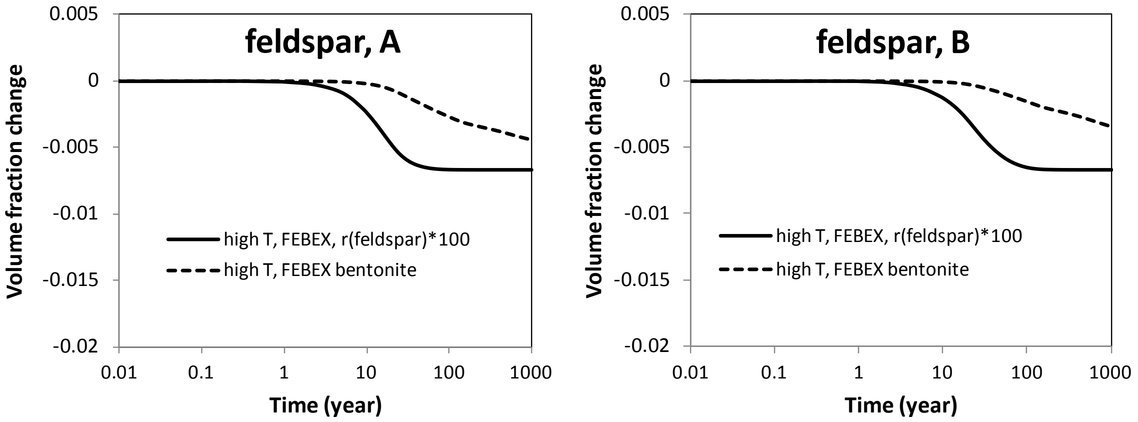

Figure 5.27. The temporal evolution of K-feldspar volume fraction at points A, B for the case with FEBEX bentonite with dissolution rate of K-feldspar being raised by two orders of magnitude.

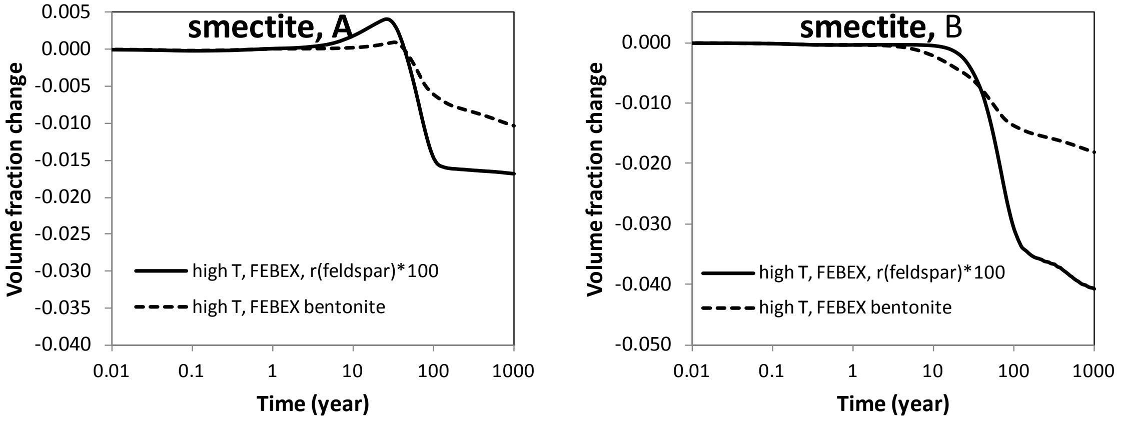

Figure 5.28. The temporal evolution of smectite volume fraction at points A, B for the case with FEBEX bentonite with dissolution rate of K-feldspar being raised by two orders of magnitude.

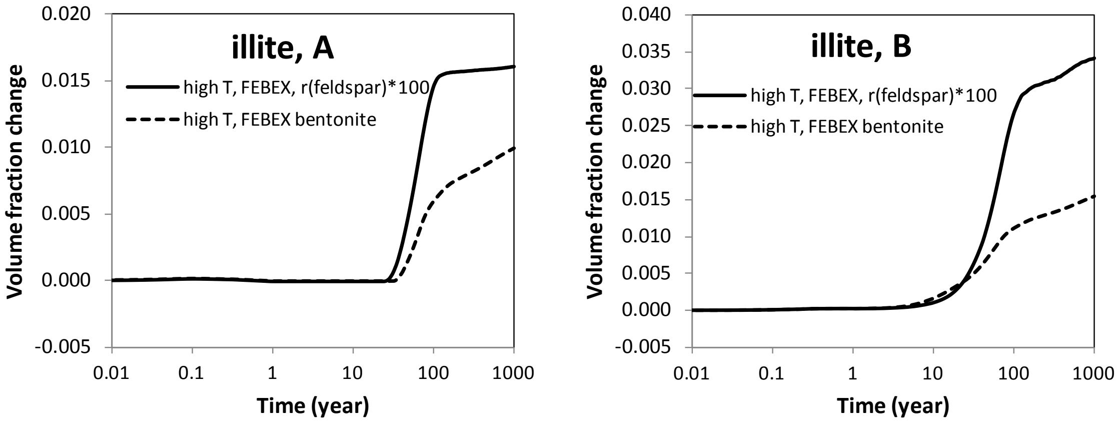

Figure 5.29. The temporal evolution of illite volume fraction at points A, B for the case with FEBEX bentonite with dissolution rate of K-feldspar being raised by two orders of magnitude.

The “high T” scenario with K-feldspar dissolution being increased by two orders of magnitude represents the worst scenario for FEBEX bentonite in terms of the swelling pressure reduction caused by chemical changes. However, even for this worst scenario, the swelling pressure reduction is still fairly moderate. As shown by the green line in Figures 5.30 and 5.31, in comparison with the swelling stress obtained by “s=f(Sl),” that swelling is the function of moisture change alone; when K-feldspar dissolution is increased by two orders of magnitude, the swelling stress decreases about 0.12 MPa, about 2.3%, at point A; and about 0.18 MPa, about 3.6%, at point B.

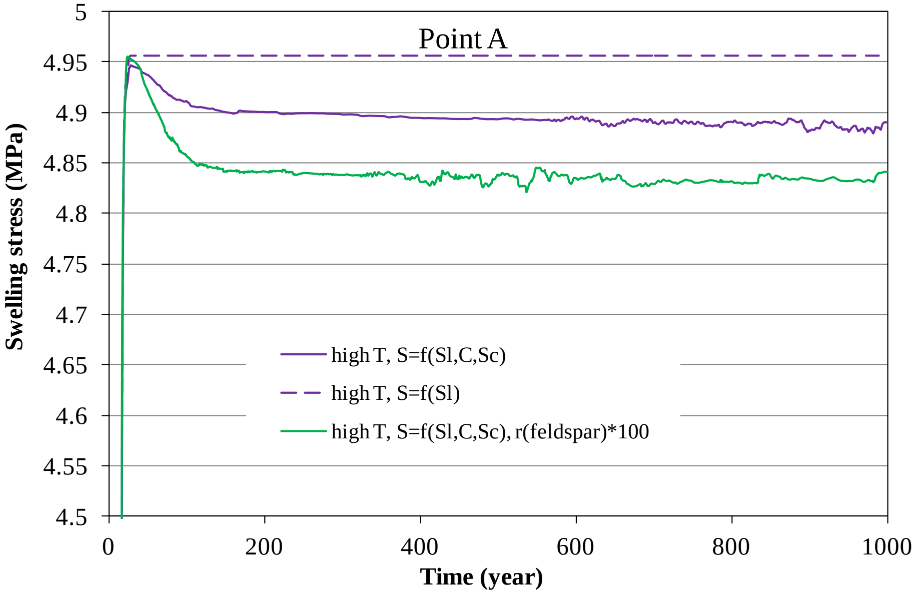

Figure 5.30. Simulation results of swelling stress at point A for the FEBEX bentonite “high T” scenario with K-feldspar dissolution being increased by two orders of magnitude, focusing on the stress range from 4.5 to 5 MPa.

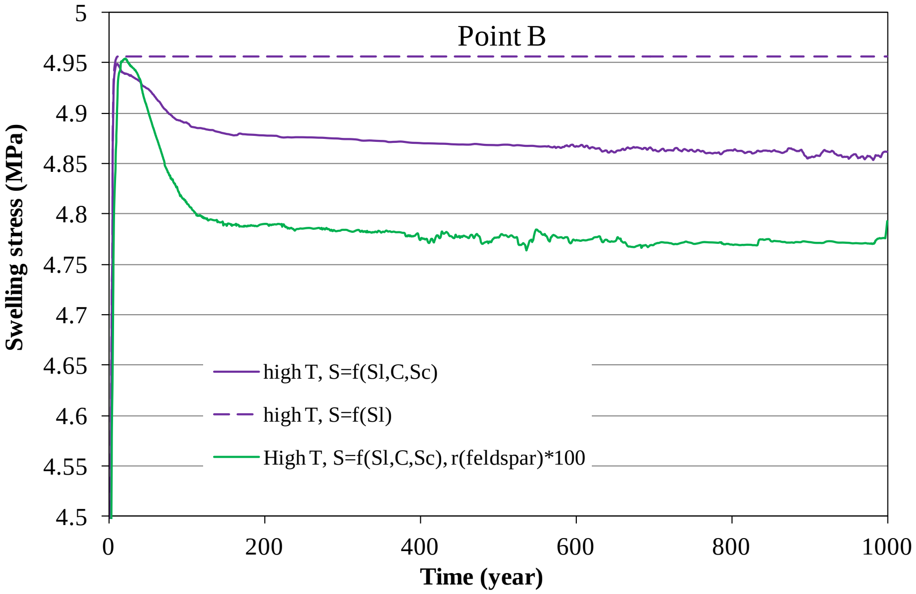

Figure 5.31. Simulation results of swelling stress at point A for the FEBEX bentonite "high T" scenario with K-feldspar dissolution being increased by two orders of magnitude, focusing on the stress range from 4.5 to 5 MPa.

5.3 High Temperature THM Experiments on Bentonite and Opalinus Clay

The primary objective of the laboratory experiments is to investigate the impact of high-T physical and chemical alterations of buffer and backfill materials (bentonite) and clay host rock on their geomechanical and hydrological properties, and on interaction between the EBS and the natural system. Our particular interest is the heat-induced chemical alteration—the illitization of smectite and cementation—within the buffer and backfill materials (bentonite) of the EBS.

Miniature core samples for the experiment were prepared from natural, untreated bentonite chips obtained from LANL and Opalinus Clay cores from Mont Terri URL through NAGRA. The bentonite containing either distilled water or aqueous KCl solution were made, which was introduced during compaction of ground bentonite powder. Both bentonite and Opalinus Clay cores were heated in sealed titanium containers over extended durations (1–3 months).

The heat-treated samples were tested for their triaxial compression strength and ultrasonic velocities. Also, a miniature indentation test setup was built to examine changes in the hardness and elastic moduli of the clay. However, the samples suffered progressive decreases in water content during heating, which indicated very slow leakage of water vapor from the pressure vessels. For this reason, the measured changes in the clay properties were strongly affected by desiccation-induced bulk volume decreases and increases in the strength. The details of the experimental results are described below.

5.3.1 Sample preparation

The Opalinus Clay cores previously obtained from Mon Terri were subcored to produce small, cylindrical core samples (Figure 5.32). Because of the strong bedding anisotropy of the clay and preexisting microcracks and inclusions, slender, well-shaped cores were difficult to obtain, and only cores drilled along the bedding planes and microcracks were recovered successfully. The drilling was conducted using a custom-made core barrel (barrel inner diameter=0.56") which was designed to reduce seizing of the drill's cutting edge by the produced debris. No water or cryogen was used during the drilling, because we needed to avoid introduction of additional water into the clay (cryogen induces condensation of water from the air). This, however, resulted in heating of the rock cores from the drilling, which may have caused additional losses of the pore water from the cores already drying from long-term storage. The density and the water content of the cores used for the experiment were 2.3 g/cm^3 and 2.2 wt%, respectively.

The bentonite samples were obtained from LANL, sharing the same batch of the material (untreated *BARA-KADE*® brand bentonite chips, Bentonite Performance Minerals) with other experiments conducted by the LANL and LBNL teams. The chips were ground and pulverized to grain sizes smaller than 75 μm, which were dried in a convection oven at 60ºC for 24 hours. According to a previously published report (Caporuscio 2013, Table 3), similar bentonite chips contained 72%wt montmollironite, 13%wt clinoptilolite, 9%wt feldspar, and 2%wt biotite. Previously, Pusch (Pusch, R. [1992], Clay Minerals, 27, 353-361) used a similar commercial bentonite compacted at ~100 MPa (~14,490 psi) with 8–14%wt of water content. This resulted in compacted clay samples with a final density of ~2.1 g/cm^3 and water content ~60%. Based upon this knowledge, our samples were designed to have a water content of 15%wt and density 2.1 g/cm^3, compacted at 100 MPa in a sample mold (Figure 5.32). Also, to examine the effect of potassium in the pore water, either distilled water or 0.5 M KCl aqueous solution (reagent grade crystals obtained from BDH) was used as the pore fluid. Three types of cylindrical cores were prepared for the experiment: (1) permeability test cores [D(diameter)=0.56", H(height)=0.25"], compacted within a titanium-2 ring (PRM), (2) seismic and indentation test cores [D=0.56", H=0.25"] (S&I); and (3) geomechanical test cores [D=0.56", H=1.1"](GEO). The actual density of the cores varied from 1.92 g/cm^3 to 2.05 g/cm^3, depending upon the core types (GEO cores were less dense than other core types).

Both compacted bentonite and Mont Terri core samples were introduced in chemically passivated miniature titanium pressure vessels (High Pressure Company, titanium grade 5 miniature reactor C), and were heated at 200ºC over planned durations (Table 5.6). However, initial pressurization of the vessels with nitrogen gas indicated that the metal-to-metal contacts of the vessels did not form tight seals. Therefore, as an alternative, a 1/32"-thick, extreme-high-temperature silicone rubber (McMaster 8632K41, durometer 70A) was used as a gasket. A preliminary test using a wet Kaolin sample (15%wt water content) indicated no loss of fluid from the vessel over 7 days, while heated at 200ºC. Once each pressure vessel reached its "maturity," the vessel was removed from the oven and stored in a separate oven at 100ºC overnight, then stored at room temperature until the tests were conducted.

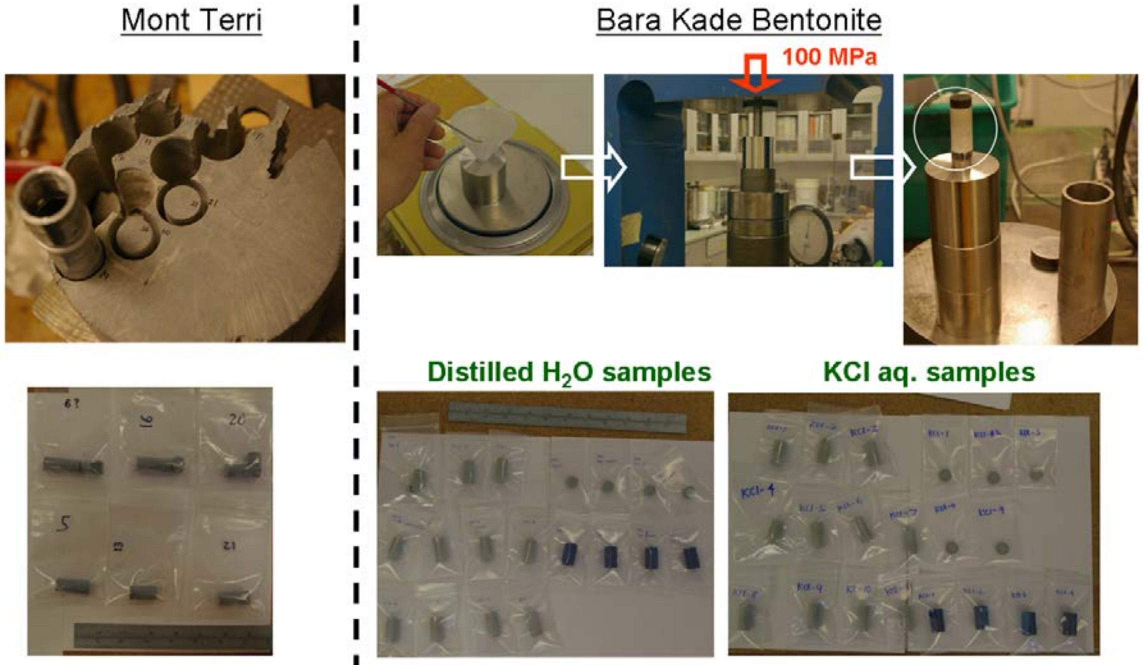

Figure 5.32. Preparation of clay cores used in the experiment. Opalinus Clay cores from Mont Terri (left) and bentonite cores (right).

Table 5.6. Core samples used for the experiments and heating durations.

		0 month	1 month	3 months	6 months (in progress)
Bentonite	Distilled Water	GEO-DW- 1, 3, 6 PRM-DW-1 S&I-DW-1	GEO-DW-2, 4, 5 PRM-DW-2 S&I-DW-2	GEO-DW-7, 8, 9 PRM-DW-3 S&I-DW-3	GEO-DW-10, 11 PRM-DW-4 S&I-DW-4
	0.5 M KCl aq.	GEO-KCL-1, 2, 3 PRM-KCL-1 S&I-KCL-1	GEO-KCL-4, 5, 6 PRM-KCL-2 S&I-KCL-2	GEO-KCL-7, 8, 9 PRM-KCL-3 S&I-KCL-3	GEO-KCL-10, 11 PRM-KCL-4 S&I-KCL-4
Mont Terri		GEO-MT-6, 13, 16 S&I-MT-16		GEO-MT-5, 20, 21 S&I-MT-20	

NOTE: DW and KCL cores indicate compacted bentonite cores. MT indicates Opalinus Clay (from Mont Terri) cores.

When the samples were examined after heating, however, slow, gradual decreases in the sample weight and water content were noticed (Table 5.7). This may be attributed to progressive degradation of the vessel seals, as indicated by accelerated loss of water in 3 months compared to 1 month (Figure 5.33).

Table 5.7. Sample weight, density, and water content changes in geomechanical test cores.

Sample	Heating Duration	Before-Heating weight and density	After-Heating weight	% lost weight
DW-2	1 month	9.23 g (1.92 g/cm^3)	9.16 g (1.91 g/cm^3)	0.68 %
DW-4		9.21 g (1.97 g/cm^3)	9.11 g (1.96 g/cm^3)	1.1 %
DW-5		9.22 g (1.92 g/cm^3)	9.13 g (1.92 g/cm^3)	1.1 %
DW-6	3 months	9.15 g (1.93 g/cm^3)	8.44 g (1.90 g/cm^3)	7.8 %
DW-7		9.20 g (1.95 g/cm^3)	8.41 g (1.91 g/cm^3)	8.6 %
DW-8		9.22 g (1.93 g/cm^3)	8.41 g (1.99 g/cm^3)	8.8 %
KCL-4	1 month	9.23 g (1.95 g/cm^3)	9.11 g (1.94 g/cm^3)	1.3 %
KCL-5		9.26 g (1.94 g/cm^3)	9.13 g (1.94 g/cm^3)	1.4 %
KCL-6		9.26 g (1.94 g/cm^3)	9.13 g (1.93 g/cm^3)	1.4 %
KCL-7	3 months	9.25 g (1.95 g/cm^3)	8.61 g (1.95 g/cm^3)	6.9 %
KCL-8		9.25 g (1.97 g/cm^3)	8.60 g (1.96 g/cm^3)	7.0 %
KCL-9		9.26 g (1.96 g/cm^3)	8.62 g (1.95 g/cm^3)	6.9 %

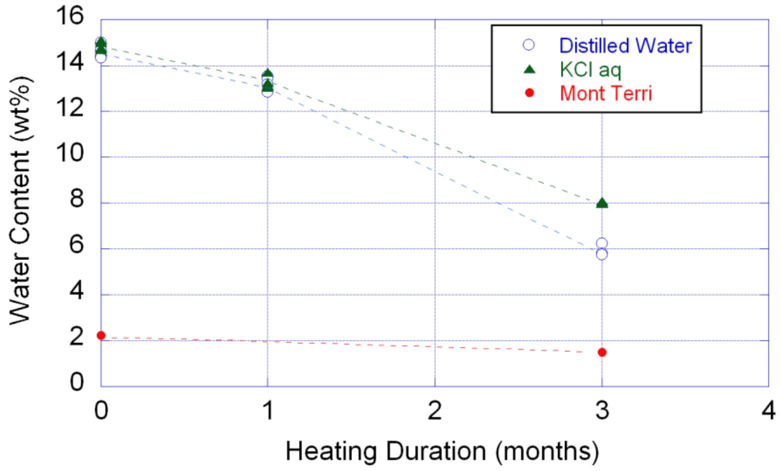

Figure 5.33. Decreases in the water content of the compacted bentonite core samples.

5.3.2 Ultrasonic velocity measurements

Ultrasonic velocity measurements were conducted on short, pill or “hockey-puck” shaped S&I samples (0.25”–0.5” in thickness). Both P-wave transducers (Panametrics, source central frequency 500 kHz) and S-wave transducers (1 MHz) were transmitted through the samples while a small load was applied through thin lead foils to improve mechanical coupling across the interfaces (Figure 5.34).

With increasing heating duration, both P and S-wave velocities of all the samples increased (Figure 5.35), as did the amplitude of the waves (Figure 5.35a). Considering the small changes in the density of the samples during heating, the observed velocity increases were mostly caused by increases in elastic moduli.

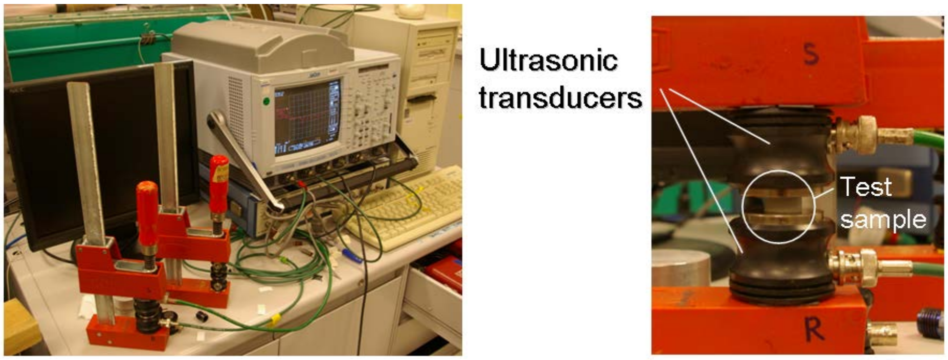

Figure 5.34. Ultrasonic velocity measurements on small clay cores. Minimal stress was applied to the surfaces through thin lead foils to establish good acoustic coupling.

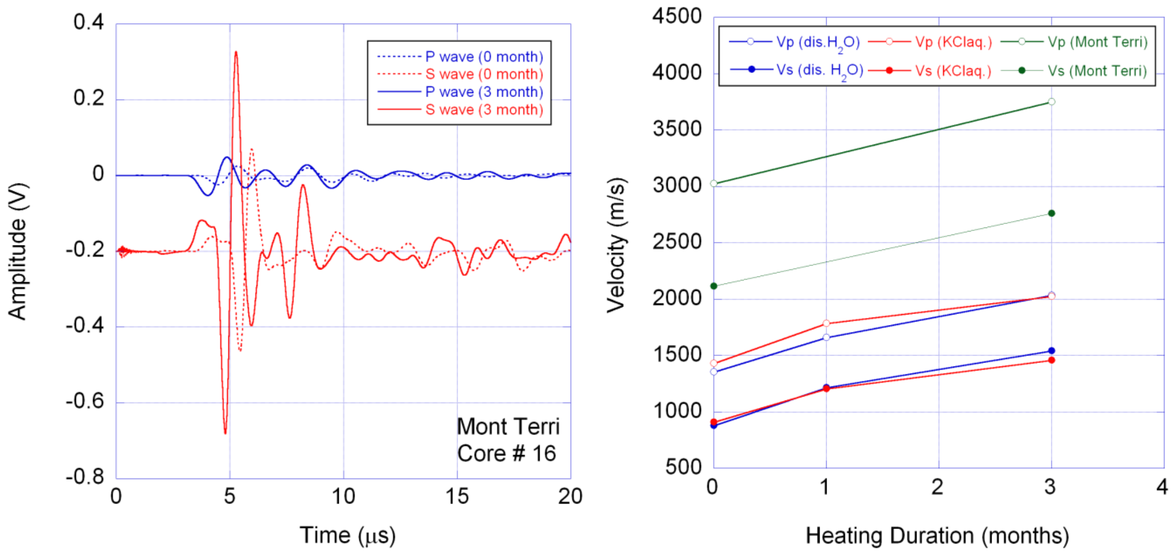

(a) (b)

Figure 5.35. An example of waveforms (a) and changes in the P and S-wave velocities (b) determined for the cores. Velocities of all the samples increased after heating.

5.3.3 Triaxial compression tests

Undrained triaxial compression tests were conducted on miniature cores with a diameter 0.56” and a length 1.1” (the length was slightly longer for the Mont Terri cores). A triaxial confining cell capable of quick exchanges of the samples between tests was built (Figure 5.36). Each sample was jacketed with a thick-walled latex tubing, and thin Teflon films were placed at the both ends of the sample to reduce the friction at the interfaces.

The tests were conducted at three different confining stresses of 10 psi, 100 psi, and 250 psi. Loading rate (strain rate) was ~3.0×10^{-5} s^{-1} for bentonite cores, and ~1.5×10^{-5} s^{-1} for Mont Terri cores. The reasons for the rather fast loading rates are the unsaturated condition of the samples and that our current focus is on the potential relative changes in the strength of heat-treated clays. The axial stress and displacement were monitored during the tests, and the dilation of the sample was determined from the volume of the fluid expelled from the confining cell and measured by a syringe pump (ISCO 500D pump).

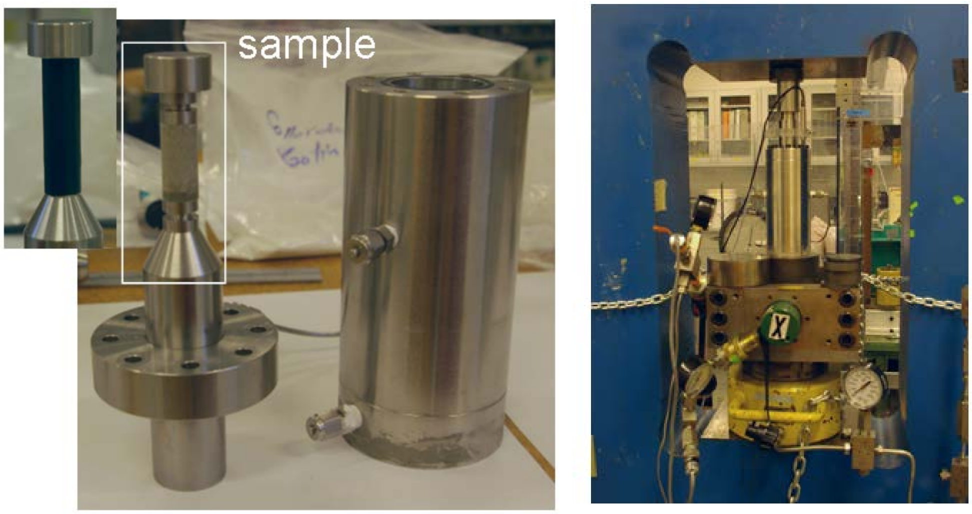

Figure 5.36. Triaxial compression tests on miniature core samples. The piston+jacketedsample assembly can be simply inserted in the confining cell through an o-ring, which does not require unbolting of the top vessel closure plate.

Both compacted bentonite and Mont Terri cores exhibited clear increases in the confined compressional strength (Table 5.8, Figures 5.37, 5.38). Brittleness of the samples also appeared to have increased somewhat, as seen from the more linear peak-failure load-displacement responses and the sudden drop in strength in the post-failure regime for the heated samples. Mohr's circles determined from the peak (failure) loads are also shown in Figure 5.39. Note that apart from the obvious increases in strength with increasing heating duration, the compacted bentonite samples showed no significant differences in strength (Figure 5.39a) or in the failure behavior (Figure 5.35) between the samples containing distilled-water and 0.5 M KCl solution.

Table 5.8. Undrained triaxial compression strength of clay samples.

Samples	Heating Duration	Confining Stress		
		10 psi	100 psi	250 psi
GEO-DW-6, 3, 1	0 month	1190.5 psi	1722.5 psi	2259.3 psi
GEO-KCL-1, 2, 3		1333.9 psi	1633.2 psi	2119.9 psi
GEO-DW-2, 4, 5	1 month	2278.9 psi	2898.7 psi	3392.0 psi
GEO-KCL-4, 5, 6		1994.4 psi	2956.8 psi	2967.0 psi
GEO-DW-7, 8, 9	3 months	3941.9 psi	5320.1 psi	5728.3 psi
GEO-KCL-7, 8, 9		4298.5 psi	5279.1 psi	5624.1 psi
MT-6, 13, 16	0 month	2213.1 psi	2957.9 psi	4093.6 psi
MT-5, 20, 21	3 months	6411.4 psi	7700.5 psi	8010.1 psi

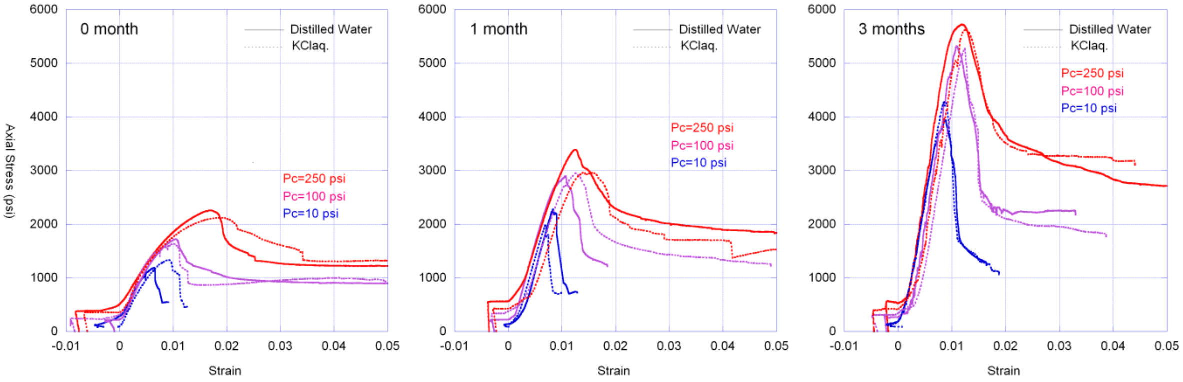

(a) No heating (b) Heated for 1 month (c) Heated for 3 months

Figure 5.37. Axial stress vs strain response of compacted bentonite samples. Solid lines indicate samples containing distilled water, and the broken lines indicate samples with 0.5 M KCl solution (Note that the concentration should have increased due to water loss). Increases in the heating duration resulted in higher compressional strength and more brittle behavior.

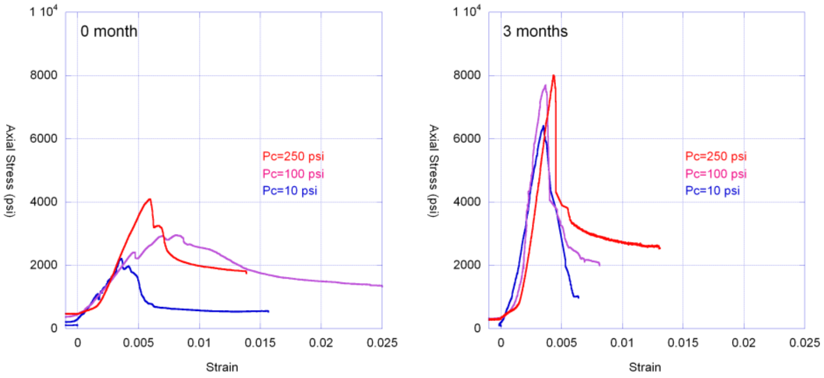

(a) No heating (b) Heated for 3 month

Figure 5.38. Axial stress vs strain response of Mont Terri core samples. Solid lines indicate samples containing distilled water, and the broken lines indicate samples with 0.5 M KCl solution (Note that the concentration should have increased due to water loss). Increases in the heating duration resulted in higher compressional strength and more brittle behavior.

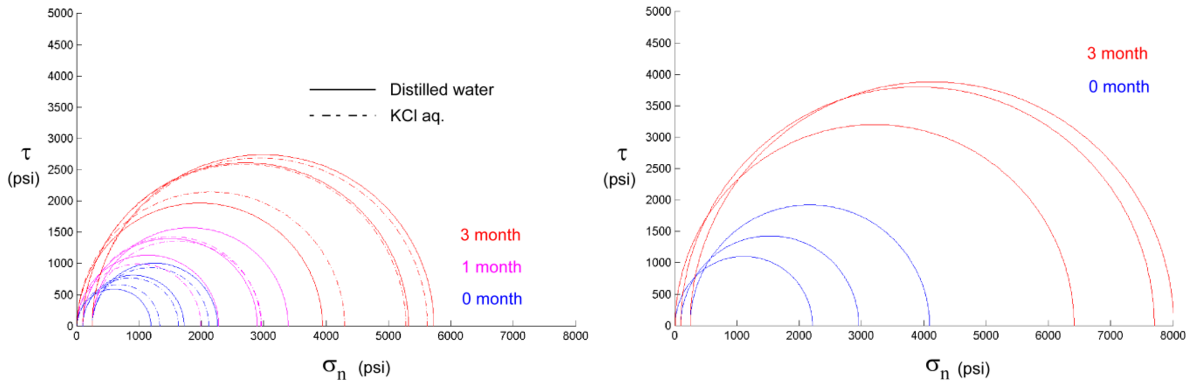

(a) Compacted bentonite cores

(b) Mont Terri cores

Figure 5.39. Mohr's circles determined from the triaxial compression tests in Figures 5.37 and 5.38.

5.3.4 Development of a miniature indentation experiment setup and some preliminary results

Because only a limited number of samples can be produced for triaxial tests, the errors in the experimentally determined geomechanical parameters, such as the cohesion and friction angle of a Mohr-Coulomb envelope, can be significantly large. Although making direct links to such engineering parameters is not well established, as supplementary information, hardness and reduced Young's modulus determined from indentation tests can be used to investigate the effect of heating on the changes in the mechanical properties of clays.

We built a miniature/micro indentation test setup that applies controlled displacement to an indenter pushed onto the surface of clay samples to determine its hardness value (=force/area during indentation) and the reduced Young's modulus. Using this setup, a diamond-tipped conical indenter is driven using a piezo linear actuator (Polytech Nexline actuator N-216.2A) and an encoder (Polytech close-loop encoder E-755.1A1), and the resulting reaction force is recorded (Figure 5.40).

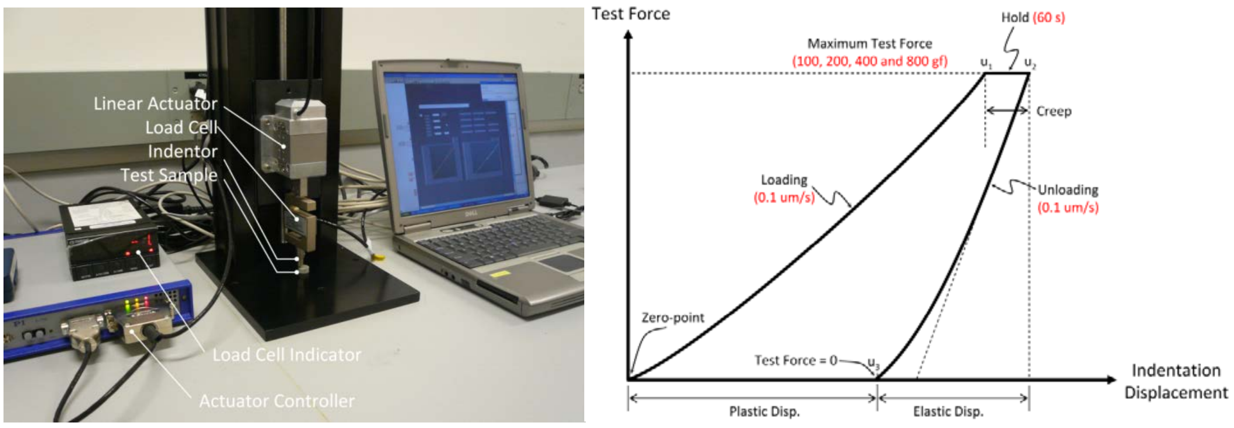

(a) Experimental setup

(b) Loading protocol currently used for our experiment

Figure 5.40. Micro indentation experiment setup. Controlled displacement is applied to an indenter and the resulting force response is measured.

Once a series of indentations with a range of maximum forces are produced, the geometry of the depression (“crater”) is determined using an optical surface profiler (Nanovea PS50) (Figure 5.41) and with image processing (Figure 5.42), which produces the area of depression used to compute the sample hardness.

Before the samples in the previous sections were made and the heating experiments were conducted, one sample of Mont Terri core was heated at 285ºC over 1 week, within one of the pressure vessels used in the experiments but without the silicon rubber gaskets. Although this resulted in severe desiccation of the sample, the result demonstrated promising performance of the new experimental system. Figure 5.43 shows a series of 2-D depression profiles (at the same gray scale for the depth) obtained from the same sample, before and after the heating experiment. The resulting hardness values are shown in Figure 5.44, as a function of the applied maximum loads. Although the results for the smallest load (250–500 gf) may not be reliable due to the noise, a series of measurements conducted over a range of loads can provide more consistent values as an average, indicating that heating increased the clay hardness to twice the original value.

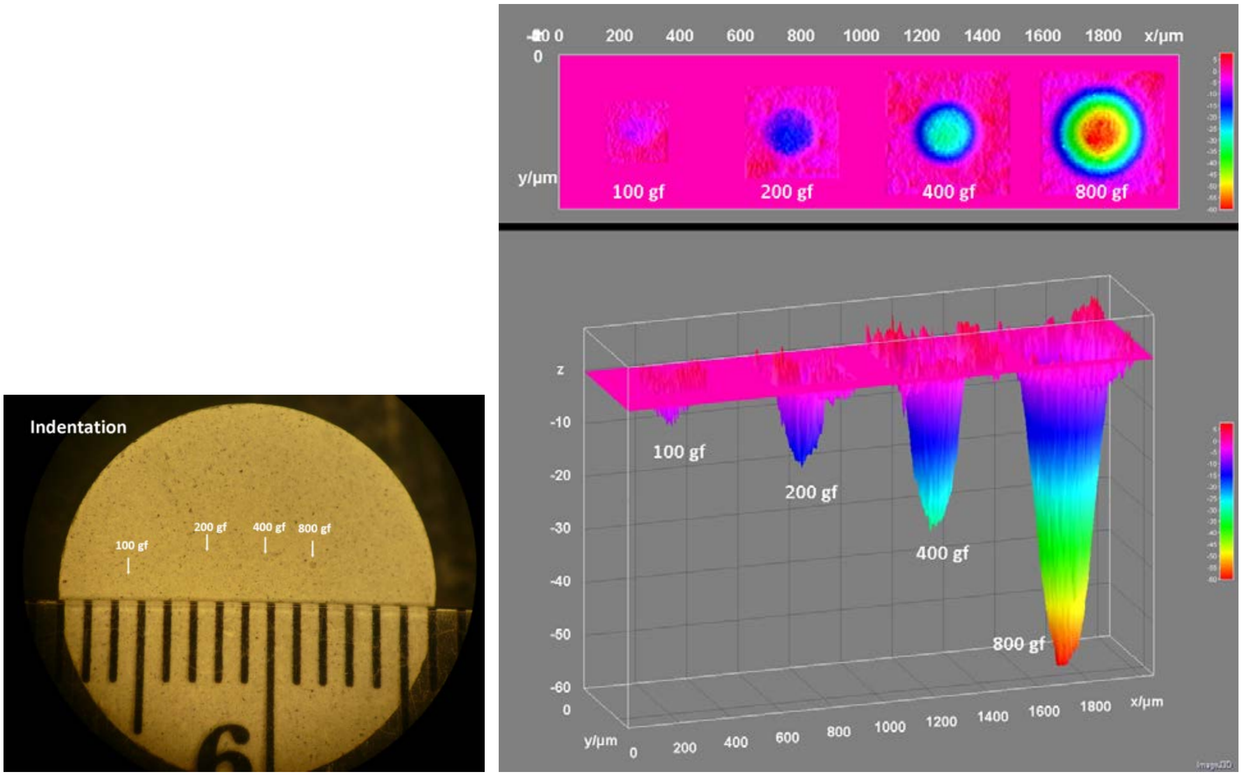

Figure 5.41. Indentations produced at different maximum forces on a compacted bentonite sample (contains distilled water. Density ~ 2.09 g/cm^3, water content ~15%wt).

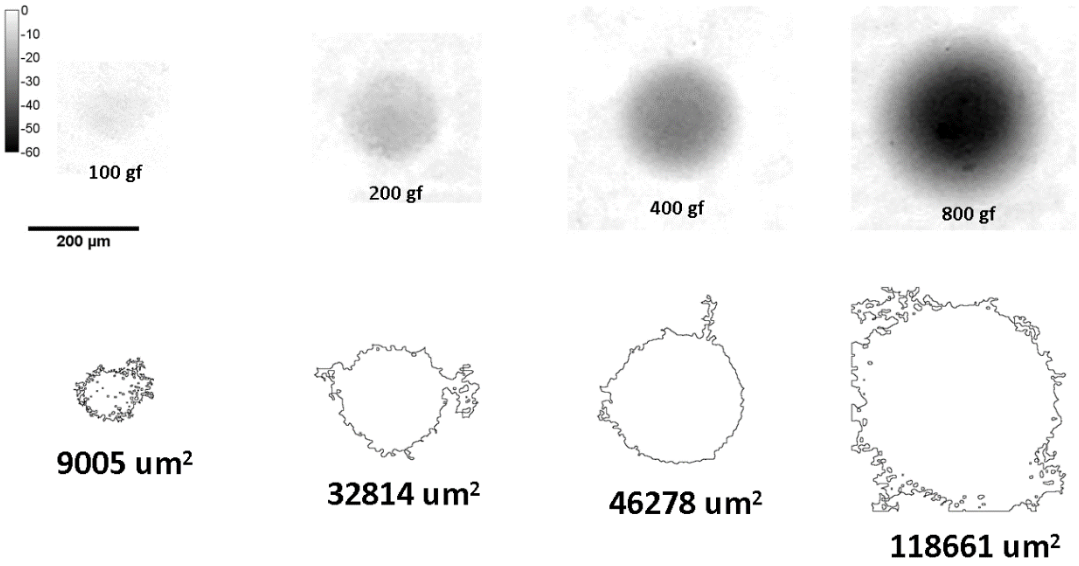

Figure 5.42. Indentations produced at different maximum forces on a compacted bentonite sample (contains distilled water. Density ~ 2.09 g/cm^3, water content ~15%wt).

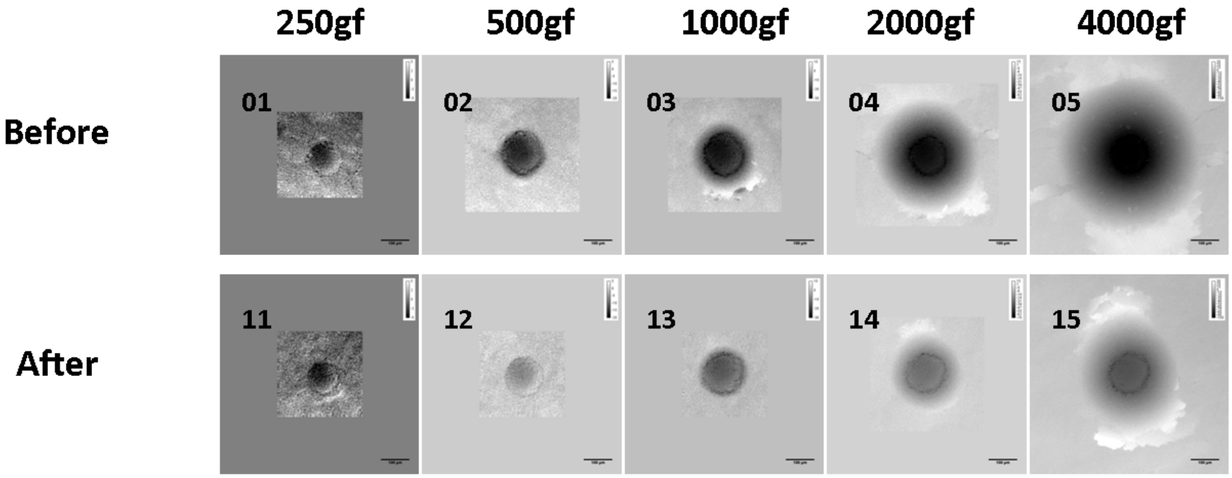

Figure 5.43. 2-D indentation profiles on a single sample of Mont Terri core before and after the sample was heated at 285°C over 1 week.

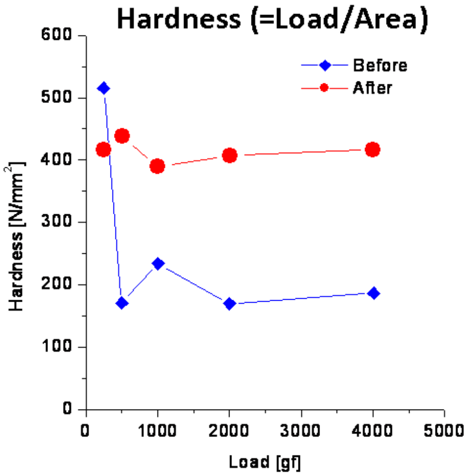

Figure 5.44. Hardness values determined from the area of indentation and the corresponding applied maximum force. The results indicate increases in the hardness of the sample due to the heating.

5.3.5 Summary and Future Work

It is highly likely that the observed heat-induced changes in the strength and failure behavior of the compacted bentonite and the Opalinus Clay from Mont Terri were caused by decreases of water content from the clay samples during heating. The effect, however, may also be superimposed by other effects such as redistribution (dissolution and re-precipitation) of quartz within the pore space and phase transformations of clay minerals. A summary of the accomplishments so far is as follows:

- Sample preparation procedures have been established and necessary tools developed.
- An efficient triaxial compression testing setup has been developed. The tests were conducted on compacted bentonite clay with different fluid chemistry and on Opalinus Clay cores from Mont Terri. However, the loss of fluid during heated resulted in ambiguities in the experimental results.
- A miniature indentation test setup has been developed. A sample hardness measurement procedure has been established and demonstrated.

Future work for the remaining months of FY14 and FY15 includes:

- Finding a solution for the slow leakage of water vapor from the pressure vessels used for heating of clay samples. Currently, use of soft metal foils (e.g., lead or tin [Sn] foils for unsaturated samples. Silver or gold if the sample is saturated.)
- Preparation of the clay samples and repeated experiments
- Chemical/mineralogical characterization of heat-treated samples. Interpretation of the results with the changes in the mechanical/hydrological properties.
- Improvement of mini indentation test setup. Currently, the reduced Young modulus of tested samples cannot be determined accurately because of large flexures in the loading column (particularly in the loadcell section). An additional displacement gage for determining the system deformation needs to be installed.
- Continued development of a gas permeability measurement setup for low-permeability clay samples. Current samples exhibit unusually high permeability which may be attributed to microcracks in the heated samples.

5.4 Discussion and Conclusions

5.4.1 Summary of current work

This study investigates the impact of strongly elevated temperature on the bentonite backfill and near-field clay host rock in a geologic repository for radioactive waste. We use coupled THMC modeling to evaluate the chemical alteration and associated mechanical changes in a generic repository and consider the interaction between EBS bentonite and the NS clay formation. Two main scenarios were developed for comparison: a "high T" case in which the temperature near the waste package reaches about 200°C, and a "low T" scenario in which the temperature peaks at about 100°C.

Our model results indicate the occurrence of some degree of illitization in the NS clay formation (as previously revealed by several earlier natural analogue studies), and also show that illitization occurs in the EBS bentonite. Other chemical alterations include the dissolution of K-feldspar and calcite, and the precipitation of quartz, chlorite, and kaolinite. In general, illitization in the bentonite and clay formation is enhanced at higher temperature. However, the quantity of illitization, expressed as the smectite volume fraction change, is affected by many chemical factors and subsequently varies a great deal, which could be the reason that illitization is not consistently observed in laboratory studies. The most important chemical factors are the concentration of K and dissolution rate of K-feldspar; less important are the concentration of Na and the quartz precipitation rate. Because of the differences in chemical properties, it is conceivable that the occurrence of illitization in different bentonite is different, which was manifested in current simulations for Kunigel-VI and FEBEX bentonite. For Kunigel bentonite, the decrease in smectite volume fraction in bentonite ranges from 0.004 to a maximum of 0.085, or up to about 27% of the initial volume fraction of smectite for the 200°C scenario. For FEBEX bentonite, the decrease in smectite volume fraction in bentonite ranges from 0.01 to a maximum of 0.04 (7% of the initial amount). The smectite volume fraction in the clay formation decreases moderately in some cases, but in other cases it decreases as much as 0.035, fully depleting the initial smectite.

Higher temperature leads to much higher stress in the near field, caused by thermal pressurization in the low-permeability rock surrounding and connected to the emplacement tunnel. During this period of strong thermal stresses, smectite dissolution causes only minimal changes in the simulated total stress. Chemical changes, including changes in pore water ion concentration and smectite volume fraction, lead to a reduction in swelling stress. But such reduction seems to be more pronounced for Kunigel-VI bentonite than for FEBEX bentonite. For Kunigel-VI bentonite, a reduction in swelling stress is up to 16–18% for the base case, and a reduction of swelling stress up to 70% could be observed in an extreme case in which key chemical and mechanical parameters are tuned to maximize the possible swelling stress reduction and to represent the worst scenario. The results for Kunigel-VI bentonite seem to suggest that the swelling stress reduction could compromise the ability of EBS bentonite to provide mechanical support to the tunnel walls and to seal any fractures in the disturbed rock zone. However, for FEBEX bentonite, the base case shows only about 1.5% reduction in swelling stress and 3.6% reduction in swelling stress in the worst scenario, which is much less than that for Kunigel-VI bentonite. The reasons are (1) FEBEX bentonite undergoes less degree of illitization; (2) FEBEX bentonite has higher swelling capacity so that the relative reduction in swelling stress is fairly small.

Chemical alteration and the subsequent changes in mechanical properties are among the determining factors for establishing the thermal limit of a repository with a clay-based EBS. A thermal limit of about 100°C is imposed unanimously in all disposal concepts throughout the world—without rigorous studies to back up the choice. THMC simulations were conducted in FY13 (Liu et al., 2013b) and FY14 to answer the question whether an argillite repository with bentonite EBS can sustain higher than 100°C. While further refinement of the THMC models is needed and laboratory studies are recommended, the modeling work in FY13 and FY14 leads to a tentative conclusion that an argillite repository with bentonite EBS could sustain higher than 100°C as far as illitization concerns, with the following reasons:

1. Despite illitization in the bentonite and clay formation is enhanced at higher temperature, such enhancement is fairly limited even at 200 °C due to other constrains of illitization such as the supply of K and Al.
2. Illitization causes only moderate decrease of swelling pressure and thus compromise insignificantly the functionality of EBS such sealing the gap. Although for the bentonite having low swelling capacity (e.g., Kunigel-VI bentonite), chemical changes could results relatively large reduction in swelling pressure in the worst scenario, for bentonite with high swelling capacity (e.g., FEBEX bentonite) chemical changes could only lead to about a few percent reduction of swelling pressure. Using bentonite with high swelling capacity could diminish the undesirable consequence (if there is any) of illitization.
3. Illitization in EBS could be suppressed by relatively easy engineering method such as increasing the concentration of Na in the pore water of bentonite.

For the laboratory investigations, it is highly likely that the observed heat-induced changes in the strength and failure behavior of the compacted bentonite and the Opalinus Clay from Mont Terri were caused by decreases in water content from the clay samples during heating. The effect, however, may also be superimposed by other effects, such as redistribution (dissolution and re-precipitation) of quartz within the pore space and phase transformations of clay minerals.

5.4.2 Reconciliation of the apparent differences regarding illitization

Illitization is one of the major considerations for determining the thermal limit for a clay repository. It is widely observed in geological systems (e.g., Pusch and Madsen, 1995) and recent modeling work also showed the occurrence of illitization in EBS bentonite and clay rock. However, this process has not been conclusively confirmed for EBS bentonite in either small-scale laboratory experiments or large-scale mockup and field tests. There are seemingly contradictory conclusions reached by geological data and models versus laboratory and field tests. For example, our model in this report shows the occurrence of illitization in Kunigel or FEBEX bentonite, whereas experimental studies at LANL under UFDC (Cheshire et al., 2014) show no illitization for Wyoming bentonite. In this section, we discuss plausible factors that contribute to such seeming controversy.

First, the reaction rate of illitization is very low, and most laboratory and field tests did not run long enough to detect the change. The Pytte's model (Pytte, 1982) and similar types of models (Elliott and Matisoff 1996; Cuadros and Linares, 1996) have been widely used to calculate the illitization rate in geological formations. In these models, the time derivative of smectite loss is related to the concentration of potassium (or the ratio of potassium to sodium concentration) and smectite mass fraction, via a rate constant that is a function of temperature. Because it is hard to know the concentration of potassium over the course of geological time or the inhibition effect from other cations, Cuadros (2006) used an "effective" potassium concentration within the following equation to match the illitization versus depth data for variety of geological formations in U.S.:

$$-dS/dt = kK^{0.25}S^{n} \tag{5.3}$$

where the proportion of smectite, S, is a fraction and has no units, t is expressed in days, and K is the effective potassium concentration in M, and k is a rate constant in $M^{-0.25}$ $days^{-1}$. Cuadros and Linares (1996) excrementally determined the rate constant, which is about 5E-6 $M^{-0.25}$ $days^{-1}$ at 100 ^{o}C and 3.3E-5 $M^{-0.25}$ $days^{-1}$ at 200°C. Cuadros (2006) used effective potassium concentration rather than the actual potassium concentration in the pore water to take into account the completion of other cations with potassium for the interlayer space and other possible inhibition effects. Effective potassium concentration, K, ranges from 10^{-10} M to 10^{-24} M, which is calibrated from illitization versus depth data. Taking the maximum K, i.e., 10^{-10} M, the smectite mass fraction decreases at a rate of 0.0006%/year at 100°C and

0.0038%/year at 200°C, which means an experiment needs to run at 200°C for around 300 years to realize about 1% changes in smectite (the detection limit of X-ray diffraction (XRD)). The models reported here show that for Kunigel bentonite, smectite dissolves about 3.5% in 1000 years, and for FEBEX bentonite, smectite dissolves only about 1% in 1000 years, which is largely aligned with those rates calibrated against geological data. The time needed to see detectable changes in smectite is probably the primary reason why most laboratory and field tests, which typically last for weeks to couple years, did not show any occurrence of illitization.

Second, illitization is a complex process and impacted by other factors, which might retard or even prevent the occurrence of illitization. This point is thoroughly discussed in Cheshire et al. (2014) when they explained the absence of illitization in their experiment. Although illitization during diagenesis is clearly evidenced by geological data, the reaction pathways are still a matter of debate (Wersin et al., 2007). In general, it is believed that the process starts with K-montmorillonite and then is followed by various stages of illite/smectite interlayer reaction**,** eventually ending up with discrete illite. The reaction mechanism could be via solid state transformation or dissolution-precipitation, depending on the water/rock ratio, fluid composition, redox state, or occurrence of microbial organism. Several factors could prevent the occurrence of illitization:

(1) The supply of K might be limited, which basically shuts down illitization. This is probably the reason why illitization was not observed in some field tests (Pacovsky et al., 2005; Pusch et al., 2010) in which K was not deliberately supplied.

(2) Illitization could be prevented by the presence of high contents of Na, Ca, and Mg, especially Na, in a water-bentonite system. It has been shown in several studies that a low supply of K with high Na activity significantly lowers the illitization rate (e.g. Roberson and Lahann 1981; Mosser-Ruck et al., 1999). As pointed out by Cheshire et al. (2014), in their system, even though high K concentration in aqueous solution is used in the experiment, the overall bentonite-water system is still Na-rich, which explains why in some experiments (Mosser-Ruck and Cathelineau 2004; Cheshire et al., 2014) using high K solution does not necessary produce illite from Na-bentonite. Also, Liu et al. (2013b) showed that if bentonite blocks are fabricated with high Na solution, the illitization is dramatically inhibited.

(3) Over the course of transforming smectite to illite, excess silicate is produced and eventually precipitates out as quartz, which has two implications. One is that high silicate concentration in the system retards illitization, as shown by several studies (Eberl 1978; Abercrombie et al. 1994). Quartz has high solubility at high temperature, which allows more silicate to remain in the aqueous solution and therefore retard illitization. This is probably a negative effect of temperature on illitization. The other is that the precipitation rate of quartz becomes a bottleneck for illitization; the precipitation rate is known to be very low.

(4) The availability of Al also interferes with illitization. Illite and smectite are both dioctahedral phyllosilicates. What make them differ so much in physical properties is the interlayer charge and cation. Smectite has a low interlayer charge, such that Al is needed to substitute silicates in the tetrahedral layer to increase the interlayer charge as a precursor of forming illite. However, Al is involved in many minerals, and therefore the availability of Al for illitization faces competition from other minerals, which could inhibit the formation of illite.

5.5 Future Work

While the modeling exercise improves our understanding of the coupled processes contributing to chemical and mechanical alteration in EBS bentonite and NS argillite formation, our results should be taken cautiously, because of the limitations/assumptions in the model. These limitations and model refinements that could be conducted to overcome these limitations in the remaining month of FY14 and FY15 are as follows:

- First, illitization is simulated as a dissolution-precipitation process, i.e., the dissolution of smectite and neo-formation of illite, with the illitization rate calibrated against field data (Pusch and Madsen 1995). It is known that illitization could also occur through solid state transformation by substitution of intracrystal cations (e.g., Cuadros and Linares 1996), which is not considered in our model. Illitization through solid state transformation could be implemented in the model to evaluate the long-term illitization in the EBS bentonite and argillite.
- Second, since the mechanical-chemical coupling in bentonite is calculated via an extended linear elastic swelling model, a more rigorous approach to link chemistry to mechanics is needed for more accurate calculations. More comprehensive links between chemistry and mechanics taking advantage of the framework provided by a dual-structure model was implemented in TOUGHREACT-FLAC (Rutqvist et al., 2014), and could be used to simulate the chemical-mechanical coupling in EBS bentonite in the future.
- Third, the current mechanical model for the NS clay formation is not tied with chemical variables, i.e., mechanical-chemical coupling is only considered in the EBS bentonite. Constitutive relationship to link the chemistry with mechanics for clay formation needs to be developed and implemented in the THMC models.
- Fourth, in the current model, the canister serves only as a heat source; chemical changes on the surface of the canister are neglected for simplification. Further model analysis is needed to consider chemical changes in the canister, specifically the release of Fe^{+2}, which might enhance the dissolution of smectite by forming chlorite.

For laboratory programs, future work needs to address the slow leakage of water vapor from the pressure vessels used for heating of clay samples. Currently, soft metal foils are used (e.g., lead or tin [Sn] foils for unsaturated samples; silver or gold if the sample is saturated). Better methods are needed for preparation of the clay samples, so that they can be reliably repeated. Chemical/mineralogical characterization of heat-treated samples is also needed for interpretation of the results regarding the changes in mechanical/hydrological properties. Regarding characterization, the mini-indentation test setup requires improvement. Currently, the reduced Young modulus of tested samples cannot be determined accurately because of large flexures in the loading column (particularly in the load cell section). An additional displacement gauge for determining the system deformation needs to be installed. Finally, development of a gas-permeability-measurement setup for low-permeability clay samples needs to be completed. Current samples exhibit unusually high permeability, which may be attributed to microcracks in the heated samples.

6. Transport in Clay and Clay Rock

6.1 Ion diffusion through clays

Clay minerals are high-surface-area lamellar aluminosilicates that possess a large capacity for retaining dissolved metal ions, which can be incorporated within interlayer spaces or adsorbed to external surfaces within the Electrical Double Layer (or EDL). However, metal ions associated with clay particles are not permanently sequestered, but may be mobile via diffusion. This task examines the role of the EDL in diffusion through clays, integrating microscopic characterization, molecular modeling, and mesoscale continuum models.

To date, we have developed two complementary approaches to modeling ion diffusion through clays, which are briefly summarized below. The first makes use of a Donnan Equilibrium or Mean Electrostatic Approach, in which a mean electrostatic potential is defined for the electrical double layer to balance the fixed negative charge of the clays. The volume of the EDL required for mass-balanced-based transport calculations is the product of the surface area of the clays and the width of the EDL, normally calculated as some multiple of the Debye length. Thus, the width of the EDL (and thus the volume) is a function of the ionic strength. The second approach involves the use of the Nernst-Planck and Poisson-Boltzmann equation (termed the Poisson-Nernst-Planck or PNP equation). In the PNP approach, the electrical potential as a function of distance from the charged clay surfaces is resolved. Both approaches predict that the electrical potential in the space between two clay layers does not decay to zero when the clay layers or interlamellae are closely spaced, and thus the water within the space does not have the same properties as "bulk water." The lack of electroneutrality in the clay interlamellae results in a swelling pressure that can now be quantified for the general multicomponent case (i.e., for systems that do not consist of a symmetric electrolyte).

6.2 Theoretical Background for Treatment of Electrostatic Effects

A rigorous model for the electrical double layer (EDL) can be derived from the combination of several equations, including the Poisson equation describing the distribution of electrical potential, ψ, in water:

$$\nabla^2 \psi = -\frac{\rho_z}{\varepsilon}, \tag{6.1}$$

where ε is the permittivity and ρ_z is the volumetric charge density given by

$$\rho_z = e \sum_i z_i C_i . \tag{6.2}$$

In Equation (6.2), e is the elementary charge of the electron, z_i is the valence of the ion, and C_i is the concentration bulk solution. The Boltzmann distribution gives an expression for the concentration, $C_i^{EDL}(z)$, in the electrical double layer as a function of distance from the charge solid surface, z,

$$C_i^{EDL}(z) = C_i \exp\left(\frac{-z_i e \psi(z)}{k_B T} \right), \tag{6.3}$$

and where C_i is here the concentration in the bulk solution, k_B is the Boltzmann constant, and T is the absolute temperature. Combining Equation (6.3) with the Poisson equation (Equation 3.1) yields the Poisson-Boltzmann equation (Schoch et al., 2008):

$$\nabla^2 \psi = \frac{-e}{\varepsilon} \sum_i z_i C_i \exp\left(\frac{-z_i e \psi(z)}{k_B T} \right) \tag{6.4}$$

which can be solved exactly for various simple formulations (e.g., the Gouy-Chapman model, which assumes a symmetric electrolyte).

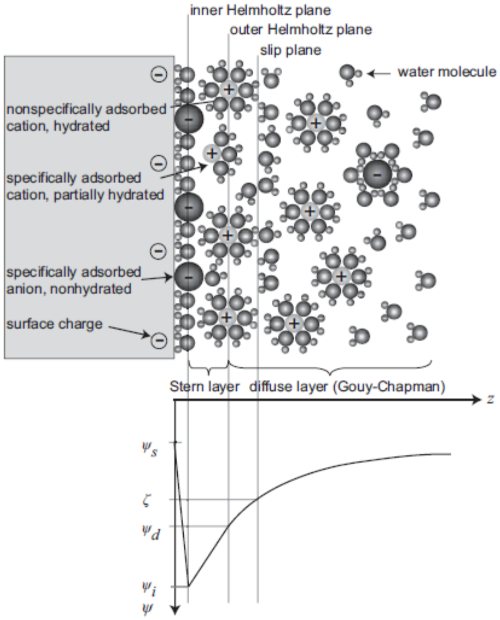

Figure 6.1. Schematic illustration of the Gouy-Chapman-Stern model of the solid-electrolyte interface, with the potential distribution $\psi(z)$ versus distance from the charged solid surface. The solid is illustrated with a negative surface potential ψ_s, described by three layers in solution. The inner Helmholtz plane layer ψ_i consists of nonhydrated co-ions and counterions (inner sphere complexes), whereas the outer Helmholtz plane layer ψ_d is built up of only hydrated counterions (outer sphere complexes). The diffuse layer is defined beyond the outer Helmholtz plane (from Schoch et al., 2008).

6.2.1 Mean Electrostatic Approach

Integrating the Poisson-Boltzmann equation over nanometer length scales from charged mineral surfaces, however, was not practical in the present version of CrunchEDL, because of the desire to consider larger length scales. So an alternative approach is used, based on a Donnan Equilibrium model (Wersin et al., 2004; Leroy and Revil, 2004; Appelo and Wersin, 2007; Leroy et al., 2007; Appelo et al., 2008; Birgersson and Karnland, 2009; Tournassat and Appelo, 2011). The electrical double layer is conceptualized as consisting of two parallel layers of charge, one being the surface charge associated with direct sorption at the mineral surface (the Stern layer, typically divided into an inner and outer Helmholtz layer), and the other being the diffuse layer charge, a swarm of counterbalancing ions (Figure 6.1).

In the approach taken in CrunchEDL, the chemical potentials of the species in the diffuse layer and the bulk solution are equated. Writing equations for the chemical potentials of the species *i* in the bulk solution (or macroporosity) (superscript “B”) and electrical double layer (superscript “EDL”) respectively, we have

$$\begin{aligned} \mu_i^B &= \mu_i^{B,0} + k_B T \ln a_i^B \\ \mu_i^{EDL} &= \mu_i^{EDL,0} + k_B T \ln a_i^{EDL} + q_i \psi_m \end{aligned} \tag{6.5}$$

where the superscript *0* (first term on the right-hand side) refers to the chemical potential at the reference state, a_i are the species activities, q_i, is the charge of an ion (the elementary charge of a particle, *e*, multiplied by the valence of the ion, z_i), k_B is the Boltzmann constant, and ψ_m is the mean electrical potential in the electrical double layer. The condition of Donnan Equilibrium implies that

$$\begin{aligned}\mu_i^{EDL} &= \mu_i^{B} \\ \mu_i^{EDL,0} &= \mu_i^{B,0}\end{aligned} \tag{6.6}$$

Combining Equations (6.3), (6.5), and (6.6) and assuming that the activity coefficients for the diffuse layer and bulk solution are the same gives the Boltzmann distribution for the ion activities in the electrical double layer, C_i^{EDL}:

$$C_i^{EDL} = C_i^{B} \exp\left(\frac{-z_i e \psi_m}{k_B T}\right). \tag{6.7}$$

The diffuse layer charge balances the charge within the Stern layer, Q^{SL}, which may consist in CrunchEDL of either a fixed mineral charge due to vacancies in the mineral structure (as in the case of classical ion exchange), or of fixed mineral charge modified by inner sphere and outer sphere complexes developed within the Stern layer calculated with a surface complexation model:

$$\phi^{EDL} \sum_i z_i C_i^{EDL} = Q^{SL} \tag{6.8}$$

where ϕ^{DL} is the volume (or porosity) of the electrical double layer. The left-hand side of Equation (6.8) gives a volumetric charge density in units of charge equivalents per unit volume porous medium. The surface charge is given by

$$Q^{SL} = \sum_k^{Ns} z_k \Gamma_k \tag{6.9}$$

where Γ_k is the concentration in units of moles sorbed species per unit volume porous medium and z_k is the valence of the surface complex. In the CrunchEDL approach, therefore, one new equation is introduced (Equation 6.8), with one new unknown, the mean electrostatic potential of the diffuse layer, ψ_m. Note that in this formulation, the concentrations of the ions in the diffuse layer are dependent (or secondary) species that are calculated algebraically from the knowledge of the bulk solution composition and the mean electrostatic potential. A kinetic treatment of the diffuse layer ions would require that they be considered as primary unknowns.

Several approaches are available for calculating the fixed or Stern layer charge that is balanced by an electrical double layer. Even if the full Poisson-Boltzmann (PB) equation is used, special consideration needs to be given to the charge present in the Stern layer, a feature not always seen in the simpler implementations of the Poisson-Boltzmann equation. The starting point is the fixed mineral charge, which is normally given by the cation exchange capacity. If no Stern layer sorption occurred, the fixed mineral charge would provide a Dirichlet boundary condition for the electrostatic potential, ψ_f, at the solid surface:

$$\psi(0) = \psi_f \tag{6.10}$$

In the case of no Stern layer sorption, therefore, the PB equation can be integrated across the entire thickness *z* of the electrical double layer. In the case where the charged bentonite particles are bordered by bulk water, this would be the point in space where the local solution becomes electroneutral (where the electrostatic potential goes to zero). In the case of overlapping double layers, as considered by Goncalves et al. (2007) and Schoch et al. (2008), this would be the midpoint between the two charged clay (or solid) surfaces.

6.2.2 Dynamic Calculation of Electrical Double Layer Thickness

CrunchEDL also now includes a dynamic calculation of the electrical double layer porosity, ϕ^{EDL}, based on the diffuse layer thickness as a function of ionic strength according to

$$\phi^{EDL} = A_{clay}\lambda_{DL}D_L = A_{clay}\lambda_{DL}\frac{\beta_{DL}}{\sqrt{I}} \tag{6.11}$$

where D_L is the Debye length, λ_{DL} gives the multiples of the Debye length used in calculating the electrical double layer porosity (as in the approach of Tournassat and Appelo, 2011), β_{DL} is a temperature-dependent factor (= $2.15\text{x}10^{-10}$ meters at 25°C), I is the ionic strength of the bulk solution, and A_{clay} is the surface area of the charged mineral surfaces (normally clays). The Debye length provides an approximate measure of the width of the electrical double layer, although in their Donnan or mean electrostatic model, Tournassat and Appelo (2011) included as many as five Debye lengths to describe the EDL porosity.

Previously, we have presented results in which the ionic strength is constant over the domain. It is also possible, however, to consider transient cases in which a salinity front propagates through the domain, changing the Debye length and thus the diffuse layer porosity dynamically. Note that in this case, the EDL thickness and thus the transport properties of the compacted bentonite are modified by the changing ionic strength. The effect is different from the swelling behavior described in Section 2, and may in fact work in the opposite way.

In the CrunchEDL approach in which solute mass is tracked in both the bulk porosity and the diffuse layer (EDL) porosity, this gives an accumulation term (neglecting liquid saturation) of

$$\frac{\partial\left[\phi^B C_i^B + \phi^{EDL} C_i^{EDL}\right]}{\partial t} = \frac{\partial\left[\phi^B C_i^B + \left(A_{clay}\lambda_{DL}\beta_{DL}\big/\sqrt{I}\right)C_i^{EDL}\right]}{\partial t}. \tag{6.12}$$

In this case, the bulk porosity is treated as a constant, or at least as separately determined or fixed. Since the total porosity then can increase or decrease as the EDL thickness changes, special considerations need to be made to conserve mass in the system. Alternatively, it is preferred to treat the total porosity (bulk and EDL) as constant, in which case the bulk and EDL porosities would be updated according to:

$$\frac{\partial\left[\left(\phi^{Tot} - \phi^{EDL}\right)C_i^B + \phi^{EDL} C_i^{EDL}\right]}{\partial t} \tag{6.13}$$

where ϕ^{Tot} is the total porosity = $\phi^B + \phi^{EDL}$.

6.2.3 Modified Poisson-Nernst-Planck Equation for Ion Transport in Clays

The primary objective here is to develop improved models for the distribution of ions between the EDL and the Stern layer (inner and outer sphere sorption) on planar and edge sites in the clay. The novelty of the research is in the integration of a molecular modeling and characterization approach that quantifies the distribution and mobility of ions in the various domains (Stern layer, EDL, water film) and to use this, along with the transport experiments described below, to develop improved micro-continuum models for ion distributions and mobility in clays. The micro-continuum model will be based on a modified Poisson-Boltzmann description of the electrical double layer (EDL) within the context of a multicomponent reactive transport code that accounts for Nernst-Planck (electrochemical migration) effects. In the PNP equation, the Poisson-Boltzmann equation (Equation 6.4) is combined with the Nernst-Planck equation given by:

$$J_i = -D_i \nabla C_i - \frac{z_i F}{RT} D_i C_i \nabla \psi \tag{6.14}$$

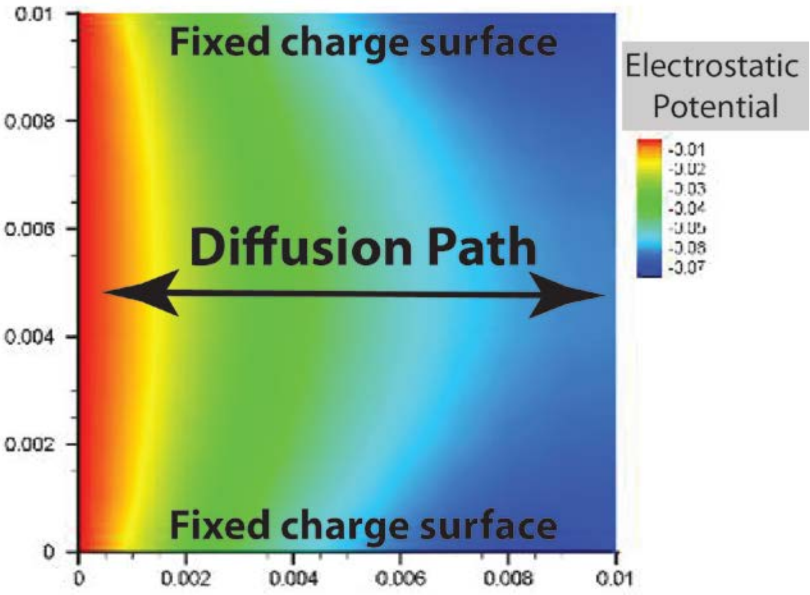

Figure 6.2. Calculation of the electrostatic potential by solving the Poisson-Nernst-Planck equation with fixed potential (Dirichlet) boundary conditions of fixed charge (0.001 mV) at the top and bottom. The gradient in potential in the diffusion direction is due to the different diffusion rates of the charged ions. The axis scales are microns and the electrostatic potential is dimensionless ($F\psi / RT$).

Classical Poisson-Boltzmann treatments perform reasonably adequately for monovalent ions, but they cannot handle as well the interactions between divalent ions (resulting in ion pairing) or the steric effects associated with the finite size of the ions (Lee et al.2012). Recently, however, modified Poisson-Nernst-Planck (PNP) models have been proposed that address the steric effects, as well as the interactions between multivalent ions in asymmetric electrolyte solutions (Grochowski and Trylska 2007; Wang et al. 2013). One possible formulation has been proposed by Wang et al. (2013) that accounts for steric and other thermodynamic (excess free energy) effects:

$$J_i = -D_i \nabla C_i - \frac{z_i F}{RT} D_i C_i \nabla \psi - D_i C_i \nabla \ln \gamma_i \tag{6.15}$$

where γ_i are the activity coefficients for the ith species. This is a general formulation that could be used to account for any excess free energy term, derived as it is from the chemical potential. Wang et al. (2013) proposed a form that accounted for steric (ion size) effects, suggesting an activity coefficient given by:

$$\gamma_i = \frac{1}{1 - \sum_i^N \frac{C_i}{C_{i,\max}}} \tag{6.16}$$

where $C_{i,max}$ is defined by the maximum concentration attainable with closest packing of the ions:

$$C_{i,\max} = \frac{1}{N_A a_i^3} \tag{6.17}$$

in which a_i is the diameter of the ion and N_A is Avogadro's number. Wang et al. (2013) have successfully compared their modified PNP model against results from cyclic voltammetry for a range of electrolyte compositions.

6.3 Benchmarking of CrunchEDL versus PHREEQC

In this section, we present the results of some preliminary benchmarking of CrunchEDL against PHREEQC, each using the Donnan or Mean Electrostatic approach. We have devised a simple test problem in which the system is comprised of both EDL and bulk water porosity (or macroporosity). The boundary conditions at both ends of this 1D system are no-flux, but diffusive transport can occur within the domain and between the two types of porosity. Two cases are considered: (1) Case 1, in which the properties of Porous Media 1 and 2 are the same; and (2) Case 2, in which the charge in EDL 1 is decreased relative to EDL 2 by a factor of 100. The total system length is 10 cm with porous media 1 and 2 having the same length (5 cm). Concentration profiles are monitored as a function of time for the numerical cells from both side of the interface and for the cells being centered on the positions at 4.5 cm and 5.5 cm.

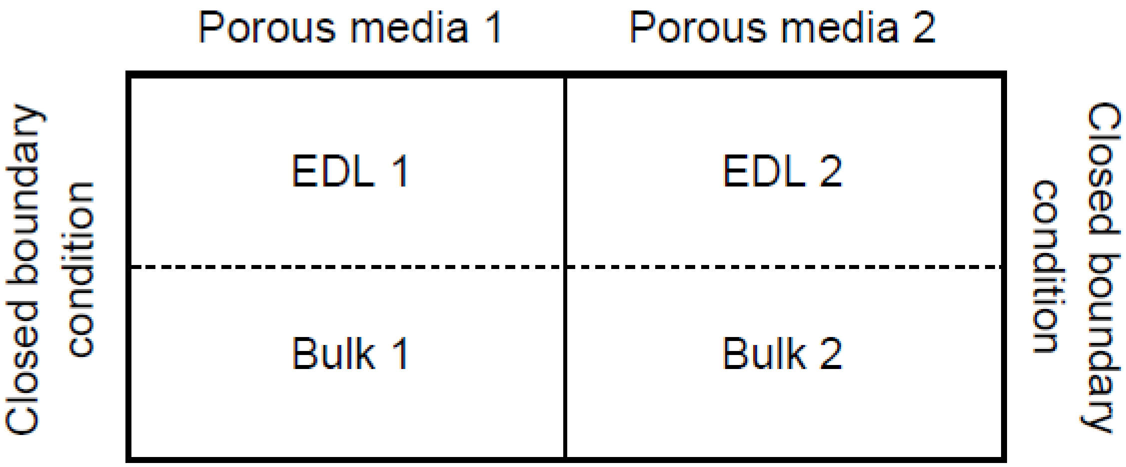

Figure 6.3. Schematic diagram of model system used for benchmark.

The volume (or porosity) of the EDL is the same as the volume of the bulk water. The initial solution composition in the bulk water is NaCl 0.01 mol kg-1 in porous media 1 and 2 (no salinity gradient, no activity coefficients gradient in bulk water), tracer A (Ac+ and Aa-) 10^{-6} mol kg^{-1} in bulk water of porous media 1 and 10^{-7} mol kg-1 in bulk water of porous media 2. The concentration gradient is opposite for tracer B (Bc+ and Ba-). Tracers Ac+ and Bc+ have the same chemical and transport parameters as Na+. Tracers Aa- and Ba- have the same chemical and transport parameters as Cl-.

6.3.1 Case 1: EDL charge the same in compartments 1 and 2

The EDL charge is -0.333 mol kg^{-1} in porous media 1 and 2. PHREEQC and CrunchEDL results are in perfect agreement (at least 3 digits) for the EDL mean composition (Table 6.1). Concentration gradients in the EDLs are in the same direction as in the bulk water. The diffusion coefficient was set to 10^{-9} m^2 s^{-1} for all species in bulk and in EDL water. PHREEQC and CrunchEDL results are consistent for a given grid refinement. A grid with 50 cells seems to be sufficient to ensure good calculation accuracy.

Table 6.1. Case 1. Comparison of mean concentrations in the EDL of the two porous media according to PHREEQC and CrunchEDL initial equilibrium calculations.

	Concentrations in EDL (mol kg^{-1}) Porous Media 1		Concentrations in EDL (mol kg^{-1}) Porous Media 2	
	PHREEQC	CRUNCH	PHREEQC	CRUNCH
Na^+	$3.336\ 10^{-1}$	$3.336\ 10^{-1}$	$3.336\ 10^{-1}$	$3.336\ 10^{-1}$
Cl^-	$2.998\ 10^{-4}$	$2.998\ 10^{-4}$	$2.998\ 10^{-4}$	$2.998\ 10^{-4}$
Ac^+	$3.336\ 10^{-5}$	$3.336\ 10^{-5}$	$3.336\ 10^{-6}$	$3.336\ 10^{-6}$
Ac^-	$2.998\ 10^{-8}$	$2.998\ 10^{-8}$	$2.998\ 10^{-9}$	$2.998\ 10^{-9}$
Bc^+	$3.336\ 10^{-6}$	$3.336\ 10^{-6}$	$3.336\ 10^{-5}$	$3.336\ 10^{-5}$
Bc^-	$2.998\ 10^{-9}$	$2.998\ 10^{-9}$	$2.998\ 10^{-8}$	$2.998\ 10^{-8}$

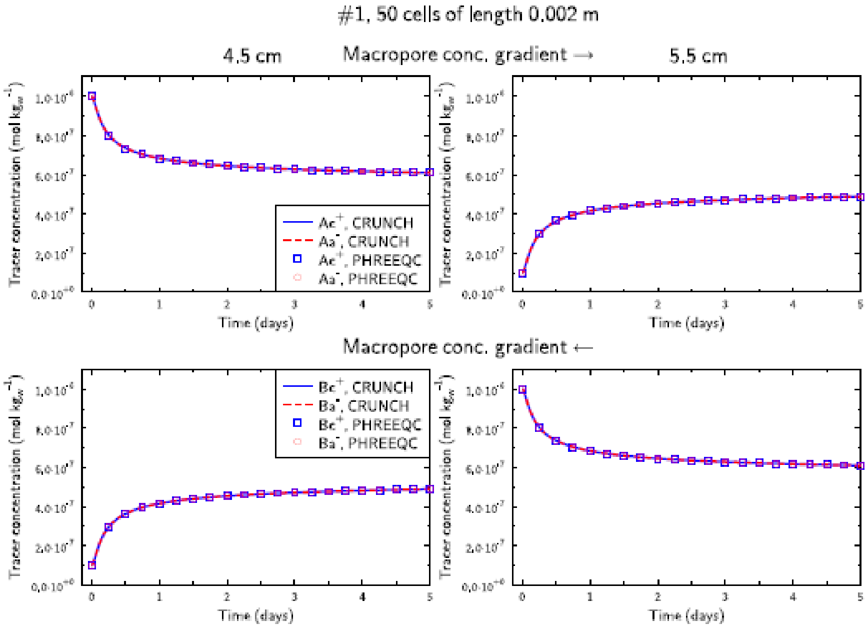

Figure 6.4. Comparison of bulk water (macropore) concentrations at 4.5 and 5.5 cm for Case 1 in which the two porous media have the same EDL charge of -0.333 equivalent moles/kgw.

6.3.2 Case 2: EDL charge different in porous media 1 and 2

This simulation is the same as the Case 1 simulation, except that the charge in the EDL of the porous media 1 is decreased by two orders of magnitude: -0.00333 mol kg-1. The agreement between CrunchEDL and PHREEQC for the initial calculation of the composition of the EDL is perfect again (Table 6.2). In this configuration, we can see now that the concentration gradients in the EDL are different from the concentration gradients in the bulk solution: Ac+ is less enriched is the EDL of porous media 1 due to the decrease of the EDL electrostatic potential, and its concentration is now lower in the EDL of porous media 1 than in the EDL of porous media 2 despite the lower bulk concentration in porous media 2 (Table 6.2). In other words, the Ac+ concentration gradient in the EDL is opposite to the chemical potential gradient. All other tracers EDL concentration gradients remain of the same sign as their related chemical potential gradients.

PHREEQC and CrunchEDL predict the same trends of concentrations evolutions: tracer Ac+ is depleted more rapidly from porous media 1 than previously in case 1 where there were uniform EDL properties along the system. Anionic and cationic tracers now behave differently. With a 50-cell grid refinement, CrunchEDL and PHREEC results exhibit significant differences in concentration prediction as a function of time. Those discrepancies can be lowered by increasing the number of cells in the CrunchEDL calculation grid, but those discrepancies cannot be eliminated even by refining the grid to 0.1 mm cells. A grid where only the cells at the interface are refined (40 cells of 0.1 mm) provides results as good as the 1000-cell grid.

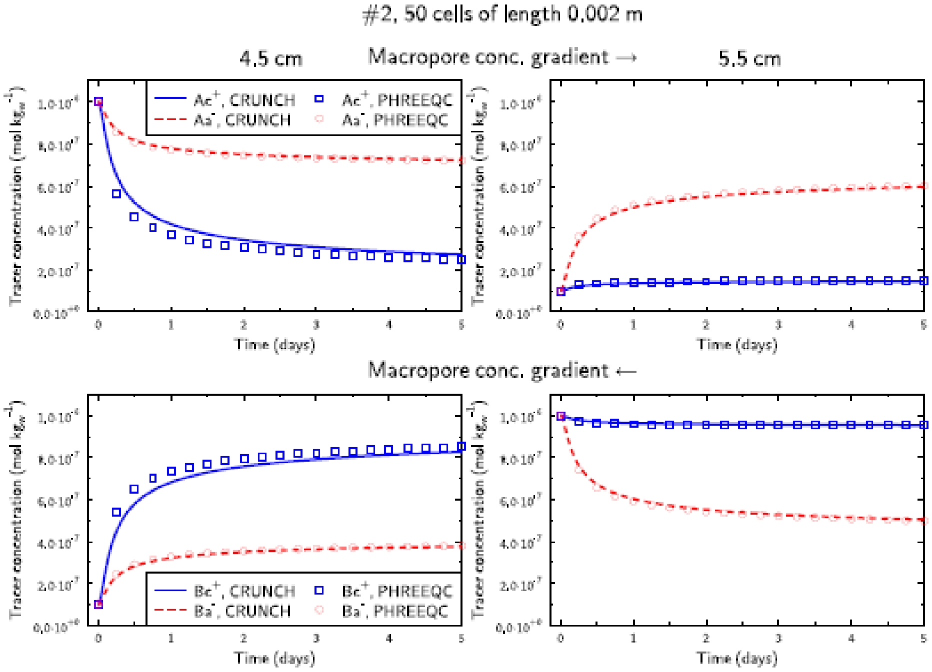

Figure 6.5. Comparison of bulk water (macropore) concentrations at 4.5 and 5.5 cm for Case 2 in which porous media 1 has an EDL charge 100 times lower than in porous media.

In addition, it can be shown that the mass balance is nearly exact in the case of PHREEQC, while CrunchEDL shows a mass imbalance in this case (unlike Case 1). The explanation is that CrunchEDL currently neglects the longitudinal gradient in the mean electrostatic potential, despite the fact that it contributes to the overall chemical potential. In the present implementation in CrunchEDL, the gradient in the electrostatic potential only accounts for the “diffusion potential” due to the diffusion of the charged ions at different rates, and not to any gradients in the electrostatic potential due to the clay charge concentration. In other words, all contributions to the electrostatic potential need to be included in the Nernst-Planck equation (Equation (6.14)). The fix for this will be completed soon.

Table 6.2. Case 2 in which the charge in porous media 1 is 100 times lower than in 2.

	Concentrations in EDL (mol kg^{-1}) Porous Media 1		Concentrations in EDL (mol kg^{-1}) Porous Media 2	
	PHREEQC	CRUNCH	PHREEQC	CRUNCH
Na^+	$1.180\ 10^{-2}$	$1.180\ 10^{-2}$	$3.336\ 10^{-1}$	$3.336\ 10^{-1}$
Cl^-	$8.471\ 10^{-3}$	$8.472\ 10^{-3}$	$2.998\ 10^{-4}$	$2.998\ 10^{-4}$
Ac^+	$1.180\ 10^{-6}$	$1.180\ 10^{-6}$	$3.336\ 10^{-6}$	$3.336\ 10^{-6}$
Ac^-	$8.471\ 10^{-7}$	$8.471\ 10^{-7}$	$2.998\ 10^{-9}$	$2.998\ 10^{-9}$
Bc^+	$1.180\ 10^{-7}$	$1.180\ 10^{-7}$	$3.336\ 10^{-5}$	$3.336\ 10^{-5}$
Bc^-	$8.471\ 10^{-8}$	$8.471\ 10^{-8}$	$2.998\ 10^{-8}$	$2.998\ 10^{-8}$
	Concentrations in bulk water (mol kg^{-1})		Concentrations in bulk water (mol kg^{-1})	
Ac^+	10^{-6}	10^{-6}	10^{-7}	10^{-7}
Ac^-	10^{-6}	10^{-6}	10^{-7}	10^{-7}
Bc^+	10^{-7}	10^{-7}	10^{-6}	10^{-6}
Bc^-	10^{-7}	10^{-7}	10^{-6}	10^{-6}

6.4 Application to the DR-A Diffusion Test at Mont Terri, Switzerland

To test the EDL transport model developed and described here, we have used it to simulate nonreactive and reactive transport processes in the DR-A experiment at Mont Terri in Switzerland. The Mont Terri site consists of Opalinus Clay, a primarily marly claystone with differing proportions of sand and carbonates, and is about 180 million years old. The stratigraphic section in which the Mont Terri site is located is shown in Figure 6.6. The Opalinus Clay is characterized by very low permeability, which makes diffusion the dominant mode of solute transport (in this respect, similar to compacted bentonite under normal conditions).

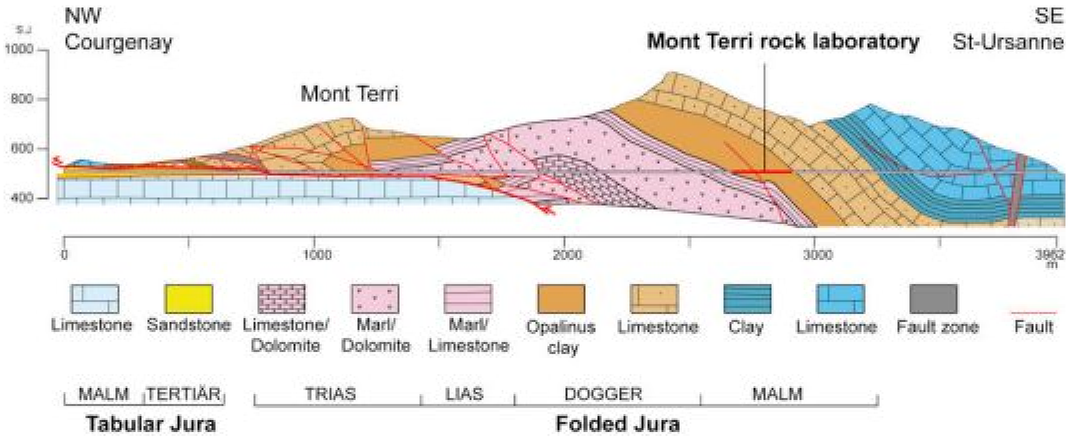

Figure 6.6. Stratigraphic section of the Jura Mountains in which the Mont Terri rock laboratory is located.

The DR-A test has consisted of a single borehole drilled in the Opalinus Clay that contains a constant ionic strength cocktail and anions, cations, and nonreactive tracers like tritium (HTO). Figure 6.7 shows the location of the DR-A niche in map view. Figure 6.8 shows the experimental setup used for the earlier DI-A test at Mont Terri, similar in setup to what has been used for the DR-A test. A volume of cocktail in excess of the actual cylindrical volume of the borehole is used as reservoir. This is treated in CrunchEDL by defining a capacity factor, α (= 2.175), that represents the additional volume needed to accommodate the extra solution volume (11.2 L) available to the actual borehole volume (Figure 6.8). In the first stage through Day 189, the borehole cocktail is a 0.384 M ionic strength solution dominated by sodium (Table 6.4). At Day 189, a higher ionic strength solution (1.135M) was circulated in the borehole apparently without diluting the tracers (HTO, iodine, and bromine) in the cocktail. The higher ionic strength was made up of both Na^+ (0.50M) and K^+ (0.56M) and Cl^- (1.13M) and was allowed to diffuse out of the borehole through Day 412.

6.4.1 CrunchEDL Simulation of DR-A Test

6.4.1.1 DR-A Simulation Parameters

In the simulations, a total porosity of 0.15 was assumed for the Opalinus Clay. The total porosity was treated as fixed, with partitioning between the "bulk" and "EDL" porosities governed by the Debye length (determined by the ionic strength, and thus variable over the course of the 412 day experiment). The additional volume needed to accommodate the extra solution volume (11.2L) available to the actual borehole volume (Table 6.3) was treated in CrunchEDL by defining a capacity factor, α (= 2.175).

For the simulation, a preliminary estimate of the illite specific surface area (200 m^2/g) and volume fraction (0.25) was made for the Opalinus Clay, which is the material expected to provide most of the retardation. A fixed mineral charge of 200 μequivalents/g illite was assumed, all of which is compensated by the electrical double layer (i.e., no Stern Layer sorption was allowed). Cylindrical coordinates were used in the simulations, with the assumption that the system was axisymmetric—thus, the system is modeled in a 1D plane.

A high value for the diffusion coefficient of solutes in the filter has been used to avoid a limitation on the rate of loss from the borehole due to this material. A diffusion coefficient of 2.7×10^{-10} m^2/s was initially assumed for all of the species in the Opalinus Clay, with the exception of the anions, for which a value of 1.25×10^{-10} m^2/s was used. As an initial test, the same values for the diffusion coefficients were used in the bulk and EDL porosity, although this assumption will be relaxed in later simulations so as to optimize the fit to the ionic strength effect.

Table 6.3. Physical parameters for DR-A test.

Length of injection interval	104 cm
Length of filter screen	67 cm
Volume of circulation system	11.2 L
Borehole diameter	76 mm
Filter, outer diameter	70 mm
Filter, inner diameter	62 mm
Filter, porosity	45%
Gap between filter and borehole wall	3 mm
Central tube, outer diameter	61 mm
Dip of bedding	32.5º
Porosity of Opalinus Clay	15%

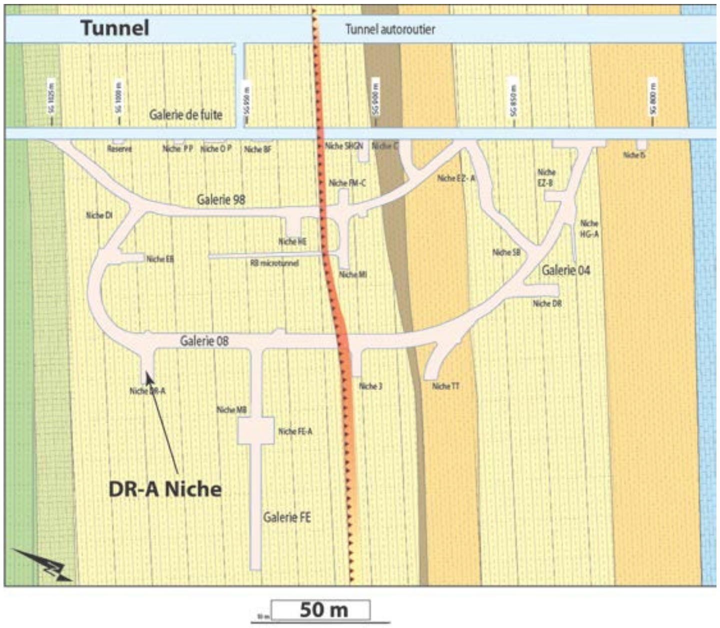

Figure 6.7. Plan view of the Mont Terri site showing location of DR-A niche.

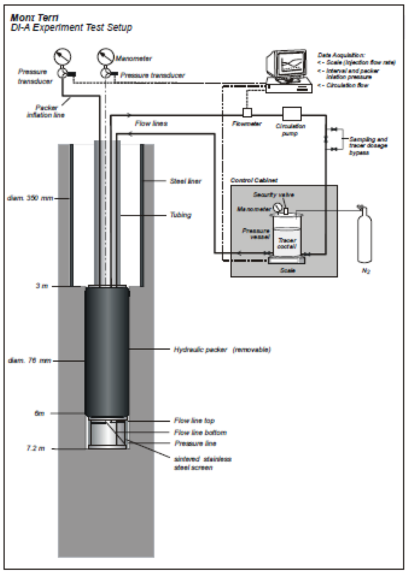

Figure 6.8. Schematic of the experimental setup from the DI-A test, similar in concept to the DR-A test.

Table 6.4. Geochemistry of borehole solution, with higher ionic strength used 189-413 days.

Species (Total)	0-189 Days	189-413 Days
	(M)	(M)
Ionic Strength	0.384	1.135
pH	4.16	7.60
Ca^{2+}	0.0188	0.0230
Mg^{2+}	0.0180	0.0147
Na^{+}	0.259	0.500
K^{+}	0.0016	0.560
Cl^{-}	0.300	1.113
SO_4^{2-}	0.0137	0.00024
HCO_3^{-}	0.00328	0.00050
Sr^{2+}	0.00051	0.00045
Cs^{+}	0.00027	0.0000062
I^{-}	0.0109	0.0109
Br^{-}	0.0109	0.0109
HTO	1.000	1.000

6.4.1.2 DR-A Simulation Results

Preliminary results from the simulations, including the increase in ionic strength in the borehole-reservoir system at Day 189, are shown in Figure 6.9. It should be noted that the anion (iodide and bromide) breakthrough data shows a slight increase in the rate of loss from the borehole starting about Day 189, the time when the ionic strength was increased. The simulation results show only a very small increase in the rate of loss from the borehole (solid line red for iodide), likely the result of the use of the same diffusion coefficients for the iodide and bromide in the EDL and bulk porosity. One expects that diffusion rates of anions in the EDL are smaller because of the greater tortuosity for the negatively ions versus the bulk fluid. Note that the data shows a stronger effect of the ionic strength, with the rate of loss from the hole increasing more dramatically for the anions at about Day 290. This effect is in keeping with a decrease in the thickness of the EDL, and thus an increase in bulk versus EDL porosity that follows from Equation (6.11). This is in contrast to some of the predictions based on swelling behavior alone that would have the effect of an increase in ionic strength reducing the bulk porosity. If the only effect of an increase in ionic strength were on the swelling behavior of the clays, then one would expect a less (not more) rapid loss of anions from the borehole. Here, the increase in diffusive loss of anions in particular from the borehole is attributed to the decrease in the EDL thickness, and thus to the increase in the proportion of bulk to EDL porosity. Properties of the Opalinus Clay considered in the simulation over time and predicted results are summarized in Table 6.5.

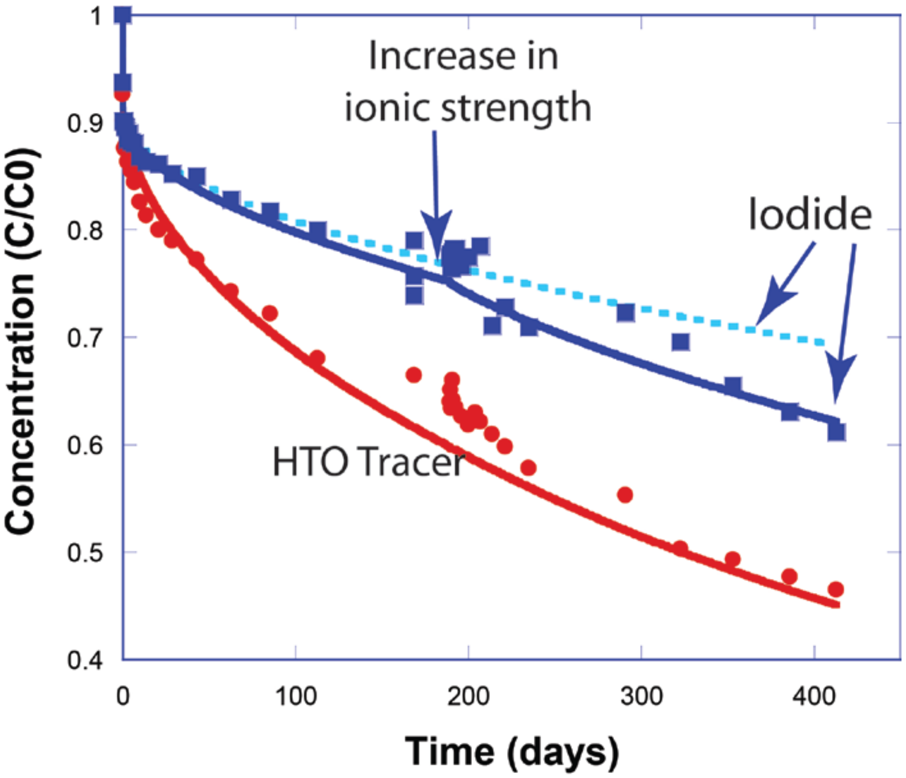

Figure 6.9. Data (symbols) versus simulation results (solid lines) for the DR-A test through Day 412. An increase in ionic strength (Na^+, K^+, and Cl^-) occurred at Day 189, which produces an increase in the rate of loss of the tracer anions iodide and bromide from the borehole. The pale blue dashed line represents the case for the anions where the EDL thickness and porosity is not affected by ionic strength.

Table 6.5. Opalinus Clay Properties and Simulation Results.

	0-189 Days	189-413 Days
Illite Specific Surface Area	200 m^2/g	200 m^2/g
Illite Volume Fraction	0.25	0.25
Fixed Charge of Illite	200 μeq/g	200 μeq/g
EDL Porosity (equilibrated w/ borehole)	0.076	0.049
Total charge in EDL (equivalents /m^3)	38.390	38.390
Na^+ Concentration in EDL (equilibrated)	0.253	0.661
K^+ Concentration in EDL (equilibrated)	0.0029	0.335
I^- Concentration in EDL (equilibrated)	0.0046	0.0049

7. Summary

(1) Development and validation of constitutive relationships for permeability, porosity and effective stress (Chapter 2)

The stress-dependent hydromechanical properties of low-permeability sedimentary rock are important for engineering. Accurate mathematical representations of stress-dependence of rock porosity and permeability are fundamental for studying the coupled hydromechanical processes of the underground rock, especially for understanding the evolution of permeability in EDZ for an argillite repository. In the work presented here, a new theoretical approach, a two-part Hooke's Model (TPHM), has been used. TPHM is based on the basic concept that the elastic deformation in a rock can be more accurately represented as a combination of two material types, a harder (or stiffer) material and a softer material. The small deformation approximation, used to linearize Hooke's law, is implemented exclusively for the harder (or stiffer) material type. Specific accomplishments are as follows:

- Existing stress-dependent formulations for porosity and permeability were reviewed, along with relationships between porosity and permeability.
- A series of rock stress-porosity and rock stress-permeability relationships based on the TPHM have been developed.
- Our preliminary evaluation of the model against published data produced encouraging results.

Recommended work for FY15 includes:

- Conduct testing of porosity and permeability as a function of effective stress to supplement the available published data.
- Use this data to perform additional validation analyses.
- Implement these constitutive relationships into our simulator TOUGHREACT-FLAC3D and conducted coupled processes simulation to evaluate the evolution of the hydromechanical properties in EDZ for an argillite repository.

(2) Discrete fracture network (DFN) approach for fractures in argillaceous rock (Chapter 3)

This study uses the RBSN approach to model geomechanical behavior including fracturing. The model provides a discrete representation of material elasticity and fracture development, and in that respect, it is considered to be suitable for the DFN approach to investigate fracturing processes. However, the original RBSN is limited to macroscopically modeling isotropic materials, or requires additional treatments in partitioning the domain (e.g., layering of individually isotropic materials) for introducing directivity of mechanical properties. Specific accomplishments are as follows:

- Linkage between TOUGH2 for simulating heat and mass transport and the RBSN method for simulating geomechanical responses, including the initiation and propagation of discrete fractures.
- Elastic spring coefficients and strength parameters have been systematically formulated for individual lattice elements, based on the principal bedding direction, which facilitate a straightforward representation of anisotropy.
- Uniaxial compression tests have been simulated for a transversely anisotropic material, the Opalinus Clay, to demonstrate the validity of the new modeling scheme.
- A simulation of fracture damage around the EDZ of the HG-A microtunnel has been conducted and has been found to qualitatively agree with the physical observations, in which nonuniform damage, due to the anisotropic mechanical characteristics, forms around the excavation wall.
- The capabilities of the TOUGH-RBSN simulator for strongly coupled hydro-mechanical processes have been shown through a simulation of hydraulic fracturing, which produces realistic hydromechanical behavior for the fracturing process.

Recommended work for FY15 includes:

- The original development of the RBSN model was mainly concerned with tensile failure. The model requires additional modifications to consider fracture surface forces that are important for compressive failure.
- Also, use of the Mohr-Coulomb fracture criterion involves brittle failure response. More realistic representation of failure response is needed for gradual degradation of strength parameters.
- Hydrological properties of discrete fractures will be estimated on the basis of the fracture geometry, so that quantitative simulations of flow and mass transport within discrete fracture networks can be conducted.
- Fracture nodes and the associated connections are defined for all the Voronoi cell boundaries from the beginning of simulations, which burdens the computational expense by increasing degrees of freedom to be calculated. The modeling scheme needs to be improved for dynamic introduction or event-based activation of the fracture components.
- A parallel version of TOUGH-RBSN is needed for computational efficiency to enable its use on larger field-scale 3-D problems.

(3) THM Modeling of Underground Heater Experiments (Chapter 4):

The UFDC is utilizing previous experience and existing models (TOUGH-FLAC and ROCMAS) that are extended to predict the long-term THM and THMC evolution of a multibarrier nuclear waste repository system involving backfilled emplacement tunnels in argillite host formations. Specific accomplishments are as follows:

- Completed implementation of constitutive models for the coupled geomechanical behavior of bentonite-based buffer material, including most recently the advanced dual-structure model.
- Verification and testing of the implemented geomechanical constitutive models for bentonite-based buffer material by modeling laboratory experiments and long-term behavior of a generic repository.
- Validation of TOUGH-FLAC and characterization of THM properties for two types of bentonite-based buffer materials through modeling of CIEMAT laboratory column experiments.
- Development of full-scale 3D TOUGH-FLAC models of the Horonobe EBS experiment and Mont Terri FE experiment and initial model predictions of temperature and saturation evolutions.
- Benchmarking associated with the Horonobe EBS experiment achieving good agreement with the results of other international modeling teams, providing code-to-code verification of TOUGH-FLAC.

Published one journal paper (Rutqvist et al., 2014) on THM modeling of nuclear waste disposal in argillite and submitted one journal paper on the use of the dual-structure model for modeling long-term behavior of a nuclear waste repository (Vilarrasa et al., 2014). (((Recommended work for FY15 includes:

- Full-scale 3D model predictions for the three *in situ* heater experiments; the Mont Terri HE-E experiment, the Horonobe EBS experiment, and the Mont Terri FE experiment, and compare with data and with the results of other international modeling teams in the DECOVALEX and Mont Terri projects
- Collaborate with the UPC (Barcelona) modeling team in application of the BBM and dual-structure models to the Mont Terri FE experiment.
- Validation of models against these field experiments as well as characterization of parameters for BBM and dual-structure constitutive models from laboratory data that are now becoming available in the various projects.

- Review of THM properties of bentonite-based buffer and backfill materials in these field experiments (and in nuclear waste isolation in general) and identify critical parameters and experimental data needs.
- Participate and present simulation results at DECOVALEX and Mont Terri workshops.

(4) Investigation of the maximum allowable temperature and detailed impacts of a high temperature on repository performance (Chapter 5):

Chemical alteration and the subsequent changes in mechanical properties are among the determining factors for establishing the thermal limit of a repository with a clay-based EBS. A thermal limit of about 100°C is imposed unanimously in all disposal concepts throughout the world—without rigorous studies to back up the choice. More rigorous studies are needed to answer the question whether an argillite repository with bentonite EBS can sustain higher than 100°C.We use coupled THMC modeling to evaluate the chemical alteration and associated mechanical changes in a generic repository and consider the interaction between EBS bentonite and the NS clay formation. Specific accomplishments are as follows:

- Coupled THMC models were developed, with properties of clay formation from Opalinus Clay, and two types of EBS bentonite—Kunigel-VI and FEBEX bentonites—are considered to understand the difference in chemical and mechanical changes in these two bentonites.
- Two main scenarios were developed for comparison: a “high T” case in which the temperature near the waste package can reach about 200°C and a “low T” scenario in which the temperature peaks at about 100°C.
- Sensitivity analyses to key parameters were conducted

For the laboratory investigations, it is highly likely that the observed heat-induced changes in the strength and failure behavior of the compacted bentonite and the Opalinus Clay from Mont Terri were caused by decreases of water content from the clay samples during heating. The effect, however, may also be superimposed by other effects such as redistribution (dissolution and re-precipitation) of quartz within the pore space and phase transformations of clay minerals. A summary of the accomplishments so far is as follows:

- Sample preparation procedures have been established and necessary tools developed.
- An efficient triaxial compression testing setup has been developed. The tests were conducted on compacted bentonite clay with different fluid chemistry and on Opalinus Clay cores from Mont Terri. However, the loss of fluid during heating resulted in ambiguities in the experimental results.
- A miniature indentation test setup has been developed. A sample hardness measurement procedure has been established and demonstrated

Recommended work for FY15 includes:

- Conducting THMC simulations using more comprehensive links between chemistry and mechanics provided by a dual-structure model. In current models, the mechanical-chemical coupling in bentonite is calculated via an extended linear elastic swelling model, a more rigorous approach to link chemistry to mechanics is needed for more accurate calculations.
- Developing constitutive relationship to link the chemistry with mechanics for clay formation and considering it in the THMC models. The current mechanical model for the NS clay formation is not tied with chemical variables, i.e., mechanical-chemical coupling is only considered in the EBS bentonite.

- Considering chemical changes in the canister in the THMC model. In the current model, the canister serves only as a heat source; chemical changes on the surface of the canister are neglected for simplification.
- Integrating THMC modeling work with other laboratory studies (e.g. Cheshire et al. 2014) in UFDC. The finding from laboratory studies can be used to constrain the reaction paths and rate of key chemical reactions.
- Finding a solution for the slow leakage of water vapor from the pressure vessels used for heating of clay samples. Currently, use of soft metal foils (e.g., lead or tin [Sn] foils for unsaturated samples. Silver or gold if the sample is saturated) is considered.
- Preparation of the clay samples and repeated experiments.
- Chemical/mineralogical characterization of heat-treated samples. Interpretation of the results with the changes in the mechanical/hydrological properties.
- Improvement of mini-indentation test setup. Currently, the reduced Young modulus of tested samples cannot be determined accurately because of large flexures in the loading column (particularly in the loadcell section). An additional displacement gauge for determining the system deformation needs to be installed.
- Continued development of a gas permeability measurement setup for low-permeability clay samples. Current samples exhibit unusually high permeability, which may be attributed to microcracks in the heated samples.
- Illitization mechanisms in the current model need to be expanded to include solid state transformation by substitution of intracrystal cations (e.g., Cuadros and Linares 1996)
- The current mechanical model for the natural system clay formation needs to be coupled with chemical variables, i.e., mechanical-chemical coupling, as done for EBS bentonite.
- Mechanical-chemical coupling in bentonite is calculated via an extended linear elastic swelling model, therefore, a more rigorous approach to link chemistry to mechanics is needed for more accurate calculation.
- Chemical changes on the surface of the canister need to be considered, specifically the release of Fe+2, which might enhance the dissolution of smectite by forming chlorite.
- Finding a solution for the slow leakage of water vapor from the pressure vessels used for heating of clay samples. Currently, use of soft metal foils (e.g., lead or tin [Sn] foils for unsaturated samples; silver or gold if the sample is saturated.) is considered.

For the laboratory investigations, it is highly likely that the observed heat-induced changes in the strength and failure behavior of the compacted bentonite and the Opalinus Clay from Mont Terri were caused by decreases of water content from the clay samples during heating. The effect, however, may also be superimposed by other effects such as redistribution (dissolution and re-precipitation) of quartz within the pore space and phase transformations of clay minerals. A summary of the accomplishments so far is as follows:

(5) Investigation of the maximum allowable temperature and detailed impacts of a high temperature on repository performance (Chapter 6):

Modeling techniques based on electric double-layer theory have been developed and tested against experimental results from the DR-A test at Mont Terri. A summary of the accomplishments so far is as follows:

- Two complementary approaches to modeling ion diffusion through clays have been developed. The first makes use of a Donnan Equilibrium or Mean Electrostatic Approach, in which a mean electrostatic potential is defined for the electrical double layer to balance the fixed negative charge of the clays. The second approach involves the use of the Nernst-Planck and Poisson-Boltzmann equation (termed the PNP method).

- The Donnan Equilibrium or Mean Electrostatic Approach was tested in benchmark studies using the software codes CrunchEDL versus PHREEQC. Differences between the calculations in one of the benchmark studies were found to be a result of the neglect of the longitudinal gradient in the mean electrostatic potential in CrunchEDL.
- Comparisons between CrunchEDL calculations and DR-A test results provide evidence that the electric double layer influences anion diffusion rates in the Opalinus Clay.

Recommended work for FY15 includes:

- Modify CrunchEDL to account for the longitudinal gradient in the mean electrostatic potential.
- Conduct further analyses of the DR-A test results using the modeling techniques developed here.

Acknowledgment

Funding for this work was provided by the Used Fuel Disposition Campaign, Office of Nuclear Energy, of the U.S. Department of Energy under Contract Number DE-AC02-05CH11231 with Lawrence Berkeley National Laboratory.

References

Abercrombie, H. J., I. E. Hutcheon, J. D. Bloch and P. de Caritat 1994. Silica activity and the smectite-illite reaction. Geology 22(6): 539-542.

Alonso EE, Gens A, Josa A (1990) A constitutive model for partially saturated soils. Geotechnique. 40: 405-430.

Appelo, C.A.J. and Wersin, P., 2007. Multicomponent diffusion modeling in clay systems with application to the diffusion of tritium, iodide, and sodium in Opalinus Clay. Environmental Science and Technology 41, 5002-5007.

Appelo, C.A.J., Vinsot, A., Mettler, S. and Wechner, S., 2008. Obtaining the porewater composition of a clay rock by modeling the in- and out-diffusion of anions and cations from an in-situ experiment. Journal of Contaminant Hydrology 101, 67-76.

Arcos, D.; Fidel, G.; Domenech, C.; Fernández, A.M.; Villar, M.V.; Muurinen, A.; Carlsson, T.; Sellin, P.; Hernan, P. 2008. “Long-Term Geochemical Evolution of the Near Field Repository: Insights from Reactive Transport Modelling and Experimental Evidences,” Journal of Contaminant Hydrology, 102, 196-209.

Armand, G., A. Noiret, J. Zghondi, and D.M. Seyedi. (2013). Short- and long-term behaviors of drifts in the Callovo-Oxfordian claystone at the Meuse/Haute-Marne Underground Research Laboratory. Journal of Rock Mechanics and Geotechnical Engineering 5, no. 3: 221-230.

Asahina, D., Landis, E.N. and Bolander, J.E. (2011). Modeling of phase interfaces during pre-critical crack growth in concrete. Cement & Concrete Composites, 33, 966-977.

Athy, L. F. (1930). "Density, porosity, and compaction of sedimentary rocks." AAPG Bulletin 14(1): 1-24.

Baechler, S., J.M. Lavanchy, G. Armand, M. Cruchaudet. (2011). Characterisation of the hydraulic properties within the EDZ around drifts at level -490 m of the Meuse/Haute-Marne URL: a methodology for consistent interpretation of hydraulic tests. Physics and Chemistry of the Earth, no. 17: 1922-1931

Barnichon, J.D. and Volckaert, G. (2003). Observations and Predictions of Hydromechanical Coupling Effects in the Boom Clay, Mol Underground Research Laboratory, Belgium. Hydrogeology Journal, 11(1), 193-202.

Bear, J. (1972). "Dynamics of Fluids in Porous Media," Elsevier, New York, New York.

Berton S. and Bolander, J.E. (2006). Crack band model of fracture in irregular lattices. Computer Methods in Applied Mechanics and Engineering, 195, 7171-7181.

Biot, M.A. and Willis, D.G. (1957). The elastic coefficients of the theory of consolidation. Journal of Applied Mechanics, 24, 594-601.

Birgersson M., Karnland, O., 2009. Ion equilibrium between montmorillonite interlayer space and an external solution - Consequences for diffusional transport. Geochimica et Cosmochimica Acta 73, 1908-1923.

Blümling, P., Bernier, F., Lebon, P. and Martin, C.D. (2007). The excavation damaged zone in clay formations time-dependent behaviour and influence on performance assessment. Physics and Chemistry of the Earth, 32, 588-599.

Bock, H. (2001). RA Experiment Rock Mechanics Analyses and Synthesis: Data Report on Rock Mechanics, Mont Terri Project, Technical Report 2000-02.

Bolander, J.E. and Saito, S. (1998). Fracture analyses using spring networks with random geometry. Eng Fract Mech, 61, 569-591.

Börgesson, L., Chijimatsu, M., Nguyen, T.S., Rutqvist, J., Jing L. (2001) Thermo-hydro-mechanical characterization of a bentonite-based buffer material by laboratory tests and numerical back analyses. Int. J. Rock Mech. & Min. Sci. 38, 105-127.

Bossart P. (2011) Characteristics of the Opalinus Clay at Mont Terri, http://www.mont-terri.ch/internet/mont-terri/en/home/geology/key_characteristics.html

Bossart, P. (2012). Characteristics of the Opalinus Clay at Mont Terri, http://www.montterri.ch/internet/montterri/en/home/geology/key_characteristics.parsys.49924.DownloadFile.tmp/characteristicsofopa.pdf

Bossart, P., Meier, P.M., Moeri, A., Trick, T. and Mayor, J.-C. (2004). Structural and hydrogeological characterisation of the excavation-disturbed zone in the Opalinus Clay (Mont Terri Project, Switzerland). Applied Clay Science, 26, 429- 448.

Brighenti, G. (1989). Effect of Confining Pressure On Gas Permeability of Tight Sandstones. ISRM International Symposium, International Society for Rock Mechanics.

Bucher, F., and Müller-Vonmoos, M. (1989) Bentonite as a containment barrier for the disposal of highly radioactive waste. Applied Clay Science, 4(2): 157–177.

Byrnes, A. (1996). "Reservoir characteristics of low-permeability sandstones in the Rocky Mountains."

Byrnes, A. P. (1997). "Reservoir characteristics of low-permeability sandstones in the Rocky Mountains." The Mountain Geologist.

Byrnes, A. P. and J. W. Castle (2000). Comparison of core petrophysical properties between low-permeability sandstone reservoirs: Eastern US Medina group and Western US Mesaverde group and Frontier formation. SPE Rocky Mountain Regional/Low-Permeability Reservoirs Symposium and Exhibition, Society of Petroleum Engineers.

Caporuscio, F. A. (2013) EBS Report - LANL Experimental update of buffer/backfill at elevated P,T. LA-UR-13-27015 2013-09-09.

Castellanos, E., M. V. Villar, E. Romero, A. Lloret and A. Gens 2008. Chemical impact on the hydro-mechanical behaviour of high-density FEBEX bentonite. Physics and Chemistry of the Earth, Parts A/B/C 33, Supplement 1(0): S516-S526.

Chen, Y., C. Zhou and L. Jing 2009. Modeling coupled THM processes of geological porous media with multiphase flow: Theory and validation against laboratory and field scale experiments. Computers and Geotechnics 36(8): 1308-1329.

Cheshire, M., F. Caporuscio, M. Rearick, C. Jove-colon and M. K. McCarney 2014. Bentonite evolution at elevated pressures and temperatures: an experimental study for generic nuclear repository designs. American Mineralogist: in press.

Chijimatsu M, Nguyen TS, Jing L, de Jonge J, Kohlmeier M, Millard A, Rejeb A, Rutqvist J, Souley M, Sugita Y (2005) Numerical study of the THM effects on the near-field safety of a hypothetical nuclear waste repository – BMT1 of the DECOVALEX III project. Part 1: Conceptualization and characterization of the problems and summary of results. Int. J Rock Mech & Min Sci 42:720–730.

Cosgrove, J.W. (2001). Hydraulic Fracturing during the Formation and Deformation of a Basin: A Factor in the Dewatering of Low-Permeability Sediments. AAPG Bulletin, 85(4), 737-748.

Cuadros, J. 2006. Modeling of smectite illitization in burial diagenesis environments. Geochimica et Cosmochimica Acta 70(16): 4181-4195.

Cuadros, J. and J. Linares 1996. Experimental kinetic study of the smectite-to-illite transformation. Geochimica et Cosmochimica Acta 60(3): 439-453.

Cui, X., et al. (2007). "Adsorption-induced coal swelling and stress: Implications for methane production and acid gas sequestration into coal seams." Journal of Geophysical Research: Solid Earth 112(B10): B10202.

David, C. and M. Darot (1989). Permeability And Conductivity of Sandstones. ISRM International Symposium, International Society for Rock Mechanics.

David, C., et al. (1994). "Laboratory measurement of compaction-induced permeability change in porous rocks: Implications for the generation and maintenance of pore pressure excess in the crust." Pure and Applied Geophysics 143(1-3): 425-456.

David, C., et al. (2001). "Mechanical compaction, microstructures and permeability evolution in sandstones." Physics and Chemistry of the Earth, Part A: Solid Earth and Geodesy 26(1): 45-51.

Davies, J. and D. Davies (2001). "Stress-dependent permeability: characterization and modeling." SPE Journal 6(02): 224-235.

Dewhurst, D. N., et al. (1998). "Compaction-driven evolution of porosity and permeability in natural mudstones: An experimental study." Journal of Geophysical Research-Solid Earth 103(B1): 651-661.

Dong, J.-J., et al. (2010). "Stress-dependence of the permeability and porosity of sandstone and shale from TCDP Hole-A." International Journal of Rock Mechanics and Mining Sciences 47(7): 1141-1157.

Eberl, D. 1978. Reaction series for dioctahedral smectites. Clays and Clay Minerals 26(5): 327-340.

Elliott, W. C. and G. Matisoff 1996. Evaluation of kinetic models for the smectite to illite transformation. Clays and Clay Minerals 44(1): 77-87.

ENRESA 2000. Full-scale engineered barriers experiment for a deep geological repository in crystalline host rock FEBEX Project, European Commission: 403.

Evans, J. P., et al. (1997). "Permeability of fault-related rocks, and implications for hydraulic structure of fault zones." Journal of Structural Geology 19(11): 1393-1404.

Ewing J. and Senger R. (2011) Evolution of Temperature, Pressure, and Saturation in the Bentonite Buffer: Scoping Calculations in Support of the Design of the Full-Scale Emplacement Experiment at the Mont Terri URL. NAGRA NAB 10-38, September 2011.

Feng Xia-Ting, Pan Peng-zhi, Zhou Hui (2006) Simulation of rock microfracturing process under uniaxial compression using elasto-plastic cellular automata. Int J Rock Mech & Min Sci 43: 1091–1108.

Fernández, A. M., B. Baeyens, M. Bradbury and P. Rivas (2004). Analysis of the porewater chemical composition of a Spanish compacted bentonite used in an engineered barrier. Physics and Chemistry of the Earth, Parts A/B/C 29(1): 105-118.

Fernández, A. M., Turrero, M. J., Sánchez, D. M., Yllera, A., Melón, A. M., Sánchez, M., Peña, J., Garralón, A., Rivas, P., Bossart, P. and Hernán, P. (2007) On site measurements of the redox and carbonate system parameters in the low-permeability Opalinus Clay formation at the Mont Terri Rock Laboratory. Physics and Chemistry of the Earth, Parts A/B/C 32(1-7): 181-195.

Fernández, A., Cuevas, J., Rivas, P., 2001. Pore water chemistry of the FEBEX bentonite. Mat. Res. Soc. Symp. Proc. 663, 573–588.

Fouche, O., Wright, H., Cleach, J.L. and Pellenard, P. (2004). Fabric Control on Strain and Rupture of Heterogeneous Shale Samples by Using a Non-Conventional Mechanical Test. Applied Clay Science, 26, 367-387.

Gangi, A. F. (1978). Variation of whole and fractured porous rock permeability with confining pressure. International Journal of Rock Mechanics and Mining Sciences & Geomechanics Abstracts, Elsevier.

Garitte B. and Gens A. (2012) TH and THM Scoping computations for the definition of an optimal instrumentation layout in the Full-scale Emplacement (FE) experiment NAGRA NIB 10-34, March 2012.

Garitte, B. (2012) HE-E experiment - In situ Heater Test, Presentation given at 1th DECOVALEX 2015 workshop, April 2012, Berkeley.

Gens A, Sánchez, M Sheng, D (2006) On constitutive modelling of unsaturated soils. Acta Geotechnica. 1, 137-147

Gens, A, Alonso, E. A framework for the behaviour of unsaturated expansive clays. Can. Geotech. J. 29, 1013–1032 (1992).

Gens, A., Sánchez, M., Guimaraes, L.D.N., Alonso, E.E., Lloret, A., Olivella, S., Villar, M.V., Huertas, F. (2009) A full-scale in situ heating test for high-level nuclear waste disposal: observations, analysis and interpretation. Geotechnique 59, 377–399.

Ghabezloo, S., et al. (2009a). "Effective stress law for the permeability of a limestone." International Journal of Rock Mechanics and Mining Sciences 46(2): 297-306.

Ghabezloo, S., et al. (2009b). "Evaluation of a permeability–porosity relationship in a low-permeability creeping material using a single transient test." International Journal of Rock Mechanics and Mining Sciences 46(4): 761-768.

Gonçalvès J., Rousseau-Gueutin P., Revil A. Introducing interacting diffuse layers in TLM calculations: A reappraisal of the influence of the pore size on the swelling pressure and the osmotic efficiency of compacted bentonites. J. Colloid Interface Sci., 316, 92-99 (2007).

Grochowski, P. and J. Trylska, 2007 Continuum molecular electrostatics, salt effects, and counterion binding—A review of the Poisson-Boltzmann theory and its modifications. Biopolymers 89: 93-113.

Hama, K., Kunimaru, T., Metcalfe, R., Martin, A.J. 2007. The Hydrogeochemistry of Argillaceous Rock Formations at the Horonobe URL Site, Japan, Physics and Chemistry of the Earth, 32, 170–180.

Herbert, H.-J., J. Kasbohm, H. Sprenger, A. M. Fernández and C. Reichelt 2008. Swelling pressures of MX-80 bentonite in solutions of different ionic strength. Physics and Chemistry of the Earth, Parts A/B/C 33, Supplement 1(0): S327-S342.

Hicks, T.W., White, M.J. and Hooker, P.J. (2009) Role of Bentonite in Determination of Thermal Limits on Geological Disposal Facility Design, Report 0883-1, Version 2, Falson Sciences Ltd., Rutland, UK, Sept. 2009.

Hoholick, J. D., et al. (1984). "Regional variations of porosity and cement: St. Peter and Mount Simon sandstones in Illinois Basin." AAPG Bulletin 68(6): 753-764.

Holditch, S. A. (2006). "Tight gas sands." Journal of Petroleum Technology 58(6): 86-93.

Horseman S.T. and McEwen, T. J. (1996) Thermal constrains on disposal of heat-emitting waste in argillaceous rocks, Engineering Geology 41, 5-16.

Houseworth J., Rutqvist J., Asahina D., Chen F., Vilarrasa V., Liu H.H., Birkholzer J. Report on International Collaboration Involving the FE Heater and HG-A Tests at Mont Terri. Prepared for U.S. Department of Energy, Used Fuel Disposition Campaign, FCRD-UFD-2014-000002, Lawrence Berkeley National Laboratory (2013).

Itasca, 2009. FLAC3D, Fast Lagrangian Analysis of Continua in 3 Dimensions, Version 4.0, Minneapolis, Minnesota, Itasca Consulting Group.

Itasca, FLAC3D V5.0, Fast Lagrangian Analysis of Continua in 3 Dimensions, User’s Guide. Itasca Consulting Group, Minneapolis, Minnesota (2011).

Jaeger, J.C. (1960). Shear failure of anisotropic rocks. Geologic Magazine, 97, 65-72.

Jasinge, D., et al. (2011). "Effects of effective stress changes on permeability of Latrobe Valley brown coal." Fuel 90(3): 1292-1300.

JNC, Japan Nuclear Cycle Development Institute. (2000) H12: project to establish the scientific and technical basis for HLW disposal in Japan: supporting report 2 (respiratory design and engineering Technology). Japan Nuclear Cycle Development Institute, Tokyo.

Jones, F. O. and W. W. Owens (1980). "A Laboratory Study of Low-Permeability Gas Sands." Journal of Petroleum Technology 32(9): 1631-1640.

Jones, S. C. (2013). "Two-Point Determinations of Permeability and PV vs. Net Confining Stress." SPE Formation Evaluation 3(01): 235-241.

Karnland, O., Olsson, S. and Nilsson, U. (2006) Mineralogy and sealing properties of various bentonites and smectite-rich clay materials, SKB Technical Report TR-06-30.

Kawai, T. (1978). New Discrete Models and their Application to Seismic Response Analysis of Structures. Nuclear Engineering and Design, 48, 207-229.

Kilmer, N. H., et al. (1987). "Pressure sensitivity of low permeability sandstones." Journal of Petroleum Science and Engineering 1(1): 65-81.

Kirsch, G. (1898). Die Theorie der Elastizität und die Bedürfnisse der Festigkeitslehre. Zeitschrift des Vereines deutscher Ingenieure, 42, 797-807.

Klinkenberg, L. (1941). "The permeability of porous media to liquids and gases." Drilling and production practice.

Kolditz O, Bauer S, Beinhorn M, de Jonge J, Kalbacher T, McDermott C, Wang W, Xie M, Kaiser R, Kohlmeier M (2003) ROCKFLOW - Theory and Users Manual, Release 3.9, Groundwater Group, Center for Applied Geosciences, University of Tübingen, and Institute of Fluid Mechanics, University of Hannover.

Komine, H., and Ogata, N. (1996) Prediction for swelling characteristics of compacted bentonite. Canadian Geotechnical Journal, 33: 11–22.

Konecny, P. and A. Kozusnikova (2011). "Influence of stress on the permeability of coal and sedimentary rocks of the Upper Silesian basin." International Journal of Rock Mechanics and Mining Sciences 48(2): 347-352.

Kristensson O, Åkesson M (2008) Mechanical modeling of MX-80 – Quick tools for BBM parameter analysis. Phys Chem Earth, Parts A/B/C. 33, Supplement 1: S508-S515.

Kwaśniewski, M.A. and Mogi, K. (2000). Faulting in an anisotropic, schistose rock under general triaxial compression. 4th North American Rock Mechanics Symposium, Seattle, WA.

Kwon, O., et al. (2001). "Permeability of Wilcox shale and its effective pressure law." Journal of Geophysical Research-Solid Earth 106(B9): 19339-19353.

Lanyon, G.W., Marschall, P., Trick, T., de La Vaissière, R., Shao, H. and Leung, H. (2009). Hydromechanical Evolution and Self-Sealing of Damage Zones around a Microtunnel in a Claystone Formation of the Swiss Jura Mountains. American Rock Mechanics Association, ARMA 09-333.

Laredj, N., Missoum, H. and Bendani, K. (2010) Modeling the effect of osmotic potential changes on deformation behavior of swelling clays. Journal of Porous Media 13(8): 743-748.

Lauber, M., B. Baeyens and Bradbury, M. H. (2000) Physico-Chemical Characterisation and Sorption Measurements of Cs, Sr, Ni, Eu, Th, Sn and Se on Opalinus Clay from Mont Terri. PSI Bericht Nr. 00-10 December 2000 ISSN 1019-0643.

Lee, J.W., R.H. Nilson, J.A. Templeton, S.K. Griffiths, A. Kung, B.M. Wong, 2012, Comparison of molecular dynamics with classical density functional and Poisson-Boltzmann theories of the electrical double layer in nanochannels. Journal of Chemical Theory and Computation 8: 2012-2012.

Lei, Q., et al. (2008). Analysis of stress sensitivity and its influence on oil production from tight reservoirs, Lawrence Berkeley National Laboratory.

Leroy P., Revil, A., Altmann, S., Tournassat, C., 2007. Modeling the composition of a pore water in a clay-rock geological formation (Callovo-Oxfordian, France). Geochimica et Cosmochimica Acta 71, 1087-1097.

Leroy, P., Revil, A., 2004. A triple-layer model of the surface electrochemical properties of clay minerals. Journal of Colloid and Interface Science 270, 371-380.

Li, L., et al. (2014). "The use of two-part Hooke’s Model (TPHM) to model the mine-by test at Mont Terri Site, Switzerland." Computers and Geotechnics 58(0): 28-46.

Li, X., et al. (2008). Multi-stage fracturing stimulations improve well performance in tight oil reservoirs of the Changqing Oilfield. International Petroleum Technology Conference.

Liu, H. H., et al. (2011). "Constitutive Relationships for Elastic Deformation of Clay Rock: Data Analysis." Rock mechanics and rock engineering 44(4): 463-468.

Liu, H.-H., et al. (2009). "On the relationship between stress and elastic strain for porous and fractured rock." International Journal of Rock Mechanics and Mining Sciences 46(2): 289-296.

Liu, H.-H., et al. (2013a). "Normal-stress dependence of fracture hydraulic properties including two-phase flow properties." Hydrogeology Journal 21(2): 371-382.

Liu, H.H., Houseworth, J., Rutqvist, J., Zheng, L., Asahina, D., Li, L., Vilarrasa, V., Chen, F., Nakagawa, S., Finsterle, S., Doughty, C., Kneafsey, T. and Birkholzer, J. (2013b). Report on THMC modeling of the near field evolution of a generic clay repository: Model validation and demonstration. (FCRD-UFD-2013-000244), U.S. DOE Used Fuel Disposition Campaign.

Louis, L., et al. (2005). "Microstructural control on the anisotropy of elastic and transport properties in undeformed sandstones." International Journal of Rock Mechanics and Mining Sciences 42(7–8): 911-923.

Marschall, P., Distinguin, M., Shao, H., Bossart, P., Enachescu, C. and Trick, T. (2006). Creation and Evolution of Damage Zones Around a Microtunnel in a Claystone Formation of the Swiss Jura Mountains. Society of Petroleum Engineers, SPE-98537-PP.

Marschall, P., Trick, T., Lanyon, G.W., Delay, J. and Shao, H. (2008). Hydro-Mechanical Evolution of Damaged Zones around a Microtunnel in a Claystone Formation of the Swiss Jura Mountains. American Rock Mechanics Association, ARMA 08-193.

Martin, C.D. and Lanyon, G.W. (2003). Measurement of In-Situ Stress in Weak Rocks at Mont Terri Rock Laboratory, Switzerland. International Journal of Rock Mechanics & Mining Sciences, 40, 1077-1088.

Mazurek, M., Pearson, F.J., Volckaert, G., and Bock, H. 2003. Features, Events and Processes Evaluation Catalogue for Argillaceous Media. ISBN 92-64-02148-5. Nuclear Energy Agency.

McGuire, W. and Gallagher, R.H. (1979). “Matrix Structural Analysis,” John Wiley & Sons, New York.

McKee, C. R., et al. (1988). "Stress-dependent permeability and porosity of coal."

McLamore, R. and Gray, K.E. (1967). The mechanical behavior of anisotropic sedimentary rocks. J Manuf Sci Eng, Trans ASME, 89(1), 62-73.

McLatchie, A., et al. (1958). "The effective compressibility of reservoir rock and its effects on permeability." Journal of Petroleum Technology 10(06): 49-51.

Meier, P., Trick, T., Blumling, P. and Volckaert, G. (2000). Self-Healing of Fractures within the EDZ at the Mont Terri Rock Laboratory: Results after One Year of Experimental Work. In: Proceedings of the International Workshop on Geomechanics, hydromechanical and Thermomechanical Behavior of deep argillaceous Rocks: Theory and Experiments, Paris, October11-12, 2000.

Metwally, Y. M. and C. H. Sondergeld (2011). "Measuring low permeabilities of gas-sands and shales using a pressure transmission technique." International Journal of Rock Mechanics and Mining Sciences 48(7): 1135-1144.

Mohiuddin, M., et al. (2000). Stress-dependent porosity and permeability of a suite of samples from Saudi Arabian sandstone and limestone reservoirs. SCA2033, 2000 Symposium of Core Analysts, Abu Dhabi, UAE.

Morrow, C. A., et al. (1984). "Permeability of fault gouge under confining pressure and shear stress." Journal of Geophysical Research: Solid Earth 89(B5): 3193-3200.

Mosser-Ruck, R. and M. Cathelineau 2004. Experimental transformation of Na, Ca-smectite under basic conditions at 150 C. Applied Clay Science 26(1): 259-273.

Mosser-Ruck, R., M. Cathelineau, A. Baronnet and A. Trouiller 1999. Hydrothermal reactivity of K-smectite at 300 C and 100 bar: dissolution-crystallization process and non-expandable dehydrated smectite formation. Clay Minerals 34(2): 275-290.

Nater P. (2012) Mont Terri / FE-Experiment Geomechanische Modellierung des Vortriebs. NAGRA AN 12-184.

Nutt, M. (2011). Used Fuel Disposition Campaign Disposal Research and Development Roadmap (FCR&D-USED-2011-000065 REV0), U.S. DOE Used Fuel Disposition Campaign.

Ochs, M., Lothenbach, B., Shibata, M. and Yui, M. (2004) Thermodynamic modeling and sensitivity analysis of porewater chemistry in compacted bentonite. Physics and Chemistry of the Earth, Parts A/B/C 29(1): 129-136.

Ohnishi Y, Kobayashi A (1996) THAMES. In O. Stephansson, L. Jing, and C.-F. Tsang, editors, Coupled Thermo-hydro-mechanical Processes of Fractured Media, Developments in Geotechnical Engineering, Elsevier, 79:545–549.

Okabe, A., Boots, B., Sugihara, K. and Chiu, S.N. (2000). Spatial tessellations: Concepts and applications of Voronoi diagrams, 2nd ed. Probability and Statistics. Wiley, NYC. 671 pages.

Olivella S., Gens A. Vapour transport in low permeability unsaturated soils with capillary effects. Transport in Porous Media 40: 219–241, 2000.

Ostensen, R. (1983). "Microcrack permeability in tight gas sandstone." Society of Petroleum Engineers Journal 23(6): 919-927.

Pacovsky, J., Svoboda, J. and Zapletal, L. (2005) Saturation development in the bentonite barrier of the mock-up CZ geotechnical experiment. Clay in Natural and Engineered Barriers for Radioactive Waste Confinement—Part 2. Physics and Chemistry of the Earth, 32(8–14). Elsevier, Amsterdam, pp. 767–779.

Pan Peng-zhi, Feng Xia-Ting, Huang Xiao-Hua, Cui Qiang, Zhou Hui (2008) Study of coupled THMC processes in crystalline rock in the EDZ using an ECPA code. Environmental Geology.

Pariseau, W.G. (2006). “Design Analysis in Rock Mechanics,” Taylor & Francis, London, UK.

Patriarche, D., Ledoux, E., Simon-Coincon, R., Michelot, J. and Cabrera, J. (2004). Characterization and Modeling of Diffusive Process for Mass Transport through the Tournemire Argillites Aveyron, France. Applied Clay Science, 26, 109-122.

Perry, F.V., Kelley, R.E., Dobson, P.F., Houseworth, J.E. 2014. Regional Geology: A GIS Database for Alternative Host Rocks and Potential Siting Guidelines (FCRD-UFD-2014-000068), U.S. DOE Used Fuel Disposition Campaign.

Pietruszczak, S. and Mroz, Z. (2001). On failure criteria for anisotropic cohesive-frictional materials. Int J Numer Anal Meth Geomech, 25, 509-524.

Pusch, R. (1992) Use of Bentonite for Isolation of Radioactive Waste Products. Clay Minerals, 27: 353-361.

Pruess, K., Oldenburg, C.M., Moridis, G. (2011) TOUGH2 User’s Guide, Version 2.1, LBNL-43134(revised), Lawrence Berkeley National Laboratory, Berkeley, California.

Pusch R. and Karnland, O. (1996) Physico/chemical stability of smectite clays, Engineering Geology 41: 73-85.

Pusch, R. and Madsen, F. t. (1995) Aspects on the illitization of the kinnekulle bentonites. Clays and Clay Minerals 43(3): 261-270.

Pusch, R., Kasbohm, J. and Thao, H. T. M. (2010) Chemical stability of montmorillonite buffer clay under repository-like conditions—A synthesis of relevant experimental data. Applied Clay Science 47(1–2): 113-119.

Pytte A. 1982. The kinetics of the smectite to illite reaction in contact metamorphic shales [M.A. Thesis]. Dartmouth College: Hanover, N.H. 78p.

Ramírez, S., J. Cuevas, R. Vigil and S. Leguey 2002. Hydrothermal alteration of “La Serrata” bentonite (Almeria, Spain) by alkaline solutions. Applied Clay Science 21(5–6): 257-269.

Rizzi, M., A. Seiphoori, A. Ferrari, D. Ceresetti, and L. Laloui. 2011. Analysis of the behaviour of the granular MX-80 bentonite in THM-processes. Lausanne: Swiss Federal Institute of Technology, Orders No 7’928 and 5’160.

Roberson, Herman E., and Richard W. Lahann. "Smectite to illite conversion rates: effects of solution chemistry." Clays and Clay Minerals 29.2 (1981): 129-135.

Rutqvist, J., Börgesson, L., Chijimatsu, M., Kobayashi, A., Nguyen, T.S., Jing, L., Noorishad, J., Tsang, C.-F. (2001a) Thermohydromechanics of partially saturated geological media – Governing equations and formulation of four finite element models. Int. J. Rock Mech. & Min. Sci. 38, 105-127.

Rutqvist J., Börgesson L., Chijimatsu M., Nguyen T. S., Jing L., Noorishad J., Tsang C.-F. (2001b) Coupled Thermo-hydro-mechanical Analysis of a Heater Test in Fractured Rock and Bentonite at Kamaishi Mine – Comparison of Field Results to Predictions of Four Finite Element Codes. Int. J. Rock Mech. & Min. Sci. 38, 129-142.

Rutqvist J. and Tsang C.-F. (2002). A study of caprock hydromechanical changes associated with CO2-injection into a brine formation. Environmental Geology, 42, 296-305.

Rutqvist, J., Wu, Y.-S., Tsang, C.-F. and Bodvarsson, G. (2002). A modeling approach for analysis of coupled multiphase fluid flow, heat transfer and deformation in fractured porous rock. International Journal of Rock Mechanics & Mining Sciences, 39, 429-442.

Rutqvist J., Chijimatsu M., Jing L., De Jonge J., Kohlmeier M., Millard A., Nguyen T.S., Rejeb A., Souley M., Sugita Y. and Tsang C.F. Numerical study of the THM effects on the near-field safety of a hypothetical nuclear waste repository – BMT1 of the DECOVALEX III project. Part 3: Effects of THM coupling in fractured rock Int. J. Rock Mech. & Min. Sci, 42, 745-755 (2005).

Rutqvist J. and Tsang C.-F. Review of SKB’s Work on Coupled THM Processes Within SR-Can: External review contribution in support of SKI’s and SSI’s review of SR-Can. Swedish Nuclear Power Inspectorate (SKI) Technical Report 2008:08 (2008).

Rutqvist J., Barr D., Birkholzer J.T., Fujisaki K., Kolditz O., Liu Q.-S., Fujita T., Wang W. and Zhang C.-Y. A comparative simulation study of coupled THM processes and their effect on fractured rock permeability around nuclear waste repositories. Environ Geol, 57, 1347–1360 (2009)

Rutqvist J. Status of the TOUGH-FLAC simulator and recent applications related to coupled fluid flow and crustal deformations. Computers & Geosciences, 37, 739–750 (2011).

Rutqvist, J., Ijiri, Y. and Yamamoto, H. (2011). Implementation of the Barcelona Basic Model into TOUGH-FLAC for simulations of the geomechanical behavior of unsaturated soils. Computers &Geosciences, 37, 751-762.

Rutqvist, J., Leung, C., Hoch, A., Wang, Y. and Wang, Z. (2013a). Linked multicontinuum and crack tensor approach for modeling of coupled geomechanics, fluid flow and transport in fractured rock. J Rock Mech Geotech Eng, 5, 18-31.

Rutqvist J., Steefel C., Chen F., Houseworth J., Vilarrasa V., Liu H.-H., Birkholzer J. THM and Reactive Transport Model Development and Evaluation: International Activities. Prepared for U.S. Department of Energy, Used Fuel Disposition Campaign, FCRD-UFD-2013-000372, Lawrence Berkeley National Laboratory (2013b).

Rutqvist, J., Zheng, L., Chen, F., Liu, H.-H. and Birkholzer, J. (2013c) Modeling of Coupled Thermo-Hydro-Mechanical Processes with Links to Geochemistry Associated with Bentonite-Backfilled Repository Tunnels in Clay Formations. Rock Mechanics and Rock Engineering: 1-20.

Rutqvist J., Zheng L., Chen F, Liu H.-H, and Birkholzer J. Modeling of Coupled Thermo-Hydro-Mechanical Processes with Links to Geochemistry Associated with Bentonite-Backfilled Repository Tunnels in Clay Formations. Rock Mechanics and Rock Engineering, 47, 167–186 (2014).

Sadhukhan, S., et al. (2012). "Porosity and permeability changes in sedimentary rocks induced by injection of reactive fluid: A simulation model." Journal of Hydrology 450–451(0): 134-139.

Sánchez, M., Gens, A., Guimarães, L. do N., Olivella, S. A double structure generalized plasticity model for expansive materials. Int. J. Numer. Anal. Meth. Geomech., 29, 751–787 (2005).

Schoch, R.B., Han, J., Renaud, P., 2008. Transport phenomena in nanofluidics. Reviews of Modern Physics 80, 840-883.

Shanley, K. W., et al. (2004). "Factors controlling prolific gas production from low-permeability sandstone reservoirs: Implications for resource assessment, prospect development, and risk analysis." AAPG Bulletin 88(8): 1083-1121.

Shi, Y. and C. Y. Wang (1986). "Pore pressure generation in sedimentary basins: overloading versus aquathermal." Journal of Geophysical Research: Solid Earth (1978–2012) 91(B2): 2153-2162.

Soeder, D. J. and P. L. Randolph (2013). "Porosity, Permeability, and Pore Structure of the Tight Mesaverde Sandstone, Piceance Basin, Colorado." SPE Formation Evaluation 2(02): 129-136.

Somerton, W. H., et al. (1975). "Effect of stress on permeability of coal." International Journal of Rock Mechanics and Mining Sciences & Geomechanics Abstracts 12(5–6): 129-145.

Sonnenthal, E. Chapter 5 in: Birkholzer, J. Rutqvist, E. Sonnenthal, and D. Barr, Long-Term Permeability/Porosity Changes in the EDZ and Near Field due to THM and THC Processes in Volcanic and Crystalline-Bentonite Systems, DECOVALEX-THMC Project Task D Final Report, 2008.

Spencer, C. W. (1989). "Review of characteristics of low-permeability gas reservoirs in western United States." AAPG Bulletin 73(5): 613-629.

Tanikawa, W. and T. Shimamoto (2009). "Comparison of Klinkenberg-corrected gas permeability and water permeability in sedimentary rocks." International Journal of Rock Mechanics and Mining Sciences 46(2): 229-238.

Thomas, R. D. and D. C. Ward (1972). "Effect of overburden pressure and water saturation on gas permeability of tight sandstone cores." Journal of Petroleum Technology 24(02): 120-124.

Tournassat, C., Appelo, C.A.J., 2011. Modelling approaches for anion-exclusion in compacted Na-bentonite. Geochimica et Cosmochimica Acta 75, 3698-3710.

Tsang, C.-F., et al. (2005). "Geohydromechanical processes in the Excavation Damaged Zone in crystalline rock, rock salt, and indurated and plastic clays—in the context of radioactive waste disposal." International Journal of Rock Mechanics and Mining Sciences 42(1): 109-125.

Tsang, C.-F., J.D. Barnichon, J.T. Birkholzer, , X.L. Li, H.H. Liu, X. Sillen, and T. Vietor. (2012). Coupled Thermo-Hydro-Mechanical Processes in the Near-Field of a High-Level Radioactive Waste Repository in Clay Formations. International Journal of Rock Mechanics and Mining Sciences 49: 31-44

Vairogs, J., et al. (1971). "Effect of rock stress on gas production from low-permeability reservoirs." Journal of Petroleum Technology 23(09): 1,161-161,167.

van Genuchten, M.T. 1980. A closed-form equation for predicting the hydraulic conductivity of unsaturated soils. Soil Science Society of America Journal 44, : 892-898.

Vietor T. (2012).Mont Terri Project - FE Experiment Modelling Kick-off Meeting. February 9, 2012, Mont Terri, Switzerland. NAGRA Technical Discussion TD-217

Vilarrasa, V., Bolster, D., Olivella, S. and Carrera, J. (2010). Coupled hydromechanical modeling of CO2 sequestration in deep saline aquifers. Int J Greenhouse Gas Control, 4, 910-919.

Villar, M.V. (2012) THM Cells for the HE-E Test: Setup and First Results; PEBS Report D2.2.7a. CIEMAT Technical Report CIEMAT/DMA/2G210/03/2012; Euratom 7th Framework Programme Project: PEBS: Madrid, Spain.

Villar, M.V., P.L. Martín, and F.J. Romero. 2014. Long-term THM tests reports: THM cells for the HE-E test: Update of results until February 2014. CIEMAT Technical Report, CIEMAT/DMA/2G210/2014.

Volckaert, G., Bernier, F., Sillen, X., Van Geet, M., Mayor, J.-C., Göbel, I., Blümling, P., Frieg, B. and Su, K. (2004). Similarities and Differences in the Behaviour of Plastic and Indurated Clays, The Sixth European Commission Conference on 'The Management and Disposal of Radioactive Waste: Euradwaste '04', held on 29-31 March 2004 in Luxembourg.

Walls, J. D., et al. (1982). "Effects of pressure and partial water saturation on gas permeability in tight sands: experimental results." Journal of Petroleum Technology 34(04): 930-936.

Walsh, J. and W. Brace (1984). "The effect of pressure on porosity and the transport properties of rock." Journal of Geophysical Research: Solid Earth (1978–2012) 89(B11): 9425-9431.

Wang W, Xie M, Nowak T, Kunz H, Shao H, Kolditz O (2006) Modeling THM coupled problem of Task D of the DECOVALEX project. Proc. GEOPROC2006 International symposium: 2nd International Conference on Coupled Thermo-hydro-mechanical-chemical processes in Geosystems and Engineering, HoHai University, Nanjing, China, May 22-25, 2006, 226–232, HoHai University.

Wang, H., A. Thiele, L. Pilon, 2013, Simulations of cyclic voltammetry for electric double layers in asymmetric electrolytes: A generalized modified Poisson-Nernst-Planck model. Journal of Physical Chemistry 117: 18286-18297.

Wang, Y. (2011). Research & Development (R&D). Plan for Used Fuel Disposition Campaign (UFDC). Natural System Evaluation and Tool Development, U.S. DOE Used Fuel Disposition Campaign.

Wei, K., et al. (1986). "Effect of Fluid Confining Pressure and Temperature on Absolute Permeabilities of Low-Permeability Sandstones." SPE Formation Evaluation 1(04): 413-423.

Wersin P., Johnson, L.H. and McKinley, I.G. (2007) Performance of the bentonite barrier at temperature beyond 100oC: A critical review, Physics and Chemistry of the Earth 32: 780-788.

Wersin, P., Curti, E. and Appelo, C.A.J., 2004. Modelling bentonite-water interactions at high solid/liquid ratios: swelling and diffuse double layer effects. Applied Clay Science 26, 249-257.

Wibberley, C. A. and T. Shimamoto (2005). "Earthquake slip weakening and asperities explained by thermal pressurization." Nature 436(7051): 689-692.

Wieczorek, K., Miehe, R. (2010): Measurement of Thermal Parameters of the HE-E Buffer Materials, Deliverable D2.2-5 of the PEBS project.

Wieczorek, K., R. Miehe, and B. Garitte. 2013. Thermal characterisation of HE-E buffer. PEBS, FP7 24968.

Witherspoon, P., et al. (1980). "Validity of cubic law for fluid flow in a deformable rock fracture." Water Resources Research 16(6): 1016-1024.

Wolery, T. J., 1993. EQ3/6, A software package for geochemical modelling of aqueous systems, Version 7.2. Lawrence Livermore National Laboratory, USA.

Wu, W.-J. and J.-J. Dong (2012). "Determining the maximum overburden along thrust faults using a porosity versus effective confining pressure curve." Tectonophysics 578(0): 63-75.

Wyble, D. (1958). "Effect of Applied Pressure on the Conductivity Porosity and Permeability of Sandstones." Journal of Petroleum Technology 10(11): 57-59.

Xu, T., Sonnenthal, E. Spycher, N., Pruess, K., 2006. TOUGHREACT, A simulation program for non-isothermal multiphase reactive geochemical transport in variably saturated geologic media. Computers and Geosciences 32, 145-165.

Xu, T., Spycher, N., Sonnenthal, E., Zhang, G., Zheng, L. and Pruess, K. (2011) TOUGHREACT Version 2.0: A simulator for subsurface reactive transport under non-isothermal multiphase flow conditions. Computers & Geosciences 37(6): 763-774.

Yale, D. P. and A. Nur (1985). Network modeling of flow storage and deformation in porous rocks. 1985 SEG Annual Meeting, Society of Exploration Geophysicists.

Zhang, K., Wu, Y.S., Bodvarsson, G.S. and Liu, H.H. (2004). Flow focusing in unsaturated fracture networks: a numerical investigation. Vadose Zone Journal, 3, 624-633.

Zhao, Y. and H.-H. Liu (2012). "An Elastic Stress–Strain Relationship for Porous Rock Under Anisotropic Stress Conditions." Rock mechanics and rock engineering 45(3): 389-399.

Zheng, L., J. Samper and L. Montenegro 2011. A coupled THC model of the FEBEX in situ test with bentonite swelling and chemical and thermal osmosis. Journal of Contaminant Hydrology 126(1–2): 45-60.

Zheng, L., Li, L., Rutqvist, J., Liu, H. and Birkholzer, J.T., (2012). Modeling Radionuclide Transport in Clays. Lawrence Berkeley National Laboratory. FCRD-URD-2012-000128

Zimmerman, R. and G. Bodvarsson (1996). "Hydraulic conductivity of rock fractures." Transport in Porous Media 23(1): 1-30.

Zhu, C., 2005. Feldspar dissolution in saturated aquifers, in situ rates. Geochimica et Cosmochimica Acta 69(6), 1435-1453.